ABSTRACT

Title of Dissertation: HIGH RESOLUTION REMOTE SENSING OBSERVATIONS OF SUMMER SEA ICE

Ellen Margaret Buckley
Doctor of Philosophy, 2022

Dissertation directed by: Associate Professor Sinéad Louise Farrell
Department of Atmospheric and Oceanic Science

During the Arctic summer melt season, the sea ice transitions from a consolidated ice pack with a highly reflective snow-covered surface to a disintegrating unconsolidated pack with melt ponds spotting the ice surface. The albedo of the Arctic decreases by up to 50%, resulting in increased absorption of solar radiation, triggering the positive sea ice albedo feedback that further enhances melting. Summer melt processes occur at a small scale and are required for melt pond parameterization in models and quantifying albedo change. Arctic-wide observations of melt features were however not available until recently.

In this work we develop original techniques for the analysis of high-resolution remote sensing observations of summer sea ice. By applying novel algorithms to data acquired from airborne and satellite sensors onboard IceBridge, Sentinel-2,

WorldView and ICESat-2, we derive a set of parameters that describe melt conditions on Arctic sea ice in summer.

We present a new, pixel-based classification scheme to identify melt features in high-resolution summer imagery. We apply the classification algorithm to IceBridge Digital Mapping System data and find a greater melt pond fraction (25%) on sea ice in the Beaufort and Chukchi Seas, a region consisting of predominantly first year ice, compared to the Central Arctic, where the melt pond fraction is 14% on predominantly multiyear ice. Expanding the study to observations acquired by the Sentinel-2 Multispectral Instrument, we track the variability in melt pond fraction and sea ice concentration with time, focusing on the anomalously warm summer of 2020.

So as to obtain a three-dimensional view of the evolution of summer melt we also exploit ICESat-2 surface elevation measurements. We develop and apply the Melt Pond Algorithm to track ponds in ICESat-2 photon cloud data and derive their depth. Pond depth measurements in conjunction with melt pond fraction and sea ice concentration provide insights into the regional patterns and temporal evolution of melt on summer sea ice. We found mean melt pond fraction increased rapidly in the beginning of the melt season, peaking at 16% on 24 June 2020, while median pond depths increased steadily from 0.4 m at the beginning of the melt season, to peaking at 0.97 m on 16 July, even as melt pond fraction had begun to decrease. Our findings may be used to improve parameterization of melt processes in models, quantify freshwater storage, and study the partitioning of under ice light.

HIGH RESOLUTION REMOTE SENSING OBSERVATIONS OF SUMMER SEA ICE

by

Ellen Margaret Buckley

Dissertation submitted to the Faculty of the Graduate School of the
University of Maryland, College Park, in partial fulfillment
of the requirements for the degree of
Doctor of Philosophy
2022

Advisory Committee:
Associate Professor Sinéad Louise Farrell, Chair
Professor James Carton
Assistant Professor Laura Duncanson
Research Assistant Professor Melinda Webster
Professor Tatiana Loboda, Dean's Representative

© Copyright by
Ellen Margaret Buckley
2022

Acknowledgements

First, I'd like to acknowledge my brilliant advisor Dr. Sinead Farrell. Sinead has not only given me the opportunity to work on the most interesting projects, but has provided me all of the tools to become a successful and productive researcher. She has ushered me into her network of sea ice scientists and remote sensing experts, encouraged me to sign up for all the relevant trainings/ workshops/ hackweeks that I wanted, meticulously edited my manuscripts and proposals, and passed along her knowledge and contagious passion for sea ice and remote sensing.

Dr. Jim Carton has been the most reliable academic advisor, offering words of encouragement and practical advice when I needed it the most. Not to mention he is also an excellent scientist with great questions and comments on my research.

I am grateful for Dr. Melinda Webster and Dr. Don Perovich, our go-to melt ponds experts, for sharing their knowledge of melt ponds with me. Both are very enthusiastic and collaborative scientists that we are lucky to have in the field. I also thank Melinda for her feedback on my research throughout my time as a graduate student, her participation on my prospectus and dissertation committee, acting as a great role model and mentor, and giving sound career advice.

I express my sincere gratitude to all of my committee: Dr. Sinead Farrell, Dr. Jim Carton, Dr. Melinda Webster, Dr. Laura Duncanson, and Dr. Tatiana Loboda for their interest in my work and time and energy spent reviewing my thesis and attending my dissertation.

I am very grateful for the ICESat-2 Science Team for including me in the regular telecons, and the in-person meetings. I've learned so much from these meetings and scientists and I am very fortunate to have had this exposure as a graduate student. I have worked with so many excellent scientists. Thank you to Dr. Ute Herzfeld for sharing her knowledge of surface tracking algorithms, and Dr. Tom Trantow and Matt Lawson for working so hard on our collaborative projects. I'm very grateful to have worked with Josh King and the team at Environment Canada. I am grateful for the opportunity to have met with and discussed my research with sea ice experts: Cecilia Bitz, Jackie Richter-Menge, Bonnie Light, Don Perovich.

I would like to acknowledge the opportunity to work alongside the researchers at the NOAA Laboratory for Satellite Altimetry. I'm grateful to John Kuhn for fixing everything computer related issue from answering simple python questions to formulating the data products we produced. Thanks to Dr. Larry Connor for helping with IceBridge data, and for the much-needed running breaks. Thanks to Kyle Duncan for answering so many questions, entertaining me during the work day, keeping the mood light, sharing code and advice, and being an all-around great coworker.

To Oliwia Baney and Reint Fischer, thanks for the comments and questions on my work and for making me a stronger scientist. I'm grateful for our River Road walks, extended happy hours, and bonfires.

A big thank you to Tammy Hendershot for supporting every graduate student emotionally and academically, and for coordinating so many things- probably more

than I even realize. Thanks to the administrative office in AOSC for all of their support and behind-the-scenes work.

I can't even begin to describe the endless love and support from my closest college and high school friends. Thanks for the inspiration, encouragement, happy hours, dog walks, girls' weekends, and so much more.

I am very fortunate to have an incredible mom, Nita Reigle who supported me throughout my time in grad school, and especially in the last month of dissertation writing. Thanks for all the carrot cookies, pep talks, and for having the best dog, Peyton. Thanks to my sister Gwen Buckley and my brother-in-law Greg Lancaster for their long-distance support, hosting great getaways, and for having the other best dog, Stella. Thank you, Billy, for your love and support, and to the cat Bee, thanks for nothing.

Table of Contents

List of Tables

List of Figures

List of Abbreviations

AMSR-2	Advanced Microwave Scanning Radiometer 2
AMSR-E	Advanced Microwave Scanning Radiometer for the Earth Observing System
APLIS	Applied Physical Laboratory Ice Station
ATLAS	Advanced Topographic Laser Altimeter System
ATM	Airborne Topographic Mapper
CAMBOT	Continuous Airborne Mapping By Optical Translator
CDR	Climate Data Record
CESM	Community Earth System Model
CMIP	Coupled Model Intercomparison Project
DDA	Density Dimension Algorithm
DMS	Digital Mapping System
DMSP	Defense Meteorological Satellite Program
ECV	Essential Climate Variable
ESA	European Space Agency
FYI	First Year Ice
GCOM-W	Global Change Observation Mission - Water
GeoTIFF	Georeferenced Tagged Image File Format
ICESat	Ice, Cloud, and land Elevation Satellite
ICESat-2	Ice, Cloud, and land Elevation Satellite - 2
ISSIC	ICESat-2 Summer Sea Ice Campaign
JAXA	Japan Aerospace Exploration Agency
MIZ	Marginal Ice Zone
MODIS	Moderate Resolution Imaging Spectroradiometer
MOSAiC	Multidisciplinary drifting Observatory for the Study of Arctic Climate
MPA	(UMD) Melt Pond Algorithm
MPF	Melt Pond Fraction
MSI	MultiSpectral Instrument
MYI	Multiyear Ice
NDWI	Normalized Difference Water Index
NIR	Near Infrared
NSIDC	National Snow and Ice Data Center
OIB	Operation IceBridge

OW	Open Water
PCF	Pond Color Fraction
PCFD	Pond Color Fraction Dark
PCFL	Pond Color Fraction Light
PCFM	Pond Color Fraction Medium
PGC	Polar Geospatial Center
RGB	Red, Green, Blue
SAR	Synthetic Aperture Radar
SHEBA	Surface Heat Budget of the Arctic
SIC	Sea Ice Concentration
SMOS	Soil Moisture and Ocean Salinity
SSMI	Special Sensor Microwave Imager
SSMIS	Special Sensor Microwave Imager and Sounder
SSMR	Scanning Multichannel Microwave Radiometer
WMO	World Meteorological Organization
WV	WorldView

Chapter 1: Introduction

This chapter gives a background on sea ice, why it is important, the observed trends, and the state of knowledge of summer Arctic sea ice. The motivation for our work and an outline for the thesis is provided at the end of the chapter.

1.1 Geographic Location of Sea Ice

Sea ice is the frozen ocean found in the polar regions. Globally, the average annual cycle of sea ice extent ranges from a minimum of 18.2 million km^2 to 26.6 million km^2 based on average monthly sea ice extents (Parkinson, 2014). Figure 1.1 shows the average month extent over the period 1979-2013 for Arctic, Antarctic and global sea ice. The amplitude of the Antarctic sea ice extent is greater than that of the Arctic sea ice, with a greater maximum extent and a smaller minimum extent. A map of sea ice concentration (SIC), defined as the percentage of the ocean covered in sea ice (see section 3.8.1), for the month of the Arctic maximum and minimum extent is shown in Figure 1.2. At its annual maximum extent, Arctic sea ice is ~ 15 million km^2 in area, an extent approximately 1.5 times the size of the entire United States. At its minimum, sea ice extent drops to ~ 3 - 5 million km^2, closer to the size of India.

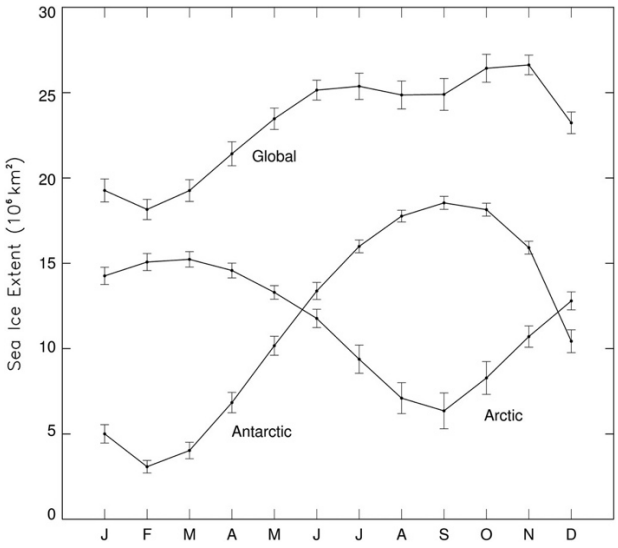

Figure 1.1. Average monthly extent for Arctic, Antarctic, and global sea ice over the period 1979–2013. Bars are plotted for one-standard-deviation of each data point. Figure from Parkinson, 2014.

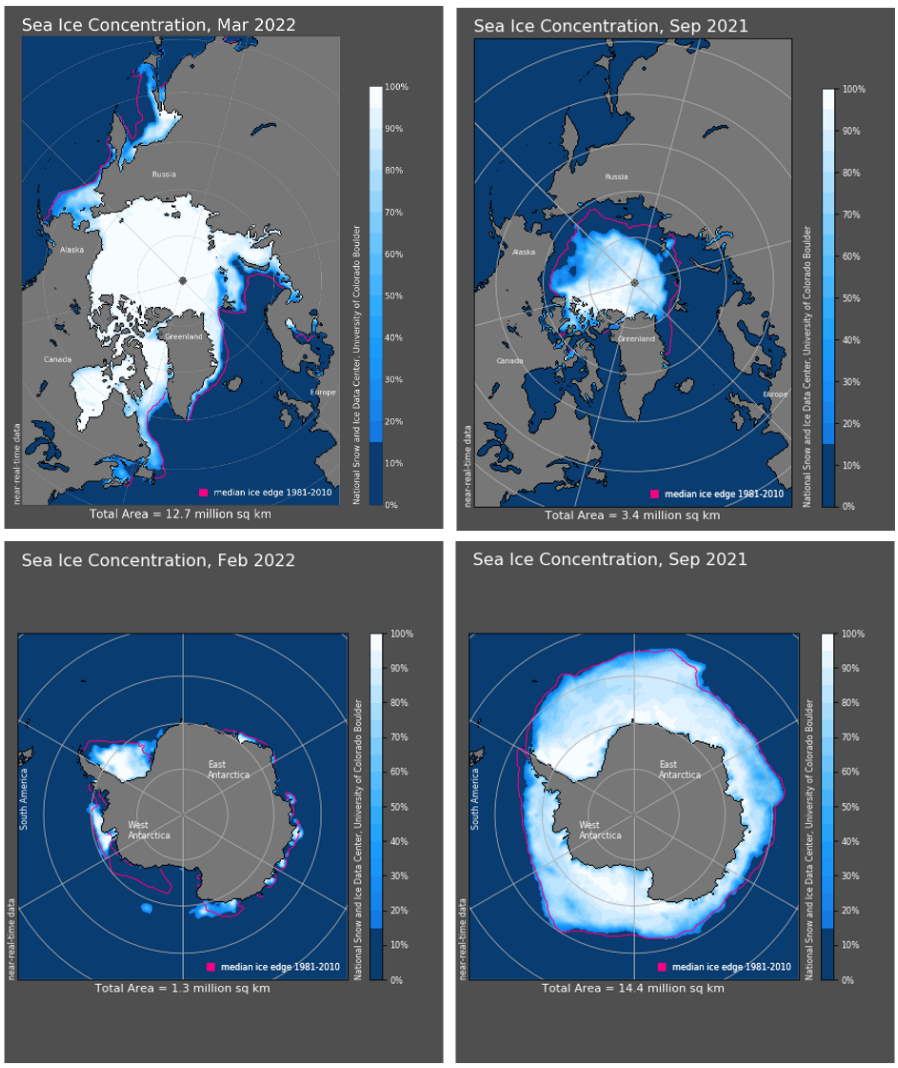

Figure 1.2. Sea ice concentration at annual minimum and maximum showing the geographic location of the ice. Top row shows Arctic SIC in the month with the maximum extent (March) and the month with the minimum extent (September). Bottom row shows Antarctic SIC in the month with the minimum extent (February) and the month with the maximum extent (September). The median ice edge from the time period 1981-2010 is shown in magenta. Figures are from NSIDC.

Figure 1.2 shows the asymmetries of the ice cover in the two polar regions, primarily related to the geography of the polar regions (Simmonds, 2015). In the Arctic, the polar region is ocean surrounded by land. The opposite is true for the South Pole; the Antarctic continent is surrounded by expansive ocean. Ice motion in the Arctic is confined by the land masses and ice often collides, deforms and thickens

(Haas, 2017). In Antarctic, the ice drift around Antarctic is divergent, resulting in opening of leads and polynyas allowing young new ice to form. Ice drifts in the Arctic for a few years on average before exist the Arctic Basin (Rampal et al., 2009). Thus, it is confined in high latitudes, mostly greater than 70° N. In contrast, with the divergence drift in the Antarctic the ice drifts towards lower latitudes and melts, resulting in minimal summer ice coverage (Figure 1.2). In the austral winter, ice in the Antarctic region extends as far north as 55° S. The land masses surrounding the Arctic Ocean contribute freshwater inflow, warm air masses, and pollution that effect the sea ice formation and melt. There is a fresh mixed layer in the Arctic that prevents mixing from warmer water beneath (Aagard et al., 1981). In the Southern Ocean such a freshwater layer does not exist and the ocean heat is transported much more efficiently. The ocean surrounding the Antarctic sea ice provides moisture for extensive snowfall and accumulation (Haas, 2017). Snow atop the sea ice insulates the sea ice and ocean below from the freezing air temperatures and slow thermodynamic ice growth. Typical snow accumulation on Antarctic sea ice can reach up to 1 m, whereas typical snow depths for Arctic sea ice is 30 cm (Blanchard-Wrigglesworth et al., 2018). Because of the lower latitudes of Antarctic sea ice and less solar radiation in the summer combined with the dry winds coming off the Antarctic shelf, the iconic melt ponds that spot the Arctic sea ice in the summer, are rarely seen on Antarctic sea ice (Andreas and Ackley, 1982). From here on, we will focus on the Arctic sea ice.

1.2 Arctic Sea Ice Processes and Properties

1.2.1 Characteristics of the Sea Ice Cover

As sea ice forms and grows, brine is retained in pockets between the ice crystals. These brine inclusions scatter light due to the contrast in refractive index (Petrich & Eicken, 2017). As the ice ages, brine drains through the ice into the ocean below, and thus older ice has lower salinity than new ice (Comiso, 2009). Sea ice is not uniform; it is subject to the forces of the ocean and experiences divergence and convergence. Figure 1.3 illustrates the convergence and divergence of sea ice. Diverging ice creates cracks that grow into leads where new ice can form and thicken. Convergence causes ice floes to collide resulting in ice fragmentation and pressure ridge formation. Heavily deformed ice floes can reach thicknesses greater than 6 meters at the location of the pressure ridges (von Albedyll et al., 2021). In the Arctic, the thickest sea ice is located along the coast of Greenland and the Canadian Archipelago. Drift patterns near the Canadian Archipelago and Greenland push ice against the coast, causing convergence and dynamic thickening (Haas, 2017).

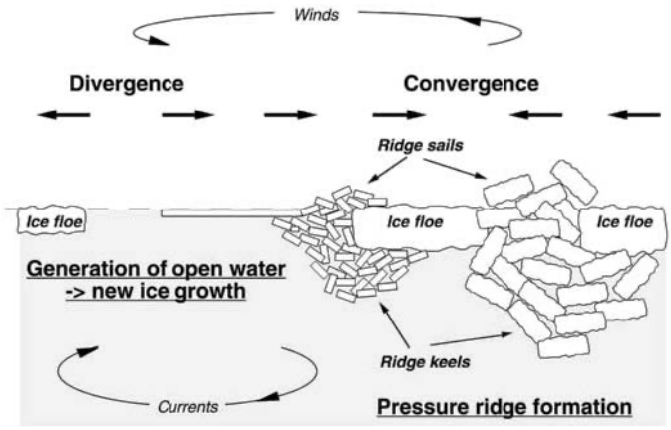

Figure 1.3. Illustration of dynamics of sea ice (convergence and divergence) that dynamically affect the distribution of sea ice thickness. Figure from Haas, 2009.

Sea ice can be divided into two age categories: first year ice and multiyear ice. First year ice (FYI) is ice of not more than a winters growth and has not yet survived a summer melt season, typically 0.30 m – 2 m thick (WMO). First year ice is mostly found at the edges of the ice pack. Multiyear ice (MYI) is defined here as ice that has survived a melt season and includes second year ice (WMO). It is typically at least 3 m thick (WMO) and tends to be less saline than first year ice. With the extra thickness it is more resilient to dynamic and thermodynamic forcings and thus is a measure of the health of the Arctic (Perovich and Richter-Menge, 2015). More examples of the differences between FYI and MYI are discussed in the next section, section 1.2.2.

Arctic sea ice reaches a maximum extent in March, then melts throughout the summer months, reaching an annual minimum extent in September (Figure 1.2). During the summer, Arctic temperatures increase to above the freezing temperature, and the snow and sea ice begin to melt. Snow meltwater drains vertically through the

ice, horizontally off the ice, or stays on the ice, pooling into low-lying areas, forming melt ponds.

1.2.2 Melt Ponds on First Year Ice and Multiyear Ice

Melt ponds manifest differently depending on the ice type on which they form. Their albedo and color depend on pond depth, ice thickness, and sub-ice algal growth (e.g., Light et al., 2015; Lu et al., 2018; Perovich et al., 1998). Pond albedo evolves throughout the melt season as ponds deepen and drain, ice porosity increases, and ponds link to the ocean and eventually refreeze (Perovich & Polashenski, 2012).

First year ice having only experienced one growth season (WMO, 1970), has low topographic relief (Petrich et al., 2012; Webster et al., 2015) and thus snow settles in a relatively homogenous layer. Melt pond area increases throughout the season because the flat topography allows for the melt ponds to expand horizontally (Grenfell and Perovich, 2004). The ability to expand on first year ice can lead to the melt out of thin ice by the end of the melt season (Fetterer and Untersteiner, 1998). The albedo of dark melt ponds typically found on first year ice (Figure 1.4a) is less than 0.2 (Figure 1.7).

The topography of multiyear ice is undulating due to a long deformation history and thus, lateral spread of melt ponds across the surface is limited (Eicken et al., 2004; Petrich et al., 2012). Instead, drainage channels form, connecting the ponds, allowing melt water to travel across the ice and pool in the lowest-lying topographic features (Figure 1.4b). Later in the summer, the melt water drains through pores that develop in the ice, resulting in a decreasing pond area (Fetterer and Untersteiner,

1998). Ponds on multiyear ice have higher albedo than ponds on first year ice due to the thickness of the underlying ice (Grenfell and Perovich, 2004). Pond albedo has been found to be ~ 0.35 on multiyear ice (Figure 1.7; Perovich, 2017).

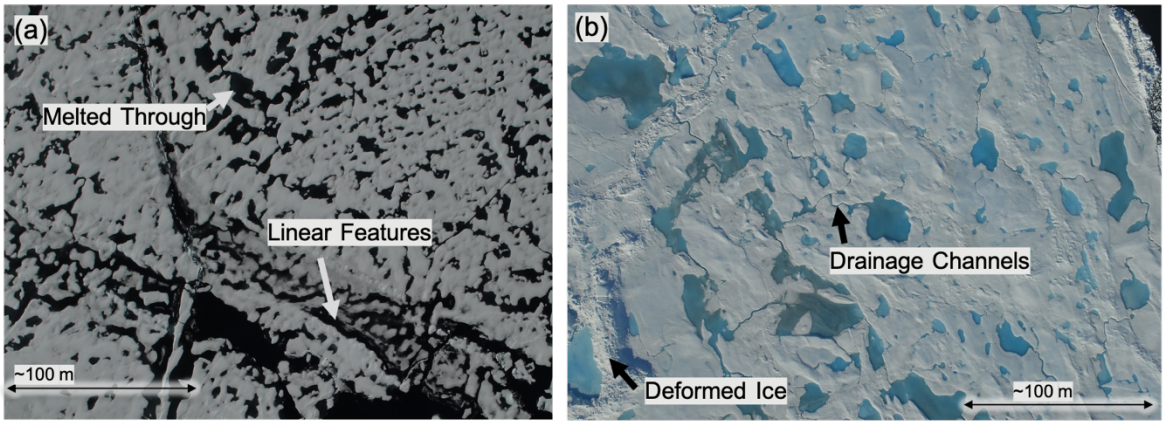

Figure 1.4. High resolution imagery of melt ponds on different ice types (a) first year ice in the Beaufort Sea on 14 July 2016, and (b) multiyear ice north of Ellesmere Island on 24 July 2017. Figure from Buckley et al., 2020a.

Webster et al. (2015) conducted a study of sea ice in the Beaufort and Chukchi seas and found maximum ponds fractions on of 53% and 38% on first year and multiyear ice, respectively. Based on the evidence of the observed strongly negative trends of multiyear ice area and extent in favor of predominantly seasonal ice (Maslanik et al., 2007; Comiso, 2012), we would expect changes in melt pond coverage and resulting ice albedo. The disparity between melt pond formation on first year and multiyear ice has implications for a changing Arctic and indicate that understanding pond formation, evolution, and impact on the climate system is not a simple task. As the ice transitions to a younger and thinner ice cover, we expect to see changes in melt pond areal fraction, albedo, depth, and volume.

1.2.3 Melt Pond Formation and Evolution

We use this section to discuss the evolution of ponds throughout the summer melt season. Figure 1.5 from Perovich and Polashenski (2012) shows the stages of ponds on first year ice (left column) and multiyear ice (second column). The photographs of multiyear ice are from the Surface Heat Budget of the Arctic (SHEBA) campaign discussed in more depth in section 1.5.1. Figure 1.6 from Webster et al., 2015 shows the observed MPF (light blue) in a study of predominantly multiyear ice (1.6a) and predominantly first year ice over the Applied Physics Laboratory Ice Station (APLIS) (1.6b). At the onset of pond formation, there is a rapid rise in pond coverage (Figure 1.6), as the snow melts and accumulates on the sea ice surface (Figure 1.5c). The spring sea ice topography prior to melt, determined by deformation, snow drifting and other mechanisms, guides the meltwater distribution on the ice surface (Fetterer & Untersteiner, 1998; Polashenski et al., 2012). Webster et al. (2022a) found that the largest and deepest ponds formed near pressure ridges at the lowest elevations measured in the April prior to melt observed during the Multidisciplinary drifting Observatory for the Study of Arctic Climate (MOSAiC), a field campaign occurring from September 2019 to October 2020 (discussed in more depth in section 1.5.1). Melt ponds are on the order of 10 m^2 in area (Perovich et al., 2002b) but can grow much larger if the conditions allow. In the next stage of pond evolution, melt water percolates through the ice (Eicken et al., 2002), and drains through horizontal channels (Figure 1.5d). The pond surface elevation reaches that of the local sea level. In this stage, the areal pond coverage decreases as ponds deepen and drain (Figure 1.6). As the summer progresses, ponds

continue to melt the underlying ice, and can completely melt through the ice exposing the open ocean (Polashenski et al., 2012; Webster et al., 2022a). At the end of the season, the ponds begin to freeze, starting with the formation of an ice lid on the surface (Figure 1.5e). Note that ponds do not go through the stages at one time; i.e., on one sea ice floe, one pond may be draining through to the ocean, while another is still accumulating volume from meltwater inflow.

Figure 1.5. Photographs showing evolution of ponds for seasonal ice (left column) and multiyear ice (right column). Seasonal ice photographs are from Barrow, Alaska and multiyear ice are from SHEBA. The sequence is: (a) cold snow, (b) melting snow, (c) initial melt pond formation, (d) melt pond evolution, and (e) fall freezeup. Figure from Perovich and Polashenski (2012).

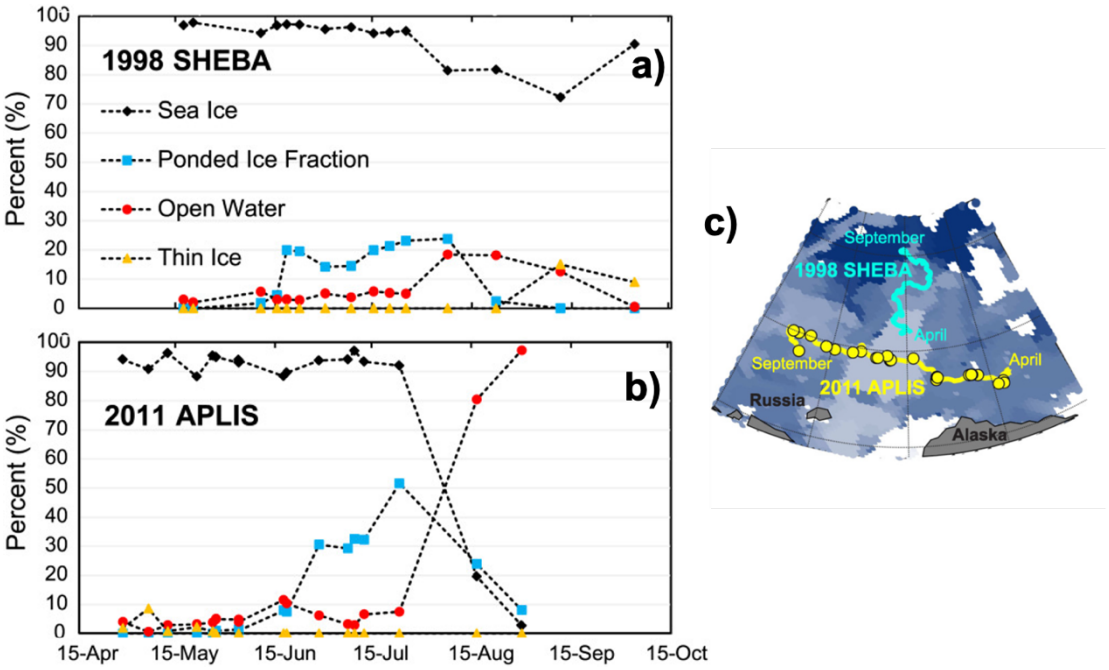

Figure 1.6. Sea ice, open water, and thin ice as a percentage of total image area from (a) the SHEBA campaign over predominantly multiyear ice (Perovich et al., 2002), and (b) over the APLIS site, predominantly first year ice. The ponded ice fraction is shown as the percentage of sea ice covered by ponds. (c) shows the locations of these studies. Figures from Webster et al., 2015.

The summer snow melt introduces a flux of freshwater to the sea ice- ocean system, whether the freshwater is stored in the ponds or drains laterally or vertically into the upper ocean. The fate of meltwater on Arctic sea ice is has not been widely studied (Perovich et al., 2021), though has a significant influence on the evolution of sea ice in the summer. Perovich et al. (2021) found that of the meltwater produced from rain, snow melt and ice bottom and lateral melt, approximately 15% was stored in ponds, equivalent to a 12 cm thick layer of meltwater below the ice. As meltwater percolates through the ice, it reduces the salinity of the ice and affects the thermal and optical properties of the ice (Perovich et al., 1998). Melt pond drainage also contributes to the surface freshwater flux, enhancing the stratification of the ocean

water column (Perovich and Maykut, 1990), and can limit under-ice algal growth, as meltwater is low in nutrients (Eicken et al., 2002). Melt pond volume increases with snow and ice melt and therefore is representative of a specific change in energy balance (Zhang et al., 2018).

1.3 Sea Ice in the Earth System

It is essential we study sea ice as it plays an important role in the Earth's system and changes in the state of the sea ice are both a cause and effect of climate change.

1.3.1 Albedo

The ice reflects sunlight and thus prevents a large portion of the incoming solar radiation from being absorbed by the Earth. Albedo, the reflectance of a surface, is an important factor in the heat budget of the earth. Figure 1.7 shows the spectral albedo of summer sea ice surfaces. The thin lines show the albedo at each wavelength and the large dot shows the spectral albedo. Surfaces with high reflectance values such as snow and ice, reflect a majority of the incoming solar radiation and reduce surface heat flux (Figure 1.7, gray, red, green, and purple thin lines). In contrast, the open ocean has one of the lowest values of albedo on Earth and absorbs a significant amount of incoming radiation (Figure 1.7 black line, Perovich, 2017). With and albedo of up to ten times greater than the surrounding open ocean, the snow-covered ice reduces the amount of solar absorption by the Earth (Curry et al. 1995).

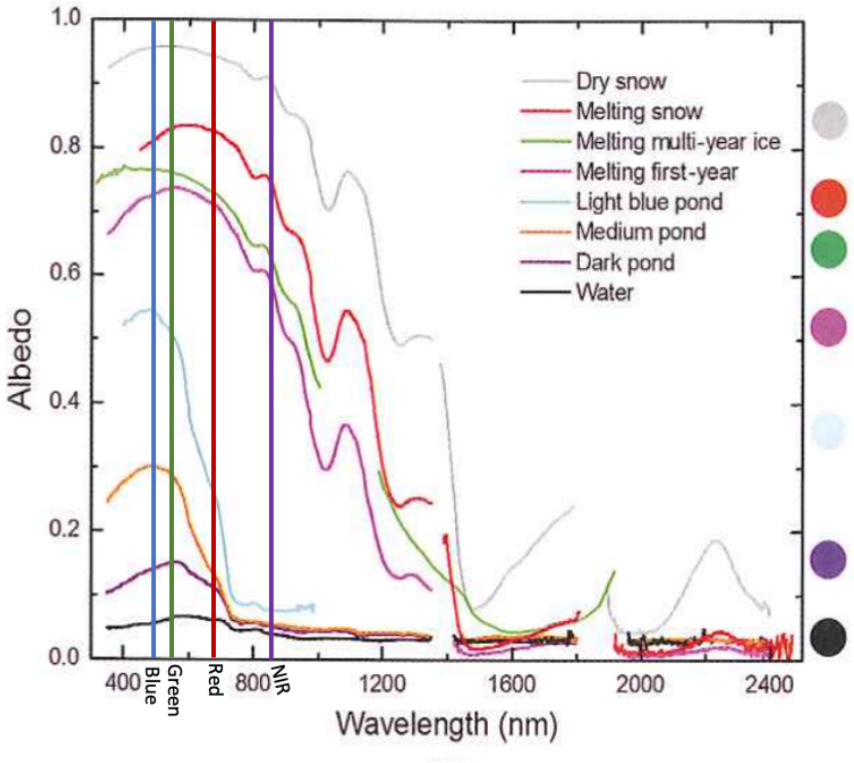

Figure 1.7. Spectral albedos for ice and water surfaces present during the summer melt season. The dots show the wavelength-integrated albedo for that surface. Vertical lines show the location of the spectral bands: blue, green, red and near infrared (Sentinel-2 A central bandwidths given for example). Figure from Perovich, 2017, annotations added.

While sea ice has an albedo of 0.8 to 0.9, melt ponds have a much lower albedo around 0.3-0.6 (Figure 1.7, Rösel et al, 2012; Perovich, 2017). Formation of melt ponds and areas of lower albedo results in more surface absorption and heat uptake, and thus more localized melting (Perovich, 2002; Perovich and Polashenski, 2012). Melt pond formation and increased absorption of heat reinforce one another and creates a positive feedback (Perovich et al, 2002). Figure 1.8 from Perovich and Polashenski (2012) shows the albedo evolution over the summer and the relationship between albedo and the timing of melt pond processes for seasonal (first year ice) and multiyear ice.

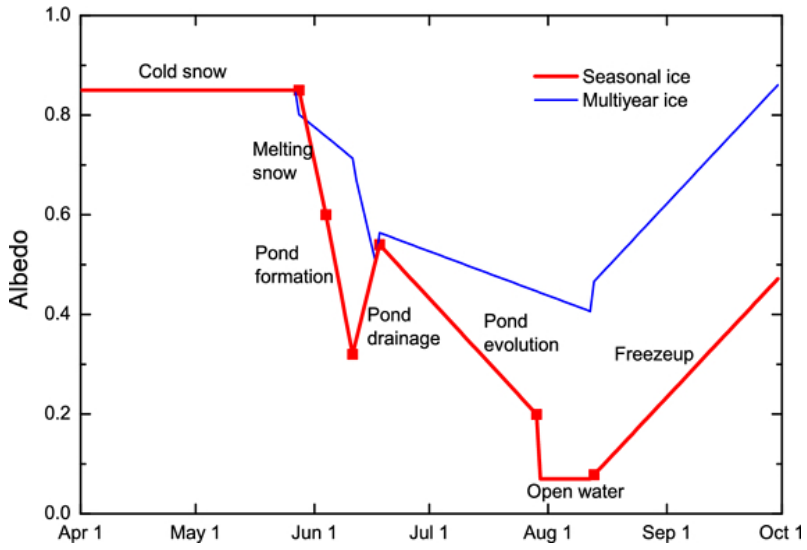

Figure 1.8. Time series of the evolution of albedo corresponding to melt phases for first year (red) and multiyear (blue) ice. Figure from Perovich and Polashenski, 2012.

Prior to melt, the snow-covered sea ice has a high albedo (>0.8). Figure 1.8 shows a sharp drop in the albedo with the onset of melt as snow melt water spread across the surface. The decrease in albedo in the first-year ice is more significant than multiyear ice as the deformations on multiyear ice limit the spread of meltwater (Perovich and Polashenski, 2012) (Figure 1.8). A drainage event reduces the MPF and the albedo increases. Then the albedo decreases as ponds continue to melt. In the case of the first year ice in Figure 1.8, ponds melt through the ice and the open ocean is exposed, reducing the albedo to those of open water. When freeze-up commences, the albedo slowly increases as the new ice thickens and fresh snow falls on the ice (Perovich and Polashenski, 2012).

1.3.2 Heat and Moisture Flux

The frozen ocean acts as a barrier between the ocean and the atmosphere by limiting and controlling interactions between the ocean and the atmosphere. When sea ice is not present, the ocean is a source of moisture for the lower atmosphere. Evaporation over open water can be tens of times greater than that over sea ice (Launiainen and Vihma, 1994). The formation of clouds causes a release of heat, warming the air. Low-level clouds can trap outgoing radiation resulting in a higher net radiance compared to a cloudless scenario (Boisvert et al, 2013). Melt ponds alter ocean-atmosphere heat fluxes in summer, providing an additional source of moisture to the atmosphere (Boisvert et al., 2013).

The sea ice cover also controls heat flux. Not only does the presence of ice reduce the absorption of incoming solar radiation (section 1.3.1), it reduces the turbulent heat fluxes. The heat flux over the open ocean is two orders of magnitude greater than that over the sea ice (Smith et al., 1990). It has been shown that sea ice extent is negatively correlated with heat flux in autumn and early winter (Vihma, 2014). With more heat and moisture available to the atmosphere, a continuous cloud cover is present over much of the Arctic during the summer months (Eastman and Warren, 2010).

1.3.3 Thermohaline Circulation

The presence of sea ice in the Arctic is also an important factor in the thermohaline circulation. When the ocean freezes, salt is rejected from the ice crystals and brine pockets form in the structure (Aagaard and Carmack, 1989). As the brine is

expelled, the salty dense water sinks (Cottier et al., 2017). This creates a large stratification between fresh melted sea ice at the surface and the salty dense water at lower depths, known as North Atlantic Deep Water. This downwelling initiates the thermohaline circulation- the conveyor belt circulation that transports heat in the warm surface waters near the equator poleward (Clark et al., 2002). The strong density gradient limits mixing, preventing ocean heat flux, and ultimately protecting the sea ice cover from the warmer waters below (Cottier et al., 2017).

1.3.4 Ecosystem

The sea ice is a unique ecosystem providing habitat for marine animal and biological activity. Algal communities utilize sea ice to remain and grow in the upper ocean where sunlight and nutrients are plentiful (Arrigo, 2017). Algae is the base of the food web for Arctic marine life, sustaining life through the winter months when other food sources are lacking (Arrigo, 2017). Melt ponds that form on the ice regulate this light available under the ice for photosynthesis. Light et al. (2015) found that ponded first year ice transmits or absorbs more than three-quarters of incoming solar radiation, whereas, unponded, bare ice reflects more than three-quarters of solar radiation. The light transmitted through heavily ponded sea ice is enough to support the growth of under-ice phytoplankton blooms (Arrigo et al., 2012). Sea ice also provides a hunting ground for Arctic mammals such as seals, whales, walruses and polar bears (Laidre and Regehr, 2017). These marine mammals are particularly vulnerable to changes in the climate because of their reliance on the state of the sea ice (Laidre et al., 2015) (see trends in Arctic sea ice in section 1.5).

1.3.5 Socioeconomics

Sea ice also has a socio-economic impact. The extent of the ice determines the ability for naval operations and navigation. The presence of sea ice impedes navigation of commercial shipping vessels, and routes across the Arctic are usually limited to summer months when the sea ice is thinner and less extensive (Zhang et al., 2019). Arctic communities rely on the ice for everyday activities. Sea ice that is fastened to the land (shorefast or landfast ice) is a platform for transportation for travel to and from hunting sites (Dammann et al., 2018). The ice may also be used for the construction of ice roads for transportation to and from resource extraction industries (Dammann et al., 2018). Coastal sea ice protects the shores from erosion and in its absence, coastal communities may be affected by enhanced erosion (Eicken et al., 2009). Monitoring sea ice conditions and understanding sea ice trends is essential for the native Arctic communities (Huntington et al., 2017).

1.4 Arctic Sea Ice Trends

1.4.1 Sea Ice Essential Climate Variables

Climate research relies on long term monitoring of the Earth's systems. The Global Observing Climate System, set up under the United Nations developed the concept of Essential Climate Variables (ECV) (Bojinski et al., 2014). An ECV is defined as 'a physical, chemical or biological variable or group of linked variables that critically contributes to the characterization of Earth's climate.' Each ECV is able to be observed or derived with established methods. These variables fall into one of the following categories: land, ocean, atmosphere. Falling within the ocean sphere,

the sea ice related variables are concentration, extent/edge, thickness and drift. Monitoring ECVs is required to understand the evolution of Earth's climate, and predict future conditions to assess risk and guide mitigation (Bojinski et al., 2014). Throughout the rest of this section, we discuss trends in Arctic sea ice change that are pertinent to the work presented in this thesis.

1.4.2 Extent and Area

Satellite passive microwave observations of Arctic sea ice extent reveal a negative trend in every month for the time period 1979-2012 (Stroeve et al., 2012). Summer sea ice extent has been decreasing at a rate of 12.7% per decade relative to the 1981-2010 average (Meier et al., 2021). In March, at the sea ice maximum, the trend in the annual maximum is -2.7% per decade, a smaller rate of decline than in summer (Meier et al., 2021). There is evidence that the rate of September sea ice loss is accelerating and Comiso et al. (2008) has split the trend line into two periods: prior to 2007 and from 2007 onward, as we have done in Figure 1.9. The first period (1978-1996) has a trend of -4.8% per decade, the second period (1997-2021) shows a trend of -14.9% per decade.

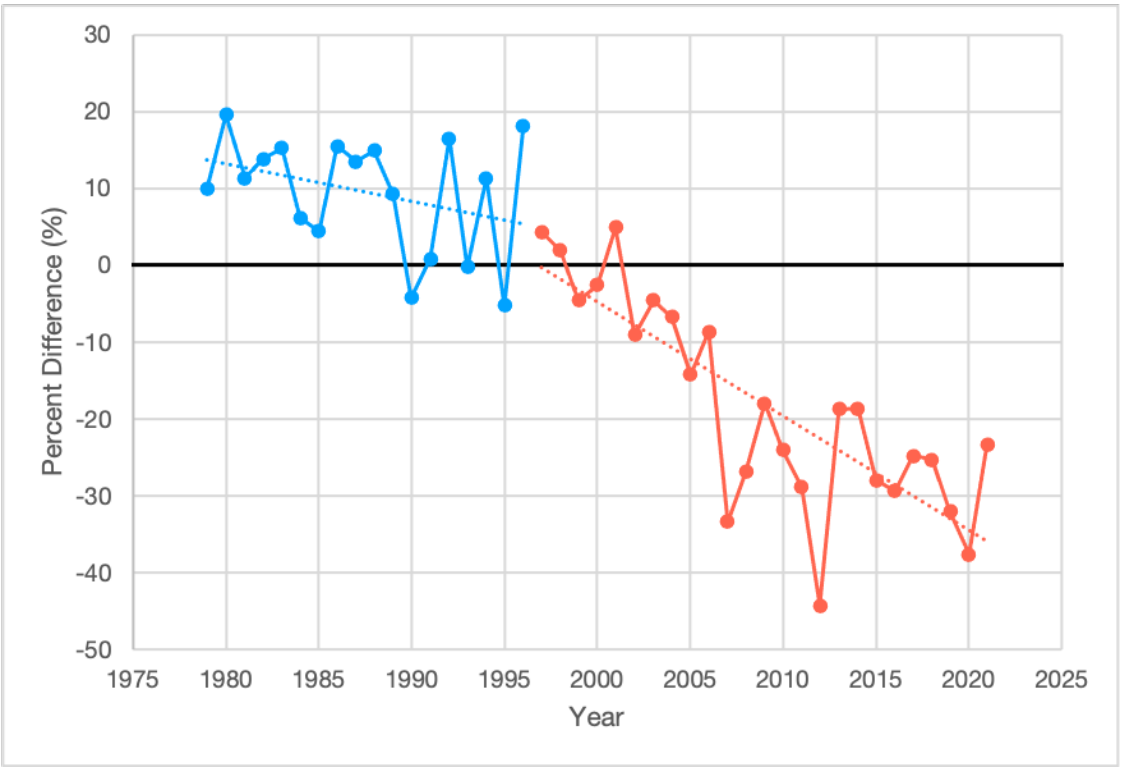

Figure 1.9. Monthly September sea ice extent anomalies from 1979 to 2021. Anomalies are relative to the 1981 to 2010 average. Data from Fetterer et al., 2017.

Models can be used to predict the future of sea ice given different climate change scenarios. Figure 1.10 shows the predictions of September sea ice area with three different emission scenarios for all available Coupled Model Intercomparison Project (CMIP6) models. Although the multimodel ensemble mean captures the trend in observations, there is a large spread in predictions of when the Arctic will see an ice-free summer (Notz and Community, 2020). These discrepancies suggest that some summer sea ice processes are not well understood or represented in models (Flocco et al. 2012). Sea ice models continue to evolve as higher order processes are incorporated (Hunke et al., 2010).

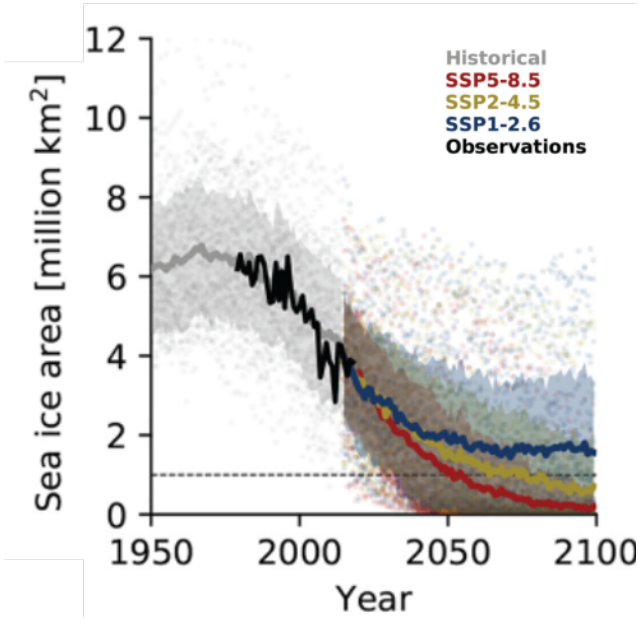

Figure 1.10. Evolution of September sea ice area from three emission scenarios. Thick lines show the multimodel ensemble mean, shading indicates one standard deviation, and the dots correspond to the first ensemble member of each model. From Notz and Community, 2020.

Although this thesis is focused on Arctic sea ice, it is important to note the trends of Antarctic sea ice here. Over the same 43-year record, Antarctic sea ice has seen a positive trend in average annual sea ice extent, however since the record high ice extent in 2014 in the Antarctic, there has been a steep decline in sea ice extent. (Parkinson et al., 2019).

1.4.3 Age, Thickness, and Volume

The negative trends in Arctic sea ice extent are accompanied by a transition to a predominantly younger (Comiso, 2012), and thinner (Kwok and Rothrock, 2009; Laxon et al., 2013) ice cover. The sea ice cover of the Arctic Ocean comprised ~55% first year ice in 1985, which has increased to ~77% in 2018 (Perovich et al., 2018). This extreme trend suggests an overall decline in mean thickness and volume of the

Arctic sea ice and a more vulnerable ice pack (Comiso, 2012). Figure 1.11 shows the interannual variability in the mean winter and fall ice thickness. Kwok and Rothrock (2009), found a decrease in mean winter sea ice thickness of 1.75 m from 3.64 m in 1980 to 1.89 m in 2008. The mean winter thickness from the CryoSat record was 2.22 m in 2018. Other studies confirm this, and show that the total sea ice volume is also trending downward. Laxon et al. (2013) shows a decrease in both winter and autumn ice volume from the 2003-2012 satellite record. ICESat-2 extends these records and Kacimi and Kwok (2022) report an Arctic sea ice volume loss of 251 (414) km^3 per year in winter (fall).

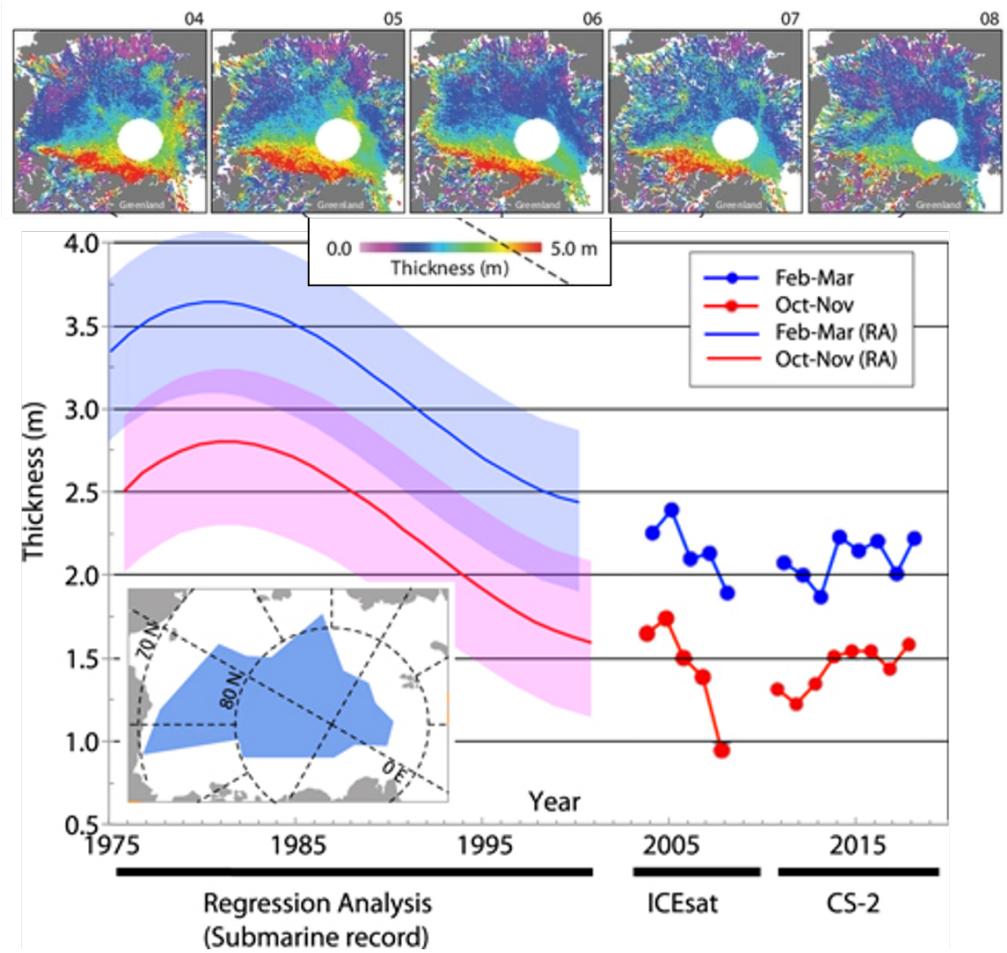

Figure 1.11. Mean fall and winter ice thickness from a regression analysis of submarine records, ICESat, and CryoSat-2. Maps at the top show the thickness distribution from the five years of ICESat measurements. Figures from Kwok (2018) and Kwok and Sulsky (2010).

1.4.4 Melt Season Length

Markus et al. (2009) shows an earlier melt onset and a later freeze up of the Arctic sea ice. In the Arctic as a whole, the melt season increased by 20 days over the period 1979 - 2009. In some areas of the Arctic, the melt season is increasing by as much a 10 days per decade. Stroeve et al. (2014) extends this study and confirms the increase in the length of the melt season, showing an increase in the Arctic wide melt season length at a rate of 5 days per decade. The earlier dates of melt onset results in an increase of solar input to the Arctic ice-ocean system (Perovich et al., 2007). Further, Laxon et al. (2003) shows that the average winter thickness is correlated to the length of the summer melt season.

1.5 Knowledge of Melt Ponds on Sea Ice

In this section we discuss our current state of knowledge of the melt ponds that form on summer Arctic sea ice. In situ, aircraft and satellite measurements of the ice are necessary to gain a full understanding of the melting surface. All have benefits and drawbacks, but are necessary to piece together the processes and mechanisms that contribute to the sea ice melt.

1.5.1 In Situ Observations

The majority of our understanding of melt ponds is derived from in situ field studies, particularly the Surface Heat Budget of the Arctic Ocean (SHEBA) program,

a drifting ice camp in the Beaufort Sea from October 1997 to October 1998 (Uttal et al., 2002). SHEBA measurements of both first year and multiyear ice, advanced the understanding of melt pond albedo, fraction, size distribution (Perovich et al., 2002) and meltwater transport (Eicken et al., 2002), and provided input for MPF and melt pond depth parameterization in modeling efforts (e.g., Curry et al., 2001).

The Multidisciplinary drifting Observatory for the Study of Arctic Climate (MOSAiC) was a yearlong ship-based expedition from September 2019 to October 2020 to measure sea ice, ocean, and atmosphere conditions as the ship drifted with the sea ice through the Central Arctic and out the Fram Strait. The goal of MOSAiC was to develop a better understanding of the processes that have contributed to the observed changes of sea ice extent and type. MOSAiC observations included a central observatory on the ship, a regional network around the ship, and coordinated observational activities with other remote sensing studies. Webster et al. (2022a), synthesizes MOSAiC melt pond observations with sea ice modeling results, setting the groundwork for improving representation of summer sea ice processes and interactions in climate models.

1.5.2 Airborne Observations

Aircraft based studies provide observations over a larger region than in situ studies can be used to scale up field campaigns and tie together observations from in situ data and satellite data. A benefit of airborne campaigns is that aircrafts have the ability to selectively maneuver around or below clouds to collect unobscured data. Similar instruments can be found on aircraft studies and satellite studies so the

aircraft instrument can be used to validate its' satellite counterpart. For example, the Operation IceBridge (OIB) Campaign was used to tie together observations from satellites the Ice, Cloud, and land Elevation Satellite (ICESat) and the Ice, Cloud, and land Elevation Satellite 2 (ICESat-2). A brief summary of the OIB campaign and description of the OIB data used in this work is provided in Chapter 2.2.

Previous studies have demonstrated the ability to extract sea ice melt pond parameters from airborne studies but most are limited in spatial extent and temporal evolution (Buckley et al., 2020a). For example, Miao et al. (2015) classified images collected in the Arctic Pacific sector in one summer (2010) only, while Perovich et al. (2002) and Tschudi et al. (2001) analyzed aerial imagery collected during the 1998 SHEBA campaign. Wright and Polashenski (2018) demonstrated a classification algorithm using 66 images collected in the Beaufort and Chukchi Seas region in 2009, 2014, and 2016. This work was further expanded to imagery collected from 87 OIB flights from 2010 to 2018 (Wright et al., 2020).

Airborne imagery has also been used to validate studies of melt pond fraction from the lower resolution satellite observations discussed in Section 1.5.3. Tschudi et al. (2008) used an unmanned aerial vehicle to capture high resolution imagery. They then classified this imagery and compared the melt pond fraction derived from the aerial imagery to that from the Moderate Resolution Imaging Spectroradiometer (MODIS) satellite imagery. Airborne imagery can also be used to understand the evolution surface conditions at a wider scale over fields sites as in Polashenski et al., 2012.

1.5.3 Satellite Observations

Satellite observations provide surface measurements over a larger area and time period as compared to airborne and field campaigns. Polar orbiting satellites collect data in the visible, infrared and microwave ranges of the electromagnetic spectrum. Active and passive sensors emitting and receiving at these wavelengths measure different aspects of sea ice (See Chapter 2 for more details on techniques of remote sensing). A benefit of satellite measurements, is the ability to provide a long-term record. For example, the NASA melt onset product derived from passive microwave data, has allowed for the quantification of the positive trend of melt season over the satellite record from 1979 to present (Markus et al., 2009).

Altimeters measure the height of the Earth's surface and since the launch of the European Remote Sensing satellite (ERS) in 1991, we have been able to measure sea ice height over large regions (e.g., Laxon et al., 2003). However, until recently, satellite altimetry measurements were not suitable for providing information on individual ponds as footprints were too large, or the along track repetition was not suitable (Farrell et al., 2011, 2020). The high resolution of ICESat-2, described in more detail in Chapter 2, section 2.6.3, allows us to examine the small-scale melt features on the summer sea ice.

Similarly, satellite imagery provides greater coverage than airborne studies, but often sacrifices resolution. Since melt ponds are less than 1 meter at melt onset (Perovich et al., 2002) and expand in area with melt, high-resolution imagery is required to resolve their geophysical features and evolution. Fetterer and Untersteiner

(1998) classified high resolution National Technical Means (NTM) satellite imagery and airborne Arctic Ice Dynamics Joint Experiment (AIDJEX) photographs to understand evolution of areal melt pond coverage throughout the summers of 1993,1994, and 1995. They combined these observations with surface air temperature from drifting buoy data and passive microwave data to understand the timing of pond formation relative to the air temperatures and the emissivity measured by passive microwave radiometers. This study emphasizes the need for continued studies of melt ponds on Arctic sea ice in order to model albedo as an internal variable in sea ice models. High resolution (<5 m) commercial imagery such as the NTM can resolve melt features, but is not easily accessible, and not available on a large scale. The Copernicus Sentinel-2 imagery (described in Chapter 2.4.2) provides 10-meter resolution imagery, which can resolve melt features on the sea ice.

Although lower resolution satellite imagery does not resolve individual melt ponds, they can provide information about the MPF, and overall changes in surface albedo during the summer melt period. The Moderate Resolution Imaging Spectrometer (Rösel et al., 2012; Rösel & Kaleschke 2011; Tschudi et al., 2008), Medium Resolution Imaging Spectrometer (Istomina et al., 2015; Zege et al., 2015), Landsat 7 Enhanced Thematic Mapper (Markus et al., 2002, 2003), and Environmental Satellite synthetic aperture radar imagery (Mäkynen et al., 2014), have all proven useful for studying melt ponds. There are additional errors associated with lower resolution, and products derived from satellite imagery may not provide the detail necessary for model parameterization or albedo calculation.

1.5.4 Obstacles to Observing Summer Sea Ice

Although measurements of summer sea ice have provided us with a wealth of knowledge, there are significant limitations to the observational methods. Due to the expanse of the Arctic and the difficulty of working in the extreme environment, field studies are spatially and temporally limited (Cohen et al., 2018). In situ observations on ice can be dangerous with unknown ice thicknesses and melt locations. Studies are limited to small areas over relatively short time frames.

Remote sensing from satellites or aircraft sensors can measure large-scale aspects of the Arctic without the danger of field surveys. However, remote sensing observations also have their drawbacks. Cloud cover is higher than average in the summer in the Arctic (Curry et al., 1996), and can obstruct satellite and airborne campaigns.

Clouds and bad weather often postpone planned survey flights and even on clear days, low lying clouds can contaminate the data retrieved from an airborne platform. Satellites do not have the ability to maneuver around weather systems and avoid cloudy regions. Therefore, satellite sensors that are not able to penetrate the cloud cover are extremely limited in summer. It is a challenge to create an accurate cloud mask in polar regions because both clouds and snow/ice have a strong reflectance and sometimes are nearly indistinguishable (Rösel et al, 2012). Another inherent difficulty is varying light conditions. Reflectance of the surface is highly dependent on solar zenith angle, cloud cover, season, and sensor angle and height (Miao et al, 2015). A melt pond may look very different depending on these factors

and therefore it is difficult to create a classification algorithm that takes all these factors into account.

Further, melt ponds are difficult to resolve from satellite data. With lower resolution and larger pixels, a single pixel may contain multiple surfaces such as ice and pond, which when classifying imagery, may easily be misclassified as an ice pixel. In other summer sea ice imagery such as radar and laser altimetry, passive and active microwave measurements, melt ponds are difficult to distinguish from open water, as they have similar radiometric properties

Aircraft-based studies may be used to validate the satellite observations. Validation flights are aligned in time and space in order to minimize the lag between aircraft observations and satellite observations. This is challenging to plan and observed data must be drift corrected to align properly. In the summer unconsolidated sea ice is common, and freely drifts with the wind and ocean currents. Errors are introduced during the drift correction due to uncertainties in drift magnitude, direction and variance.

Satellite observations cover large areas but have low spatial and temporal resolution. For example, a satellite with a 90-day orbit repeat period would not be able to capture the evolution of a single melt pond. In contrast, images from aircrafts have much higher resolution but cannot cover the extent that satellites do. Both methods of retrieving aerial imaging require a tremendous amount of data processing to correct for cloud cover, receiver saturation, timing, pitch and roll, and more.

1.5.5 Melt Ponds in Sea Ice Models

Melt ponds are typically represented in global climate models through adjustment of the overall sea ice albedo in the summer months (Hunke et al., 2010). However, this does not account for variability in melt ponds with respect to regional ice type and sea ice topography, nor the observed range in melt pond albedo (Flocco et al., 2012), and an improved treatment of summer melt processes is required (Lüthje et al., 2006; Skyllingstad et al., 2009). Ebert and Curry (1993) introduced melt pond parameterization into sea ice models, incorporating the energy balance of ponds at variable depths and surface fractions. Recent advances in parametrizing melt ponds have improved their representation in sea ice models (e.g., Flocco et al., 2010, 2012; Schröder et al., 2014) and in coupled ice-ocean models (e.g., Zhang et al., 2018). It has been shown that sea ice model predictions are sensitive to melt ponds inclusion (Flocco et al., 2010; Flocco et al., 2012; Tsamados et al., 2015), and inclusion of ponds in models reduces the surface albedo and enhances the ice-albedo feedback (Holland et al., 2012). Figure 1.12 shows the findings from Holland et al. (2012) where they found simulations with aerosol deposition and melt ponds reduce ice area and thickness compared to simulations those with just aerosol deposition. Flocco et al. found 13% lower minimum ice extent and 40% lower ice volume in simulations with melt ponds compared to those without ponds (Flocco et al., 2012). Schröder et al. (2014) also showed that MPF can be used to predict summer minimum extent. Rösel et al. (2012) found that early melt pond formation may contribute to the decline of September sea ice minimum extent. Incorporating melt pond formation and evolution processes in numerical models has a significant effect on the predicted sea

ice thickness and extent (Flocco et al., 2010). Sea ice modeling is essential to help us understand interactions between processes contributing to the rapid sea ice loss.

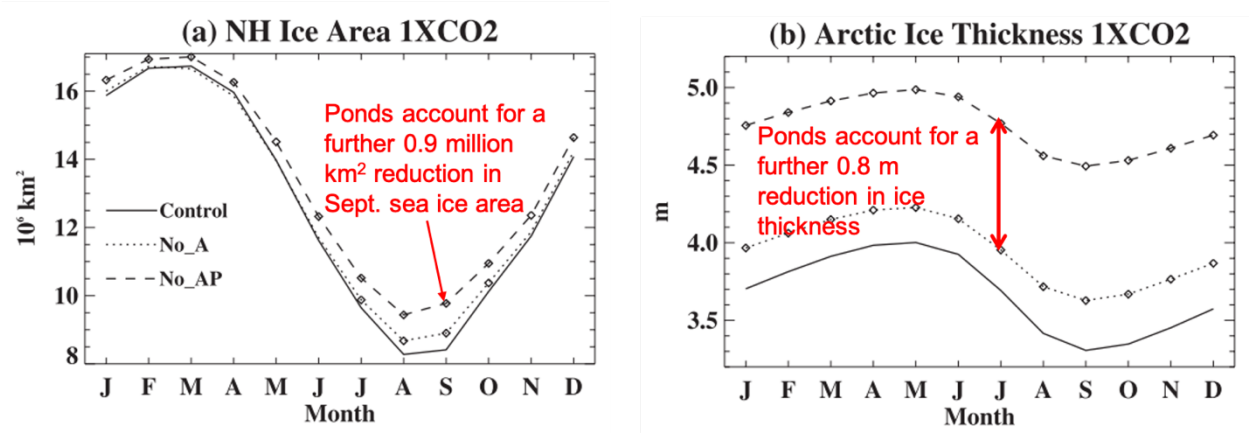

Figure 1.12. Annual cycle of Arctic sea ice area (a) and ice thickness (b) for the control simulation, the simulation that excludes aerosols, and the simulation that excludes ponds and aerosols. Figure from Holland et al., 2012, annotations added.

1.6 Dissertation Motivation and Goals

Previous work has demonstrated the potential to extract sea ice melt pond parameters from airborne and satellite imagery (Fetterer and Untersteiner, 1998; Markus et al., 2003; Tschudi et al., 2008; Rösel et al., 2012; Webster et al., 2015). However, this work was limited by both the resolution and aerial coverage of the observations. Some studies were limited to small regions of the Arctic (Miao et al., 2015), while others are limited by low pixel resolution (30m-250m) of the imagery (Markus et al., 2003; Tschudi et al., 2008). There are many studies estimating melt pond area or areal fraction, but information of melt pond depth and volume is lacking. Because of these limitations, gaps remain in our knowledge of melt pond characteristics at an Arctic-wide level.

Given the importance of Arctic sea ice in the climate system, paired with the downward trends in sea ice extent and thickness, we are motivated to better understand the summer sea ice evolution and fill in the knowledge gap of melt pond properties and processes. The observations from the OIB summer campaigns allow us to derive melt parameters and compare regional patterns. New satellite remote sensing observations from Sentinel-2 and ICESat-2 allow us to scale up the observations of melt features and monitor the evolution throughout the melt season. The work presented in this dissertation thesis will aim to:

- Develop techniques for deriving melt parameters from new high resolution remote sensing imagery and altimetry
- Understand MPF on multiyear and first year ice types
- Consider the evolution of melt through the summer season, and asses the timing and relationships between these parameters
- Produce novel data products describing the summer sea ice to help inform new scientific studies of melt season processes.

This thesis is organized as follows:

- Chapter 2 describes the remote sensing techniques and datasets used in this work: high resolution imagery, passive microwave radiometry, and laser altimetry.
- Chapter 3 describes the methods used for classification of sea ice imagery during summer melt. We describe the algorithm used for the classification of

IceBridge Digital Mapping System imagery and the modifications required to apply this algorithm to Sentinel-2 and WorldView imagery.

- Chapter 4 provides results from the classification of high resolution IceBridge summer imagery. This section includes comparisons with lower resolution existing datasets.
- Chapter 5 describes the altimetric observations of sea ice and methods for sea ice surface retracking and retrieving melt pond depth.
- Chapter 6 provides results of pond depth and pond fraction derived throughout the 2020 summer melt season in the multiyear ice region. We discuss temporal evolution of melt pond characteristics.
- Chapter 7 offers conclusions of the dissertation work and describes the impact of the work, as well as proposed future work.

Chapter 2: Techniques for Remote Sensing of Sea Ice

2.1 Motivation and Goals

In Chapter 1, we presented an overview of sea ice, describing the importance of sea ice in the climate system, the properties and processes of Arctic sea ice, and an overview of the observations of summer sea ice. We described the knowledge gap of large-scale observations of summer Arctic sea ice. In Chapter 2, we present the remote sensing techniques and newly available airborne and satellite datasets, that we use to fill this critical knowledge gap in our understanding of summer sea ice. This chapter is not an attempt to describe all available methods of remote sensing of sea ice. Instead, we summarize the pertinent techniques and describe the datasets used in the work presented in this thesis. The novelty of our study is its use of high-resolution remote sensing observations to improve understanding of small-scale processes driving sea ice melt and to better characterize sea ice conditions during the summer. We do however also employ lower-resolution datasets for the purposes of comparison and for setting the scene across a regional scale.

The goals of this chapter are as follows:

- summarize the techniques used to acquire the remote sensing observations utilized in the work presented in this thesis.
- Detail the specifications of the datasets used in our work.

The chapter begins by describing the methods for remote sensing of sea ice and the differences between passive and active sensing (section 2.2). Section 2.3 details the

Operation IceBridge campaign and describes the campaign's spatial and temporal span, major accomplishments, and contribution to our knowledge of sea ice. The following sections focus on the techniques used to produce the datasets used in this study, and the description of those datasets: high resolution imagery (section 2.4), passive microwave radiation (section 2.5), and laser altimetry (section 2.6). Chapter conclusions are offered in Section 2.7.

2.2 Passive and Active Remote Sensing

Passive and active remote sensors operate in the visible, infrared and microwave channels of the electromagnetic spectrum, giving us multiple looks of the ice surface. Figure 2.1 shows the electromagnetic spectrum indicating the wavelengths that these sensors observe. Passive remote sensing relies on energy that is either emitted from Earth or energy that originates in space and reflects off Earth's surface (i.e., solar illumination) (Shuchman and Onstott, 1990). Observations obtained from passive remote sensing that are used for the work described in this thesis include visual and infrared imagery and passive microwave radiometry. Active remote sensing instruments provide their own illumination of the Earth's surface and include altimeters, scatterometers, and synthetic aperture radars (SARs) (Shuchman and Onstott, 1990). The primary active remote sensing instruments used for the studies described in this thesis are laser altimeters. In this section we describe the fundamentals of the acquisition of these datasets.

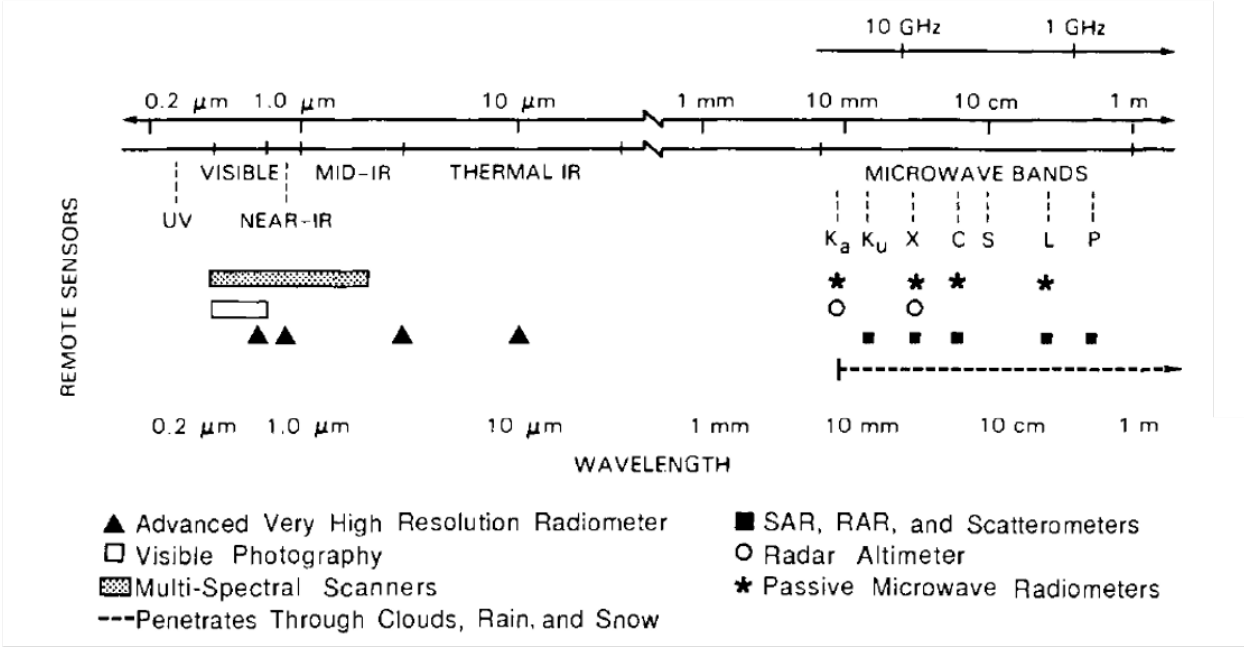

Figure 2.1. The electromagnetic spectrum. Location of the visible, infrared, and microwave ranges are noted. Figure from Shuchman and Onstott, 1990.

Combining altimetry, passive microwave radiometry, and imagery datasets allows for a deeper, three-dimensional understanding of the summer Arctic sea ice. Figure 2.2 illustrates the primary satellite and airborne sensors that collected the data used in this work.

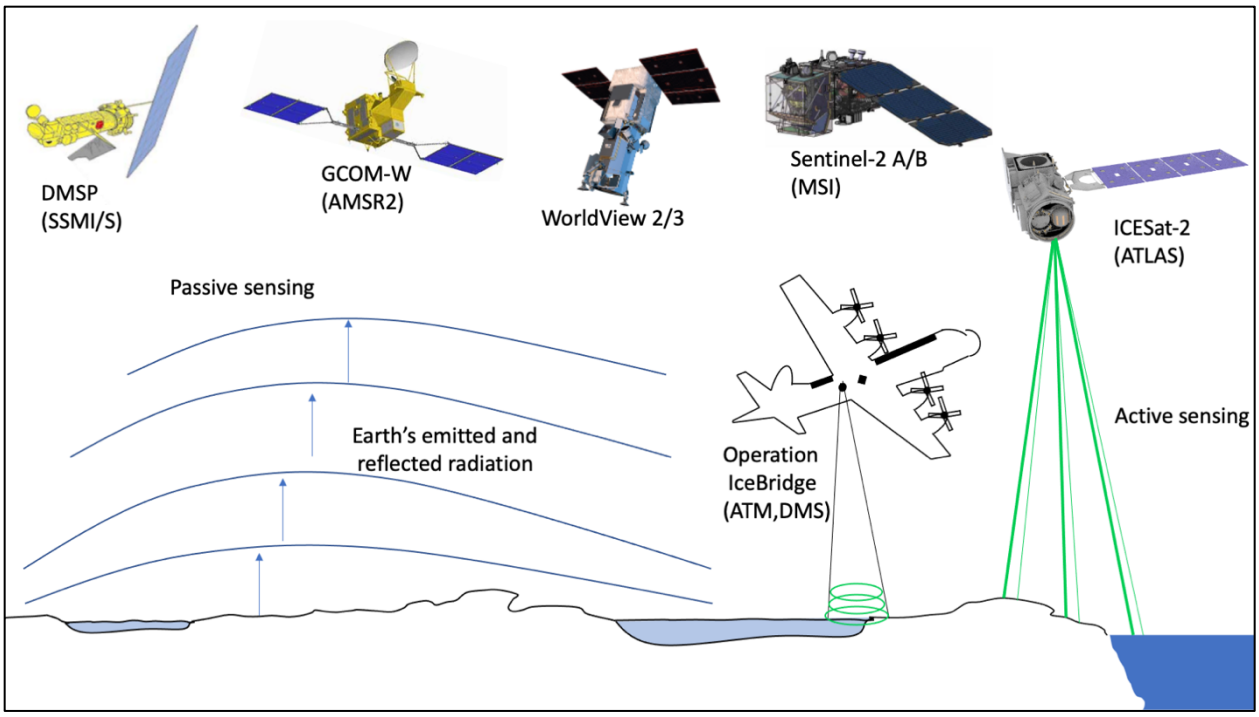

Figure 2.2. Multiple looks of the melting sea ice surface. We use high resolution imagery from OIB DMS, Sentinel-2 and WorldView, sea ice concentration products derived from passive microwave radiometry from AMSR2 and SSMI/S, and laser altimetry measurements from OIB ATM and ICESat-2 to obtain a three dimensional view of the sea ice.

2.3 Operation IceBridge

NASA's Operation IceBridge (OIB) airborne campaign was designed to fill the gap between the ICESat satellite (decommissioned in 2009) and the ICESat-2 satellite (launched in 2018) (Koenig et al., 2010). The goal of OIB was to continue measurements of glaciers, sea ice and ice sheets, in fast-changing areas of both the Arctic and Antarctic as they respond to climate change (Koenig et al., 2010). Regular surveys were designed to under-fly and thereby link the satellite altimeters CryoSat-2, ICESat and ICESat-2 to support both the continuation and intercomparison of laser and radar altimeter observations (MacGregor et al., 2021). From 2009 to 2019, a suite of instruments mounted on an aircraft captured high detail measurements over the polar regions, including Antarctica, Greenland, Alaska, and sea ice in the Arctic and

Antarctic. The instruments included: radar sounders, gravimeters, magnetometers, altimeters, and cameras (MacGregor et al., 2021). There were over 968 flights, 124 of which were focused on Arctic sea ice (MacGregor et al., 2021). Overall, Operation IceBridge was highly successful in advancing the state of knowledge of Arctic sea ice, providing information on snow depth distribution on sea ice, estimates of ice topography and roughness including new knowledge on pressure ridges, validating satellite estimates of thickness, and providing estimates of spring sea ice thickness for summer ice forecasting (MacGregor et al., 2021). The work presented in this thesis focuses on two sea ice campaigns, one in the Beaufort and Chukchi Seas and one in the Central Arctic. Figure 2.3 shows the OIB flight paths in black, and Table 2.1 provides technical specifications of the OIB data.

During the two OIB summer sea ice campaigns, the NASA 524 HU-25C Guardian aircraft operated at a nominal flight altitude of ~460 m and was equipped with a snow radar (Yan et al., 2017), laser altimeter (Krabill et al., 2002), and a digital camera (Dominguez, 2010) with positioning capabilities. The campaigns were conducted in different regions of the Arctic, exploring distinct ice regimes. The July 2017 campaign was flown over the thickest and oldest multiyear ice in the Arctic, to the north of Canada and Greenland (Sallila et al., 2019), in the Central Arctic (CA), where the regional convergence towards the coast causes dynamic thickening (Haas, 2017) and a consolidated ice cover. The July 2016 campaign targeted mixed ice types in the Beaufort and Chukchi Seas (B/C Seas), where ice drift is influenced by the Beaufort Gyre, and much of the ice does not survive the summer melt season, resulting in a thinner and younger ice cover (Richter-Menge and Farrell, 2013).

Table 2.1 Data Specifications

Mission / Company	Instrument	Measurement	Product	Data Source	Temporal coverage	Spatial coverage	Footprint / Resolution
NASA Operation IceBridge (OIB)	Airborne Topographic Mapper (ATM)	Surface elevation and topography	IceBridge ATM L1B Elevation and Return Strength (with Waveforms)	https://nsidc.org/data/ILATM1B/versions/2 https://nsidc.org/data/ILATMW1B/versions/1	July 2016 July 2017	Beaufort and Chukchi Seas (2016) Central Arctic Ocean - north of Greenland (2017)	1 m footprint
NASA Operation IceBridge (OIB)	Digital Mapping System (DMS)	Red, Green and Blue (RGB) Imagery	IceBridge DMS L1B Geolocated and Orthorectified Images	https://nsidc.org/data/IODMS1B/versions/1	July 2016 July 2017	Beaufort and Chukchi Seas (2016) Central Arctic Ocean - north of Greenland (2017)	0.1 m
NASA Ice Cloud and Land Elevation Satellite - 2 (ICESat-2)	Advanced Topographic Laser Altimeter System (ATLAS)	Surface elevation and topography	ATL03 L2A Global Geolocated Photon Data ATL07 L3A Sea Ice Height	https://nsidc.org/data/atl03 https://nsidc.org/data/atl07	Launched 2018-09-15	North to 88° N	11 m footprint
ESA Sentinel-2	Multispectral Instrument (MSI)	Top of Atmosphere Reflectance	L1C Top of Atmosphere Reflectance 100x100 km2 tiles	https://apps.sentinel-hub.com/eo-browser/	Sentinel-2A since 2015-06-23 Sentinel-2B since 2017-07-03	up to 20 km from the coast, and north to 84° N	10 m resolution
Maxar (Commercial)*	WorldView-2 (WV2) and WorldView-3 (WV3)	Top of Atmosphere Reflectance	WorldView-2 and WorldView-3 Multispectral Imagery	https://www.pgc.umn.edu/data/commercial-imagery/	WV2 Since 2009-08-10 WV3 since 2014-08-13	Up to 85° N	WV-2: 1.85 m resolution WV-3: 1.65 m resolution
Japan Aerospace Exploratory Agency (JAXA) Global Change Observation Mission - Water (GCOM-W)	Advanced Microwave Scanning Radiometer 2 (AMSR2)	Brightness Temperature	AMSR-E/AMSR2 Unified L3 Daily 12.5 km Brightness Temperatures, Sea Ice Concentration	https://nsidc.org/data/AU_SI12/versions/1	Since 2-7-2012	Up to 89.24° N	12.5 km resolution
Defense Meteorological Satellite Program	Special Sensor Microwave Imager/Sounder (SSMI/S)	Brightness Temperature	NOAA/NSIDC Climate Data Record of SIC (CDR SIC)	https://nsidc.org/data/g02202	Since 25-10-1978	Up to 89.8° N	25 km resolution

* Commercial satellite imagery provided through the Polar Geospatial Center for projects funded by the NASA Cryosphere Program. Geospatial support for this work was provided by the Polar Geospatial Center under NSF-OPP awards 1043681 and 1559691.

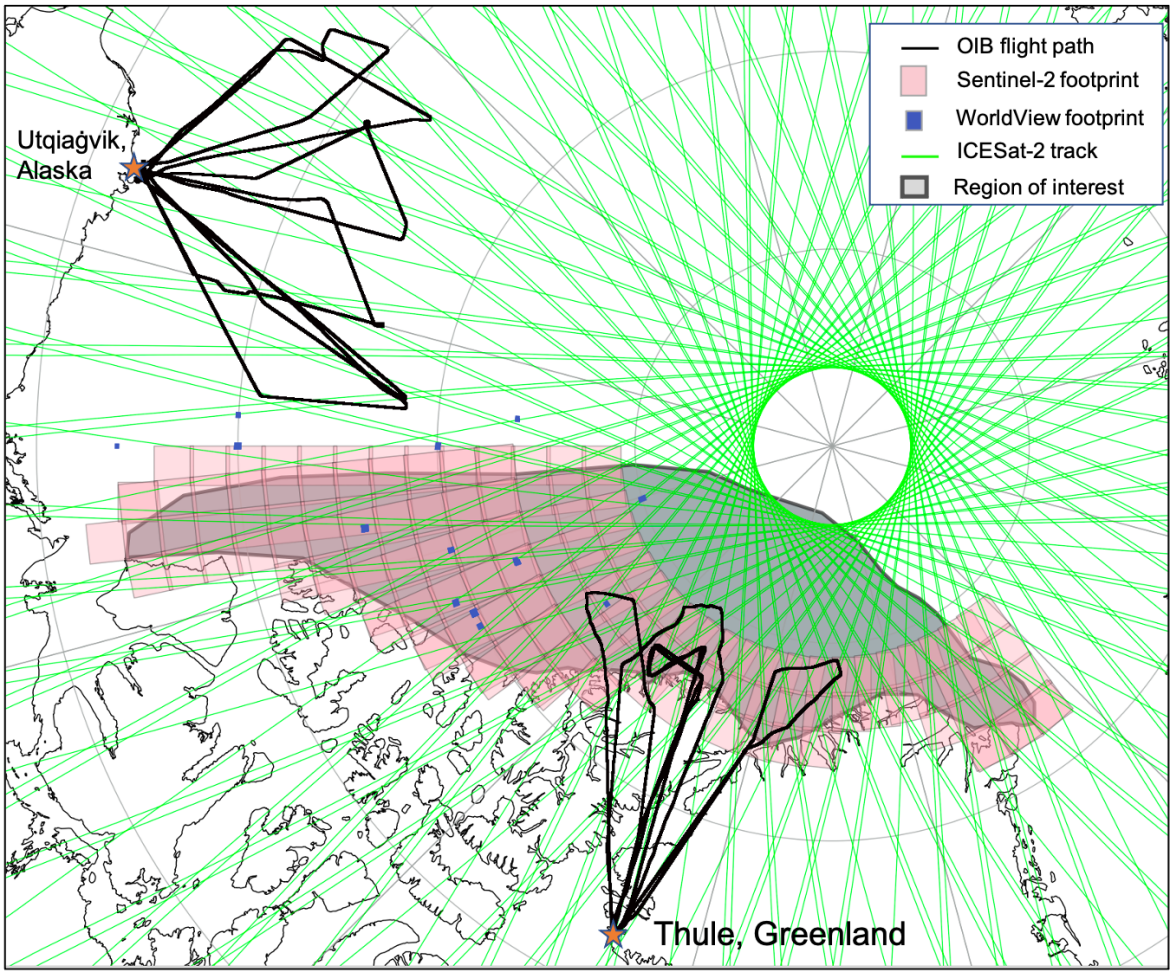

Figure 2.3. Map of the Arctic showing the location of remote sensing observations used in this work. Pink boxes are the outline of each 100 x 100 km^2 Sentinel-2 tile, clipped to the May 2020 multiyear ice region (shown in gray). Blue squares are the location of Worldview imagery scenes. Operation IceBridge campaign flight paths are shown in black and represent the locations where coincident Digital Mapping System imagery and Airborne Topographic Mapper measurements are available. These flights are based out of Utqiaġvik, Alaska and Thule, Greenland, noted by the orange stars. Green lines show ICESat-2 tracks for one week from 1 June 2020 through 7 June 2020 (~1/13 of the total tracks in a 91-day ICESat-2 repeat cycle).

2.4 High Resolution Imagery Observations

2.4.1 Fundamentals of High Resolution Imagery

Visible and infrared sensors detect the radiation at wavelengths from 0.5 μm to 1 μm and 3 μm to 15 μm, respectively (Figure 2.1) (Comiso, 2009). These are passive sensors and are sensitive to clouds as they emit and reflect radiation at these wavelengths. Visible imagery is dependent on the reflection of the incoming solar radiation and thus provides useful information during the day time only, while infrared sensors can provide useful information during the night (Comiso, 2009). Infrared imaging is useful for detecting sea ice, because the temperature of sea ice is generally much colder than the surrounding ocean. However, as snow melts on the ice surface during the summer, the surface temperature of the sea ice approaches the freezing point and becomes more difficult to distinguish from the open ocean. Clouds limit these observations, but in cloud free conditions, these sensors may provide useful information at high spatial resolution (Comiso, 2009).

2.4.2 Digital Mapping System Imagery

In this work we use the OIB Digital Mapping System (DMS) L1B Geolocated and Orthorectified Images (Dominguez, 2010) collected during the OIB Arctic summer campaigns. The DMS captured images every 5 seconds. At the nominal flight altitude of ~460 m, each image covers a surface area of ~ 575 m by ~ 400 m. DMS data consists of a compressed jpeg file suitable for quick-look viewing and quality control, and a Georeferenced Tagged Image File Format (GeoTIFF) array with a black border surrounding surface pixels. Each pixel within the image has a red,

green, and blue channel value (RGB data), with a resolution of 0.1 m at nominal altitude (Dominguez, 2010) (Table 2.1). The corrected position and attitude data collected by the Applanix 510 POS AV system flown with the DMS provide aircraft parameters that were used to apply orthorectification and geolocation to all of the images (Dominguez, 2010).

Previously, DMS data were used for lead detection (Farrell et al., 2011; Onana et al., 2013), pressure ridge sail height measurements (Duncan et al., 2019), characterization of sea ice surface morphology (Newman et al., 2014), and roughness (Webster et al., 2015). We take advantage of the high resolution of the DMS data to classify sea ice surface types during melt, including small-scale features such as melt ponds and deformed ice. Continuous sampling throughout the flights allows for calculation of along-track parameters, including sea ice concentration and melt pond fraction. These data have been obtained from the National Snow and Ice Data Center (NSIDC).

2.4.3 Sentinel-2 Multispectral Instrument Imagery

The ESA Copernicus Sentinel-2 mission consists of two satellites carrying the MultiSpectral Instrument (MSI) (Drusch et al., 2012). Sentinel-2A was launched 23 June 2015, and Sentinel-2B followed on 7 March, 2017. The satellites have a 98° inclination and coverage of all coastal waters up to 20 km from the shore, up to 84° N. The Sentinel-2 tiles are 110 km x 110 km. The Level 1C Top of Atmosphere Reflectances are provided in 13 spectral bands ranging from visible (490 – 665 nm) to short wave infrared (2190 nm). We utilize the 10 m resolution visible and near

infrared bands B02, B03, B04, and B08 in this work (Table 2.1). Table 2.2 provides the central wavelength and bandwidth for each of the bands we use in this work. Figure 2.3 shows the locations of the Sentinel-2 tiles in the multiyear ice region, the area of interest for the 2020 summer melt study (Chapter 6). Figure 2.4 shows a section of a Sentinel-2 tile that is 3.5 km by 2.5 km, where (a) shows the true color composite (RGB), and (b) shows the near infrared band. These data are available online at the Copernicus Open Access Hub, with a 24-hour latency.

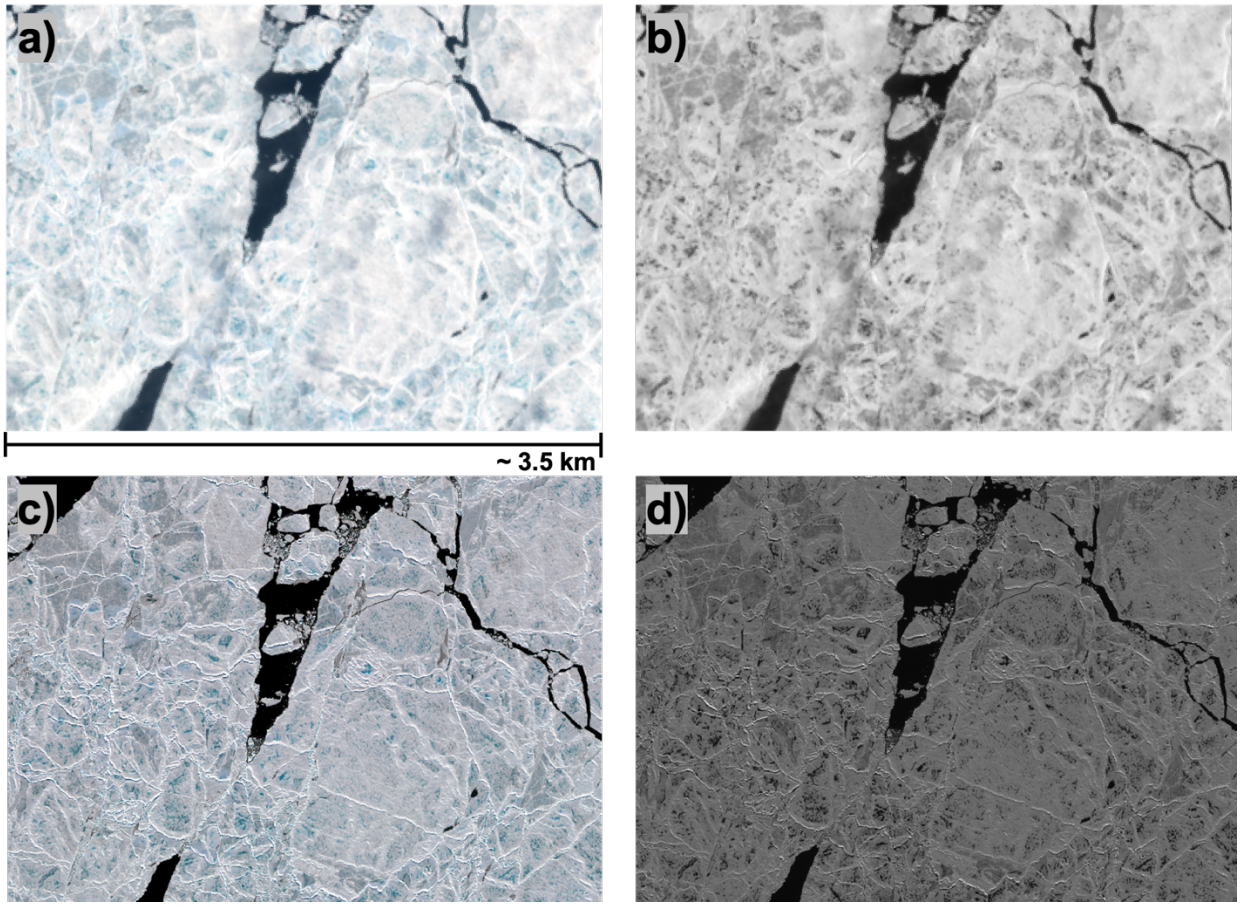

Figure 2.4. A 3.5 km x 2.5 km section of coincident Sentinel-2 (a-b), and WorldView (c-d) imagery. (a) Sentinel-2 red, green and blue band composite (B04, B03, B02). (b) Sentinel-2 near-infrared band (B08). (c) WorldView true color composite of red, green, and blue bands (B05, B03, B02) coincident with (a). (d) WorldView near infrared band (B07) coincident with (b). Both the Sentinel-2 and WorldView imagery was captured on 16 June, 2020 and are located west of Prince Patrick Island along the

Canadian Archipelago (-125.3 °W, 77 °N) (WorldView imagery copyright 2020 Maxar).

2.4.4 WorldView Imagery

The Maxar (formerly DigitalGlobe) WorldView commercial satellite constellation provides high-resolution panchromatic and multispectral imagery. The WorldView-2 satellite was launched 8 October 2009, and provides 8 multispectral bands at 1.85 m resolution (Maxar, 2020a). WorldView-3, launched on 13 August 2014, also has 8 multispectral bands at 1.24 m resolution (Maxar, 2020b). For research investigations funded through the NASA Cryosphere Program, access to the Maxar Worldview imagery archive is available via the Polar Geospatial Center. In this work, we utilize the high-resolution WorldView imagery to validate the lower resolution Sentinel-2 imagery. We use four spectral bands from this dataset: blue (B02), green (B03), red (B05), and near infrared (B07). Table 2.2 summarizes the sensor bands of the two WorldView satellites. Figures 2.4 c-d show an example of the high-resolution WorldView imagery as a RGB composite (c) and the near infrared channel (d). Comparing the top row and bottom rows of Figure 2.4, the small melt ponds and edges of the sea ice are better resolved in the higher resolution WorldView images (1.24 – 1.85 m resolution) than the Sentinel-2 images (10 m resolution).

Table 2.2. WorldView and Sentinel-2 spectral band specifications.

`	WorldView-2	WorldView-3	Sentinel-2 A	Sentinel-2 B
Blue	B02: 450-510 nm	B02: 445–517 nm	B02: 459-525 nm	B02: 459-525 nm
Green	B03: 510-580 nm	B03: 507–586 nm	B03: 542-578 nm	B03: 541-577 nm
Red	B05: 630-690 nm	B05: 626–696 nm	B04: 649-680 nm	B04: 649-680 nm
Near IR	B07: 770-895 nm	B07: 765–899 nm	B08: 780-886 nm	B08: 780-886 nm

2.5 Passive Microwave Observations

2.5.1 Fundamentals of Passive Microwave Remote Sensing of Sea Ice

Both active and passive microwave remote sensing of sea ice may be used for estimating sea ice concentration (SIC) and ice types (Shuchman and Onstott, 1990). Here we focus on the techniques of passive microwave remote sensing. Radiometers are passive sensors that measure the intensity of the radiation emitted from Earth. The structural properties of the sea ice and ocean create unique microwave signatures. Microwave emission from open water is very low and highly polarized, whereas emission from sea ice is greater and has weaker polarization (Markus and Cavalieri, 2009). Specific emissivity values are dependent on the microwave wavelength observed as well as the ice properties, such as crystalline structure and salinity, and thus provide information about the age and history of the sea ice (Shuchman and Onstott, 1990). Microwave signatures respond quickly to the melt and freeze cycles of the upper surface of sea ice (Shuchman and Onstott, 1990), and thus can be used to determine melt and freeze onset (Markus et al., 2009). Passive microwave sensors are able to operate at night because they are not reliant on reflection of solar radiation,

and are not affected by cloud coverage as clouds do not emit much radiation at low to mid-range microwave frequencies (Meier et al., 2017). However, due to the low energy level of passive microwave radiation, the radiation values must be collected over a large region, resulting in coarse spatial resolution (typically ~25 km x 25 km) (Comiso, 2009).

SIC can be derived from passive microwave radiometer data utilizing the ratios of brightness temperatures (typically 37 GHz v 19 GHz), taking advantage of the contrast in emissivity of ice and open water (Markus and Cavalieri, 2009). However, the melting sea ice surface complicates the retrieval of SIC values in the summer, and results in an underestimation of the SIC (Comiso and Kwok, 1996).

There is a long history of passive microwave sea ice data; there is a nearly 43-year continuous record of sea ice area and extent extending back to 1978 (Parkinson et al, 1999). These measurements of Arctic sea ice are one of the longest-running remotely sensed climate indicators (Meier et al., 2017), allowing scientists to understand long term trends and variability of the sea ice.

2.5.2 Sea Ice Concentration Climate Data Record

The NASA Scanning Multichannel Microwave Radiometer (SSMR) onboard Nimbus-7 was the first passive microwave sensor to provide measurements of sea ice, operating from 1978 to 1987 (Meier et al., 2022). The record continued with a series of satellites from the U.S. Defense Meteorological Satellite Program (DMSP) satellites carrying the Special Sensor Microwave Imager (SSMI) and the Special Sensor Microwave Imager and Sounder (SSMI/S) (Meier et al., 2022). These operations began in 1987 and continue through present (2022).

The NOAA/NSIDC Climate Data Record of SIC (CDR SIC), is a 25 km product derived using the Special Sensor Microwave Imager/Sounder (SSMI/S) brightness temperature measurements, and which, for each grid cell, selects the higher concentration value derived from the NASA Team and NASA Bootstrap algorithms (Meier et. al., 2017) (Table 2.1).

2.5.3 JAXA Advanced Microwave Scanning Radiometer 2

The NASA/ Japan Aerospace Exploration Agency (JAXA) Advanced Microwave Scanning Radiometer for the Earth Observing System (AMSR-E) (2002-2011) and the JAXA Advanced Microwave Scanning Radiometer 2 (AMSR2) (2012-present) employ larger antennas than previous microwave radiometers and are able to provide higher resolution data (12.5 km x 12.5 km) (Meier et al., 2022). AMSR2 is the sole instrument onboard the Global Change Observation Missions – Water (GCOM-W) satellite operated by JAXA (Imaoka et al., 2012). We use the AMSR2 Daily 12.5 km SIC (AMSR2 SIC) product, created using AMSR-2 brightness temperatures processed with the NASA Team 2 algorithm (Meier et. al., 2017) (Table 2.1).

2.6 Laser Altimetry Observations

2.6.1 Fundamentals of Laser Altimetry of Sea Ice

The main objective of altimetry is to measure the range (distance) from the satellite or aircraft to the surface (Chelton et al., 2001). The technique involves measuring the timing of short pulses for two-way travel at the speed of light between

the spacecraft or aircraft and the target surface (Bufton et al., 1989). Laser and radar altimeters provide their own source of electromagnetic illumination and thus are considered active remote sensors (Shuchman and Onstott, 1990). Radar altimeters require pulse averaging, whereas with the high energy laser pulses, no pulse averaging is required, and each individual pulse is meaningful (Bufton et al., 1989). Laser altimeters are able to provide higher resolution measurements of the sea ice surface compared to radar altimeters (Bufton et al., 1989). Laser altimeters have footprints on the order of tens of meters in diameter, where a radar footprint is at least an order of magnitude greater (Bufton et al., 1989). Figure 2.5 shows a schematic of the laser waveform transmitted and received pulse.

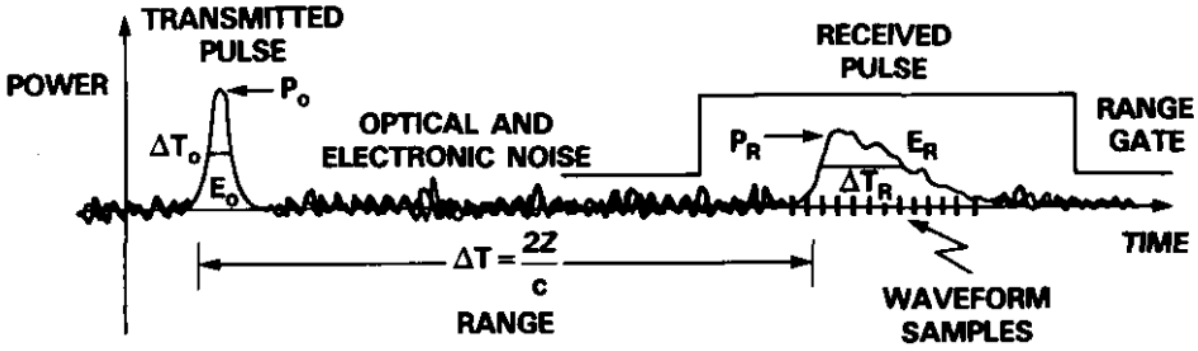

Figure 2.5. Schematic showing transmitted and received pulses. From Bufton et al., 1989.

The range to the surface, Z can be calculated:

$$Z = \frac{c\,\Delta T}{2} \tag{2.1}$$

Where *Z*, the slant range to the surface (in kilometers), is the product of the speed of light (*c*, in kilometers per second) and the time between pulses (ΔT, in seconds), divided by two to account for the round-trip travel. The range must be corrected for

instrument, atmospheric, and geophysical impacts. Once the corrected range is determined, the location of the reflecting surface is determined with knowledge of the instrument position vector (altitude and pointing of the satellite relative to the Earth) and the laser pointing vector (range and direction from the satellite to the reflecting surface).

Laser altimeters operate at different wavelengths. ICESat had an infrared laser operating at 1064 nm for surface altimetry. It is understood that laser altimeters reflect at the air-snow interface on snow covered sea ice (Kwok et al., 2004, Giles et al., 2007), off the water surface, and in the case of a green laser, such as ICESat-2, are able to penetrate the water and reflect off the ice on the bottom of the pond (Farrell et al., 2020). The ICESat 1064 nm infrared laser was not able to penetrate the water column. Figure 2.6 shows a schematic the ICESat-2 laser returns from these surfaces.

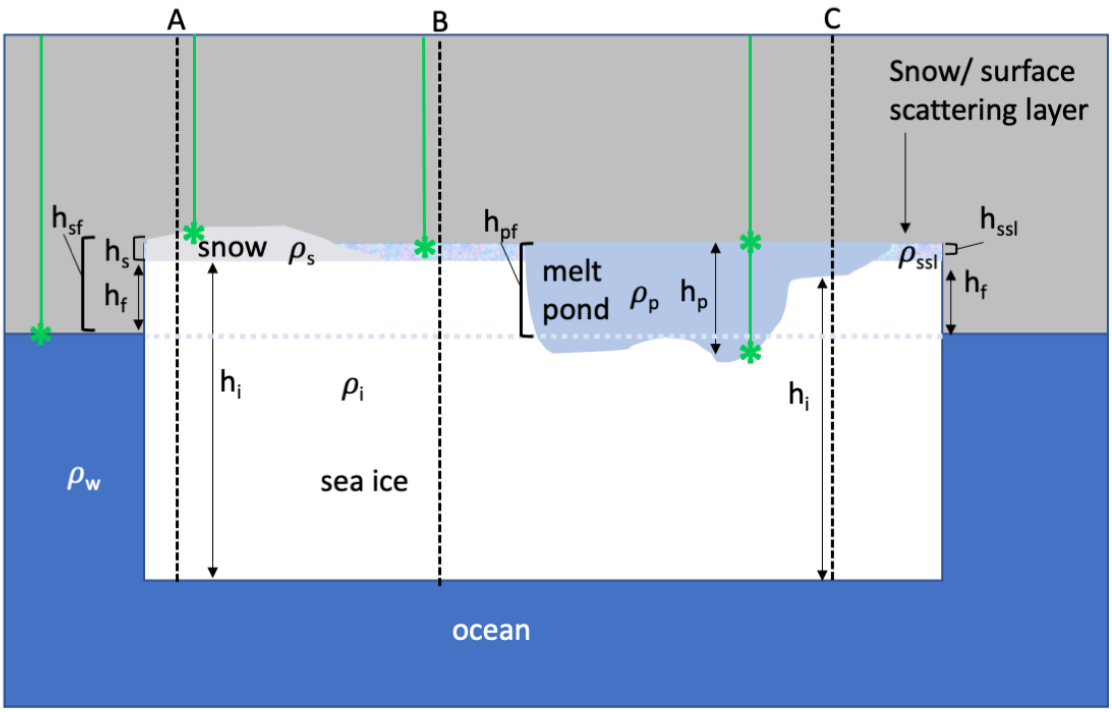

Figure 2.6. Schematic showing the summer sea ice diagram. An example sea ice floe is shown in white, with the surface scattering layer show in a textured blue, and snow in a light gray. A melt pond is shown in light blue, and the ocean is in dark blue. The parameters shown are the densities (ρ) and thicknesses (h) of each layer.

Sea ice thickness is an essential climate variable and is linked to the integrity of the ice pack. Ice thickness measurements are essential for understanding mass balance, validating models, and monitoring trends in Arctic sea ice (see Chapter 1, section 1.4). Typically, laser-derived sea ice thickness is given by:

$$h_i = h_{sf}\left(\frac{\rho_w}{\rho_w - \rho_i}\right) + h_s\left(\frac{\rho_s - \rho_w}{\rho_w - \rho_i}\right) \tag{2.2}$$

Where h_i is the thickness of the ice, h_{sf} is the snow freeboard, h_s is the snow depth, ρ_w is the density of ocean water, ρ_i is the density of sea ice, and ρ_s is the density of snow (Giles et al., 2006). This equation is derived from the assumption of hydrostatic equilibrium and is valid for a simplified one-dimensional thickness approximation at location A in Figure 2.6.

On summer sea ice, when the snow cover has melted, the topmost layer of the ice is a surface scattering layer (SSL), a bright white layer with a crumbly texture (Light et al., 2008). This is an important aspect of summer sea ice as it has been estimated that the scattering coefficient of this layer is approximately twice that of the interior ice (Light et al., 2008). This layer is on the order of a few centimeters thick (Light et al., 2022) and has a lower density than the interior ice. Light et al. (2008) found the density to be 420 kg m^{-3}, a density closer to that of snow (Warren, 1999). In order to calculate the sea ice thickness for the vertical profile at B in Figure 2.6, we replace the snow density (ρ_s) and depth (h_s) with the SSL density (ρ_{ssl}) and depth (h_{ssl}), and the freeboard (h_{sf}) is the ice and SSL freeboard ($h_{ssl} + h_f$), as the SSL is now the reflective surface measured by the laser.

The final summer thickness profile scenario is in the case of a melt pond (Figure 2.6, location C). To derive this equation, we start with first principles: the weight of the ocean water displaced is equal to the weight of the object:

$$\rho_w(h_i - h_f) = \rho_p(h_p) + \rho_i(h_i) \tag{2.3}$$

Where the variables are the same as above, ρ_p is the density of the pond water, and h_p is the depth of the pond. The total freeboard, h_{pf}, is the height of the pond surface above the local sea surface and can be related to the pond depth and the ice freeboard:

$$h_{pf} = h_f + h_p \tag{2.4}$$

Where the variables are the same as above, and h_f is the ice freeboard, which may be negative if the pond bottom is below the sea surface. Combining equations (2.3) and (2.4), we get:

$$\rho_w h_i - \rho_w(h_{pf} - h_p) = \rho_p h_p + \rho_i h_i \tag{2.5}$$

Dividing and rearranging equation, we get:

$$h_i = h_{pf}\left(\frac{\rho_w}{\rho_w - \rho_i}\right) + h_p\left(\frac{\rho_p - \rho_w}{\rho_w - \rho_i}\right) \tag{2.6}$$

Where h_i is the thickness of the ice, h_{pf} is the total freeboard in the presence of a pond, that is, the height of the pond surface above the local sea surface, h_p is the pond depth, ρ_w is the density of ocean water, ρ_i is the density of sea ice, and ρ_p is the density of the freshwater in the melt pond (Figure 2.6). The derivation of pond depth from laser altimetry measurements is described in Chapter 5, sections 5.2 and 5.3. The average thickness of a sea ice floe can be estimated by integrating these equations across the length of the floe, using the appropriate equation and values when necessary.

We described the derivation of sea ice thickness and discuss the impact of melt ponds on this calculation, as it has motivated our work to derive melt pond parameters such as melt pond depth, width and fraction.

2.6.2 Airborne Topographic Mapper

The Airborne Topographic Mapper (ATM) is a conically scanning laser altimeter (Krabill et al. 2002), that measures surface height. The ATM operates at 532 nm, a green laser, at the same wavelength as ICESat-2 (Table 2.1). The ATM has been essential in studies of sea ice thickness (e.g., Farrell et al., 2015; Kurtz et al.,

2013), and for validating thickness estimates from satellite altimeters: ICESat (Connor et al., 2012), CryoSat-2 (Laxon et al., 2013), and ICESat-2 (Kwok et al., 2019). The high-resolution elevation measurements can provide additional details of the sea ice surface such as roughness (Farrell et al., 2012; Kwok, 2015). In the work presented in this thesis, we use ATM observations over melt ponds to demonstrate the feasibility of extracting melt pond depth from the data.

For the summer 2016 and 2017 data, the ATM uses a narrow angle scan (5-degree full scan angle), corresponding to a swath width of ~ 30 m on the sea ice surface. Figure 2.7 shows an example of a DMS image with the ATM lidar elevations overlain. The data are provided in the form of surface height elevation and return strength. For the summer 2017 campaign, the waveform data are available (Studinger, 2018). In the work presented in this thesis, we use the ATM Return Strength and Elevation with Waveforms product from the 2017 campaign to detect pulses returned from the surface and bottom of melt ponds. For each measurement, the transmitted laser pulse and the received backscatter pulse are detected by the waveform digitizer (Studinger, 2018). The uncalibrated range is calculated using Equation 2.1 described in section 2.6.1, and further processing is required to derive the surface height above the ellipsoid (Studinger, 2018). Figure 2.8 shows an example of the ATM return waveform in the case of a single mode (a) and two modes (b). Modes are counted when they exceed the threshold defined as 35% of the maximum amplitude. The bimodal waveform indicates a complex surface such as a pressure ridge or a melt pond. We specifically look at the data over melt ponds to detect the modes

corresponding to the surface of the pond and the bathymetry of the pond (Chapter 5, section 5.2).

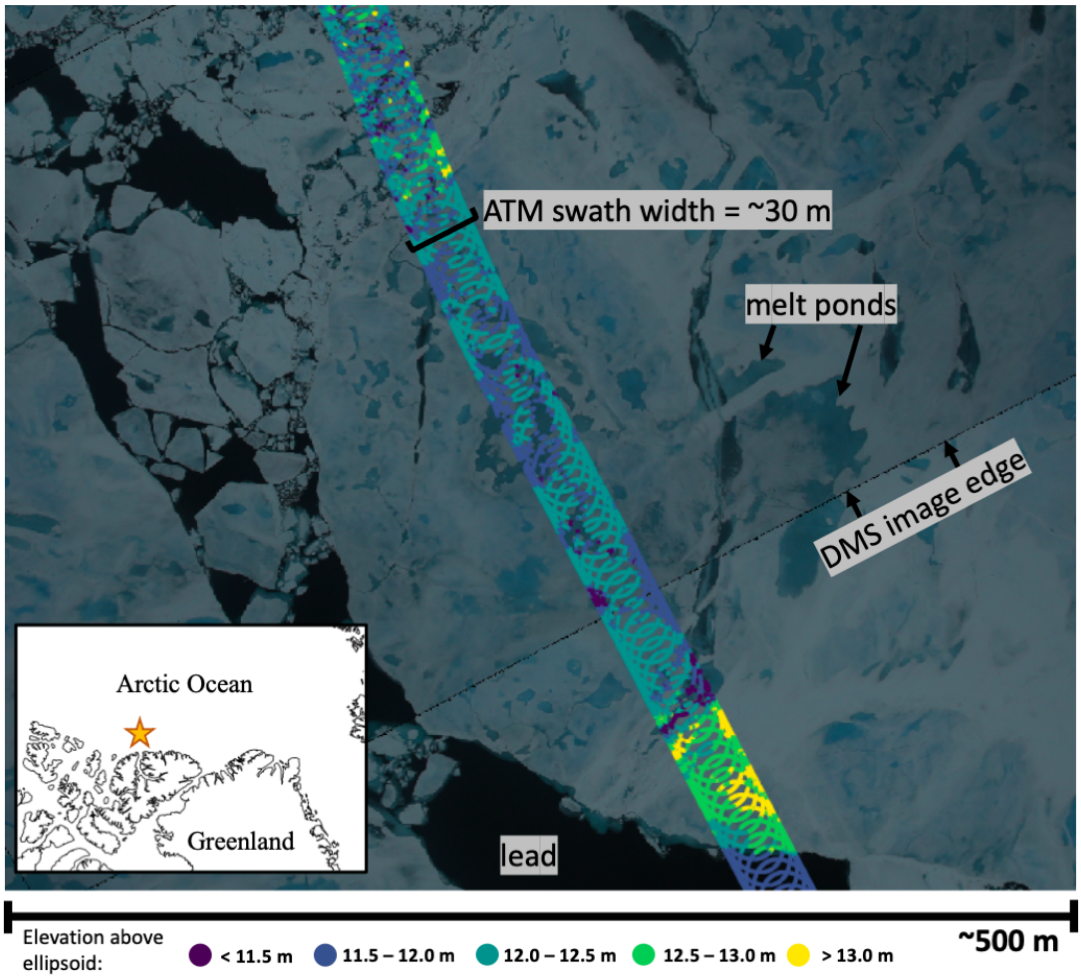

Figure 2.7. DMS imagery (background) and the conically scanning ATM track colored by the elevation above the ellipsoid. The DMS images are approximately 400 x 575 m. The ATM narrow scan swath width is approximately 30 m. The map inset shows the location of these data.

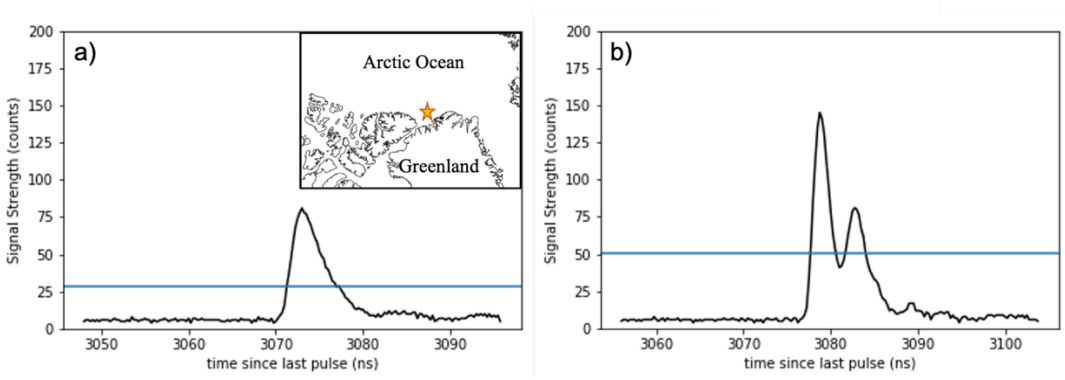

Figure 2.8. Example of ATM return waveforms over sea ice. a) shows a single mode where b) shows a bimodal return. The blue horizontal line corresponds to 35% of the maximum amplitude which is the threshold for defining a mode. The map inset shows the approximate location in the Lincoln Sea of both of these waveforms. These waveforms were observed on 24 July 2017.

2.6.3 ICESat-2

On 15 September 2018, NASA's Ice Cloud and land Elevation Satellite 2 (ICESat-2) was launched, carrying the Advanced Topographic Laser Altimeter System (ATLAS), a photon counting altimeter (Neumann et al., 2019). ICESat-2 is the follow-on mission to ICESat, in operation from 2003-2009, which was the first laser altimeter in polar orbit (Schutz et al., 2005). With a polar inclination of 92 ° and a 91-day repeat track orbit, ATLAS on ICESat-2 obtains surface height measurements across the Arctic up to 88 °N (Table 2.1). Figure 2.9 shows the ATLAS beam configuration. Each orbital track has a reference ground track (RGT) at the nadir of the predicted orbit and is numbered from 1 to 1387 (Smith et al., 2019). ATLAS has 3 beam pairs with 90 m spacing within the pairs, and 3.3 km pair separation (Figure 2.9). The RGT falls between the central beam pair (Figure 2.9). Each beam pair consists of a strong spot and a weak spot with an energy ratio of 4:1 (Neumann et al., 2019). In this work we refer to the track and beam as RGT #### GTNX, Where ####

is the track number, N is the beam pair number and X is L (left) or R (right) are the ground tracks. In this work we exclusively use the strong beams, as the weak beams do not provide enough energy for our studies. ATLAS operates at 10 kHz, resulting in measurements every 0.7 m along track (Markus et al., 2017). With a footprint of ~11 m (Magruder et al., 2020), the instrument over-samples the surface providing high fidelity surface measurements. ICESat-2 delivers improved spatial coverage and resolution when compared to ICESat which had a latitudinal limit of 86 ºN, and a footprint diameter of 50-70 m and 172 m along-track sampling (Markus et al., 2017). The altimeter has the ability to measure time of flight for individual photons (Neumann et al., 2019). For the strong beam, the expected photon return per shot is 2.8 - 8.5 photons over sea ice, and 0.2 to 1 photon over leads (Kwok et al., 2019).

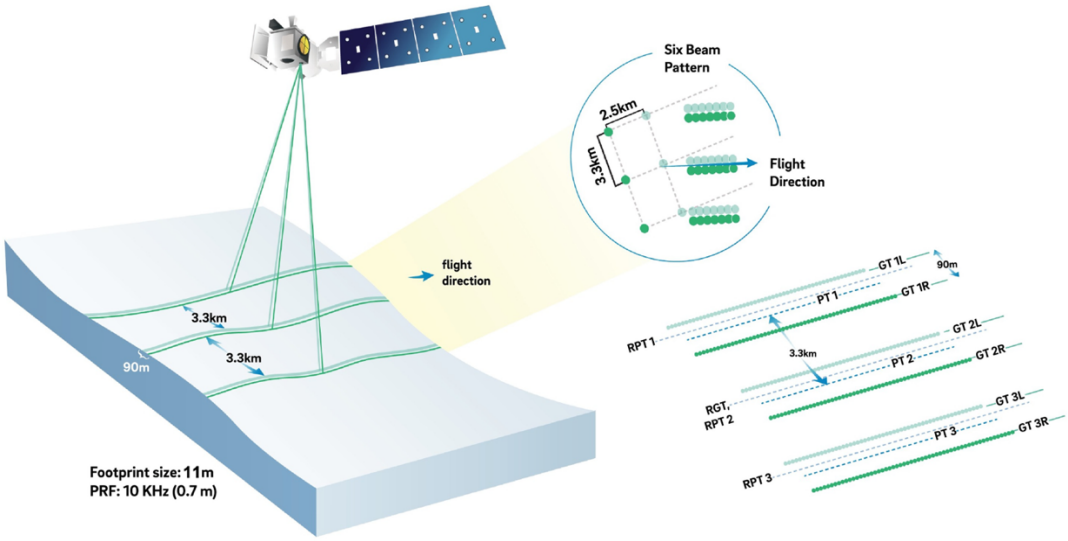

Figure 2.9. Schematic showing the ATLAS pattern. Figure modified from Smith et al., 2019. The distance between beam pairs is 3.3 km and the distance within pairs is 90 m.

Studies with ICESat-2 data have already demonstrated the instrument's ability to measure the Earth's surface in high resolution. Brunt et al. (2019) demonstrate that

the ICESat-2 data products map Antarctica's ice sheets with high precision (<9 cm). Fricker et al. (2021) derive the depth of melt lakes on the Amery ice shelf using ICESat-2's measurements. The dense sampling frequency and precise measurements have provided us new information about the complex sea ice surface, and has changed the way we observed small features on sea ice. Farrell et al. (2020) describe the measurements of complex sea ice surface features such as melt ponds, pressure ridges and leads. Tilling et al., 2020 examined ICESat-2's response to the melting sea ice surface and the effect of melt ponds on the summer sea ice height and freeboard retrievals. Although ICESat-2 was designed for the measurement of elevation in Earth's polar regions, it has been useful for other Earth science studies. Parrish et al. (2019) revealed ICESat-2's ability to map nearshore bathymetry and Neuenschwander et al. (2020) demonstrated the ability to map boreal forests.

The ICESat-2 Level 2 Geolocated Photon Data (ATL03) product includes time, latitude, longitude, and height relative to the ellipsoid, for each photon downlinked from ATLAS and is available at the National Snow and Ice Data Center (NSIDC) (Neumann et al., 2021). Figure 2.10 shows the elevation relative to local level sea ice surface of each geolocated photon. The high-resolution data is able to resolve small features such as pressure ridges and melt ponds (annotated in Figure 2.10).

The Level 3A Sea Ice Height Product (ATL07) provides along-track surface height and surface type. The segment lengths vary as they are determined based on a 150-photon aggregate. Segment lengths for the strong beams are on average ~15 m (Kwok et al., 2019). The ATL07 segment sea ice heights are shown in Figure 2.10b

and 2.10d. As the ATL07 product only tracks one surface, it either tracks the bathymetry of the pond, as in Figure 2.10b, or the surface of the ponds, as in Figure 2.10d (Farrell et al., 2020). The ATL07 product includes cloud statistics that are inputs from ATL09, the Level 3A Atmospheric Layer Characteristics Product (ATL09). We used these statistics to understand how clouds effect the photon returns and use them to limit the use of ATL03 surface measurements to cloud-free regions (data quality control is described in Chapter 5, section 5.3).

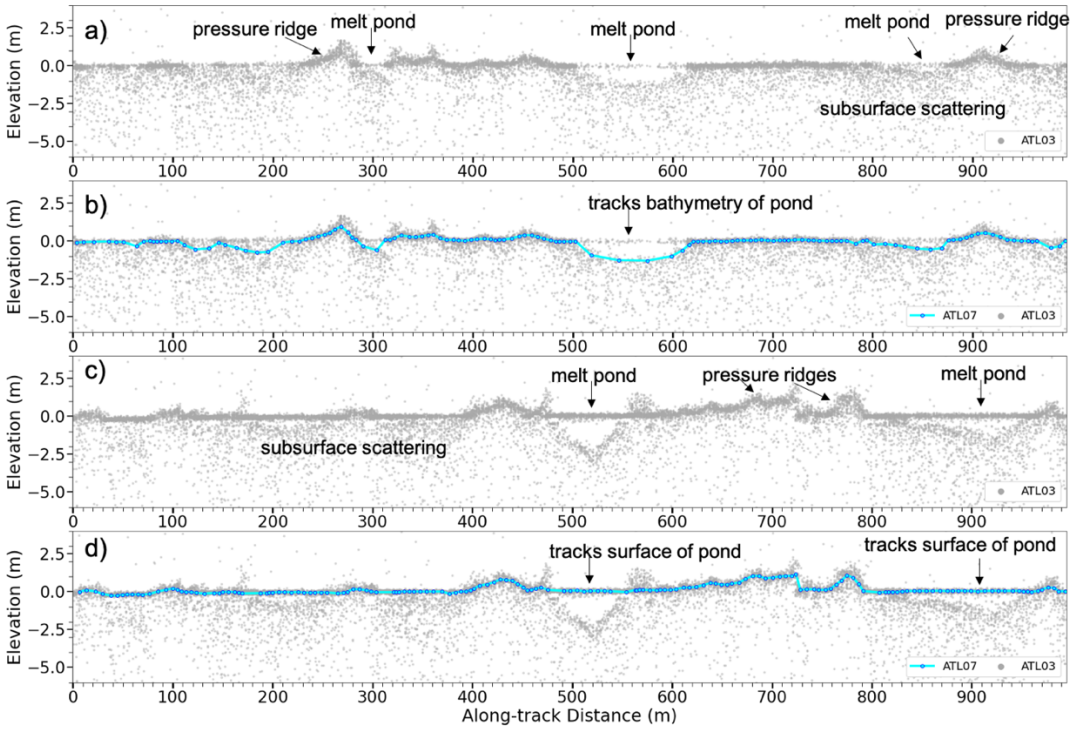

Figure 2.10. ICESat-2 data. (a) and (c) show ATL03 geolocated photon data (gray dots). (b) and (d) show the same ATL03 data as a) and c) in addition to the ATL07 sea ice height (cyan dots). Both 1 km segments are observed in the Lincoln Sea, (a)-(b) on 17 June 2019 at (-60.3 °W, 82.5 °N), and (c)-(d) on 18 June 2019 at (-55.5 °W, 82.9 °N).

2.7 Chapter Summary

In this chapter we described the main differences between passive and active remote sensing of sea ice (Section 2.2). A summary of Operation IceBridge focusing on the summer sea ice flights was provided in section 2.3. We discussed basic techniques for obtaining high resolution imagery, and described the DMS, WorldView and Sentinel-2 data products used in this work in section 2.4. Section 2.5 described the fundamentals of passive microwave radiometry and determining sea ice concentration, and we described the SIC data we use. Section 2.6 detailed the fundamentals of laser altimetry, the derivation of sea ice thickness, and the complications that the summer melt brings to that calculation. We described the ATM waveform data and the ICESat-2 laser altimetry data. The following chapters focus on the methodology and results of our work using the data and techniques described here.

Chapter 3: Image Classification Methodology

3.1 Motivation and Goals

The goal of this work is to understand the state of sea ice, asses regional and temporal variability of derived parameters, and compare findings with existing sea ice products to understand shortcomings of lower resolution datasets.

This chapter focuses on methodologies to derive sea ice concentration (SIC), melt pond fraction (MPF), and pond color fraction (PCF) from high resolution imagery. Previous studies have demonstrated the ability to extract sea ice melt pond parameters from airborne studies but most are limited in spatial extent and temporal evolution. See Chapter 1, sections 1.5.2 and 1.5.3 for a summary of the previous studies. The current deficiencies in observing melt pond characteristics at high resolution motivate our work to investigate the extraction of summer melt signatures from newly available airborne remote sensing data. The NASA Operation IceBridge (OIB) airborne mission obtained high-resolution measurements of the melt season in different regions of the Arctic in July 2016 and 2017.

In this chapter our goals are to:

- Describe the classification algorithm used to derive features from OIB imagery (as in Buckley et al., 2020a)
- Detail the algorithm modifications required for application to Sentinel-2 and WorldView imagery.
- Discuss the potential pixel misclassifications and impact.

- Describe the derivation of parameters: SIC, MPF, PCF.

First we provide background information on image classification methodology both broadly and related specifically to sea ice classification in Section 3.2. In this chapter we describe the methodology used in Buckley et al. (2020a) to classify OIB DMS imagery (sections 3.3 - 3.6). This methodology is adaptive to other high resolution RGB imagery and we apply this classification algorithm to Sentinel-2 and WorldView images. Sentinel-2 image acquisition and preprocessing is described in subsection 3.6.1. Then we describe the minor modifications made to the DMS classification algorithm to take advantage of the near-infrared channel in Sentinel-2 (subsection 3.6.2) and account for the lower resolution of the Sentinel-2 dataset (subsection 3.6.3). We also discuss the decision to not classify melt pond color in the Sentinel-2 imagery in subsection 3.6.4. We apply this modified classification algorithm to Sentintel-2. The application of the algorithm to WorldView imagery classification is described in section3.7. And finally, from the pixel classification we may derive SIC, MPF, PCF (section 3.8).

3.2 Fundamentals of Image Classification

Remotely sensed imagery provides important geographic information to scientific communities and beyond. Image classification is useful for many environmental and socioeconomic practices (Lu and Weng, 2007, and references therein). Classification methodology has evolved as scientists develop algorithms and new higher resolution imagery becomes available.

Satellite sensors, specifically designed to monitor the Earth's surface include panchromatic, multispectral, and hyperspectral imagery (DeFries, 2008). Panchromatic imagery, combines information from the visible red, green, and blue bands to form one channel, and thus is higher resolution than the counterpart multispectral imagery from the same sensor. Multispectral imagery, such as Advanced Very High Resolution Radiometer (AVHRR), MODIS, Landsat and Sentinel-2 imagery, provides brightness values at multiple spectral bands. Hyperspectral sensors such as the Airborne Visible/Infrared Imaging Spectrometer (AVIRIS) samples over 200 spectral bands in the visible and near infrared (DeFries, 2008).

Combinations of spectral bands are commonly used for land cover classification and observations of different surface types. For example, vegetation indices are used to understand biophysical and structural properties of vegetation and the global distribution of these attributes (Huete et al., 2002). The normalized difference vegetation index (NDVI) and the enhanced vegetation index (EVI) are simple transformations of spectral bands. The NDVI utilizes the red and near infrared bands and is sensitive to chlorophyll and related to photosynthetic capacity (Tucker, 1979; Myneni et al., 1995), whereas the EVI is more sensitive to canopy structure (Huete et al., 2002). Both can be calculated from standard MODIS bands, and therefore we have an extended record of 1km and 500 m vegetation index values throughout the seasons (Huete et al., 2002). Prior to the MODIS dataset, NDVI was calculated from NOAA Advanced Very High Resolution Radiometer (AVHRR). Both Landsat and NOAA-AVHRR sensors provide vegetation index time series back

to the 1970s (Huete et al., 2002). These vegetation indices are useful for drought detection, monitoring deforestation, and land cover classification. NDVI is also an important input for global climate models and biological models (Huete et al., 2002). The normalized difference water index (NDWI) utilizes the near infrared and visible green channels to delineate water bodies in multispectral imagery (McFeeters, 1996).

3.2.1 Classification Methodology

Classification algorithms can be per-pixel, subpixel, or per-field (Lu and Weng, 2007). Per pixel algorithms involve classification of individual pixels based on spectral values and classifications are mutually exclusive. In subpixel algorithms, individual pixels are made up of multiple classification categories and are best suited for coarse resolution imagery. Per-field classifications involve grouping neighboring pixels with similar spectral features and classifying the object.

3.2.2 Classification of Sea Ice Imagery

Classification of sea ice imagery presents unique challenges because it is difficult to differentiate features on a surface that is all white with blue tones. Open water and sea ice are easy to differentiate but features such as melt ponds, drained melt ponds, and generally submerged ice are hard to distinguish from one another. A review of the studies involving sea ice image classification is given in Sections 1.5.2 (airborne) and 1.5.3 (satellite). A discussion of the obstacles of classification of sea ice imagery is briefly discussed in Section 1.5.4, and obstacles include the presence of clouds, the sub-pixel size melt features, and the limited data coverage in the Arctic.

In this work, we made the decision to develop a classification algorithm based on empirical examination of the spectral make up of sea ice features. We opted for a supervised classification methodology, with a set of training data (Buckley et al., 2020 Supplementary Information) used to fine tune the algorithm. Because of the novelty of the dataset, we chose to empirically develop a classification methodology to minimize error and ensure reproducibility. Our classified imagery may be used to advance machine learning methods in the field.

We build on previous knowledge of spectral attributes of the melting sea ice surfaces (Perovich et al., 1998; Miao et al., 2015; Rosel et al., 2012, see Section 1.5.4). When possible, we make use of the NDWI to distinguish between water (open water or melt pond) and sea ice. The classification algorithm developed in this work involves manual discarding of cloud contaminated images. The surface classification is based on our knowledge of the reflectance of surfaces at different wavelengths (see Figure 1.7). We do not account for the effects of bidirectional reflectance distribution function (BRDF) such as shadows and sun glint. Topographic shadowing is minimal as ridge features are small (a few meters compared to the large terrain on land that casts shadows). Webster et al., 2015 found shadowing to make up $< 0.5\%$ of the ice surface area in summer sea ice imagery used in their study. Further, sun angles are high in the summer, minimizing the effects of BRDF. The thresholding locations in the mentioned figures are relative to other surfaces classified in the image so that they are adaptive to the changing light conditions. Pond color is related to the average ice and open water reflectance that have been classified. The deformed sea ice is related

to the brightness of the undeformed sea ice in the image. We intentionally do not set hard thresholds of reflectivity, so that the algorithm may be adapted to other datasets.

3.3 Digital Mapping System Imagery Classification

We classified DMS surface pixels into four ice-type categories: undeformed ice, deformed ice, open water and melt pond (Figure 3.1, Buckley et al., 2020a). The DMS images are not routinely adjusted for scene brightness due to varying overhead cloud conditions and sun angle during flight, and are thus not uniformly lit. Therefore, it is essential that surface type classification criteria are not based on fixed thresholds. Rather, criteria are applied on a per-image basis, and automatically adjust to suit the specific brightness levels of each image. We utilize the RGB channel data provided in each DMS image (Cr, Cg, Cb), and the normalized pixel value, Cn, defined as:

$$Cn = (Cr - Cg)/(Cr + Cg) \tag{3.1}$$

We analyze distributions (histograms) of pixel values in these channels using a bin width of 2-pixel values for the Cr, Cg, and Cb, and 0.02 for Cn, to ensure high resolution such that the frequency distribution can be determined. Modes are defined as a collection of bins bounded by pixel count minima on either side. The modal value is defined as a bin with lower pixel counts on either side. The difference between pixel count on either side of a modal value must be greater than 0.05% of the total number of pixels counted in the histogram. This is to eliminate the detection of erroneous modes. The maxima (ma) are annotated as follows: *Cx_ma_y* where x is r

(red), g (green), b (blue), or n (normalized) and y is the mode number, counting from 1, the modal value with the lowest pixel values, to m, the modal value with the highest pixel values. For example, the second mode in Cr is labeled *Cr_ma_2*. Similarly, the minima (mi) are defined as a bin with higher pixel counts on either side and are labeled *Cx_mi_y*. We also calculate the half maximum (hm) and quarter maximum (qm) of the mode on the left (L) or right (R) side of the mode. The half (quarter) maximum is the bin at which the pixel count is equal to 0.5 (0.25) of the pixel count in the associated mode. For example, to denote the half maximum bin value on the left side of the second mode in the blue channel, we write *Cb_ma_2_hmL*.

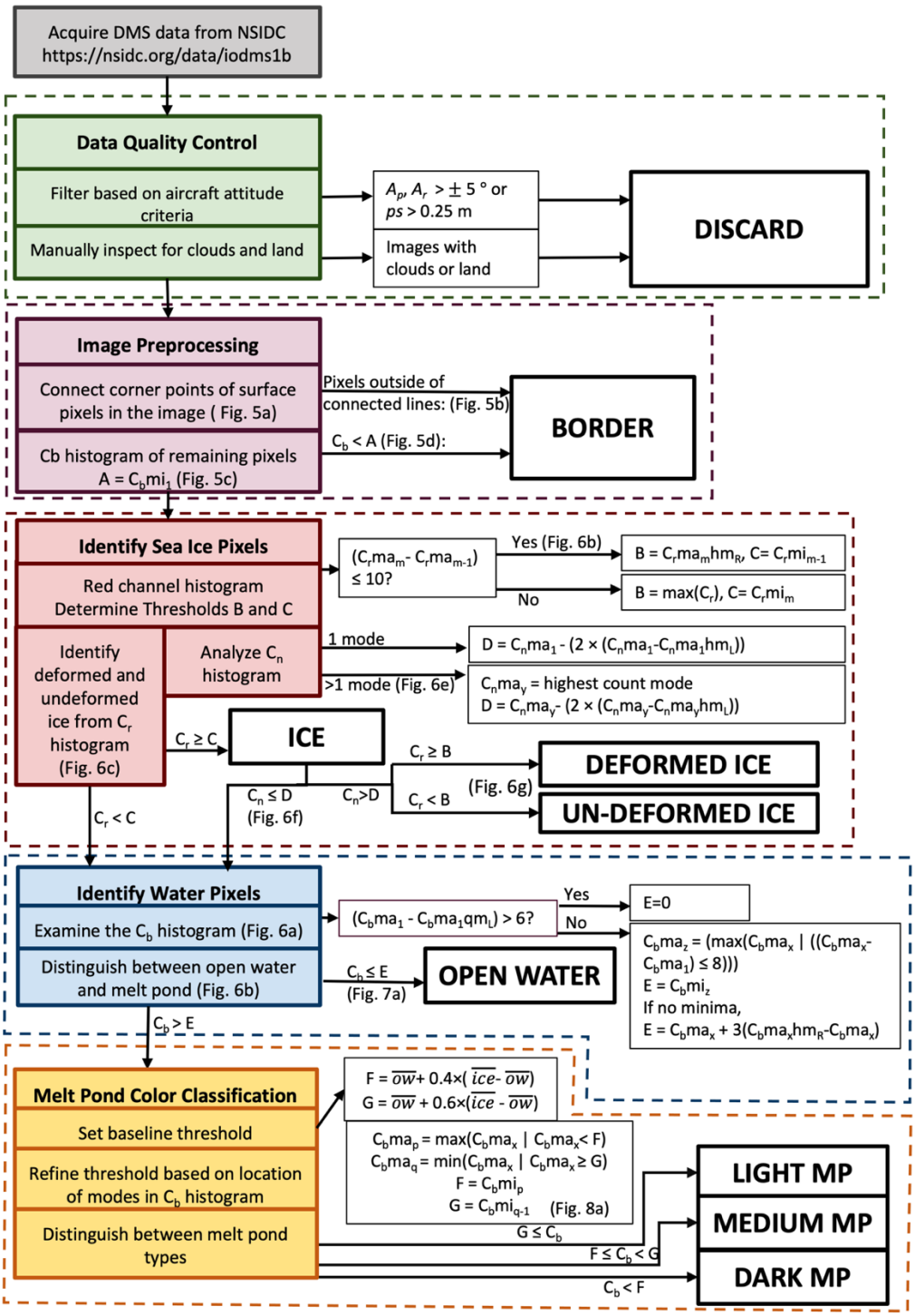

Figure 3.1. A schematic detailing the surface classification algorithm including steps to identify deformed ice, undeformed ice, open water, and melt pond pixels. Corresponding figures in Buckley et al., 2020a are noted, where applicable. The notation "|" is used to mean "such that." Colored boxes indicate the classification steps, with equations describing specific conditions and thresholds, including data

quality control (green, see text section 3.4), image preprocessing (purple, section 3.4), sea ice classification (red, subsection 3.5.1), open water classification (blue, subsection 3.5.2), and the melt pond classification algorithm (gold, subsection 3.5.3). Final outputs are indicated by white boxes with thick black outline. Figure from Buckley et al., 2020a.

3.4 Quality Control and Image Preprocessing

We retain only images acquired under normal flight conditions (nominal pitch, roll, and pixel size) by selecting data with the following attributes: pixel size < 0.25m, and roll and pitch < ±5°. These filtering steps ensure that each pixel represents a consistent surface area, simplifying calculations of the area of each sea ice parameter derived from the classified pixels. Images containing cloud and land are discarded. Of the total 46,162 DMS images collected during 11 flight surveys, 8.9% were eliminated due to roll, 6.6% due to pitch (including those eliminated in the 24 July 2017 flight segment), and 9.2% due to altitude outside of nominal conditions. Upon manual inspection, 37.5% were discarded due to the presence of clouds obscuring surface features, and less than 1% of images were eliminated due to contamination by land. In total, 17,217 images (37.3% of total data collected) remained for analysis.

The data quality control may introduce some statistical biases to the processed dataset. Clouds and sea smoke may preferentially form over areas of open water with a lower ice concentration, due to abundance of available moisture. Therefore, discarding data in cloudy regions may not fully capture the amount of open water on the survey line, biasing the dataset towards a conclusion of higher SIC.

In Figure 3.2 we demonstrated the methodology used to identify pixels associated with the black border before classifying surface pixels. We cannot simply remove border pixels using a set color threshold of zero (black), however, because border pixels near the edge of the surface pixels have brightness values greater than zero as a result of image compression. In Buckley et al., 2020a, we describe the methodology to identify border pixels by first finding the image corners (Figure 3.2a), and eliminating the pixels outside of the lines connecting the corners (Figure 3.2b), then we refine the border mask by removing the remaining low value brightness pixels (Figure 5.2c-d).

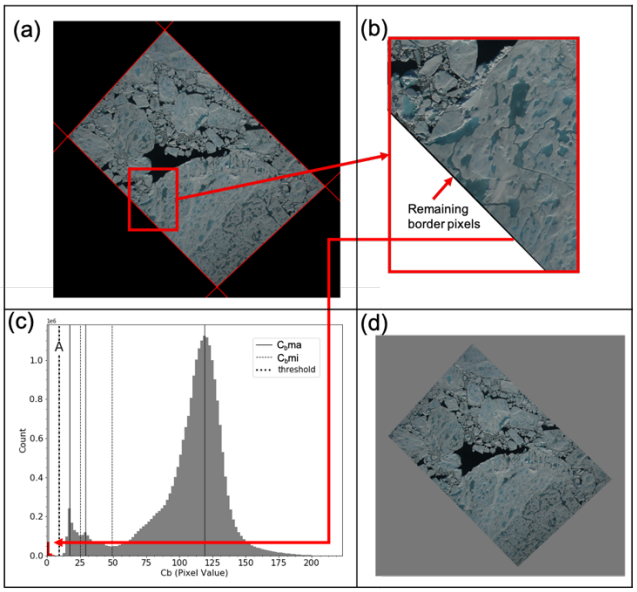

Figure 3.2. Methodology to identify DMS border pixels. (a) Original GeoTIFF image of sea ice in the Lincoln Sea at −51.6°W, 83.2°N on 24 July 2017, with the corner points of the surface pixel array connected (thin red lines). (b) Residual border pixels remain unclassified after the first identification step. (c) Distribution of Cb pixels. Residual border pixels are identified where Cb < Cbmi1 (red). (d) Same as in a but with all border pixels identified (gray), revealing the remaining surface pixels (natural color).

3.5 Classification of Melt Features on Sea Ice

After the quality control filtering and preprocessing steps, surface pixels within the remaining DMS images are classified (Figure 3.3a). Each of the four sea ice classes has a unique signature in the three color channels and it is therefore feasible to classify individual pixels based on the values of the RGB channel data relative to other pixels in the image.

3.5.1 Sea Ice

The first step is to identify sea ice. In the Cr histogram, ice pixels occupy the highest bins and form a distinct mode, *Cr_ma_m*. In images with significant amounts of deformed sea ice, there are two high-value modes in the red channel histogram (*Cr_ma_m* and *Cr_ma_m-1*) (Figure 3.3b). If deformed ice is present, the highest value modes in the red channel are within 10 bins of each other, i.e., (*Cr_ma_m* – *Cr_ma_m-1*) ≤ 10, and both modes are associated with ice pixels (Figure 3.3b). In this case, threshold B is defined as the first bin to the right of *Cr_ma_m* that is less than half of the pixel count in the modal value bin (*Cr_ma_m_hmR*, Figure 3.3b).

$$B = Cr\_ma\_m\_hmR \tag{3.2}$$

Threshold C is set as the minimum to the left of the second highest mode (Figure 3.3b):

$$C = Cr\_mi\_m - 1 \tag{3.3}$$

In the case where no deformed ice is present, i.e., where ($Cr\_ma\_m - Cr\_ma\_m\text{-}1$) > 10, threshold B is set as the maximum pixel value in the red channel:

$$B = max\ (Cr) \tag{3.4}$$

and threshold C is defined as:

$$C = Cr\_mi\_m \tag{3.5}$$

After setting thresholds B and C depending on the presence of deformed ice, we classify all snow-covered ice pixels with Cr ≥ C, and further classify undeformed ice pixels as ice pixels with Cr < B, and deformed pixels as Cr ≥ B (Figure 3.3c). The transition of melting snow to ponded meltwater is not discrete transition but rather a continuous process, and it is challenging to specifically identify the point at which the meltwater forms a melt pond. The pixels with Cr values at or near Threshold C (Figure 3.3b) demonstrates the challenge of distinguishing between melting snow, melting ice, and newly formed ponds which are optically similar.

In these steps, lighter pond pixels may be misclassified as ice (Figures 3.3d). We introduce another requirement to refine the ice mask (second iteration) to separate these light pond pixels from ice. Ponds have high green and blue channel values compared to their red channel values and thus have lower normalized pixel values (Cn) than ice pixels. In the second iteration, we analyze the Cn histogram of all surface pixels, and if there is only one mode, threshold D is set:

$$D\ =\ Cn\_ma\_1 - (2 \times\ (Cn\_ma\_1 - Cn\_ma\_1\_hmL)) \tag{3.6}$$

If there is more than one mode (Figure 3.3e), we identify the mode that has the highest pixel count (i.e., the location of the maximum Cn bin) as *Cn_ma_y*, where y = 1, 2, 3…, m-1, m, in the Cn histogram. Threshold D is set as the minimum to the left of *Cn_ma_y* (Figure 3.3e):

$$D = Cn\_mi\_y - 1 \tag{3.7}$$

All pixels with Cn ≤ D are removed from the ice mask (Figure 3.3f). A total of 286,305 pixels (1.2% of surface pixels) were removed in the second iteration (Figure 3.3g). The ice classification is complete and the remaining pixels move on to the next classification step.

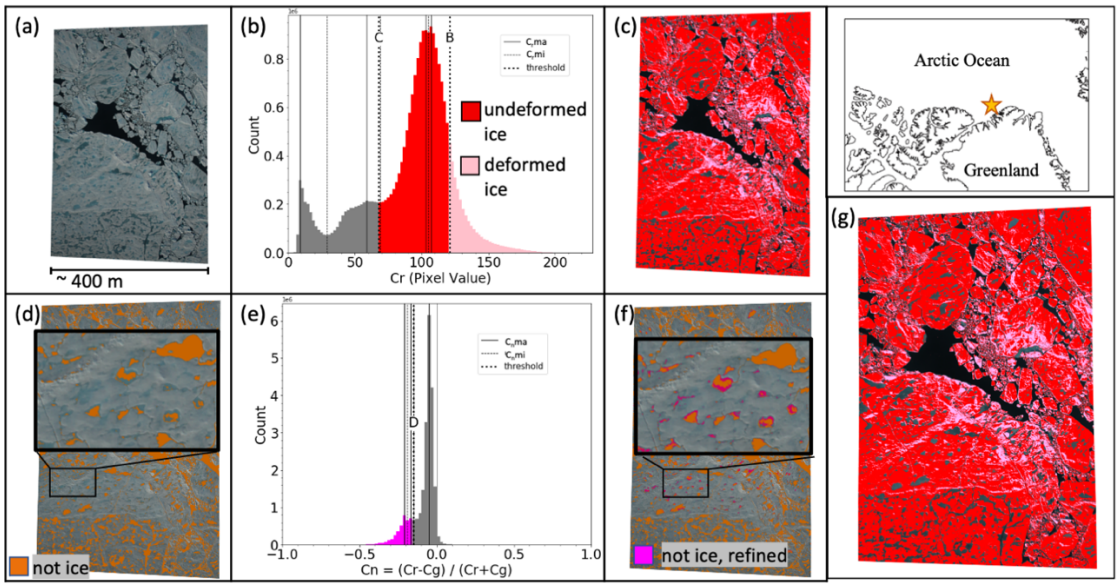

Figure 3.3. Demonstration of the methodology to identify ice (both undeformed and deformed) pixels. Same image as in 3.2. The map inset shows the location of this image (star). (a) Surface pixels (after preprocessing). (b) Distribution of surface pixels Cr, where thresholds B and C (section 3.4.1) are identified to separate ice pixels from other surface pixels (threshold C) and deformed (pink) from undeformed ice (red) (threshold B). (c) Classification of undeformed ice pixels (red), deformed ice pixels (pink), and remaining surface pixels (open water and ponded ice, natural color) after the first iteration. (d) Image distinguishing between pixels classified as ice (undeformed and deformed, natural color) and surface pixels remaining (orange),

demonstrating the need for a second iteration to remove misclassified pixels from the ice mask, refining the results of the first iteration. (e) Distribution of normalized pixel value (Cn) of all surface pixels. Pixels where Cn < D are shown in magenta and are not ice pixels. (f) Image distinguishing pixels classified as ice (natural color), pixels not classified as ice after the first iteration (orange), and pixels misclassified as ice in the first iteration and removed from ice mask in second iteration (magenta). (g) Classified image after second iteration, showing undeformed ice (red), deformed ice (pink), and unclassified pixels (natural color). Figure modified from Buckley et al., 2020a.

3.5.2 Open Water

There are two water classes, melt pond (MP) and open water (OW), which are often difficult to distinguish and define. Here, we define MPs as ponded freshwater on the sea ice surface. As soon as the ponded water melts through the ice and exposes the open ocean, it is considered open water. Light may be scattered off the melt pond edges and lighten the open water patch within a melt pond, but large melted-through ponds have similar pixel values to open water in all channels. Open water has the lowest value in all channels. Open water is found beyond the ice edge, in leads between ice floes, and in ponds that have completely melted through the ice.

To detect open water, we use the blue channel, Cb (Figure 3.4a). If present, open water pixels occupy the lowest value pixels in the blue channel (*Cb_ma_1*) and form a distinct narrow mode. If the quarter maximum to the left of the lowest value mode (*Cb_ma_1_qmL)* is fewer than 6 bins from the lowest value mode, there is open water in the image. In some cases, the open water pixels can occupy two closely-spaced, low-value pixel modes. For all the modes within 8 bins of *Cb_ma_1*, we define threshold E as the first minimum with a higher bin value than the highest pixel value mode of these modes (Figure 3.4a), i.e.,

$$Cb\_ma\_z = max\,(Cb\_ma\_x \;\; |\,(\,Cb\_ma\_x \;<\; (Cb\_ma\_1 \;-\; 8))) \tag{3.8}$$

$$E = Cb\_mi\_z \tag{3.9}$$

Where x, z are 1, 2, 3, …, m-1, m, in the Cb histogram. A threshold width of 8 bins was determined empirically and ensures that the mode selected is a low Cb value. If there is no open water present in the surface pixels, threshold E = 0. If there are no minima, E is defined relative to the mode:

$$E = Cb\_ma\_x + 3(Cb\_ma\_x\_fwhmR - Cb\_ma\_x) \tag{3.10}$$

Open water is classified as all the unclassified pixels with Cb < E (Figure 3.4b). Pixels with Cb ≥ E are classified as MP pixels and are further classified in the next step

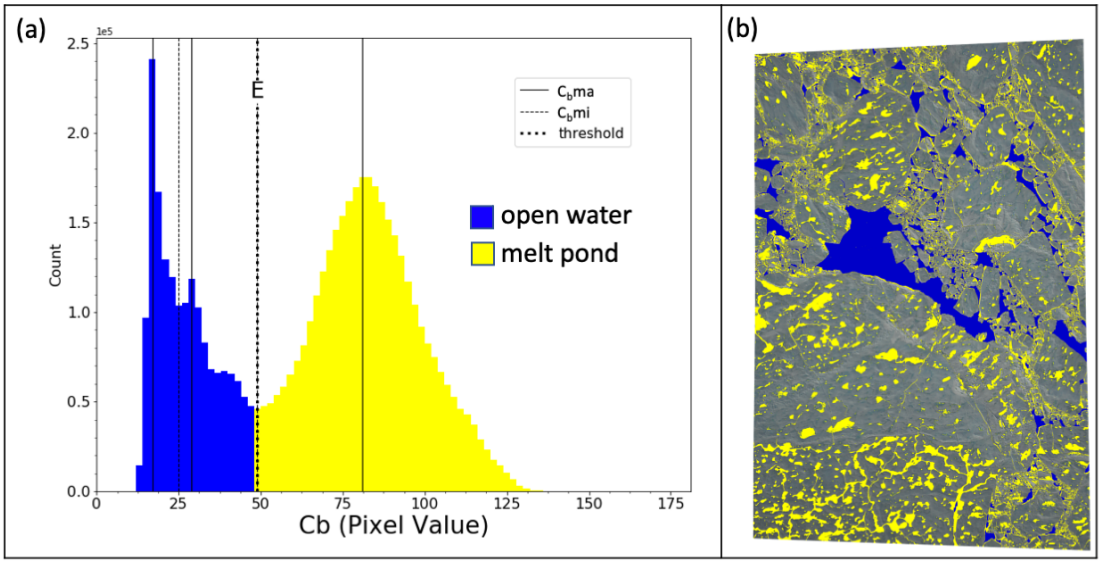

Figure 3.4. Methodology to identify open water pixels. Same DMS image as in Figure 3.2. (a) Distribution of Cb pixels remaining after ice pixels have been classified. Threshold E separates open water pixels (blue) from MP pixels (yellow). (b) Classified image showing open water pixels (blue), MP pixels (yellow), and ice pixels (natural color). Figure modified from Buckley et al., 2020a.

3.5.3 Melt Ponds

After identification of deformed ice, undeformed ice and open water pixels, all remaining pixels are classified as melt ponds (Figure 3.4b). Melt ponds range in color from light to dark blue, depending on the depth of the pond and the properties of the underlying ice (Eicken et al., 2004). Lighter ponds tend to have thick ice below and, as their depth increases, their color darkens. Due to the requirement of thick ice below, the lightest MPs are more common on thick, multiyear ice than on thinner, first-year ice.

Here, MP pixels are further distinguished as light, medium and dark ponds. For the classification of MP type, we utilize the blue channel (Cb) histogram (Figure 3.5a). Because MPs are blue in color, this channel has the widest spread of pixel values for MPs. Low Cb values indicate dark MPs, and high Cb values indicate light blue MPs. The MP color classification is based on the Cb values of the unclassified pixels relative to the values of ice and open water in the image. We calculate the average value of the ice ($\overline{ice}$) and open water ($\overline{ow}$) pixels in the image that were identified in the steps described in subsections 3.3.1 and 3.3.2. We establish the baseline thresholds for dark, F, and light, G, MP pixels as 40% and 60%, respectively, of the difference between *ow*_avg and *ice_avg* added to *ow_avg* (Figure 3.5a).

$$F = \overline{ow} + 0.4 * (\overline{ice} - \overline{ow}) \tag{3.11}$$

$$G = \overline{ow} + 0.6 * (\overline{ice} - \overline{ow}) \tag{3.12}$$

Next, we refine these thresholds based on the location of the modes in the Cb histogram (Figure 3.5a). We classify modes based on their location relative to these two values. Modes are classified as dark MP modes where $Cb\_ma\_x < F$, medium MP modes where $F \leq Cb\_ma\_x < G$, and light MP modes where $Cb\_ma\_x \geq G$.

If any dark MP modes exist, a new threshold for dark MP pixels, F, is set as the minimum to the right of the highest pixel value dark MP mode. Likewise, the threshold for light MP pixels, G, is set as the minimum to the left of the lowest pixel value light MP mode:

$$Cb\_ma\_p = max(Cb\_ma\_x \mid Cb\_ma\_x < F) \tag{3.13}$$

$$Cb\_ma\_q = min(Cb\_ma\_x \mid Cb\_ma\_x \geq G) \tag{3.14}$$

$$F = Cb\_mi\_p \tag{3.15}$$

$$G = Cb\_mi\_q - 1 \tag{3.16}$$

After determining these thresholds, we classify dark MPs as $Cb < F$, medium MPs as $F \leq Cb < G$, and light MPs as $Cb \geq G$ (Figure 3.5b). This step concludes the classification algorithm process; all surface pixels have now been classified.

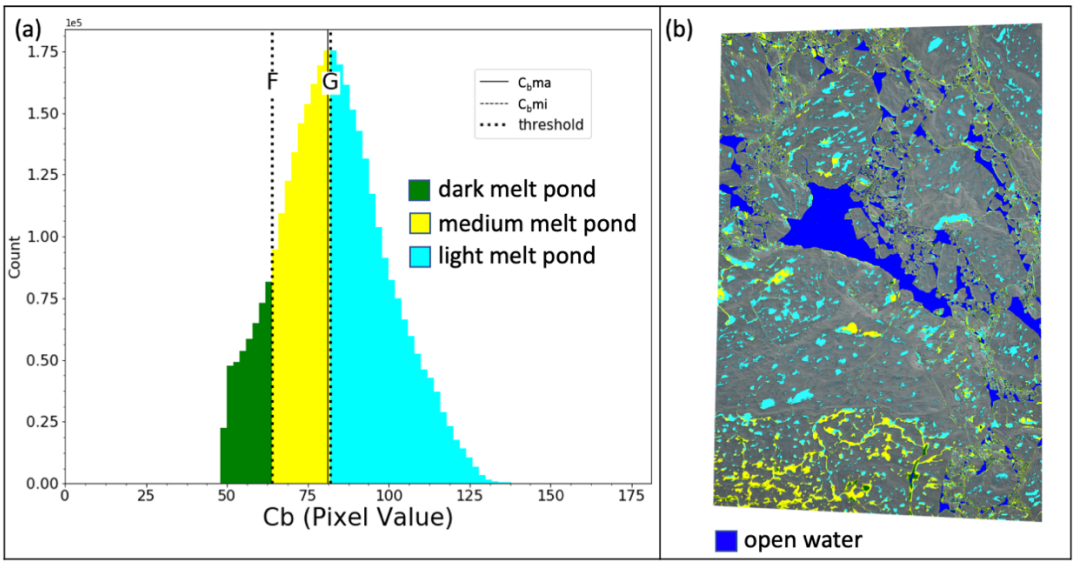

Figure 3.5. Methodology to classify MPs. Same DMS image as in Figure 3.2. (a) Distribution of Cb pixels showing thresholds for cutoff between dark (green)/medium (yellow) MPs and between medium/light (cyan) MPs, F and G, respectively. (b) Classified image showing open water (blue), dark (green), medium (yellow), and light (cyan) MPs and previously classified ice pixels (natural color). Figure from Buckley et al., 2020a.

3.5.4 Classified DMS Images

Classified images are stored as binary masks with the dimensions of the GeoTIFF and seven layers, one layer for each ice-type classification category: border (layer 0), undeformed ice (1), deformed ice (2), open water (3), dark MP (4), medium MP (5), and light MP (6). There are no unclassified pixels. Figure 3.6 shows an example of the raw DMS data (Figure 3.6a) and the classified image (Figure 3.6b).

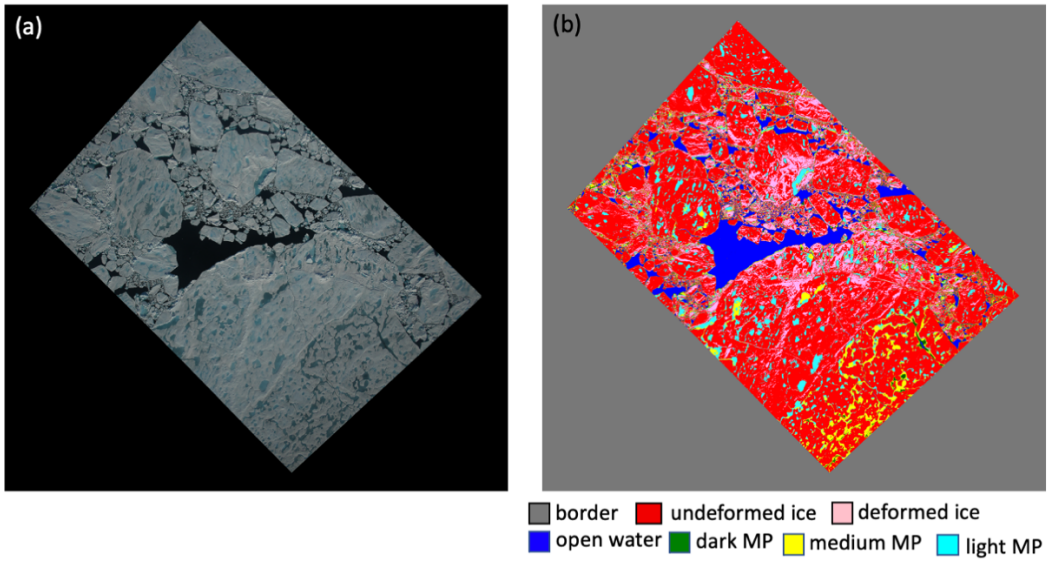

Figure 3.6. Final result of image classification algorithm. Same DMS image as in Figure 3.2. (a) Original DMS GeoTIFF (same as in Figure 5a). (b) DMS image after classification showing pixels identified as border (gray), undeformed ice (red, 64%), deformed ice (pink, 13%), open water (blue, 8%), dark MPs (green, 2%), medium MPs (yellow, 5%), and light MPs (cyan, 8%). Figure modified from Buckley et al., 2020a.

3.5.5 Classification Errors

Although the classification algorithm includes steps to differentiate hard-to-distinguish features, instances of pixel misclassification persist (Figure 3.7). Geophysical features occurring during the melt season that are not classified by the algorithm include ridge shadows, sun glint, and ice draft. The algorithm is designed to minimize errors based on its performance on a test image set (Buckley et al., 2020, Supplementary Information 1). Here, we briefly consider each of the common potential pixel misclassifications and discuss their impact (Buckley et al., 2020a).

1. Ridge shadows: The RGB values of ridge shadows fall in the middle of the spectrum, between the low values of open water and the high values of ice, and are similar to MP RGB values. Ridge shadows exhibit a higher, but overlapping, Cn

value compared to MPs, and thus, most are separated from pond pixels in the algorithm (Figure 3.3e), but some misclassifications persist (Figures 3.7a, Buckley et al., 2020a: S17, S22, S27). The results (Table 4.1) show that deformed ice comprises on average 0.5% of surface pixels, whereas MP pixels comprise 15.4% on average. Assuming the number of misclassified ridge shadow pixels are less than or equal to the number of deformed ice pixels, ridge shadows can contribute a maximum MP pixel error of 0.5%.

2. Sun glint: At the high end of the intensity spectrum, sun glint pixels in water are classified as ice or melt pond. When sunlight reflects off an open water disturbance, it can result in a specular reflection into the camera lens, which saturates the RGB values of those pixels. In our current algorithm, white pixels resulting from sun glint are misclassified as ice or dark melt ponds (Figures 3.7b, Buckley et al., 2020a: S3). However, sun glint appears only in large areas of open water, which are uncommon in our study region. We determined that sun glint is present in less than 5% of all images analyzed. We looked at three images where sun glint in open water occurred and found 2% of open water pixels were misclassified as ice or MPs. Therefore, we conclude that sun glint is a minor issue and can contribute a maximum MP pixel error of <<1%.

3. Ice draft: It is difficult to distinguish ice draft from MPs in the pixel-based, RGB-sensitive, algorithm (Figure 3.7c, Buckley et al., 2020a: S11, S12, S18, S31). The algorithm does not attempt to remove ice draft pixels from the MP pixels. Ice draft

is visible along ice edge floes, which are prevalent in images of unconsolidated ice due to a higher percentage of individual ice floes (resulting in a longer, aggregated floe perimeter), but can occur in any image. To quantify this error, we look at images with SIC < 80% (33% of all processed images). On average, 10% of pixels within these images are classified as melt pond pixels. Therefore, we can conclude that this misclassification has a moderate impact on images with SIC < 80% and has a minor impact on images with SIC ≥ 80%.

4. Open water in close proximity to dark melt ponds: Open water and dark melt ponds have similar RGB values, and in images with both, there may be a natural break (minimum) in the Cb histogram between the features (e.g., Figure 3.4, Threshold E, Equation 3.9). For 1,858 images (11% of processed image), no minima in the Cb histogram are found, and Threshold E is determined relative to the mode (Equation 3.10, Figure S41). Misclassification of open water pixels as dark melt pond may occur during this step (Figures 3.7d, Buckley et al., 2020a: S16, S20, S28, S41). To quantify the potential impact of this misclassification, we consider the statistics associated with DMP pixels in these images. We find the percentage of DMP pixels per image ranges from 0% to 24% and is on average 4% with a standard deviation of 5%. These results suggest that potential misclassification of OW pixels as DMP pixels would only occur infrequently. Since this potential misclassification can impact a maximum of 11% of the data and is expected to occur infrequently, we conclude that it has minimal impact on the derived products.

5. Very light melt ponds: In the early stages of melt pond formation, as the snow melts and meltwater collects into pools, the ponds are very light in color and may be misclassified as ice (Figures 3.7e, Buckley et al., 2020a: S30, S38). The second iteration of the ice classification step (Equations 3.6 and 3.7) was introduced to rectify this misclassification by removing light melt pond pixels from the ice mask (Figure 3.3d). In the second iteration, on average, 3% of ice pixels were removed from the ice mask and classified as melt pond pixels. With this additional iteration to refine the ice step, we expect this misclassification is infrequent and has minimal impact on the results.

Grouping pixels into object sets and considering geometric thresholding may improve the accuracy of classification and resolve some of the aforementioned misclassification errors. However, introducing these approaches in the current algorithm would increase computational processing time and may result in additional, unforeseen pixel misclassification errors. Because we did not consider any of these issues to impact the majority of the data (Buckley et al., 2020a), we did not implement any further steps to mitigate potential pixel misclassification. Where the near-infrared band is available (in Sentinel-2 and WorldView imagery), we use this band to enhance the classification pixels and introduce an 'other' category, encompassing some of these unusual circumstances where pixel reflectances don't fall squarely into a surface type classification. Section 3.6.3 and Section 4.6 discuss these steps in further detail.

In summary, we conclude that pixel misclassifications due to cases 1, 2, 4, and 5 are minor and do not significantly impact the results. Case 3 could potentially have a larger impact on the derived parameters (SIC and MPF), and this is further discussed in section 4.6.

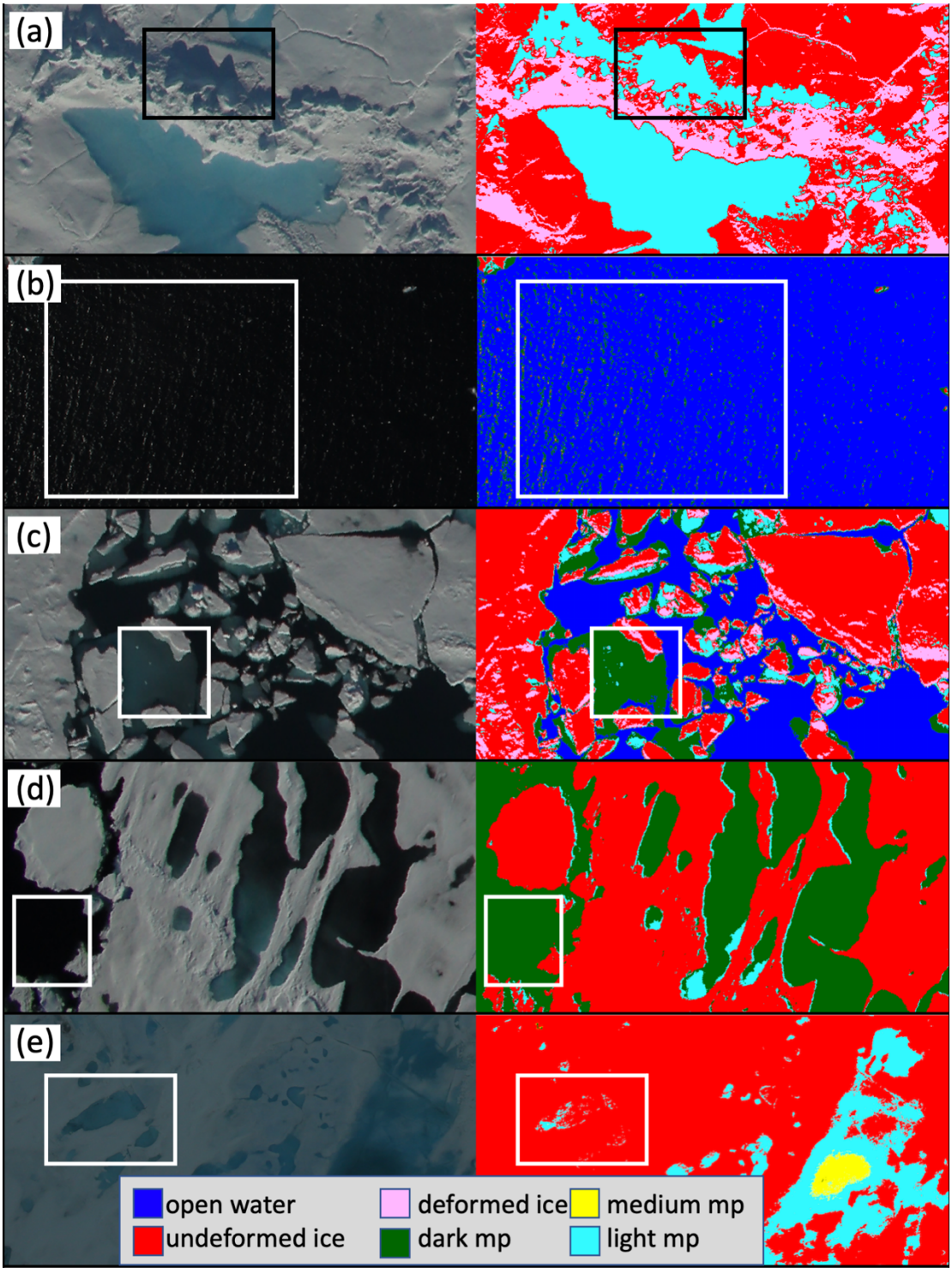

Figure 3.7. Examples of pixel misclassification. Areas with misclassified pixels are in white boxes in the zoom of original DMS GeoTIFF on the left and classified image on the right to exemplify pixel misclassifications of: (a) Ridge shadows, (b) sun glint, (c) ice draft, (d) open water, and (e) light melt ponds. Figure modified from Buckley et al., 2020a.

3.6 Sentinel-2 Imagery Classification

The algorithm developed for classification of the DMS imagery, can easily be applied to other RGB imagery, as all thresholds are adaptive to ranges of pixel values. However, a few modifications are made to the algorithm to improve the classification and account for the differences in the datasets. Figure 3.8 shows the modified algorithm flow diagram.

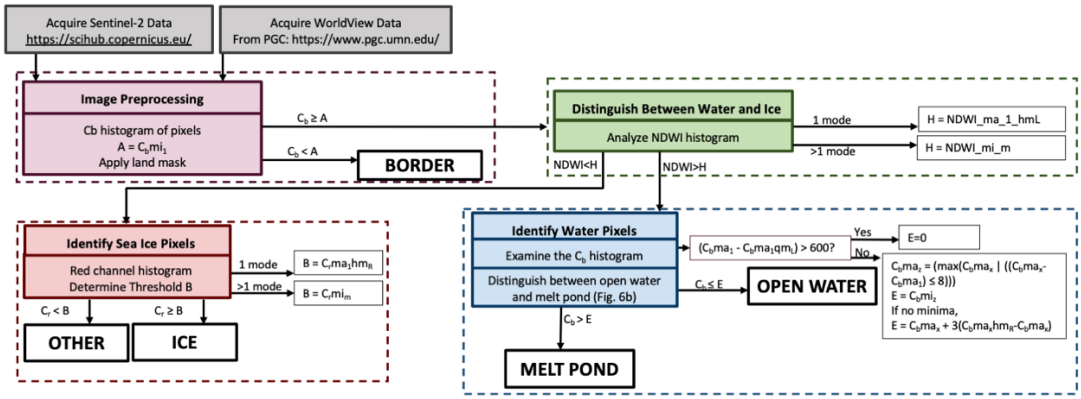

Figure 3.8. A schematic detailing the modified surface classification algorithm including steps to identify ice, open water, melt pond, and other pixels. Final outputs are indicated by white boxes with thick black outline. Figure modified from Buckley et al., 2020a.

3.6.1 Sentinel-2 Imagery Acquisition and Preprocessing

Sentinel-2 imagery is available for browsing and download via the Sentinel Hub (Copernicus Sentinel-2 Data). We requested Sentinel-2 imagery from the multiyear ice region (tile locations shown in Figure 2.3), we set the maximum cloud coverage as 10%, and downloaded all data matching these parameters from 1 June through 31 August, 2020. As in the DMS imagery preprocessing, we manually inspect Sentinel-2 images to discard images with pervasive cloud cover. In this case, we examine the near-infrared channel images, as it is easiest to differentiate clouds and ice with these

images. In the DMS preprocessing, we discarded images containing land. Here the Sentinel-2 tiles are much larger in size (100 x 100 km^2), so discarded images containing land would mean discarding large areas of useful information. Figure 3.9 shows the application of a land mask to a Sentinel-2 tile containing land. We used a GIS shapefile of the maximum sea ice extent from the National Ice Center, and modified it so that it did not include the landfast ice within the Canadian Archipelago. The inverse of this shapefile is the land and landfast ice mask; that is, everything outside of the modified shapefile is not included in the image analysis. In this example land is occupying both of the bottom corners of the tile (Figure 3.9a). When we apply the land mask, we omit the land pixels within the Sentinel-2 tiles (Figure 3.9b).

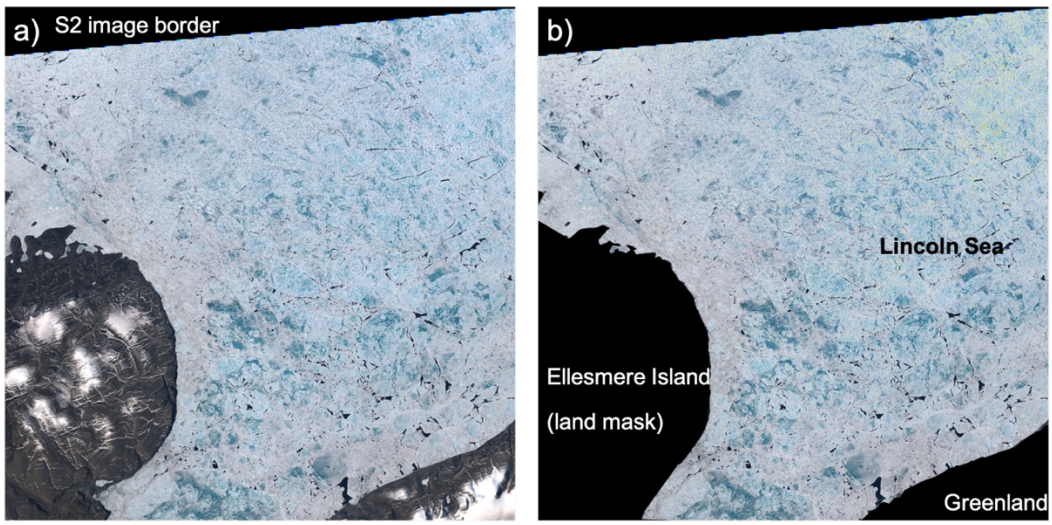

Figure 3.9. Example showing land mask application to Sentinel-2 imagery. (a) RGB composite of a Sentinel-2 tile containing land. (b) Application of Sentinel-2 land mask to remove the land pixels within the image. This image was captured on 25 June 2020 and is located in the Lincoln Sea.

3.6.2 Utilization of NIR band

The Sentinel-2 MSI measures reflected radiance in 13 spectral bands. In addition to the RGB bands, the Senteinl-2 near-infrared band is also 10 m resolution (whereas all other bands have a lower resolution). Water is very absorptive in the near infrared wavelengths (Curcio and Petty, 1951), and thus this channel can be used to discern between land and water (e.g., McFeeters 1996, 2013) (See Chapter 1, Figure 1.7). We add another step in the classification algorithm to enhance the discrimination between ponds and open water from sea ice.

Prior to the sea ice classification described in subsection 3.5.1, we introduce a step to distinguish water pixels from ice pixels. We calculate the Normalized Difference Water Index (NDWI) from McFeeters (1996):

$$NDWI = \frac{Cg - C_{NIR}}{Cg + C_{NIR}} \tag{3.17}$$

Where Cg is the green band (Band 3), and C_{NIR} is the near-infrared band (Band 8). NDWI is greater for water than for ice surfaces due to the low reflectance of water at IR wavelengths (McFeeters, 1996). In the NDWI histogram, water pixels occupy the higher value bins. If the histogram has one mode, threshold H is set as the half max on the left of the mode:

$$H = NDWI\_ma\_1\_hmL \tag{3.18}$$

If the NDWI histogram has more than one mode, we identify the highest pixel value mode as NDWI_ma_m. Threshold H is set as the minimum to the left of NDWI_ma_m:

$$H = NDWI\_mi\_m \tag{3.19}$$

All pixels with NDWI ≤ H are designated as non-water and move on to the sea ice classification step. All pixels with NDWI > H are designated as water pixels, then skip the sea ice classification step and move on to the open water classification step described in subsection 3.5.1. In this step, water pixels are classified as either melt ponds or open water.

3.6.3 Accounting for Other Pixels

Sentinel-2 has a lower resolution than the DMS imagery and with a 10 m resolution each pixel may include multiple types of surfaces. For example, a pixel that straddles the edge of a pond would contain melt pond and sea ice. We call these pixels "mixed pixels." This issue was negligible in the DMS classification due to the 0.1 m pixel size, but with the 10 m Sentinel-2 imagery, it becomes more significant. For that reason, we introduce a category of 'other' pixels, capturing both mixed pixels and pixels that do not fall into a particular category. For example, late in the summer as the ocean begins to refreeze, thin layers of ice form in the leads between sea ice floes, and this thin ice has a different spectral reflectance than thicker snow covered ice. In this section, we describe the steps added to the algorithm to take advantage of the near-infrared band and to account for the 'other' pixels.

With a larger pixel size in Sentinel-2 (10 m) than in DMS imagery (0.1 m), mixed pixels are common (Figure 3.10d) and thus must be distinguished from other classification categories. Mixed pixels are identified in the sea ice classification step. All non-water pixels enter the sea ice classification step where they are classified as

sea ice or mixed pixels. This step follows the methodology described in subsection 3.5.1. Pixels greater than the threshold in the Cr are identified as ice. Pixels less than the threshold, are identified as mixed pixels (Cr < C, see subsection 3.5.1 and Figure 3.8). Thus, mixed pixels are identified as those that are not as bright in Cr as ice, and not as high in NDWI as water pixels are. These pixels typically cover multiple surfaces, for example: sea ice edges and melt pond edges. Figure 3.10 shows an example of a full Sentinel-2 tile (a), zoom in of a 10 km section (b) and the classification of a 1 km section (c-d), and the coincident higher resolution (1.3m) WorldView imagery and classification (e-f). In the Sentinel-2 image, the larger pixel size does not resolve the small melt pond features (Figure 3.10c), as seen in the WorldView imagery (Figure 3.10e). Pixel misclassification may occur in this situation where the ponded sea ice is instead classified as sea ice (Figure 3.10d). Also, along the sea ice edge, where mixed pixels occur, the pixels are classified as 'other' (Figure 3.10d, green).

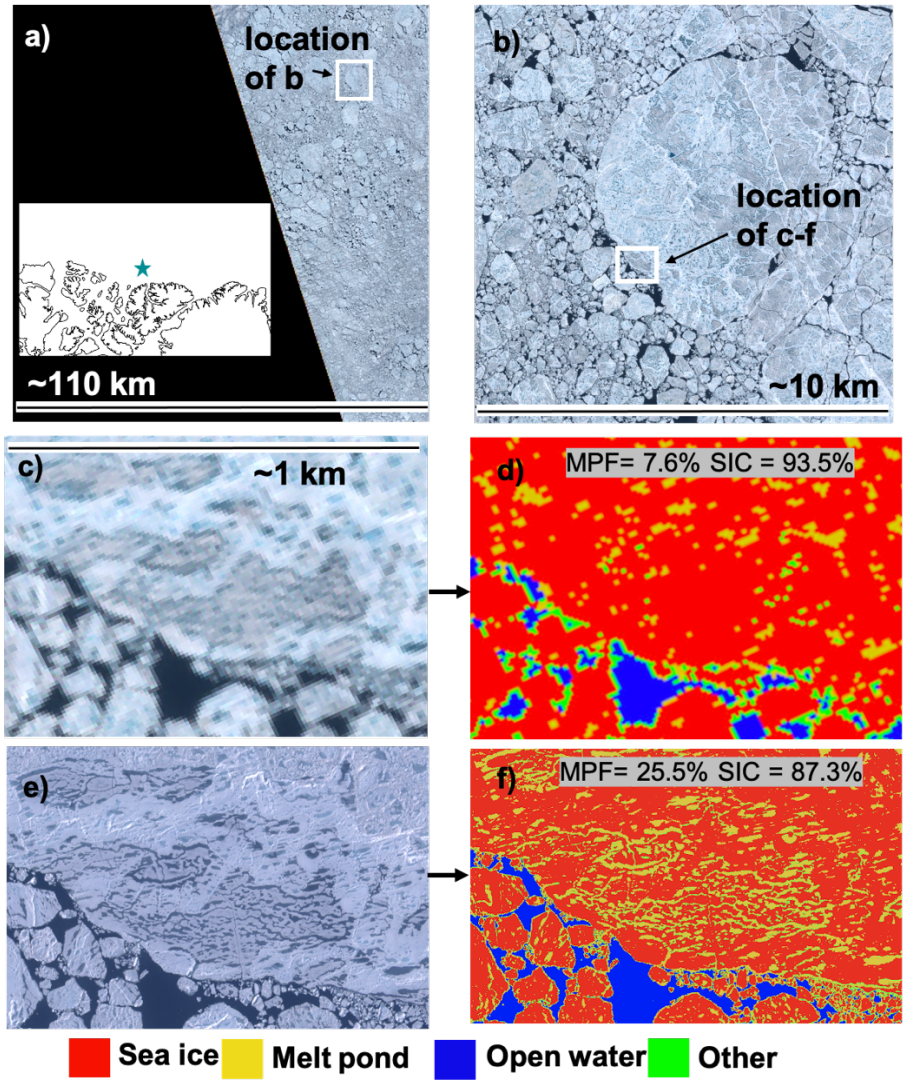

Figure 3.10. Example classification of Sentinel-2 imagery at (-110° W, 80° N) observed on 27 July 2020. (a) Sentinel-2 tile shown in true color. The white box in (a) shows the location of (b). (b) A zoom in of the Sentinel-2 image, shown in the white box in Figure a. The 1 km by 0.8 km white box in (b) shows the location of (c-f). (c) is the zoom in of (a) and (e) shows spatially and temporally coincident WorldView imagery (WorldView imagery copyright 2020 Maxar). Classification of these images are shown in (d) and (f), respectively with sea ice (red), melt ponds (yellow), open water (blue), and other (green). Figure from Buckley et al., 2022.

3.6.4 Melt Pond Color Classification

In the Sentinel-2 and WorldView imagery classification, we do not separate the melt ponds into dark, medium, and light-colored melt ponds, as we do in the DMS

imagery. That step in the DMS imagery classification is used for a comparison of melt pond colors on different ice types, but for the study presented in Chapter 6, we only work with the multiyear ice region when classifying Sentinel-2 and WorldView.

3.7 WorldView Imagery Classification

We only utilize about 20 WorldView scenes in this work, and so preprocessing and quality control is done manually. We visually inspect for lands and clouds in the imagery and use images containing only sea ice and water. The WorldView classification follows the same classification routine as the Sentinel-2 imagery. We utilize WorldView bands 5 (red), 3 (green), 2 (blue), and 7 (near-infrared). The classified WorldView images are used for comparison with coincident Sentinel-2 imagery to assess the errors and limitations that occur with the lower resolution Sentinel-2 dataset (Chapter 6, section 6.4.1).

3.8 Derived Summer Melt Parameters

After the classification of each surface pixel, we derive summer melt features on sea ice by taking ratios of ice-type pixels. SIC, MPF and PCF (for DMS imagery) are derived on a per-image basis, thus taking advantage of the highest resolution available.

3.8.1 Sea Ice Concentration

WMO (1970) defines SIC as “the amount of the sea surface covered by ice as a fraction of the whole area being considered.” Here, we calculate the percentage and define SIC as:

$$SIC = \frac{MP + ICE}{MP + ICE + OW} \times 100 \tag{3.20}$$

3.8.2 Melt Pond Fraction

MPF is the ponded area relative to the sea ice area (Webster et al., 2015). We define MPF as the ponded percentage of the sea ice area:

$$MPF = \frac{MP}{MP + ICE} \times 100 \tag{3.21}$$

Here we calculate MPF for all data collected within the ice pack, defined as areas where SIC > 15%. This minimizes the effects of submerged ice draft or brash ice contributing to the MPF parameter close to the ice edge.

3.8.3 Pond Color Fraction

For the DMS imagery where the melt pond classification is separated into light, medium and light-colored ponds, we calculate PCF as an additional statistic to normalize the pond color pixels by the total melt pond pixels per image. The number of surface pixels in each pond color classification type (light, medium, dark) is divided by the total number of MP pixels in the image to determine the make-up of pond color within the image:

$$PCF_{DARK} = \frac{DMP}{DMP + MMP + LMP} \times 100 \tag{3.22}$$

$$PCF_{MED} = \frac{MMP}{DMP + MMP + LMP} \times 100 \tag{3.23}$$

$$PCF_{LIGHT} = \frac{LMP}{DMP + MMP + LMP} \times 100 \quad (3.24)$$

3.9 Chapter Summary

In this chapter we described the classification algorithm developed to identify high resolution sea ice image pixels as sea ice, open water, and melt pond. In the DMS imagery, we further classified melt ponds into light, medium and dark-colored ponds. Sections 3.2-3.4 described the DMS imagery classification from Buckley et al., 2020a. Section 3.6 detailed the modifications made to the algorithm for application to Sentinel-2 imagery. These modifications include: a land mask (3.6.1), the incorporation of the NIR band to improve the disambiguation of water and ice pixels (3.6.2), and the introduction of the 'other' category to account for larger pixel size in the Sentinel-2 imagery, where pixels may contain multiple surface types (3.6.3). In the WorldView and Sentinel-2 imagery classification, we introduced a classification category: 'mixed pixels', to account for the larger pixels. We discussed the calculation of geophysical parameters: SIC, MPF, and pond color fraction (Section 3.8). DMS classification results are shown and discussed in Chapter 4. The classification of Snetinel-2 and WorldView images for understanding melt evolution in 2020 is presented in Chapter 6. Conclusions and suggestion of future work with the classification algorithm is offered in Chapter 7.

Chapter 4: Classification of Sea Ice Summer Melt Features in High-Resolution IceBridge Imagery

4.1 Motivation and Goals

This chapter presents the results from the classification of the Operation IceBridge Digital Mapping System (OIB DMS) imagery from the 2016 and 2017 Arctic summer campaigns (Buckley et al., 2020a). The goals of this chapter are:

- Present the results of the DMS image classification using the methodology described in Chapter 3.
- Describe patterns of melt features (open water, sea ice, melt ponds) and derived parameters: sea ice concentration (SIC), melt pond fraction (MPF), and pond color fraction (PCF).
- Put results into context of existing datasets and literature

In section 4.2, we describe the application of the algorithm to the DMS imagery and discuss the along-track patterns of the classified melt features and parameters. In section 4.3 we focus on the derived SIC and compare with existing SIC datasets. In section 4.4, we look at the MPF and compare to findings from previous studies. Section 4.5 describes the regional differences in pond characteristics, and Section 4.6 presents the impact of misclassified pixels. The chapter is summarized in section 4.7.

4.2 Feature Classification

We applied the classification algorithm to 17,033 DMS images, covering an area ~4,000 km^2 in size (Buckley et al., 2020a). The percentages of surface pixels classified in each ice-type category were automatically calculated on a per-image basis. Table 4.1 summarizes the classification statistics averaged per flight, both in terms of the percentage of ice type categories and the derived data products (SIC and MPF). Open water percentages in the B/C Seas surveys over the marginal ice zone (MIZ) (19– 38%, Table 4.1) are much greater than those in the CA region in the consolidated ice pack (4–16%, Table 4.1). MP color classification percentages are also related to the regional ice types; dark MPs are more prevalent in the B/C Seas region on first year ice; light MPs are more prevalent in CA region of multiyear ice (Table 4.1). The melt pond fraction and color are also related to the timing of surveys related to the regional melt onset date. The time elapsed between melt onset and the survey flights was greater in 2016 than in 2017, allowing ponds more time to evolve. The highest percentage of dark MPs (17%, Table 4.1) was found on 15 July 2016, a flight conducted entirely south of 75°N, in an area well into the melt season (Anderson et al., 2019). MPF results are further discussed in section 4.3.

Table 4.1. Results of automatic surface classification, averaged per flight.

	Classification Category (%)							Sea Ice Concentration (%)					Melt Pond Fraction (%)				
Flight Date	**N**	**UI**	**DI**	**OW**	**DMP**	**MMP**	**LMP**	**N**	**mean**	**5%**	**95%**	**stdev**	**N**	**mean**	**5%**	**95%**	**stdev**
13 July 2016	1759	42.9	0.2	38.4	5.1	2.5	10.9	1759	61.6	0.0	100.0	43.4	1222	31.2	12.4	67.6	16.5
14 July 2016	1523	61.2	0.5	18.9	10.3	2.6	6.5	1523	81.1	26.9	100.0	22.3	1475	23.2	10.6	40.8	11.5
15 July 2016	2540	45.6	0.6	32.2	17.2	0.8	3.6	2540	67.8	11.6	100.0	26.8	2351	31.9	17.4	61.7	14.8
19 July 2016	2774	54.1	0.4	31.5	9.2	1.1	3.7	2774	68.5	0.0	100.0	29.4	2469	20.0	8.9	33.8	8.0
20 July 2016	225	55.8	1.2	29.7	9.7	1.3	2.3	225	70.3	0.0	100.0	34.6	193	18.7	1.5	92.0	25.2
21 July 2016	654	60.5	1.3	26.6	7.0	1.1	3.5	654	73.4	0.0	100.0	32.9	577	16.3	1.4	55.0	17.8
17 July 2017	985	83.0	0.5	7.6	1.6	0.5	6.8	985	92.4	71.4	100.0	11.5	980	9.6	3.1	19.7	7.6
18 July 2017	158	84.6	1.0	4.2	1.1	1.1	8.0	158	95.8	86.7	100.0	4.6	158	10.6	4.7	23.5	5.9
24 July 2017	2268	69.8	1.0	15.9	2.2	2.8	8.3	2268	84.1	14.4	100.0	22.2	2153	15.7	9.5	22.0	5.0
25 July 2017 (a)	2120	79.3	0.3	6.7	3.0	2.5	8.2	2120	93.3	79.6	100.0	7.5	2119	14.6	6.5	23.4	6.0
25 July 2017 (b)	2027	78.5	0.0	8.9	1.2	1.4	10.0	2027	91.1	75.1	100.0	9.7	2027	13.8	7.8	19.8	4.5

Note. Percentage of surface pixels in classification categories: undeformed ice (UI), deformed ice (DI), open water (OW), dark melt pond (DMP), medium melt pond (MMP) and light melt pond (LMP). N is the total number of classified images per flight. Table from Buckley et al., 2020a.

We examine the along-track variability in the percentage of sea ice (deformed and undeformed), open water, and MPs (light, medium, dark), per image in the flight profiles. The along-track classification is more variable in the B/C Seas than in the CA (Figures 4.1a and 4.1b). Large deviations in the percentage of open water in the B/C Seas are observed (blue line, Figure 4.1) and increase to 100% for a stretch of images during the 19 July 2016 flight. More along-track consistency in the surface classification percentages is observed in the CA. There, ice cover characteristics are less variable, with consistently low percentages of OW pixels (between 0% and 20%) and high percentages of ice pixels throughout the flights (between 60% and 100%). The exception is the 24 July 2017 flight, which sampled the Lincoln Sea polynya at the northern limit of the Nares Strait, where a large area of open water contributed to a high flight-averaged open water percentage of 16% (Table 4.1). The percentage of melt pond pixels per image is dependent on the amount of ice in the image. The MP pixel percentage in the B/C Seas ranges from 0–50%, exhibiting high variability in MP pixels per image, because of the high variability in SIC in this region. The flight averaged MPFs in this region range from 16% to 32% (Table 4.1). The highest MP percentages and highest MPF (32%, Table 4.1) were observed during the 15 July 2016 survey (Figure 4.1a). MP areal percentages are lower and less variable in the CA at ~20%, resulting in flight-averaged MPFs that range from 10% to 16% (Table 4.1).

Next, we consider the MP color classification, which reveals regional differences in pond type. The along-track profiles allow us to examine the variability as the flight traverses the ice cover (Figures 4.1c and 4.1d), while the histograms

provide a summary of the PCF for the entire season (Figures 4.1e and 4.1f). Dark MPs are the predominant MP type in the 2016 surveys over the B/C Seas (Figure 4.1e), with the exception of the flight on 13 July 2016 (Figure 4.1c). The two flights that exhibit the highest fraction of dark MPs (PCFD = 79% and 65%) (Figure 4.1c), are located in the Chukchi Sea. In contrast, light MPs prevail in the CA region (Figure 4.1f). Only a small segment of the 25 July 2017 (a) flight had more dark MPs than light MPs (Figure 4.1d). On average in the B/C region, PCFD was 60%, PCFM was 9%, and PCFL was 31% (Table 4.1, Figure 4.1e). In the CA region PCFD was 16% on average, PCFM was 16%, and PCFL was 68% (Table 4.1, Figure 4.1d). These results confirm that MP color is closely related to the ice type on which the MP forms.

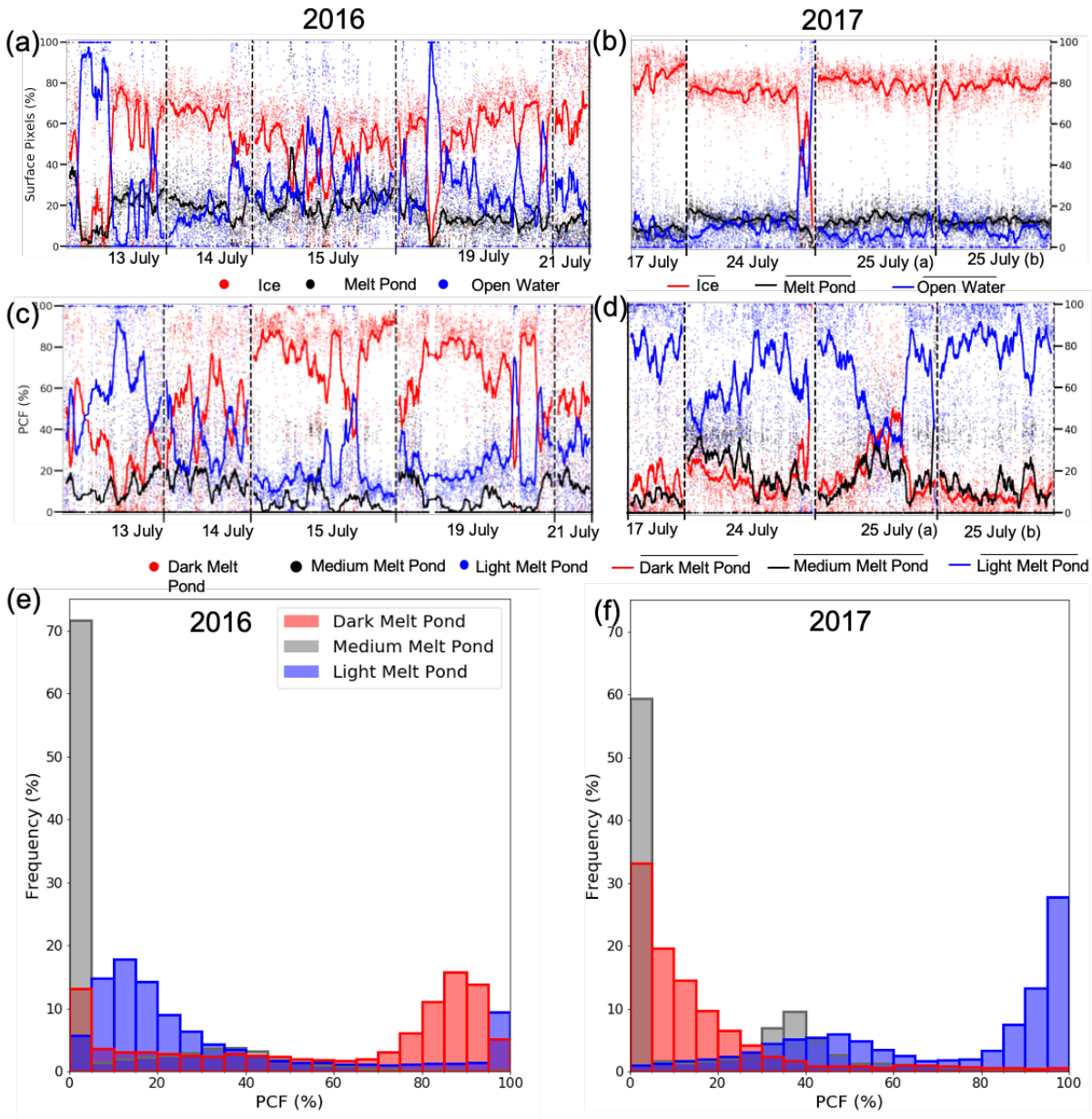

Figure 4.1. Results of DMS image classification. (Top row) Percentage of surface pixels classified as ice (red dots), MP (black dots), and open water (blue dots) in 2016 (a) and 2017 (b), with running means calculated over 100 images (solid lines). Results are presented in chronological order, with vertical dashed lines (black) separating flights. (Middle row) PCF showing percentage dark (red), medium (black), and light (blue) MPs per image in 2016 (c) and 2017 (d). Solid and dashed lines same as in top row. (Bottom row) Frequency distributions of PCF for 2016 (e) and 2017 (f). Figure from Buckley et al., 2020a.

4.3 Sea Ice Concentration

Following pixel classification, and applying Equation 3.20 (Chapter 3, subsection 3.8.1), we determine the SIC per image (Table 4.1, Figure 4.2). The high resolution of the parameters results in a wide range of values, because some images contain no open water, while others are 100% open water. We examine the fifth and 95th percentile of the SIC and MPF parameters rather than the minimum and maximum values, as they provide a more robust indication of the range, and do not rely on a single point that may be an outlier. It is interesting to note that the 95th percentile SIC of all flights was 100% (Table 4.1), as expected since these flight surveys were designed to find and measure sea ice. However, the fifth percentile provides more detail about the regional setting, with low values in 2016 in the B/C Seas, which sampled the MIZ (Figure 4.2a), an area of the ice cover affected by waves between the ice edge and the consolidated ice pack (WMO, 1970) and higher values for 2017 in the CA region, which sampled the consolidated ice pack (Figure 4.2b).

The average SIC of all the images during the summer surveys was 79%, with a standard deviation of 28% (Table 4.1). Average SIC was 69% in the B/C Seas and 90% in the CA, with standard deviations of 32% and 15%, respectively (Table 4.1). The B/C Seas flight-averaged SIC ranged from 62% to 81%, and the lowest flight-averaged SIC was observed during the 13 July 2016 survey. Mapping the SIC for that flight line, which occurred along longitude −150°W, shows that the survey crossed large areas of open water at the ice edge (Figures 2.3 and 4.1a), which reduced the

flight-averaged SIC. The fifth and 95th percentiles of SIC for this flight are 0% and 100%, respectively, confirming that this flight sampled both open water areas and the consolidated ice cover. Conversely, the 2017 campaign was conducted almost entirely within the consolidated ice pack, and flight-averaged SIC ranged from 84% to 96%, with the highest concentrations observed during the survey on 18 July 2017 (Table 4.1). However, we note that many of the images from this flight were eliminated due to clouds (46.8%) or aircraft roll (25.8%), leaving only 158 images for analysis. The lowest flight-averaged SIC of 2017 occurred on 24 July, a flight sampling the Lincoln Sea and northern Nares Strait, between Greenland and Ellesmere Island. The flight samples a long stretch of open water (the Lincoln Sea polynya) at the northern limit of the strait, reducing the average SIC observed during this flight survey (Figure 4.2b). The variability of SIC in this flight is demonstrated in Figure 4.2c, where an image at 83.4°N, −59.9°W with 65% SIC, is compared with an image at 83.9°N, −59.6°W, with 100% SIC (Figure 4.2d).

We examine the SIC distributions for the B/C Seas and CA regions in the context of satellite-derived measurements. A wide range of DMS SIC is evident when compared to coincident AMSR2 SIC (Figures 4.2a and 4.2b) and this is demonstrated in Figures 4.2c and 4.2d. We extracted the daily AMSR2 SIC and CDR SIC values, (see Chapter 2, section 2.5 for details on these data), on the same date and at the same location as each DMS image acquired along the OIB flight lines (Figure 4.2e and 4.2f), demonstrating that all data products exhibit the same regional characteristics. Our results show consistency between the DMS-derived SIC and the satellite data sets in terms of mean and modal SIC and overlapping distributions of SIC (Figures 4.2e

and 4.2f) for both regions surveyed. In both regions, the modal SIC was 95–100% for all three products. In the B/C Seas region a secondary mode exists with similar modal values for all three products (DMS SIC 75–85%, AMSR2 SIC 70–75%, CDR SIC 75–80%, Figure 4.2e). The average AMSR2 and CDR SIC in the B/C Seas are consistent at 82% and 81%, respectively, and on average, 12% greater than DMS SIC, which is 69% (Figure 4.2e). AMSR2 SIC and CDR SIC in the B/C Seas have wider distributions (Figure 4.2e) than in the CA region (Figure 4.2f), where more than 90% of the satellite-derived data have a SIC of 95% or more.

The AMSR2 SIC in the CA region shows almost entirely 100% ice concentration with the exception of the site of the Lincoln Sea polynya at the north of the Nares Strait, whereas the higher-resolution DMS SIC shows there are other areas of low ice concentration (Figure 4.2b and 4.2f). In the CA region, the mean value of SIC recorded by the DMS was 9% less than the average satellite-derived product. Due to their lower resolution compared to the airborne data, the satellite-derived products (AMSR2 SIC at 12.5 km and CDR SIC at 25 km) cannot resolve the smallest areas of open water and thus do not capture the variability of the area that is evident in the DMS SIC results (Figures 4.2a, 4.2b, 4.2e, and 4.2f). The lowest-resolution product is the CDR SIC at 25 km and this shows no ice free grid cells in the campaign region, and a SIC of 35–40% is the lowest SIC observation. In the CA, all three products agree in terms of a modal value of 100% SIC, however, the DMS SIC suggested there is a continuous distribution of SIC ranging from 60% to 100%. Previous validation of the AMSR2 SIC has shown a positive bias of 3.9% (Meier et al., 2017), which is consistent with the results shown here for the CA region.

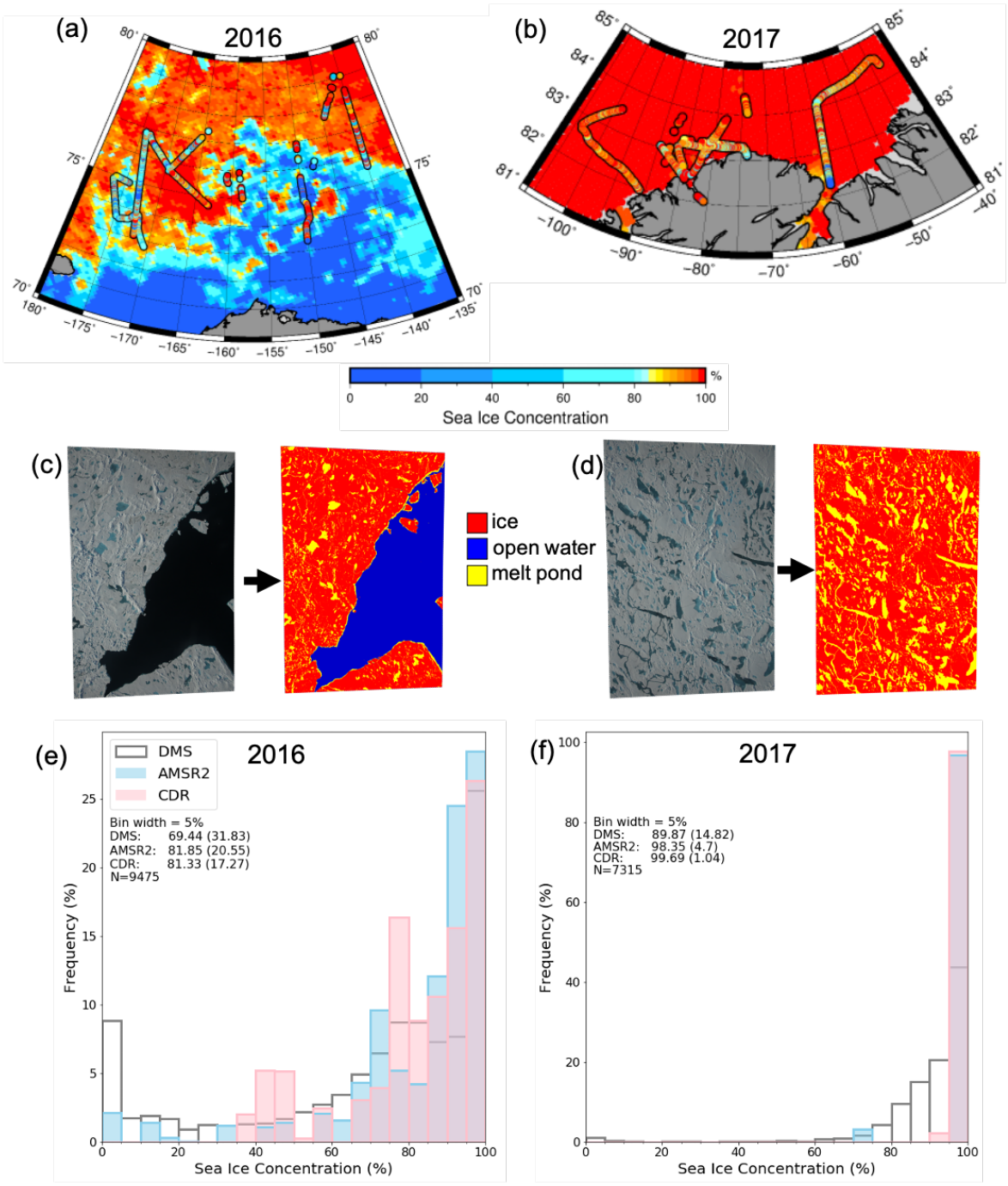

Figure 4.2. SIC results calculated per image. (a) DMS SIC overlaid on the AMSR2 SIC on 17 July 2016 and (b) 21 July 2017. (c) Sample DMS images of sea ice in the Lincoln Sea on 24 July 2017 at −59.3°W, 83.9°N with relatively low SIC (65%) and (b) −59.6°W, 83.4°N with high SIC (100%). (e) frequency distributions of DMS SIC, AMSR2 SIC and CDR SIC, extracted at the same time and location of each DMS image acquisition in 2016 and (f) 2017. Figure modified from Buckley et al., 2020a.

4.4 Melt Pond Fraction

Implementing Equation 3.18 (Chapter 3), we calculate MPF per image. On average, the MPF was 25% in the B/C Seas, and 14% in the CA region, with standard deviations of 15% and 6%, respectively (Table 4.1). The highest flight-averaged MPF was 32%, occurring on 15 July 2016. This flight surveyed sea ice in the Chukchi Sea, at the western limit of the aircraft range from Utqiaġvik, Alaska (Figure 4.3a). The entire flight line was south of 75° N and surveyed areas of ice where the melt season was well underway. Here ponds have fully developed and have laterally spread across ice floes. Conversely, the lowest flight-averaged MPF is 10%, which occurred during the flight on 17 July 2017, over the area north of Greenland and the Canadian Archipelago, an area of known ice convergence (Kwok, 2015), due to coastal boundaries that restrict ice motion (Figure 4.3b). Here, pressure ridges on deformed ice restrict the lateral spread of MPs (Figure 4.3c and 4.3d) and contribute to lower MPF. The 17 July 2017 flight was repeated one week later on 25 July, where the flight-averaged MPF was 14%, an increase of 4% over the survey of the same region one week earlier, demonstrating the temporal evolution of MPF in the CA region.

In our study MPF ranges from 16–32%, with an average of 25% (Table 4.1). This is consistent with the magnitude and variability of MPF found in previous studies. For example, Perovich et al. (2002) found a mean MPF of 18.8% in the northern Chukchi Sea in July 1998, with variability between 5% and 50% (Perovich, et al., 2002). Rösel and Kaleschke (2012) found MPFs of 40–50% in the B/C Seas in mid-July 2011. Webster et al. (2015) found MPFs ranging from 30% to 50% in a

study area on first year ice in the southern B/C Seas, overlapping with the region surveyed by OIB in 2016.

We found an average MPF of 14% in the CA region in mid-July 2017 (Table 4.1, Figure 4.3b), slightly lower than previous studies have reported. For example, Rösel and Kaleschke (2012) reported MPFs ranging from 25– 35% in mid-July 2011 in the CA region, north of Greenland and Ellesmere Island, Mäkynen et al. (2014) found MPFs ranging from 22% to 43%, averaging 34% in July 2009 in the Greenland Sea to the northeast of Station Nord, and Istomina et al. (2015) found MPFs ranging from 10% to 30% north of Greenland in mid-July 2009.

We also demonstrate the reliability of our DMS results by evaluating DMS-derived MPF using MPF derived from a Sentinel-2 image that is coincident with a section of a flight line in the Lincoln Sea over mixed sea ice conditions. On 24 July 2017, Sentinel-2 captured imagery of the Lincoln Sea and northern Nares Strait, near coincident in time to a 57 km segment of the DMS survey that occurred the same day (delta time = 4.5 hours). To assess algorithm performance, we apply our classification algorithm to a 5 km wide strip of Sentinel-2 True Color Imagery (TCI) centered on the 57 km-long section of the DMS survey. We split the Sentinel-2 TCI into 57 sections (1 km long by ~ 5 km wide) and a comparison to classification results with 398 spatially coincident DMS images in this region is shown in Figure 4.3f. The results show strong agreement in the MPF distribution derived from both DMS and Sentinel-2 imagery, which is asymmetric in both cases with a modal MPF value of 10–15% (Figure 4.3f). Mean MPF was 15% for DMS images and 13% for Sentinel-2.

We find 90% and 100% of the DMS-derived and Sentinel-2-derived MPF fall within 0–25%, respectively. Ten percent of DMS images had a derived MPF in the range 25– 60%, demonstrating the ability of high-resolution imagery to capture more variability in the ice cover at a smaller scale that is not fully captured in the lower-resolution (10 m) Sentinel-2 images. In section 6.4.3 we further discuss the impact of lower resolution data on the derived MPF and SIC is provided in section 6.4.3 where we compare the Sentinel-2 and WorldView derived parameters.

A final step is to consider images with very high MPF, inspecting those with a derived MPF greater than the 95th percentile (40% MPF) (821 images, 5% of the processed images). An example is shown of sea ice in the Lincoln Sea (Figure 4.3d), where a large pond in the upper left of the image had not yet drained through the thick, multiyear ice and had spread laterally across the relatively undeformed sea ice surface until a ridge was encountered. Previous studies have found MPFs of up to 75% on first year ice (Scharien and Yackel, 2005). In our study, less than 1% of images have MPFs of 75% or greater. Images with many small areas of submerged ice (ice draft) misclassified as MPs could also result in MPFs that are biased high (see Chapter 3, section 3.5.5).

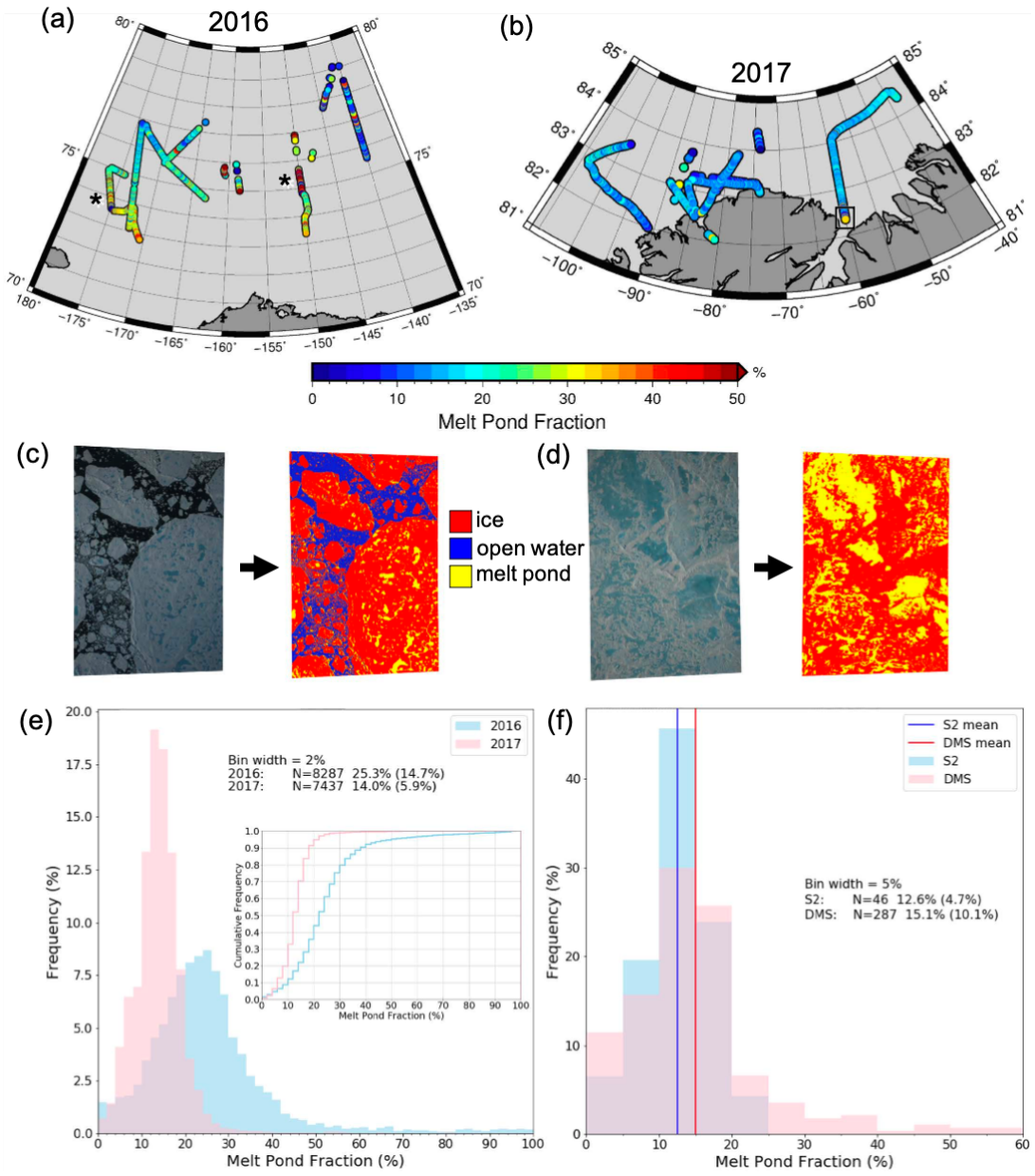

Figure 4.3. MPF results calculated per image. (a) MPF mapped for 2016, where * marks area with anomalous MPF > 40% and (b) 2017, with the black box indicating the region compared with coincident Sentinel-2 imagery. (c) Sample DMS images of sea ice in the Lincoln Sea acquired on 24 July 2017 at −59.6° W, 83.3°N with low MPF (17%) and (d) −59.9°W, 82.6°N with high MPF (50%). (e) Frequency distributions of MPF for 2016 (blue) and 2017 (pink). Inset is cumulative distribution of MPF for 2016 (blue curve) and 2017 (pink curve). (f) MPF distribution for coincident Sentinel-2 segments (light blue), DMS images (pink). The average MPF derived from Sentinel-2 strips and coincident DMS images is indicated by dark blue and red vertical lines, respectively. Figure modified from Buckley et al., 2020a.

4.5 Regional Pond Characteristics

The divergence in the 2016 and 2017 DMS classification results is not a function of time but rather related to the latitudinal location and ice types in the two areas. Compared to previous years, 2016 exhibited a lower sea ice extent the B/C Seas (Fetterer et al., 2017). On July 13, just prior to the commencement of the campaign, the Deadhorse meteorological station in Prudhoe Bay, Alaska experienced a record-setting high temperature of 29 °C (Menne et al., 2012). The melt onset in the southern Beaufort Sea occurred in late April and early May, 6 weeks prior to the average melt onset date (Anderson et al., 2019). In contrast, the 2017 surveys were conducted north of Greenland and Ellesmere Island in the CA region, an area that experiences regional ice convergence and is pushed against the continent (Haas, 2017). Here, thick, deformed ice is trapped and more likely to survive the summer melt season and continue to grow in the following winter. Thus, the CA region is composed of predominantly multiyear ice. These conditions result in a consolidated ice cover, with minimal open water for new ice to form. Melt onset in this region occurred in early to mid- June (Anderson et al., 2019). The regional differences in ice type and the timing of melt onset explain the distributions of 2016 and 2017 MPF and SIC (Figures 4.2 and 4.3).

SIC in the B/C Seas region was significantly lower than in the CA (Figures 4.2e and 4.2f), because the ice edge retreats off the north coast of Alaska early in the melt season. The 2016 flights sampled a mix of ice types primarily in the MIZ, and a mean SIC of 69% was recorded in the B/C Seas, compared to an average SIC of 90%

in the CA. The SIC distribution in the B/C Seas is bimodal due to one flight occurring in the consolidated ice pack and the others occurring in the MIZ. The sea ice in the B/C Seas region is more mobile because it is influenced by the Beaufort Gyre, creating divergence in some areas and convergence in others (Haas, 2017). For these reasons, the standard deviation of SIC in B/C Seas region was 32%, 17% greater than that in the CA (at 15%). The results validate the expectation that MPs present differently on the first year ice than on multiyear ice (Figure 4.3e). The predominantly first year ice area surveyed in 2016 exhibits a higher MPF, with more variability than the predominantly multiyear ice area surveyed in 2017. The average MPF calculated per image in the B/C Seas is 25% with a standard deviation of 15% (Table 4.1). This compares with an average MPF of 14% with a standard deviation of 6% in the CA. The B/C Seas region, although predominantly first year ice, does include multiyear floes imported into the region via the Beaufort Gyre, which may explain the wider distribution of MPF in this region.

Our results also demonstrate that the MP color distribution is closely linked with ice type, as expected. Overall dark MPs dominated in the B/C Seas regions (with an average PCFD of 60%) while light ponds dominated the CA region (with an average PCFL of 68%). Because the color of the MP is related to the albedo of the pond, which controls the amount of sunlight absorbed and transmitted by the sea ice cover, our derived MPF and PCF suggest that sunlight absorption in the Arctic is regionally variable, with lower transmission rates in the Central Arctic. We can expect an increase in light transmission as the sea ice continues to transition to a higher fractional first year ice cover (Perovich et al., 2018), although the precise

nature of future changes will also be influenced by the latitudinal location of the remaining summer sea ice and its cumulative exposure to incoming solar radiation throughout the melt season. This would have important consequences for the marine ecology of the region, where large phytoplankton blooms are expected to become more common with increasing light transmission through the sea ice (Arrigo et al., 2012; Horvat et al., 2017).

4.6 Pixel Misclassifications

In this section we discuss the impact of potential misclassification of pixels (described in section 3.5.5) on the derived SIC and MPF products. First, we consider SIC. Pixels misclassified as melt ponds due to sun glint and open water (section 3.5.5) could potentially increase SIC anomalously, while misclassification of melt pond as sea ice and vice versa do not impact the estimate of SIC since both are considered “ice: in the calculation of SIC. However, the overall consistency between the DMS SIC results and the independent and coincident AMSR2 and CDR SIC products (section 4.3, Figures 4.2a and 4.2b) demonstrates the robustness of the pixel classification technique and the reliability of the DMS SIC. In both regions, the distributions of SIC derived from the DMS, AMSR2, and CDR data have a modal value of 95–100% SIC. Moreover, the DMS SIC product shows consistent spatial gradients in SIC with the AMSR2 SIC at a regional level as well (Figures 4.2a and 4.2b). Taken together, these results suggest that the pixel misclassifications contributing to a positive SIC bias are minor, and we can discount the impact of any potential misclassification on the derived SIC results.

Next we consider the impact of pixel misclassification on MPF. The misclassification of ice and open water pixels as melt pond pixels (section 3.5.5) could increase MPF anomalously, while misclassifications of light melt ponds as ice could decrease MPF. Particular misclassifications (such as sun glint classified as ice, ice draft classified as melt pond) occur most frequently in images with low SIC. To mitigate the impact of these misclassifications, we limit the MPF calculation to images with SIC ≥15%. However, care must be taken when interpreting results with anomalously high MPF (MPF > 40%, see section 4.4), which although feasible (Figure 4.3d), may be indicative of a positive bias due to pixel misclassification. MPF > 40% is found in 821 images, (5% of processed images), 585 of which occur in the surveys on 13 July 2016 and 15 July 2016 (see survey regions marked by the symbol: * in Figure 4.3a).

4.7 Chapter Summary

In this chapter we described the results of applying the classification algorithm developed in Buckley et al., (2020a) to over 17,000 DMS images collected over sea ice undergoing melt in the summers of 2016 and 2017. We discussed the along-track variability in the percentage of sea ice, open water and melt ponds (Section 4.2). The results showed steady along-track values of classification percentages in the Central Arctic region, with more variable results in the Beaufort and Chukchi Seas. SIC averaged 69% in the Beaufort and Chukchi (B/C) Seas and 90% in the Central Arctic (CA). We found that both MPF and PCF are dependent on the ice type on which ponds form. MPF averaged 25% in the B/C Seas, where dark ponds dominated and had a PCF of 60%, compared to a PCF of 9% and 31%, for

medium and light ponds, respectively. MPF averaged 14% in the CA, where the PCF of light ponds was 68%, compared with 16% for both medium and dark ponds. Section 4.3 detailed our findings of the derived SIC and compared the results derived using DMS data with those derived from the AMSR2 and CDR datasets. We found the DMS- derived SIC had more variability than the satellite datasets, and the lower resolution AMSR2 and CDR datasets were biased high, which was consistent with previous studies. In section 4.4 we presented the MPF results and discussed them in the context of previous findings of MPF on first year ice and multiyear ice. In this section we also demonstrated the ability to apply the classification algorithm to Sentinel-2 data. We showed that although the Sentinel-2 and DMS-derived MPF values are largely consistent, the DMS-derived MPF showed more variability than that derived from coincident Sentinel-2 data. This is a key result as we consider the findings described in Chapter 5, where we apply the classification algorithm to thousands of Sentinel-2 images. The regional characteristics of the derived parameters were discussed in Section 4.5, and we found that these parameters are closely linked with ice type. We also discussed the impact of potential pixel misclassification and concluded that care must be taken when interpreting results with MPF > 40%, but the overall effects of pixel misclassification on the derived MPF and SIC were minimal. The impact of the findings presented and discussed in this Chapter are discussed in Chapter 7, Conclusions.

Chapter 5: Melt Pond Depth Retrieval from Laser Altimetry

5.1 Motivation and Goals

Measurements of the sea ice and local sea surface height allow for the calculation of sea ice freeboard, and when combined with snow depth estimates, can provide sea ice thickness estimates (e.g., Laxon et al., 2013) (see Chapter 2, section 2.6.1). Measurements of sea ice thickness from submarines combined with those from altimeters reveal that the average thickness at the end of the melt season has decreased by 53% (1.6 m) over 40 years (from 1958-2008) (Kwok and Rothrock, 2009). Despite this knowledge, we still lack the ability to derive Arctic wide summer sea ice thickness estimates. In the summer, altimetry is impacted by the melting sea ice surface (Sallila et al., 2019; Kwok et al., 2021). Because the melt ponds that form on the sea ice in the summer appear radiometrically similar to open water, algorithms to derive the sea ice freeboard and thickness break down. Furthermore, the presence of melt ponds and weight of meltwater within the ponds effect the traditional sea ice thickness calculations based on hydrostatic equilibrium (See Chapter 2, section 2.6.1). A crucial step towards adjusting algorithms to derive sea ice freeboard and thickness is understanding the altimeter response to the melting sea ice surface. The goals of this chapter are to:

- Develop a technique for deriving melt pond depth from Operation IceBridge Airborne Topographic Mapper (ATM) waveform data by utilizing the classified DMS imagery (Chapters 3 and 4).

- Develop the melt pond algorithm (MPA) to identify and track melt ponds in the ICESat-2 photon cloud.
- Describe the Density Dimension Algorithm – bifurcate – sea ice that we use to augment and compare with the MPA tracking.

We utilize altimetry to measure melt ponds that form on Arctic sea ice in the summer. Because of their small size (less than 1 meter to 100s of meters in width) (Perovich et al., 2002b), high resolution measurements of the sea ice surface are necessary. Both ATM and ATLAS have a sufficiently small footprint and high sampling frequency that the measurement of melt ponds requires. The green light (532 nm) of the both the ATM and ATLAS lasers is able to penetrate the surface of a melt pond, travel through the water column and reach the bathymetry of the pond (see Chapter 2, Figure 2.6), and thus laser energy is returned from both the pond surface and the bathymetry (Buckley et al., 2019). The chapter is organized as follows: section 5.2 describes the derivation of melt pond depth from the ATM. We describe the algorithms developed to track melt ponds in ICESat-2 section 5.3.

5.2 Analysis of Airborne Topographic Mapper Altimetry

The ATM Return Strength and Elevation with Waveforms product is available from the seven sea ice flights conducted as part of the 2017 OIB summer sea ice campaign (see Chapter 2.6.2 for more details about the dataset). In this section, we demonstrate the ability to derive melt parameters from the waveform data (Buckley et al., 2019). The section is a feasibility study, and provides a path forward for future work.

To determine the ATM returns that are associated with melt ponds, we use the classified OIB Digital Mapping System (DMS) imagery (Chapter 3). The DMS and ATM data were collected simultaneously from the OIB aircraft (Figure 5.1a). With the classified DMS imagery (Figure 5.1b) we are able to determine which coincident ATM returns are melt ponds (Figure 5.1c).

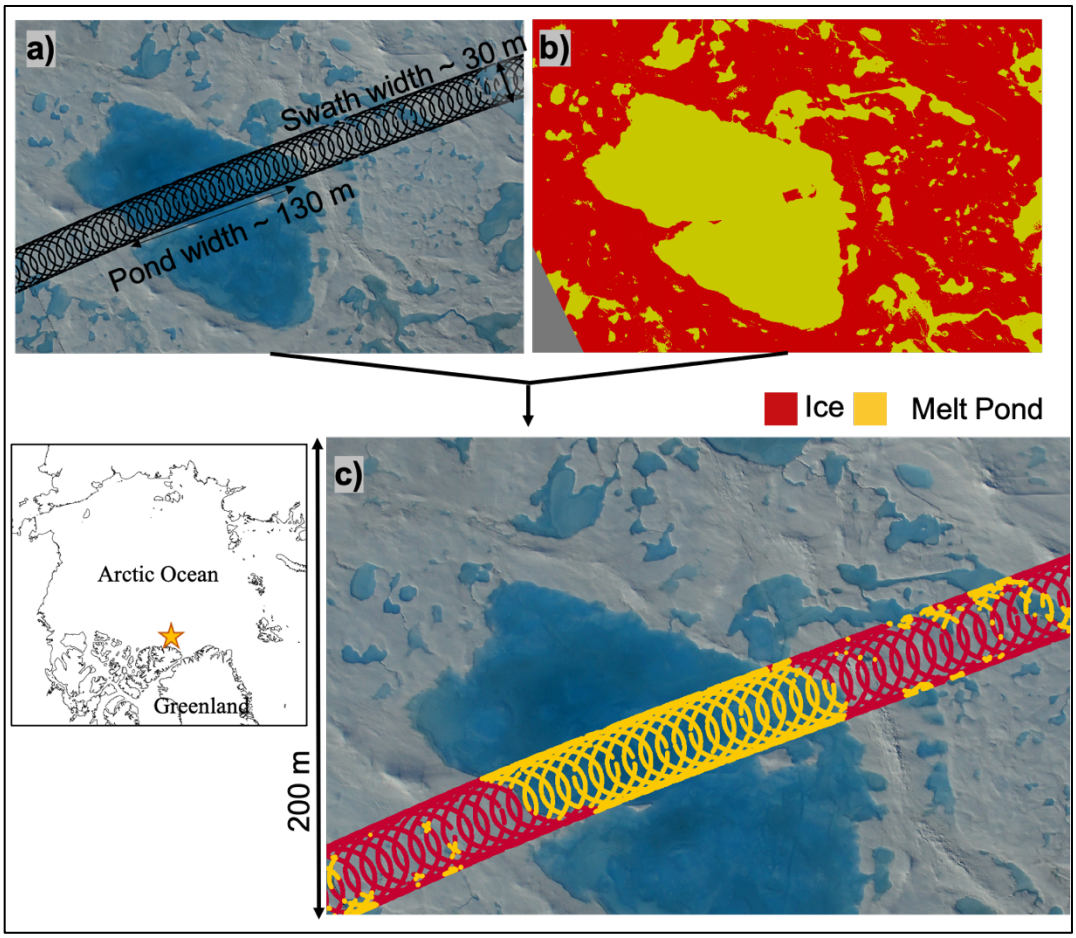

Figure 5.1. Classification of ATM measurements. a) ATM swath over coincident DMS imagery. b) DMS imagery classified following Buckley et al. (2020a), and described in Chapter 3. c) resulting ATM classification. Data were collected north of Ellesmere Island on 25 July 2017.

The ATM retrievals over a ponded surface show elevations from the bottom of a pond and the top of the pond (Figure 5.2a). These elevations are determined from the time of flight between the transmitted pulse and the centroid of the highest

amplitude mode in the returned waveform (Studinger, 2018). However, there is more information contained within the waveform product. There are several parameters that describe the return waveforms, one of which is the count parameter. This indicates the number of pulses with an amplitude greater than the threshold of 35% of the maximum amplitude (Studinger, 2018). The ATM response over melt ponds can be bimodal, where the first mode (R_xm_1) corresponds to the response from the melt pond surface, and because the green laser is able to penetrate water, the second mode (R_xm_2) corresponds to the pond bathymetry (Figure 5.2b-c).

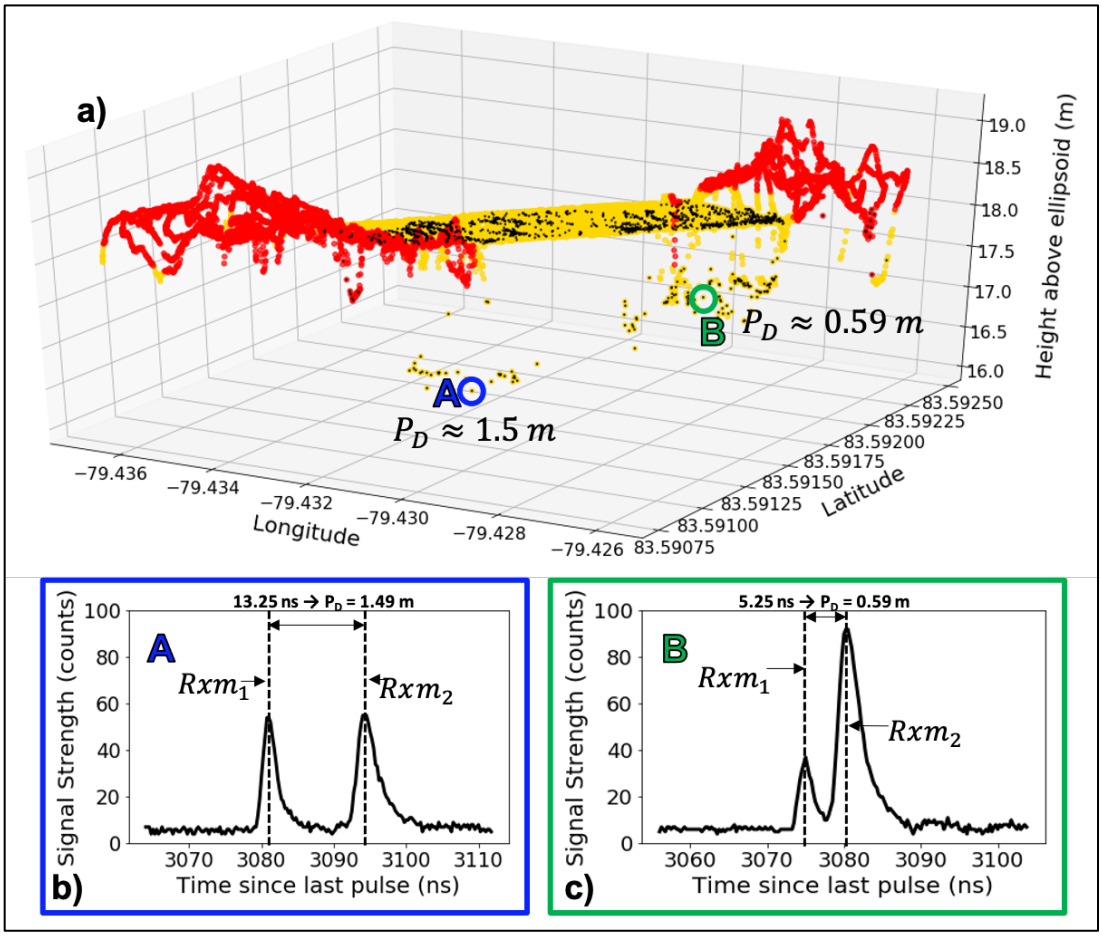

Figure 5.2. ATM laser response over melt ponds. (a) A three- dimensional view of melt pond demonstrating returns from bottom of pond and prevalence of bimodal ATM waveform returns (black dot) in the pond. (b) waveform return from deep melt

pond corresponding to a depth of 1.5 m. (c) waveform return from shallower part of melt pond indicated pond depth of 0.6 m. Same pond as in Figure 5.1.

Bimodal returns can occur over surfaces that are not melt ponds, such as pressure ridges, where the ATM footprint includes a ridge and the level sea ice surface. In this case, the first returned pulse is from the higher elevation ridge, and the second pulse, from the level ice surface. To ensure we are only looking at the bimodal returns over melt ponds, we only look at ATM returns that have been classified as melt ponds. We are able to approximate pond depth by differencing the time between the two modes and applying a correction for the refractive index of water:

$$P_D = (R_x m_2 - R_x m_2) \times \frac{\eta_a}{\eta_w} \times c \div 2 \tag{5.1}$$

where P_D is pond depth in meters, R_x is the return pulse with modes m_1 and m_2 at time since the transmit pulse, c is the speed of light, η_a is the index of refraction of light in air (~1.00) and η_w is the index of refraction of light in water (~1.33). The range is divided by two to account for two-way travel time.

This calculation is demonstrated in Figure 5.2b-c, where the pond depth was determined to be 1.5 and 0.59 m for b) and c) respectively. We establish the feasibility of deriving melt pond depth from ATM data, and create a path forward for applying this methodology to all flights in the 2017 OIB campaign.

5.3 Analysis of ICESat-2 Altimetry

In the ICESat-2 ATL03 photon cloud, we see photons outlining the two-dimensional shape of the melt ponds (see Chapter 2, Figure 2.10 and Chapter 5,

Figure 5.3a), with photons returned from both the surface of the pond and the bottom of the pond. There is currently no ICESat-2 product that is able to track both surfaces, and no automatically generated depth estimates of these ponds. However, there are currently two available methods to estimate the depth of melt ponds using ICESat-2 altimetry: the University of Maryland Melt Pond Algorithm (MPA) (Farrell et al., 2020) and the Density Dimension Algorithm (DDA) (Herzfeld et al., 2017, 2021). Both algorithms track the surface and the bathymetry of individual ponds. For each pond, we subtract the height of the pond bathymetry from the height of the pond surface at 5 m increments and apply a refraction correction to account for the change in speed of light in water as in Farrell et al. 2020. In this way, we are able to estimate melt pond depth, an important characteristic of the signature melt ponds, relating to meltwater volume and affecting the hydrostatic balance of the sea ice.

5.3.1 The University of Maryland Melt Pond Algorithm

The University of Maryland Melt Pond Algorithm (MPA) is developed to identify pond surfaces and their bathymetry in the ICESat-2 ATL03 photon cloud. Figure 5.3 demonstrates the methodology to determine the surface and bathymetry of a pond using the UMD MPA. First, we use a cloud indicator based on the apparent surface reflectance parameter (Palm et al. 2021) provided as a flag in ATL07 (Kwok et al., 2021) to identify cloud-free sections of along-track surface height data, with low, medium, and high confidence. If at least 20% of the track within the study region was cloud free, we manually examine the ATL03 photon height data for evidence of melt ponds. In the photon cloud, melt ponds have returns from the pond surface and

pond bottom (Figure 3a). We note the start and end of a pond as the point at which the two surfaces diverge and the distance from the start to the end of the pond defines the pond width. Across the width of the pond, we binned all photons into 0.1 m vertical bins (Figure 5.3b). The mode of the distribution defines h_s, the pond surface height: is (Figure 5.3b, black, Equation 2)

$$h_s = P_n\_ma \tag{5.2}$$

where P_n_ma is the bin containing the maximum count in the vertically binned histogram for all photons across the width of the pond. h_s is reset to an elevation of 0 m and the photon heights are recalculated relative to h_s (Figure 5.3c). A 2-dimensional histogram of photon height data with 0.1 m vertical elevation bins and 10 m horizontal along-track bins. For each vertical bin, we add the photon count from the bins on either side to increase the photon count for each bin. In this way, the vertical bins are overlapping with an effective bin width of 0.3 m at 0.1 m intervals. For each 10 m horizontal along-track segment (as shown in Figure 5.3c), we examine this vertical elevation histogram (Figure 5.3d). We assumed photons within the two bins on either side of the identified surface bin could be associated with the surface and discarded all photons in those bins (Figure 5.3d hatched bins). We located modes in the histogram below the surface that had at least 5% of the number of surface photons (Figure 5.3d, blue bin). If there were no modes that met this threshold, we moved on to the next horizontal segment. If there were multiple modes, we determined the one closest to the surface is associated with the bathymetry of the pond, as it is unlikely there are modes within a pond because the green laser is able to

penetrate through the water column. The elevation of the subsurface mode is the bathymetric depth of the pond (Figure 5.3c, blue, Equation 3).

$$h_b = P_{ni\_}ma_1 \tag{5.3}$$

Bathymetric elevation is determined for each 10 m horizontal section, where $P_{ni\_}ma_1$ is the vertical bin elevation of subsurface mode. The mode must contain at least half of the number of photons as the maximum photon bin in the vertically binned histogram for the section. Pond depth is estimated by differencing the pond surface and bathymetry. We then multiply this depth by the ratio of the refractive index of air to water following Parish et al., (2019) and Farrell et al., (2020).:

$$h_{mp} = (h_s - h_b) \times \frac{\eta_a}{\eta_w} \tag{5.4}$$

Where h_{mp} is the depth of the melt pond, h_s is the elevation of the pond surface, h_b is the elevation of the bathymetry, η_a is the refractive index of air (1.00029), and η_w is the refractive index of water (1.33567) (Mobley, 1995). Pond depth (h_{mp}) is determined for each 10 m along-track segment. To increase along-track resolution a linear interpolator with 5 m length is applied to obtain pond depth at 5 m intervals across the pond. The true surface height within each bin can be +/- 0.15 m from the estimated value (half bin width). When the melt pond surface and bathymetry are differenced to determine the depth, height uncertainty doubles, resulting in a total depth uncertainty of +/- 0.23 m after correction for refraction.

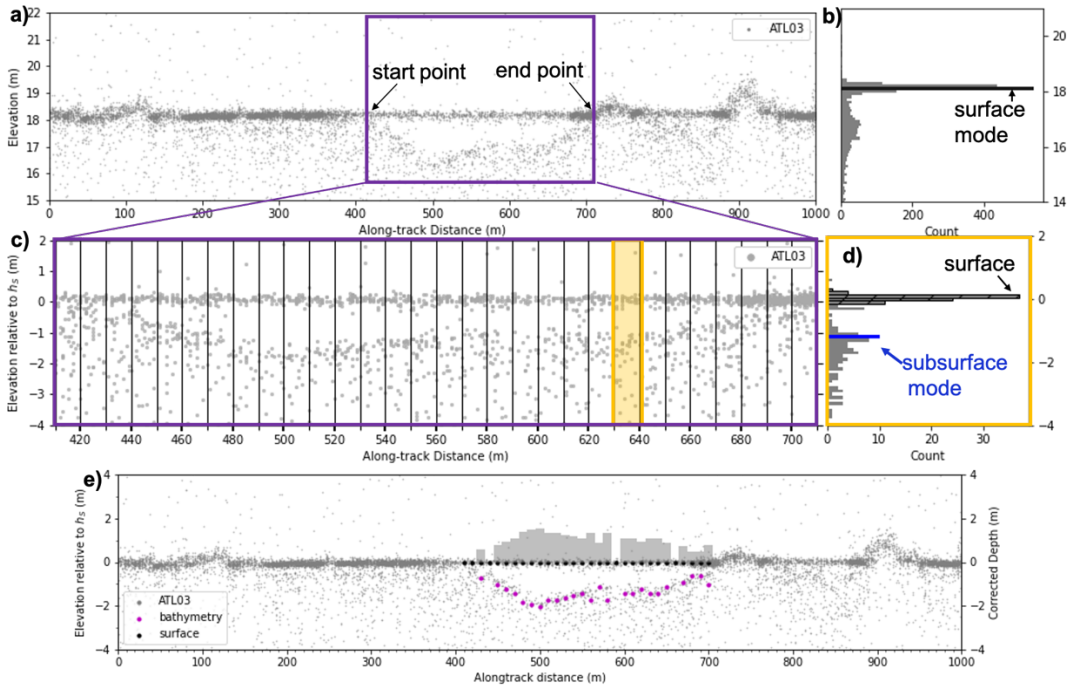

Figure 5.3. MPA methodology. a) melt pond located in the ATL03 photon cloud. The purple box shows the zoom for c). b) shows histogram of the 1 km photon cloud binned at 0.1 m vertically. The mode is identified as the surface and shown in black. c) shows the zoom in over the pond in a) and the horizontal binning at 10 m intervals. The yellow box marks the horizontal section analyzed in the vertical histogram shown in d). In d) the surface bin and two bins on either side are marked with a hatch andthe subsurface mode in blue. e) shows the tracked surface (black), bathymetry (magenta), and corrected pond depth (gray).

5.3.2 The Density Dimension Algorithm – bifurcate – sea ice

The Density Dimension Algorithm (DDA) is a family of algorithms designed to track complex surfaces in micro-pulse photon-counting lidar altimeter data, such as ICESat-2 (Herzfeld et al., 2017, 2021). The DDA- bifurcate-sea ice has the ability to track two surfaces. The algorithm is briefly described here. The DDA-bif-sea ice utilizes the full geolocated photon point cloud as provided in the ATL03 data product. The algorithm employs the calculation of a density field for data aggregation and principles of auto adaptive signal-noise thresholding and roughness determination (as

described for the DDA-ice in Herzfeld et al., 2017). Similar to the MPA, the DDA-bif-sea ice is the ability to detect bifurcating reflectors, in situations where the stronger reflector can be the lower or the higher reflector and the two reflectors may have different spatial distributions and material/reflection properties (Figure 5.4). The DDA-bifurcate-sea ice is auto-adaptive and includes a layer follower with automated adaptation to layer roughness. On rough surfaces, the DDA tracks at 2.5 m intervals, and on smooth surfaces, 5 m intervals. At least 3 depth measurements are required for a pond, so the minimum retrievable pond width is 7.5 m on a rough surface, and 15 m on a smooth surface. For comparison and consistency with the MPA, we resample the DDA tracked surfaces at 5 m intervals. The minimum elevation difference between the two tracked surfaces is adjustable within the DDA, and for the purposes of this work it is set at 0.2 m within the photon cloud, allowing for a minimum retrievable depth of 0.15 m. We use this algorithm for comparison and validation of the MPA, and to fill gaps in the melt pond database.

Upon examination of the tracked DDA surface, we notice two scenarios that frequently cause false positive melt pond detection. In the first case the DDA tracks two surfaces in between sea ice ridges (Figure 5.4a-b). As in Figure 5.4a-b, the surface tracking is not across a level pond surface, but instead, the algorithm bifurcates and the first pass connects the ridges and the second pass tracks in between the ridges. In this case, the first surface typically associated with a melt pond has an uneven, unrealistic “surface.” We filter out these false positives by discarding ponds that have surfaces with a standard deviation greater than 0.05 m. The second case occurs due to the “dead time” of the ATLAS photon detectors (Smith et al., 2019,

Figure 5.4c-d). Where there is a strong surface return, the photon detectors may be saturated, resulting in a period of 3.2 ns where no photons are detected. Following the deadtime, photons are detected and there is a secondary flat return approximately 0.5 m below the surface. In this scenario, the DDA tracks the secondary return as the bathymetry of a pond as seen in Figure 5.4c-d. To account for this false positive, we look at the mean density of the surface return. The distribution of the mean density of the surface returns reveals a bimodal histogram. We have determined that the higher mode corresponds to the scenario where the surface is saturated and a secondary surface return results in false positives in the DDA tracking algorithm. We discard false positive measurements by identifying depth measurements corresponding to the deadtime effect (0.5-0.6 m) where the surface mean density is greater than the minimum between the two modes in the mean density distribution. This process discards 9,117 of 94,543 individual ponds measurements, corresponding to 10% of the measurements, and resulting in a total of 85,426 measurements remaining for analysis.

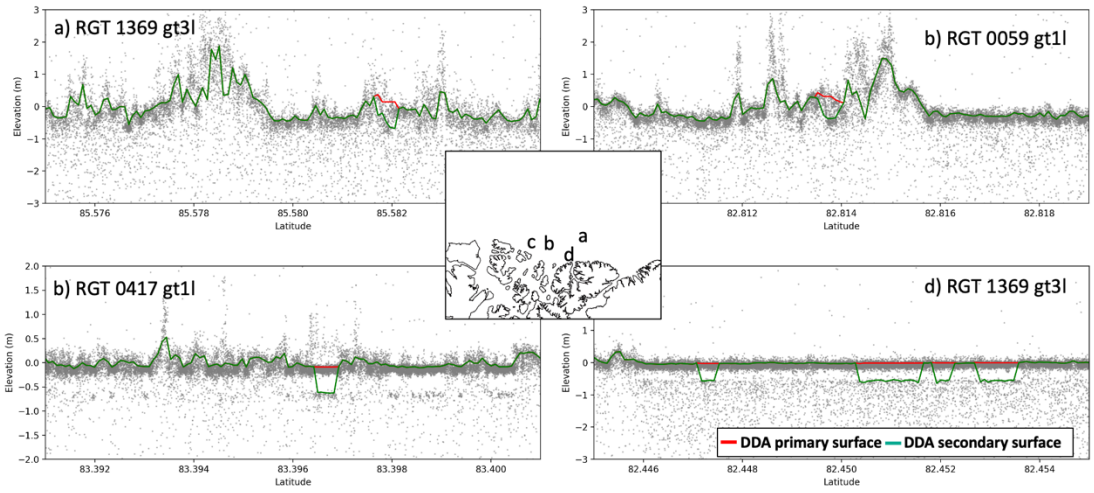

Figure 5.4. Examples of false positive melt ponds detected with the DDA tracking algorithm. a) and b) show DDA bifurcation between ridges with the primary surface connecting the ridges, and the secondary surface tracking the surface between the ridges. c) and d) show the secondary surface tracking the subsurface deadtime effect. The DDA primary surface is shown in red and the secondary surface in green.

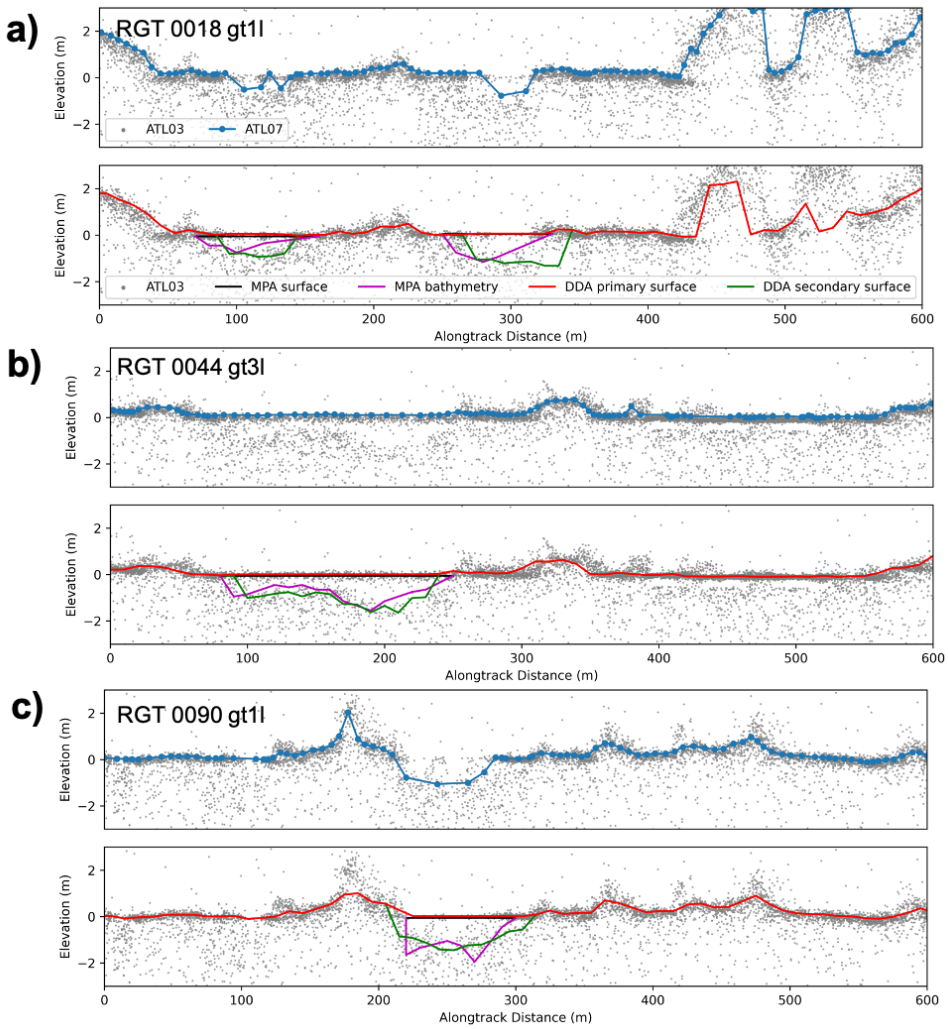

Figure 5.5. Surface tracking algorithms over a ponded surface observed on 28 June 2020, west of the Canadian Archipelago. a-c) three algorithms track the sea ice: the top panel shows the ATL07 (blue), the MPA (surface in black, bathymetry in magenta), and the DDA- bifurcate (surface in red, bathymetry in green). Figure from Buckley et al., 2022.

The top panel of Figures 5.5a-d show the ICESat-2 ATL07 surface tracking algorithm. This algorithm is not able to track two surfaces, and is not able to track pond surface and bathymetry. The ATL07 product tracks the pond surface in Figure 5.5b, the pond bathymetry in 5.5c and alternates between the bathymetry and the surface of the pond in 5.5a, and the two ponds in 5.5d. This motivates our work to

track the melt ponds on the sea ice surface, and to understand how melt ponds affect the ICESat-2 products. Examples of the MPA and DDA tracking algorithms are show in the middle and bottom panels (respectively) of Figures 5.5a-d.

5.3.3 Comparison of Pond Tracking Algorithms

The MPA is not an automated algorithm and requires manual inputs on pond locations, and thus cannot be employed for operational processing of ICESat-2 products. On the other hand, the DDA-bif-sea ice has the ability to automatically track multiple surfaces in situations of complex spatial data distributions and mathematically challenging signal-to-noise ratios. The "DDA-atmos", another algorithm in the DDA family, has been applied for identification of atmospheric layers and surface in the ICESat-2 atmospheric data product, ATL09 (Palm et al., 2021), demonstrating the ability to apply this algorithm at a large scale.

To compare the results of the two pond-depth algorithms, we have located 113 ponds that are common to both data, locations are shown in the next Chapter (Figure 6.7). Figure 5.6 shows the median depths of each pond as measured by the DDA and the MPA. We choose the median statistics to prevent anomalous depth measurements from influencing this statistic. There is good correlation between the depths derived by the two algorithms ($r = 0.78$) (Figure 5.6a), with the MPA median depths 0.05 m (sdev. 0.24 m) greater on average than those tracked by the MPA (Figure 5.6b). Although there is a small median difference between the two algorithms, the standard deviation demonstrates that there is some variability signifying uncertainty in the location of the true melt pond bottom. Because of the good agreement between the

two tracking algorithms, we combine the pond depths retrieved from both algorithms to analyze melt pond evolution throughout the summer.

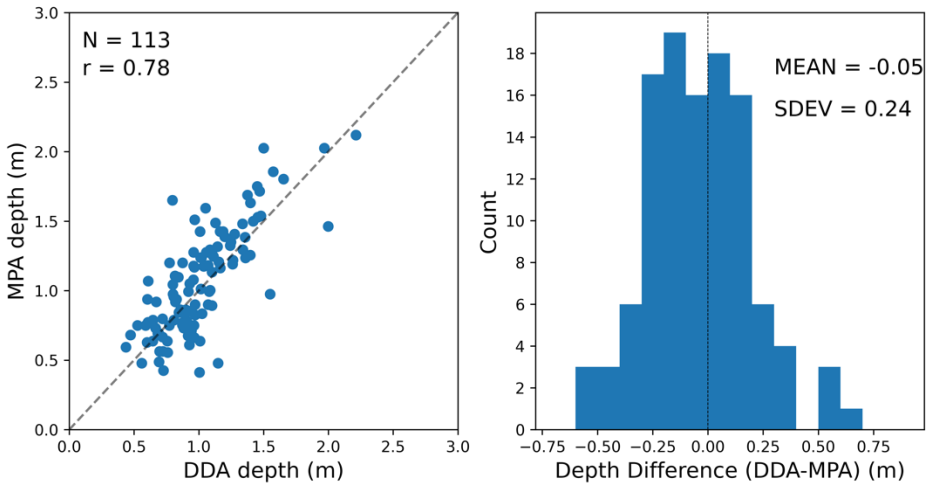

Figure 5.6. (a) scatter plot of median pond depth measurements from 113 ponds tracked by both the MPA and the DDA. (b) histogram showing the distribution of DDA – MPA residuals associated with the points in the scatter plot.

5.4 Summary

In this chapter we described the methodology used to derive melt pond depth from laser altimetry. Section 5.2 focused on the derivation of pond depth from the ATM onboard OIB flights in the 2017 Arctic sea ice summer campaign and provided a starting point for further analysis of this dataset. The methodology described is a proof of concept and can be adapted for other waveform altimetric measurements over melt ponds. Chapter 5.3 focused on the algorithms (MPA and DDA) used to

track melt ponds in the ICESat-2 photon cloud. To our knowledge, these are the first measurements of melt pond depth from a spaceborne platform. We plan to continue using these methods to retrieve melt pond depth data from airborne and spaceborne platforms.

Chapter 6: Observing the Evolution of Summer Melt on Multiyear Sea Ice with ICESat-2 and Sentinel-2

6.1 Motivation and Goals

In this chapter we examine the evolution of summer melt through observations from Sentinel-2 and ICESat-2 (Buckley et al., 2022). We are motivated by the gap in our understanding of melt evolution at a basin-wide scale. Our goals for this chapter are to:

- Describe the results of applying the classification algorithm to Sentinel-2 imagery across the multiyear ice region in the 2020 melt season.
- Discuss the results of the melt pond tracking algorithms applied to the ICESat-2 tracks across the study region and time period.
- Examine the evolution of the derived parameters throughout the summer melt season.
- Discuss our findings in context of previous studies.

Section 6.2 describes the study region and period, and section 6.3 sets the scene for our study. Section 6.4 describes the application of our classification algorithm (see Chapter 3 and Buckley et al., 2020a) to Sentinel-2 imagery within the study region. Section 6.5 discusses the application of a novel melt pond tracking algorithms (described in Chapter 5) to ICESat-2 data obtained in the study region. In section 6.6 we discuss the evolution of sea ice conditions during summer, and in

section 6.7 we discuss the relationship between MPF and melt pond depth. We summarize our findings in section 6.8.

6.2 Study Region and Period

The study region, shown in purple in the top panel in Figure 6.1, was delineated from the location of multiyear ice on 15 May 2020, prior to melt onset as defined in the EUMETSAT Ocean and Sea Ice Satellite Application Facility sea ice type product. This product is a blended passive microwave and scatterometer dataset (Breivik et al., 2012). The product is not available through the summer months due to the presence of surface melt conditions that confound the algorithm (Aaboe et al., 2021). The study region extends from just west of Banks Island in the Beaufort Sea to north of the easternmost part of Greenland, spanning the oldest and thickest ice in the Arctic. We focus on this region for two reasons. Previous studies have demonstrated the feasibility to measure melt pond depth on multiyear ice with ICESat-2 altimetry (Farrell et al., 2020). Second, Sentinel-2 imagery is more widely available throughout the multiyear ice region due to the proximity of this sea ice type to land, where Sentinel-2 acquisitions are routinely collected. The study region is consistent with the perennial ice area that persists at the end of the 2020 melt season (September 2020) and also overlaps with the "Last Ice Area" (Figure 6.1 top panel, gray), an area expected to retain multiyear ice longer than any other area in the Arctic under projected warming scenarios (Wang and Overland, 2009).

The summer melt season of 2020 is an example of a high melt year and thus provides a good time period over which to conduct our analysis of the remote sensing

data. The September average monthly sea ice extent (3.92 million km^2) was the second-lowest average monthly sea ice extent on record (Fetterer et al., 2017). The 10-year CryoSat-2/SMOS data record reveals an ice volume loss from April to October 2020 of 15,215 km^3 resulting in an October ice volume of 4,627 km^3, the lowest ice volume in the 10-year record (Perovich et al., 2020). The summer months of 2020 also represent the first summer period with the availability of continuous ICESat-2 records, since no data were collected between 26 June 2019 and 9 July 2019 when the satellite was in a temporary safe-hold configuration and the laser was turned off due to an onboard anomaly that occurred during the reorientation of the solar arrays. For these reasons, we focus on the 2020 melt season. Early melt onset, the date of the earliest observed melt conditions, occurs at different times in the region ranging from 23 May to 10 June. Melt onset, when melt was observed from this point onward, occurred in the study region on 8 to 18 June. Freeze onset, the date of the earliest observed freeze conditions, ranged from 9 to 27 August and freeze conditions, when freeze was observed from this point onward occurs 22 to 31 August (Markus et al., 2009). To ensure we capture the full melt season, we monitor melt parameters from 1 June through 30 September 2020.

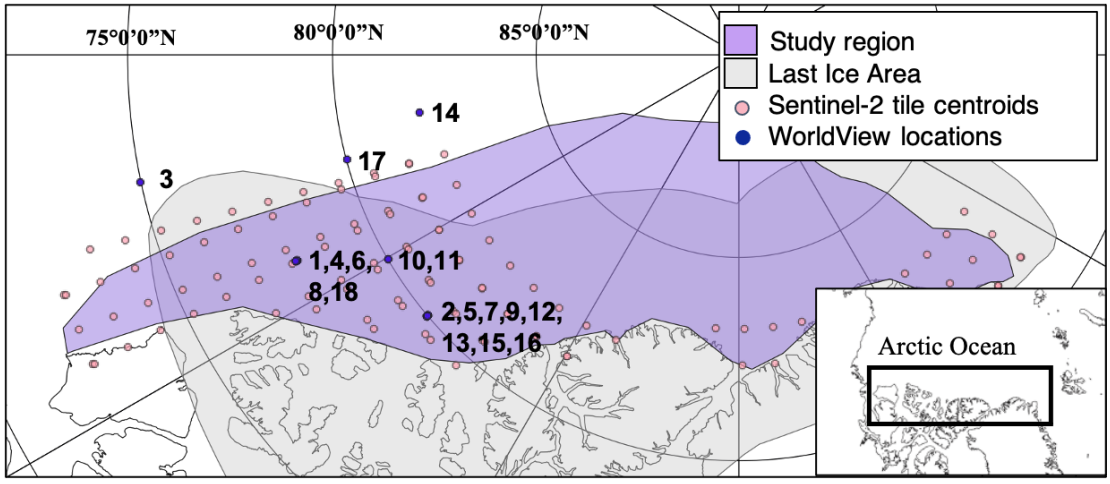

Figure 6.1. Study region north of Greenland and the Canadian Arctic Archipelago. The study region (purple) is based on the last observed multi-year ice extent in May 2020 and the overlapping last ice area (gray). Sentinel-2 tile centroids (pink circles) indicate availability of image acquisitions. WorldView imagery centroids (dark blue circles) are shown and numbered. Inset shows the location of the study region.

6.3 Setting the Scene

The 2020 melt season in the study region progressed as follows. May 2020 temperatures in the multiyear ice region were about 1 to 5 ° C greater than average (Kalnay et al., 1996). In the Central Arctic, early melt onset occurred on 3 June 2020, and melt onset occurred on 16 June 2020, both dates six days earlier than the average early melt and melt onset for the time period 1979- 2020 (Markus et al., 2009). Using WorldView imagery, we classify the stages of melt pond evolution from formation through freeze up. In Figure 6.2 we demonstrate the stages of melt pond evolution with a series of classified WorldView imagery. The WorldView shown in Figure 6.2 are from two different locations within the study region, the corresponding image numbers (Table 6.1) mark their location in the top panel of Figure 6.1. The derived parameters melt pond fraction (MPF) and sea ice concentration (SIC) from these

images are shown in Table 6.1. Figure 6.2a, on 9 June 2020, no ponds are detected in surface imagery (MPF = 0%, Table 6.1). At this point, the surface may be undergoing melt and snow metamorphism is taking place. On 17 June 2020 (Figure 6.2b), ponds have formed and the meltwater has pooled into the lowest topographic areas (MPF = 3 %, Table 6.1). By 30 June 2020 (Figure 6.2c), melt has advanced with a higher fraction of the ice covered in ponds (MPF = 23%, Table 6.1). Drainage channels that have formed between ponds by 22 July 2020 (Fig 6.2d) as ponds drain into other ponds and into the open ocean, either laterally of vertically. By 7 August 2020 (Figure 6.2e), regions of the ice have melted through, exposing the ocean, and pockets of open water have formed within the floe. In some areas, the surface of the pond has refrozen to form an ice lid. These lids increase the albedo of the pond (Flocco et al., 2015), and restrict laser penetration into the pond. Still, a large fraction of the ice is covered in ponds. On 3 September (Figure 6.2f), the majority of ponds have frozen ice lids that appear grayer in color, and are classified as ice, at this point MPF has deceased (MPF = 6%, Table 6.1). The refrozen leads are classified as other (green) in Figure 6.2f.

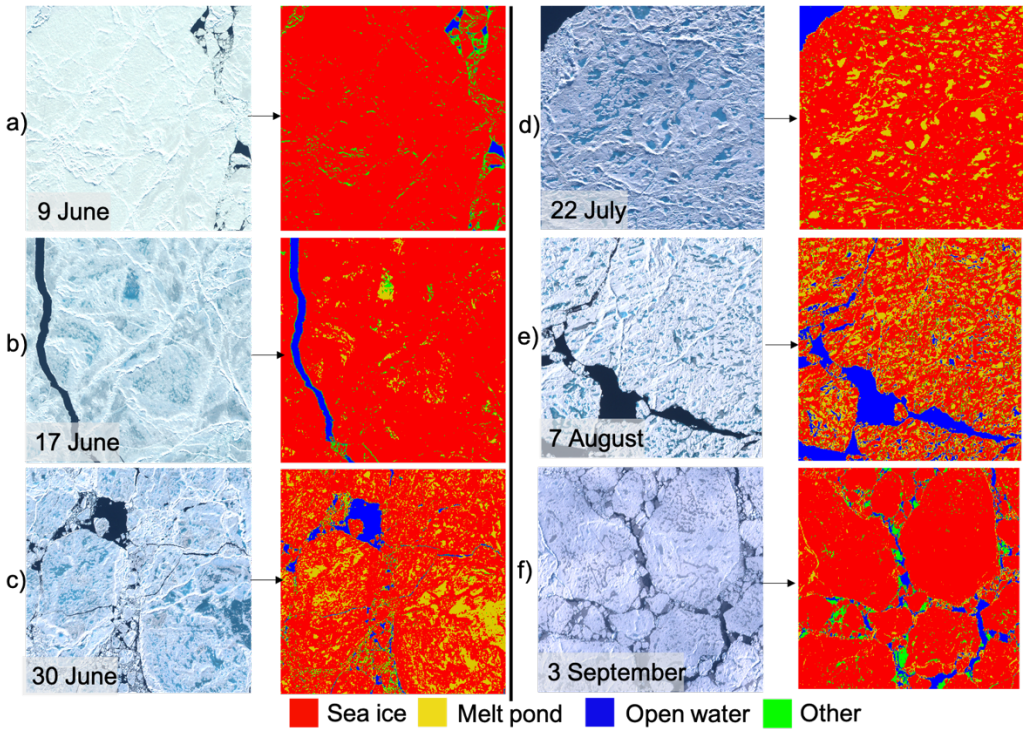

Figure 6.2. Melt evolution in 2020, based on a selection of Worldview imagery (~ 900 m x 900 m in area). Each figure shows the true color composite (RGB) of the WorldView imagery (left) and the classified image on the right. The derived MPF and SIC for each image is given in Table 6.1. (WorldView imagery copyright 2020 Maxar).

Table 6.1 Derived SIC and MPF for images shown in Figure 6.2*

Image	#	MPF	SIC
a) 9- Jun	1	0%	99%
b) 17-Jun	7	3%	97%
c) 30- Jun	8	23%	96%
d) 22-Jul	10	25%	98%
e) 7- Aug	17	32%	86%
f) 3- Sept	19	6%	95%

*# refers to corresponding image in Appendix 1.

6.4 Summer Melt Parameters Derived from Satellite Imagery

6.4.1 Feature Classification

The classification algorithm (Chapter 3) was applied to 1,775 Sentinel-2 images in the study region from 1 June 2020 to 15 September 2020. Figure 6.3 shows the evolution of surface melt conditions throughout the melt season. Vertical gray bars indicate that there are fewer than ten images in the 5-day period, due to the requirement of 90% cloud-free images (Chapter 3, section 3.6). At the beginning of the melt season a high percentage of pixels (> 90%) are classified as ice, and this is followed by a sharp drop to <80% in mid-June. The ice pixel percentage decreases through mid-August and then becomes more variable. Melt pond pixels increase from 3.0% on 13 June to 10.0% on 15 June and the max coverage is 15.3% on 24 June. The percentage of pixels classified as melt ponds remain greater than 10% until July 2, and makes up less than 5% of each image from July 23 through the end of the study period (30 September). Open water percentage is low (<5%) at the beginning of the season and then increases and becomes more variable later in the season, with the highest open water percentage from mid-July through mid-August. This indicates, increase lateral melting of floes and a more dynamic, divergent ice pack. On average, open water makes up 14% of the surface pixels in July and 17% in August. Open water percentage decreases in late August and September as leads begin to refreeze. Throughout the season the pixels classified as 'other' remain below 10%. Towards the end of the season, refrozen leads appear in the Sentinel-2 scenes and the algorithm

classifies these areas as ‘other’, explaining the increase in ‘other’ pixel percentages in September.

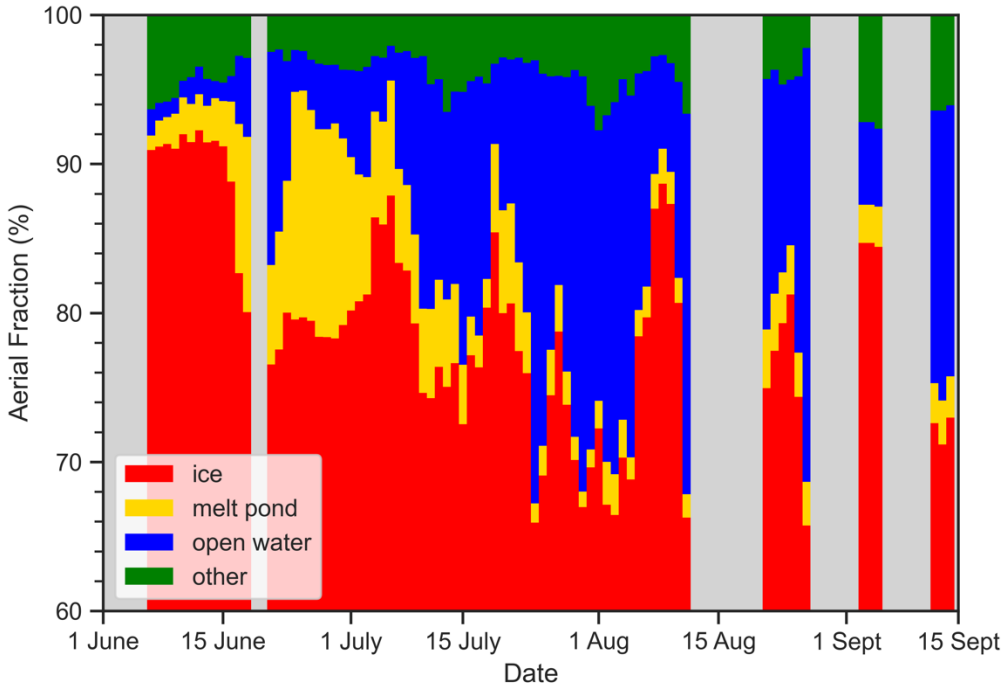

Figure 6.3 The five-day mean aerial fraction of surface types from classification of Sentinel-2 imagery throughout the melt season. Surface pixels are classified as ice (red), melt pond (yellow), open water (blue), or other (green). The gray bars indicate that there are fewer than ten images in the five-day period.

6.4.2 Melt Pond Area Distribution

We calculate melt pond size distribution for coincident Sentinel-2 and WorldView imagery to understand the limitations of the lower resolution Sentinel-2 imagery. We use the MATLAB function regionprops which evaluates a binary image (melt pond =1 , else =0), and provides the number of pixels associated with each individual object. With knowledge of the WorldView pixel size, we can determine the

area of each object in the binary image. For each WorldView image, we calculate the number of ponds, total pond area, pond perimeter, mean and median pond size, 5th and 95th percentile pond size, and circularity (Table 6.2). Figure 6.4 shows the melt pond area distribution from the 18 WorldView images. We limit our analysis to melt ponds with the area of at least 9 pixels (3 x 3 pixels), or 24.5 m^2 (30.8 m^2) for WorldView 3 (WorldView 2), as smaller scales of melt ponds are indistinguishable from noise. Circularity is measured as in Perovich et al., 2002b:

$$C = \frac{P^2}{A} \tag{6.1}$$

Where C is the circularity, P is the pond perimeter, and A is the pond area.

Table 6.2. Melt Pond Area Distribution of WorldView Imagery

Date	number of ponds	total melt pond area (m^2)	mean melt pond perimeter (m^2)	mean melt pond area (m^2)	5th percentile melt pond area (m^2)	median melt pond area (m^2)	95th percentile melt pond area (m^2)	mean circularity
9-Jun-20	972	58110.6	37.4	59.8	34.2	47.9	124.8	24.7
11-Jun-20	13644	1318542.1	55.1	96.6	34.2	58.2	277.2	33.8
12-Jun-20	877	66143.2	34.2	75.4	34.2	51.3	172.5	16.9
14-Jun-20	6249	423921.1	36.3	67.8	34.2	51.3	160.9	20.9
15-Jun-20	10130	816281.7	43.0	80.6	27.2	49.0	231.4	26.3
17-Jun-20	34839	3451221.6	43.8	99.1	34.2	61.6	284.1	21.0
30-Jun-20	168405	47213983.0	81.5	280.4	34.2	71.9	633.2	32.1
2-Jul-20	177058	34206970.3	62.3	193.2	34.2	68.5	441.5	26.4
22-Jul-20	36733	3594007.6	49.3	97.8	27.2	54.4	304.9	28.1
24-Jul-19	119124	16611644.5	56.5	139.4	34.2	75.3	438.1	25.5
24-Jul-19	95524	12228537.7	50.9	128.0	34.2	71.9	362.8	23.6
26-Jul-19	155825	39487319.6	81.2	253.4	34.2	75.3	742.7	30.4
27-Jul-20	304298	38099628.8	61.3	125.2	27.2	57.2	397.5	34.8
31-Jul-19	236057	39536174.9	67.6	167.5	27.2	79.0	536.3	32.2

4-Aug-19	164640	29114310.8	73.3	176.8	34.2	75.3	585.2	34.1
7-Aug-20	232460	29996627.5	67.4	129.0	27.2	57.2	400.2	40.7
9-Aug-20	122476	22072722.4	56.5	180.2	34.2	65.0	400.4	25.4
3-Sep-20	785	42863.4	38.0	54.6	34.2	44.5	112.9	27.5

Although these WorldView images are not all from the same melt season or same location, we see patterns related to the stage of melt evolution. As the mean melt pond area increases throughout the summer, the perimeter does as well. Towards the end of the melt season, as ponds drain, the area and perimeter decrease. As expected the number of individual ponds per image starts off low, increases mid summer, but then decreases again when freeze up occurs, as seen in the WorldView image on 3 September, 2020.

Mean pond circularity in the WorldView images ranges from 16.9 on 12 June to 40.7 on 9 August. The high end of the range is similar to the value of 41.2 found on 7 August on multiyear ice in Perovich et al., 2002. However, they found a mean pond circularity of 38.5 on 10 June. This could be due to our pixel based algorithm detecting small melt ponds which tend to have a lower circularity. Our findings also agree well with the Perovich et al., 2002b finding that the circularity increases with mean pond size. As ponds grow and become more interconnected and complex, the circularity increases.

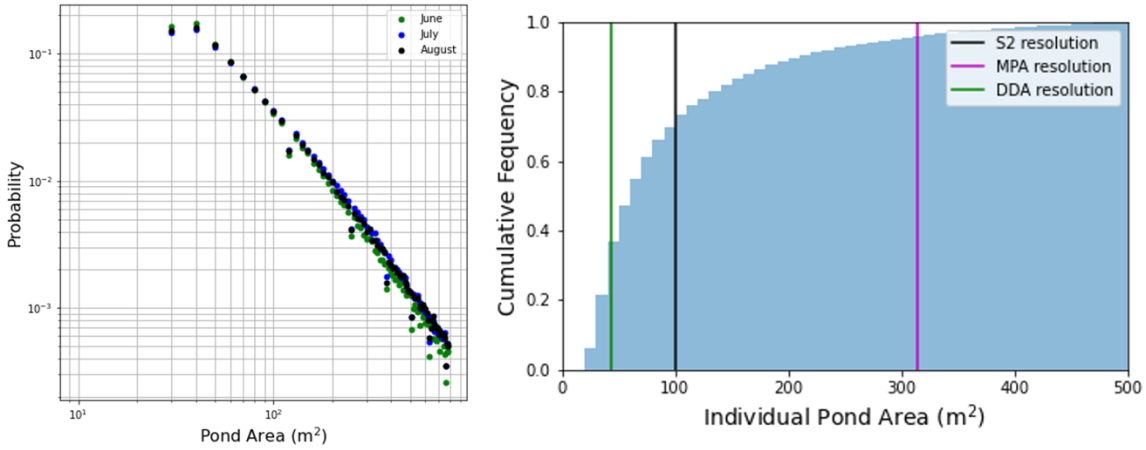

Figure 6.4. Melt pond area distributions. a) melt pond area distribution colored by month: June (green), July (blue) and August (black).Area bins of size 10 m^2 were used. b) cumulative individual melt pond area distribution. The Sentinel-2 individual melt pond area resolution (100 m^2) is shown as a solid black line. The melt pond area corresponding the minimum resolvable MPA and DDA widths (20 m, 7.5 m, respectively) and assuming circular melt ponds are shown in magenta and green, respectively.

Figure 6.4a demonstrates the prevalence of small ponds in the WorldView imagery. There is a slightly higher probability of larger ponds in Junly and August as compared to June, but the distributions from the three months show similar pond size distributions. Figure 6.4b indicates that 73% of individual ponds are not captured by the Sentinel-2 imagery. However, since these are small ponds, this accounts for 38% of the total pond area. The Sentinel-2 imagery is able to capture approximately 62% of the total pond area. In Section 6.4.3, we discuss how we can adjust the Sentinel-2 derived melt pond fraction to account for the subpixel size melt ponds.

6.4.3 Validation of Summer Melt Parameters

To validate the summer melt parameters derived from the Sentinel-2 classification, we compare with the MPF and SIC derived from the higher-resolution WorldView imagery (parameters defined in Section 3.8). To understand the impact of these biases on our data, we analyze 18 WorldView images that are coincident spatially and temporally with Sentinel-2 imagery in the 2019 and 2020 melt season (Appendix 1, Table 6.3). Although the imagery spans two years (2019-2020) we organize the findings by the day of year. We identify Sentinel-2 imagery captured within 24 hours of the WorldView imagery and we subsample the Sentinel-2 tiles to the extent of the WorldView image by matching ice features in the imagery. We demonstrate this in Chapter 3, where we show an example of an area examined in coincident WorldView and Sentinel-2 image (Figure 3.10) and found a MPF of 7.6 % and 25.5% from the Sentinel-2 image (Figure 3.10d) and WV image (Figure 3.10f), respectively. For the same image (Figure 3.10) we estimate SIC as 93.5% and 87.3% from Sentinel-2 and WorldView imagery, respectively. In this section, we discuss the results from classification of the coincident WorldView and Sentinel-2 imagery.

On average Sentinel-2 SIC is 4.2% (3.9%) higher than WorldView, and ranges from 0.5% to 15.5% ΔSIC (Sentinel-2 SIC - WorldView SIC, Table 6.3). In early June, both Sentinel-2 and WorldView SIC reveal a consolidated ice pack, with high SIC in all the images (>94%) and the Sentinel-2 imagery agrees to within 3% to the coincident WorldView imagery. As the melt season progresses, sea ice floes are more susceptible to break up due to the structural weakening induced by melt pond

formation (Arnsten et al., 2015), and the enhanced dynamics as the sea ice is able to drift more freely. For this reason, there are smaller features that appear in the imagery scenes: smaller floes, chunks of ice. Small features are not as well resolved by the lower resolution Sentinel-2 imagery and thus misclassification of pixels as well as classification of mixed pixels is more common. As the SIC decreases throughout the melt season, the Sentinel-2 bias as compared to WorldView-derived SIC increases (Figure 6.5b, Table 6.3).

On average, the MPF derived from Sentinel-2 imagery is biased low overall compared with the MPF derived from WorldView, with an average bias of -7.2% (8.6%) and ranges from -20% to +6% ΔMPF (Sentinel-2 MPF - WorldView MPF) (Table 6.3). This is likely due to small ponds going undetected or are mixed pixels in the 'other' category. We find that the magnitude of the Sentinel-2 MPF bias is greatest when small ponds are widespread across the surface. Figure 6.5 shows the Sentinel-2 bias compared to the value of the WorldView parameters. In Figure 6.5a, as MPF increases, the Sentinel-2 bias becomes more negative. For this reason, there is a seasonal trend in the Sentinel-2 MPF bias (Figure 6.5a). In early June, imagery in both data sets show little or no signs of melt (Table 6.3), and the WorldView and Sentinel-2 derived MPF show good agreement. In the five scenes in the first half of June, MPF is less than 1% in all Sentinel-2 and WorldView images. As melt progresses over the sea ice surface, melt ponds dot the surface and these new small features lead to weaker agreement in the WorldView MPF and Sentinel-2 MPF, because the lower resolution Sentinel-2 may not be able to resolve these features.

There are two cases where the MPF derived from the Sentinel-2 image is greater than that derived from the WorldView image. In the imagery collected on 17 June, 2020, the calculated MPF is 8.4 % and 2.4 % for the Sentinel-2 and WorldView images, respectively. In this scene (subset shown in Figure 6.2b), there is level bare ice that appears blue in color. In the Sentinel-2 image this area is classified as a melt pond, but in the WorldView imagery this is classified as sea ice. In the imagery captured on 3 September, 2020, there are many ice fragments smaller than the Sentinel-2 pixel size of 10 m. These pixels may be correctly classified as 'other' or can also be classified as melt ponds, falsely increasing the MPF. The WorldView images better resolve these areas and properly classify pixels as ice or open water.

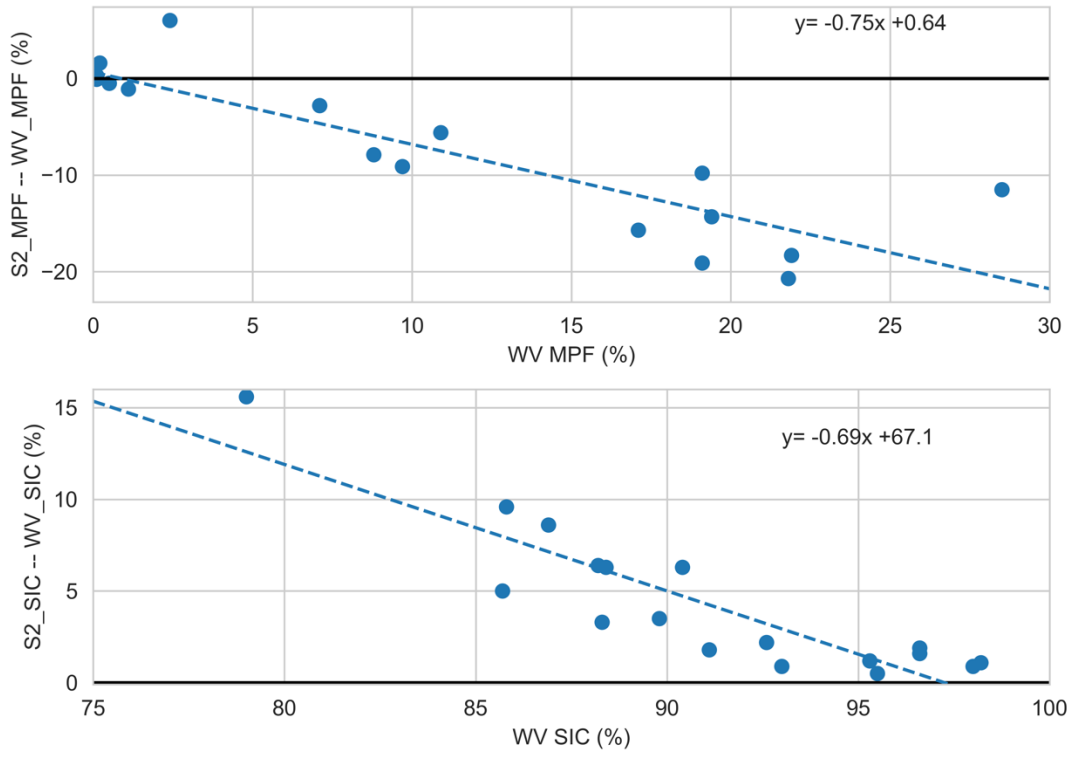

Figure 6.5. Difference between the Sentinel-2 and WorldView derived MPF (a) and SIC (b) is shown as a function of the WorldView value. Linear lines of best fits are shown as the dashed line.

The biases described in this section are consistent with previous studies (Buckley et al., 2020a and references therein) and in the findings presented in Chapter 4, sections 4.3 and 4.4, where we compare derived MPF from DMS (10 cm resolution) and Sentinel-2 imagery and SIC derived from DMS and lower resolution satellite data (AMSR2 and CDR). In section 4.3 we showed average DMS MPF was 15% and Sentinel-2 derived MPF was 13% over a 57 km stretch of the survey conducted on 24 July 2017 in the Lincoln Sea. Again, demonstrating the ability of the higher resolution data (DMS) to capture the true expanse of the small melt ponds. In section 4.4 we found that DMS derived SIC is better able to capture the SIC variability in the studied region as compared to the CDR SIC and AMSR2 SIC with pixel resolution of 25 km and 12.5km, respectively.

In order to understand the impact of pixel size on derived melt pond fraction, we look at the melt pond size distribution for each WorldView image with a coincident Sentinel-2 image, as in Section 6.4.2. We determine the total area of ponds with a size smaller than the Sentinel-2 pixel size (100 m^2). The Sentinel-2 classification cannot resolve these small features as they are smaller than the pixel size. We calculate an adjusted Sentinel-2 MPF (Equation 6.2) that adds in the unresolved melt ponds to the MPF calculation for each pair of Sentinel-2 and WorldView images where the Sentinel-2 MPF is less than the WorldView MPF:

$$S2MPF_{adj} = \frac{S2MPA + WV_{100}MPA}{S2surfA \; x \; S2SIC} \tag{6.2}$$

Where $S2MPF_{adj}$ is the adjusted Sentinel-2 MPF, *S2MPA* is the Sentinel-2 melt pond area, $WV_{100}MPA$ is the area of ponds less than 100 m^2 in size in the coincident WorldView image, *S2surfA* is the surface area in the Sentinel-2 image, and *S2SIC* is the Sentinel-2 sea ice concentration. The denominator on the right hand side of Equation 6.2 is a calculation of the total area of sea ice and melt ponds in the Sentinel-2 scene. In the case where the Sentinel-2 MPF is biased low as compared to the WorldView MPF, we make the assumption that melt ponds smaller than the Sentinel-2 pixel size are classified as ice, so when making this adjustment, we hold the sea ice concentration constant and the area of WorldView melt ponds less than 100 m^2 replaces sea ice in the original Sentinel-2 classification. Table 6.3 provides the adjusted melt pond fraction results for each pair of WorldView and coincident Sentinel-2 images. Note that this adjustment is only applied where in the original classification, the Sentinel-2 MPF is less than the WorldView MPF. Appendix 1 shows the true color imagery and classified Sentinel-2 and WorldView images used in this analysis.

Although the addition of ponds smaller than the Sentinel-2 pixel size increases the S2 MPF, making it more comparable to the WorldView-derived MPF, it does not account for the entire discrepancy between the Sentinel-2 and WorldView derived MPF. Sentinel-2 MPF, originally biased 7.2% low, is only biased 3.6% low when the sub-pixel size WorldView ponds were accounted for. Although this methodology accounts for individual small ponds identified in WorldView imagery, we have not

accounted for subpixel-size areas that are connected to larger ponds. Where the Sentinel-2 pixels may be classified as ice along the edges of ponds, the pixel could include some area that is a melt pond which is properly classified as such in the higher resolution WorldView classification. This scenario was not accounted for in the adjusted Sentinel-2 MPF, and may account for some of the remaining bias between Sentinel-2 and WorldView imagery. We also note that the Sentinel-2 derived SIC is biased high (4.3% greater than WorldView on average), and with a higher SIC and sea ice area per scene, this contributes to a lower melt pond fraction in Sentinel-2. This section describes an analysis to understand the potential error in the Sentinel-2 classification. We have not applied this adjustment to the entire dataset of classified Sentinel-2 images, as we do not have coincident WorldView imagery.

Table 6.3 Derived MPF and SIC from coincident WorldView and Sentinel-2 images.

Image Number	Date	S2 Central Latitude	S2 Central Longitude	S2 SIC (%)	WV SIC (%)	Δ SIC (S2-WV) (%)	S2 MPF (%)	WV MPF (%)	Δ MPF (S2-WV) (%)	S2 MPF adj (%)	Δ MPF adj (S2-WV) (%)
1	9-Jun-20	78.0	-125.0	94.7	92.6	2.2	0.1	0.1	0	0.5	0.3
2	11-Jun-20	80.0	-110.0	99.2	98.2	1.1	0.0	1.1	-1.1	0.6	-0.5
3	12-Jun-20	75.0	-138.0	98.2	96.6	1.6	0.0	0.1	-0.1	0.1	0.0
4	14-Jun-20	78.0	-125.0	96.4	95.3	1.2	0.0	0.5	-0.5	0.3	-0.2
5	15-Jun-20	80.0	-110.0	99.0	98.0	0.9	0.0	0.5	-0.5	0.5	0.0
6	17-Jun-20	78.0	-125.0	96.0	95.5	0.5	8.4	2.4	6.0	-	7.0
7	30-Jun-20	80.0	-110.0	98.5	96.6	1.9	17.0	28.5	-11.5	21.1	-7.4
8	2-Jul-20	78.0	-125.0	90.7	85.7	5.0	3.6	21.9	-18.3	9.4	-12.6
9	22-Jul-20	80.0	-110.0	94.6	88.2	6.4	5.3	10.9	-5.6	11.9	1.0
10	24-Jul-19	80.0	-119.8	91.6	88.3	3.3	0.9	8.8	-7.9	3.7	-5.1
11	24-Jul-19	80.0	-119.8	93.9	93.0	0.9	0.5	9.7	-9.1	3.8	-5.9
12	26-Jul-19	80.0	-110.0	93.0	91.1	1.8	1.1	21.8	-20.7	4.5	-17.4
13	27-Jul-20	80.0	-110.0	95.4	85.8	9.6	5.2	19.4	-14.3	14.5	-5.0
14	31-Jul-19	82.0	-139.7	94.7	88.4	6.3	0.0	19.1	-19.1	7.6	-11.5
15	4-Aug-19	80.0	-110.0	93.2	89.8	3.5	1.4	17.1	-15.7	5.2	-11.9
16	7-Aug-20	80.0	-110.0	94.5	79.0	15.6	9.3	19.1	-9.8	20.5	1.5
17	9-Aug-20	80.0	-135.0	96.7	90.4	6.3	4.3	7.1	-2.8	7.5	0.4
18	3-Sep-20	78.0	-125.0	95.5	86.9	8.6	1.9	0.2	1.6	-	1.8

Despite the discrepancies discussed in this section, we are confident the Sentinel-2 derived MPF and SIC parameters are reliable. We do however, warn that during the peak of the melt season, the Sentinel-2 derived MPF is likely underestimating the true MPF, and as SIC decreases throughout the melt season, the Sentinel-2 derived SIC is likely overestimating the true SIC.

6.4.4 Sea Ice Concentration

We examine the Sentinel-2 derived SIC in the study region from 1 June 2020 to 15 September 2020. We found the mean SIC for this region in Summer 2020 was 91.6% with a standard deviation of 15% and the median was 97.2%. The difference between the median and mean indicate that there are some Sentinel-2 tiles with very low SIC, or no sea ice as all. The SIC values ranged from 0-100%, with 75% of the SIC values greater than 92.8% and 25% greater than 99.0%. As the melt season progresses, individual images show more variable SIC and the median SIC value decreases. Figure 6.6 shows the seasonal evolution of the melt parameters with the SIC shown in Figure 6.6a.

SIC is consistently greater than 90% through mid-June. On 27-28 June, sea ice drift data show westward ice drift (Lavergne et al., 2010), and imagery show the ice pack separating from the landfast ice on the western coast of Greenland in the Lincoln Sea and the western coasts of the Canadian Archipelago (Vermote and Wolfe, 2021), opening leads and reducing local ice concentration. Throughout July, the sea ice continues to separate from the coast leaving large areas of open water. As the ice pack recedes, Sentinel-2 images along the edge of the pack ice capture lower SIC (<80%)

and in the lowest latitudes of the study region, SIC values drop below 20% (Figure 6.6a). The consolidated icepack evolves into a mosaic of smaller floes with leads that grow in size as the floes melt laterally. Median SIC drops below 80% in late July consistent with Perovich et al. (2002) which observed a sharp decrease from 95% to 80% SIC in early August in aerial observations over the SHEBA campaign.

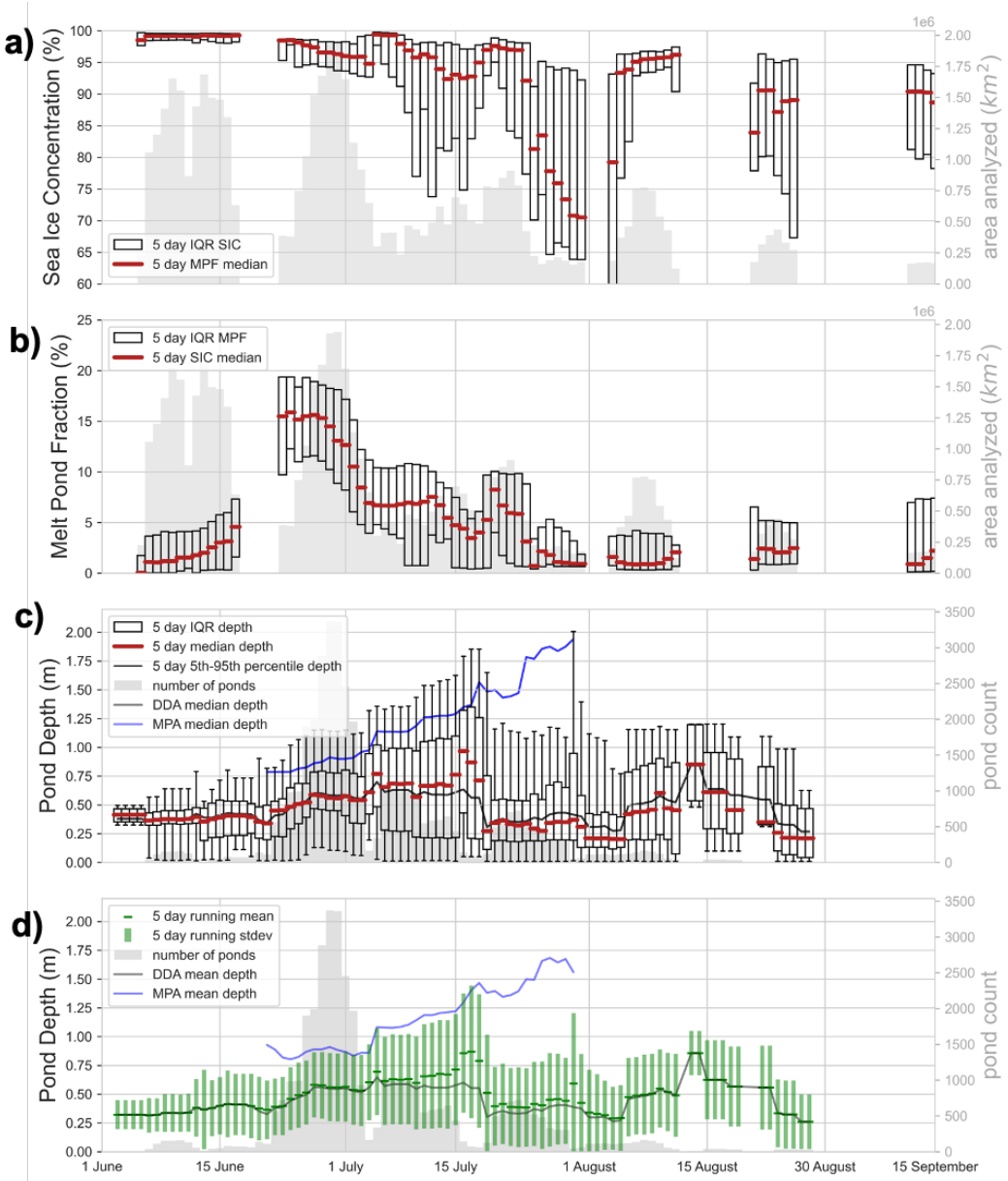

Figure 6.6. Evolution of melt features from 1 June, 2020 to 15 September, 2020 in the study region. a) box plot showing the median sea ice concentration for a 5 day

window centered on the plotted date. The box shows the interquartile range. The gray bar plot in background shows the total area of Sentinel-2 imagery analyzed per five day window. b) same as in a) but for melt pond fraction. c) box and whiskers plot with statistics from the merged DDA and MPA tracked ponds for a 5 day window centered on the plotted date. The median is shown as a horizontal red line and the interquartile range is denoted by a box. The whiskers extend from the 5th to 95th percentile. The five-day running median pond depth from just the MPA (blue line) and DDA (black line) are shown. d) 5 day running mean (solid green line) with the standard deviation (green bar). The five-day running mean pond depth from just the MPA (blue line) and DDA (black line) are shown. In c) and d) the number of ponds included in the 5 day running statistics are shown in light gray.

6.4.5 Melt Pond Fraction

We calculated MPF for the Sentinel-2 images in the study region with SIC >15% from 1 June to 15 September (Figure 6.6b). The average MPF in the region in summer 2020 was 6.5% with a standard deviation of 6.5%. The highest MPF for an individual Sentinel-2 scene was 31.6%. This image is located just outside of the mouth of Nansen Sound at (-95.3° W, 82.3° N), but far enough from that coastline that it does not contain landfast ice. Median MPF remains low, <5%, through 17 June. We then see a sharp increase to 12.1% in MPF on 18 June. The imagery is scarce between 18 and 22 June due to widespread cloud coverage (Figure 6.6b). This weather system likely enhances the melt (Mortin et al., 2016), and when it passes MPF is high, averaging 15.2% between 24 and 29 June. The peak five day running mean MPF is 15.9% on 24 June. The MPF slowly decreases in July and by August, the MPF remains below 5% for the remainder of the season. This compares well with the DMS-derived MPF results presented in Chapter 4.4, where we found a MPF of 14% (6%) on average in the Central Arctic in July 2017.

6.5 Melt Pond Depth

For each individual pond tracked by the MPA and DDA, we find the median and mean pond depth (Figure 6.6 c-d). The mean pond depth is the average depth from the interpolated ponds depths within a pond. The median pond depth is the 50^{th} percentile pond depth of the interpolated depths within a pond. We calculate statistics of a 5 day moving window for the entirety of the melt season (1 June – 30 August), as long as there are at least five melt ponds within the window. We calculate the median and interquartile range (25^{th}-75^{th} percentile) (IQR) of the median melt pond depths within the five day window (Figure 6.6c) and the mean and standard deviation of the mean melt pond depths for the five day windows (Figure 6.6d). We choose these statistics as they not affected by a single erroneous measurement that may skew other statistics such as the min and max of individual ponds to ensure a robust representation of the data. We demonstrate that the same depth evolution patterns are seen independent of the statistic chosen (mean or median) (Figure 6.6c, 6.6d). Individual ponds have complex meltwater accumulation and vertical and lateral drainage processes (Eicken et al., 2002). These processes for individual ponds are not captured in this evolution. The melt pond depth evolution is therefore not representative of a single pond, rather it is the change in pond depth statistics in the study region throughout summer 2020.

In Section 5.3.3, we show the good agreement between the melt pond tracking algorithms on the ponds that both algorithms have tracked. Therefore, in Figure 6.6, we combined the statistics for the ponds tracked by both algorithms, but we also show

the statistics for the MPA and DDA separately, the blue line and black line, respectively. The divergence of these results is due to the melt pond detection unique to the two algorithms, and the limitations of minimum pond size, as discussed in Section 6.5.3.

6.5.1 Melt Pond Algorithm

Of the 1107 tracks through the study region in from 1 June 2020 through 15 September 2020, only 850 tracks met the cloud cover requirements described in Section 2.3.1. Upon examination of these ATL03 photon cloud of these tracks, we identified 477 individual melt ponds (Figure 6.7). The MPA was applied to these ponds resulting in 11,000 individual pond depth measurements. The first pond identified was observed on 21 June, and the last pond on 8 August 2020, a shorter time period than that of the ponds tracked by the DDA due to the limitations of the manual identification process of the MPA (Figure 6.6c-d).

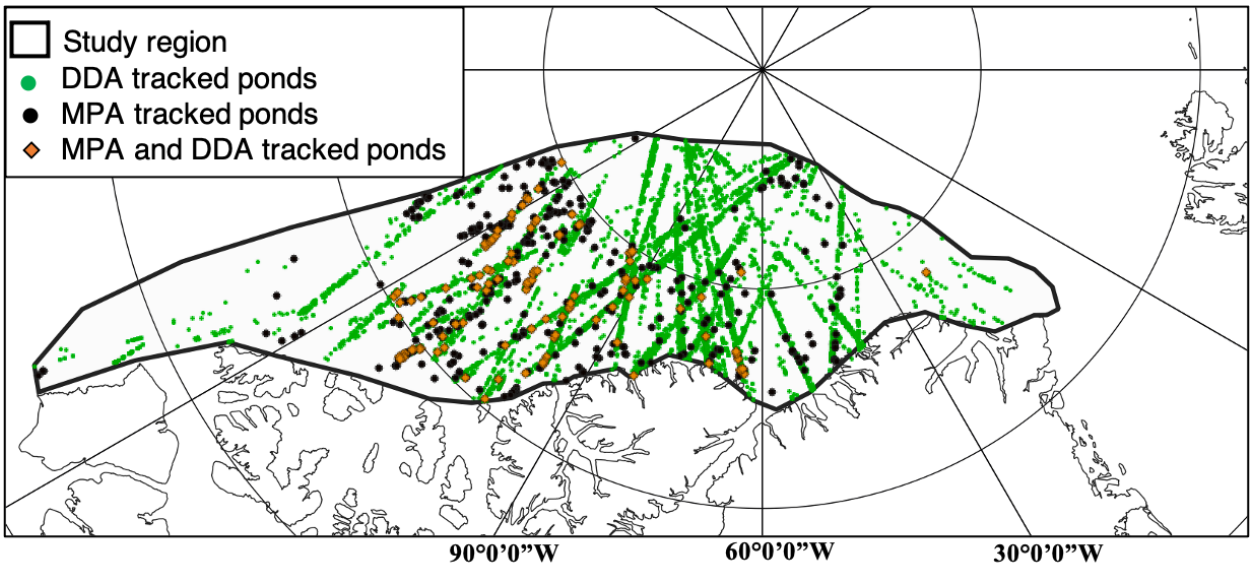

Figure 6.7. Locations of the ponds measured with the DDA (green circles), MPA (black circles), and both algorithms (orange diamonds) in the study region (black outline).

Although ponds were observed in Sentinel-2 imagery in early June, the first melt pond depth measurements from the MPA are on 21 June 2020. This indicates that the ponds present early in the season were shallow and any individual pond did not exceed both the MPA minimum retrievable pond depth of 0.23 m and minimum retrievable width of 20 m (as described in Section 5.3.1.). For ponds tracked with the MPA, we find the first observed depths on 21 June (0.79 m) increasing to a 1.94 m median depth on 30 July. There was a widening of the IQR from 0.27 m on 21 June to 0.93 m on 30 July, suggesting ponds across the area were in different stages of melt. Freeze onset in August causes the ponds to form ice lids resulting in the pond appearing radiometrically similar to ice, although there may be liquid water beneath the ice lid. We do not expect returns from the bathymetry of the ponds in these conditions, as the laser cannot penetrate the ice lid. Freeze conditions occur at different points in this region at the end of summer (Markus et al., 2009), and there are fewer pond depth measurements throughout the month of August.

The mean, mode and median pond depth derived from the MPA are all greater than reported for the 15 ponds from the 2019 melt season tracked in the Lincoln Sea in Farrell et al. (2020). This can be explained by the temporal range of melt ponds in this study extending through July and into August, whereas the Farrell et al. (2020) study only includes ponds from mid to late June.

6.5.2 Density Dimension Algorithm

The DDA was applied to 87 tracks representative in time and space of the study region and period (10% of the 850 tracks that met the cloud cover requirements described in Section 5.3.1). A total of 7,329 ponds were identified (Figure 6.7), with over 85,000 individual depth measurements. The change in melt pond depth derived from the ponds measured by the DDA is shown in Figure 6.6d. The median pond depth remains around 0.5 m through 25 June. Melt pond depths begin to increase towards the end of June, consistent with the ponds tracked by the MPA. The median depths of ponds tracked by the DDA increases to 0.78 m by 16 July. On 20 July, the pond depths decrease to a median pond depth < 0.5 m. From the end of July through early August, median pond depths are more variable ranging 0.21 to 0.49 m.

Overall, the depths derived from the 7,329 ponds found by the DDA are smaller than those from the 477 ponds found by the MPA, suggesting that the DDA was able to detect and track shallower ponds that were not manually identified as part of the MPA methodology. The MPA is limited by the manual detection of ponds, and the inability to track ponds less that 20 m in width, whereas the automated DDA finds ponds based on the photon distribution, and can track ponds as small as 7.5 m in width. The DDA can detect and track ponds where the MPA pond tracking may be limited, such as, at the beginning of the melt season.

6.5.3 Limitations of Melt Pond Depth Measurements

Similar to the analysis decribed in section 6.4.2, we use the WorldView melt pond distribution to understand the effects of tracking algorithm minimum melt pond width limitation. The minimum pond width for MPA tracking is 20 m (Section 5.3.1). Assuming a circular melt pond, the minimum detectable melt pond area is 314 m^2. Figure 6.4b shows the cumulative distribution of individual melt pond area, with the minimum retrievable pond area (assuming a circular pond) marked in magenta for the MPA and green for the DDA. Note that the cumulative distribution is shown for individual ponds, not of total ponded area. According to the WorldView imagery, approximately 83% of the total ponded area is made up of ponds with an area smaller than that, suggesting the MPA is missing a large majority of ponds. However, the DDA is able to track ponds as small as 7.5 m in width (Section 5.3.2), and the WorldView imagery melt pond distribution suggests that only 14% of the total ponded area is made up of ponds smaller than 44 m^2, the circular pond area corresponding to that width. The divergence in the MPA and DDA results are due to the inability of the MPA to track ponds smaller than 20 m in width, which makes up 96% of the melt ponds. For a systematic approach for detecting pond depth, we need an algorithm with a high resolution like the DDA that is able to detect small ponds.

6.6 Evolution of Sea Ice Melt Conditions

It is challenging to compare our findings with other studies as melt pond evolution vary based on surface conditions and regional atmospheric events that

occur throughout the melt season. Factors controlling melt progression include end of winter snow depth, ice topography, solar radiation, and weather events. In this section we put our results into context of existing literature, understanding that we cannot expect the same results as every season and region is different.

We note that the spatial domains of the Sentinel-2 imagery (Figure 6.1) and the tracked ICESat-2 melt ponds (Figure 6.7) are not exactly the same. Sentinel-2 has coverage up to 84 °N, while ICESat-2 has spatial resolution increasing with latitude up to 88 °N. Of the DDA and MPA tracked ponds, 40% and 27% (respectively) are located between 84 °N and 88 °N, out of the Sentinel-2 coverage area. No single pond or scene can be representative of the entire study area, so when considering melt feature evolution, we look at mean and median statistics for the region (Figure 6.6). Previous studies have looked at contemporaneous pond depths and pond fraction (e.g., Perovich et al., 2003; Webster et al., 2022a) to understand the physical melt processes occurring at a local level. In this work, we look more broadly at a region experiencing weather events and melt stages at different points throughout the summer. High resolution pan-Arctic observations are crucial for understanding model output (Webster et al., 2022b). In this section, we monitor the evolution of MPF alongside the evolution of the combined MPA and DDA tracked melt pond depths.

6.6.1 Early Melt

From 1 June through 17 June, MPF is less than 5% and SIC greater than 99% (Figure 6.6a-b). Figure 6.2 shows an example of an unponded ice surface on 9 June (Figure 6.2a) and early melt occurring in the image observed on 17 June (Figure

2.6b). During this time the median DDA-derived depth remains below 0.5 m and there are no ponds tracked by the MPA (Figure 6.6c-d). At the MOSAiC site, in the Fram Strait east of our study region, continuous melt started in mid-June expanding existing ponds and increasing the pond areal coverage (Webster et al., 2022a).

6.6.2 Maximum Melt

Our results show a sharp increase in MPF in mid-June (Figure 6.6a), consistent with Perovich et al. (2002) where aerial observations over the field site show a rapid increase in pond fraction over the study area from ~5% to 20% in just a few days. Scott and Feltham (2010) also find a sharp increase in the modeled MPF early in the melt season in the standard multiyear case. We find MPF greater than 10% from June 23, through July 2, with a maximum MPF of 16% on 24 June. At the MOSAiC site on primarily second year ice, ponds greater than 100 m in diameter were observed on 1 July, 2020 (Webster et al., 2022a). Maximum pond coverage occurred later in the season at SHEBA (24% on 7 August) (Perovich et al., 2002), and at MOSAiC (21% on 26 July) (Webster et al., 2022a).

In the second half of June the first ponds are tracked by the MPA (21 June), and both MPA and DDA median pond depths increase through the end of June. Similarly, at MOSAiC, melt pond depths increase through early July. Scott and Feltham (2010) found gradually increasing pond depth in their model. Morassutti and LeDrew (1996) analyze 220 pond depth measurements on multiyear ice within the Canadian Archipelago from 27 May to 26 June 1994. These ponds have a mean depth of 0.27 m with a standard deviation of 0.13 m. The MPA measurements reveal a

higher mean melt pond depth for this time period, (0.75 m +/- 0.66 m), but the is likely due to the measurement limitations and the minimum observable depth of 0.23 m from MPA, and the bias introduced in the manual identification of melt ponds in the photon cloud. The DDA measurements are more similar to the findings of Morassutti and LeDrew (1996). From 4 June through 26 June 2020, the DDA tracked ponds have a mean pond depth of 0.54 m with a standard deviation of 0.4 m.

6.6.3 Late Season Evolution

Following the maximum MPF on 24 June, we see a decrease in MPF, consistent with Eicken et al. (2002) and Polashenski et al. (2012) which describe a decrease in pond coverage as meltwater is efficiently routed through drainage channels, ice permeability increases, and meltwater percolates through the sea ice. At MOSAiC, a drainage event occurring in mid-July, reduced the pond area ~5% (Webster et al., 2022a). Eicken et al. (2002) and Perovich et al. (2002) suggest a second mode of MPF as melt ponds spread laterally and connect through drainage channels, but we did not see this in our results. This could be a result of the low resolution of the Sentinel-2 imagery where the smaller drainage channels that occur later in the melt season are not resolved well in the imagery (Chapter 3, Figure 3.10c-d) and melt pond pixels are classified as ice pixels instead.

The MPA tracked median pond depth increases throughout July, from 0.9 m on 1 July to 1.94 on 30 July, whereas the DDA depth increases through 16 July, reaching a median depth of 0.78, then is less than 0.5 m from 19 July through 14 August. These contrasting results demonstrate the bias of the MPA toward

identification of larger melt ponds, and inability to track smaller ponds. However, evolution is highly dependent on local weather (Webster et al., 2022a), and it is likely that the MPA and DDA are tracking ponds under different atmospheric conditions. The simulated pond depth in Scott and Feltham (2010) surpasses 1 m in early July, and remains above 1 m for the remainder of the melt season, agreeing well with the MPA observations. The gradual increase in melt pond depth throughout the season was also observed at SHEBA (Perovich et al., 2003). Observations at MOSAiC show that pond depth increased over time and melted through the first year ice by late July (Webster et al., 2022a).

6.6.4 Refreeze

The formation of lids on pond is a sudden process, as below freezing temperatures will quickly freeze the top layer of the pond, drastically reducing pond fraction (Webster et al., 2022a). Small, shallow ponds form lids before larger, deeper ponds (Webster et al., 2022a). At MOSAiC, MPF is greater than 30% on September 4, and all ponds had refrozen by September 6, 2020, effectively reducing MPF to 0%.

The number of melt ponds tracked by the MPA and DDA (gray histogram in 6.5c-d), significantly decreases toward the end of August indicating ponds have either drained or a lid has formed, preventing the laser penetration into the pond. This is consistent with our findings of low MPF during this period. The WorldView image observed on September 3 (Figure 6.2e), shows light gray ponds, indicative that a pond lid that has formed.

6.6.5 Regional Results in a Pan-Arctic Context

The results presented in this chapter are specific to the multiyear ice region in the 2020 melt season. Although this can provide us with information regarding the melt process, it is not representative of all ice conditions and melt seasons. Melt pond formation and evolution progresses differently on first year ice (Section 1.2.2), and regional synoptic events affect the timing of melt formation and drainage. Nonetheless, these spaceborne measurements of sea ice melt across a large region, can help us understand how spatially smaller studies (such as in situ studies) may or may not be representative of a larger area. This study only captures the 2020 melt season. The summer of 2020 was a unique melt season, where the Arctic experienced above average surface air temperatures (Section 6.3). We recoginize that this study is not representative of all melt seasons, however it does provide insight on the stages of melt progression. Satellite measurements are limited by lower sampling frequency as compared to in situ studies, limiting the ability to capture short lived events (Webster et al., 2022b). Also, unlike in situ measurements, satellite measurements are impacted by cloud cover, skewing our results towards clear-sky melt conditions which may be different than cloud-covered melt conditions. We emphasize the importance of the network of summer sea ice measurements to understand local melt processes, the spatial and temporal scalability, and long term trends of summer sea ice melt.

In Section 7.3.4, we suggest expanding this work to study larger regions over longer time periods. The image classification methodology has proven successful at classifying first year ice imagery (Buckley et al., 2020a), but further melt pond tracking algorithm testing and validation of pond depth retrieval is required to

determine if tracking shallow ponds from spaceborne altimetry is feasible (Section 7.3.4).

6.7 Relationship Between Melt Pond Fraction and Depth

We consider our MPF and depth evolution results in context of previous studies of the melt pond depth-area relationship. Perovich et al. (2003) presents a time series of depth and fraction observations obtained from a 200-m albedo line at SHEBA in 1998 (Figure 6.8a, circles). The SHEBA observations reveal a constant linear relationship between pond fraction and pond depth (Perovich et al., 2003).

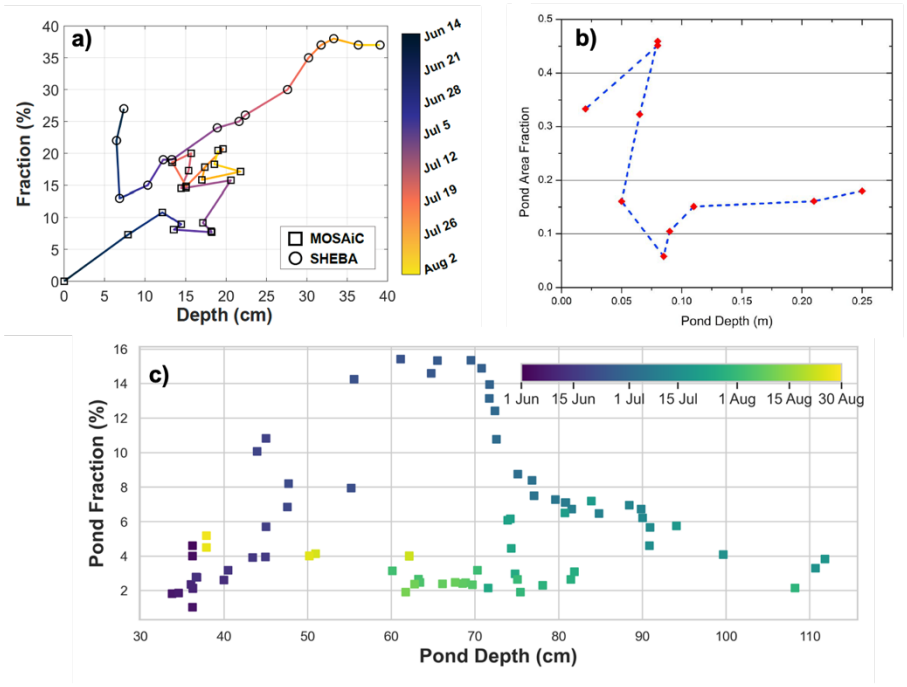

Figure 6.8. Figures showing evolution of pond depth and fraction. a) Observations from MOSAiC in 2020 (squares) showing evolution of pond fraction and depth colored by time, with the same results from SHEBA in 1998 (circles) from Perovich et al. (2003), figure from Webster et al., 2022a. b) relationship of pond area fraction to pond depth from Polashenski et al. (2012). c) relationship of pond fraction to pond depth from this study.

The ratio between pond area and pond depth from Perovich et al. (2003) is used to parameterize ponds in the CESM and level-ice formulation available in CICE (Holland et al., 2012, Hunke et al., 2013). As defined in Holland et al. (2012):

$$h_p = 0.8 \times MPF \tag{6.1}$$

Where *MPF* is melt pond fraction as a percent (%) and h_p is pond depth in centimeters. However, Webster et al. (2022a) do not show a clear relationship between pond depth and area (Figure 6.8a, squares), as pond fraction increases depth increases until early July when MPF increases but mean pond depth remains fairly consistent. Polashenski et al. (2012) show that in their study over landfast ice off of northern Alaska in 2009, the relationship between pond fraction and depth cannot be described by any function (Figure 6.8b). In this study, we also do not see a clear linear relationship between mean pond fraction and depth (Figure 6.8c), instead we see an increase in both pond fraction and pond depth early in the melt season, and then a decrease in pond fraction as the depth continues to increase. In August, pond depth decreases, while pond fraction remains consistently low.

More work is needed to understand the evolution of these parameters at small local scales and Arctic-wide. We have only applied the DDA to a small subset of available ICESat-2 tracks, and further analysis may provide additional information to better characterize this relationship. The study presented here shows the feasibility of conducting such analysis over large regions of the ice cover.

6.8 Chapter Summary

In this chapter we presented our findings on the evolution of summer melt on multiyear ice in 2020 using Sentinel-2 and ICESat-2 data (Buckley et al., 2022). The study region includes the area of the thickest ice in the Arctic that has experienced deformation as it is push along the Canadian and Greenland coasts.

We applied the classification algorithm to Sentinel-2 imagery and derive MPF and SIC from the classified images. We validated the MPF and SIC derived from Sentinel-2 (10 m resolution) with those derived from coincident higher resolution WorldView images (~1.5 m resolution). We found on average the Sentinel MPF and SIC is -7.2% lower and 4.2% higher, respectively, than that of WorldView imagery. These biases have a seasonal trend, as melt pond fraction increases, the MPF bias increased in magnitude, and as sea ice concentration decreases, the SIC bias decreases in magnitude. After validating our derived parameters and acknowledging potential biases, we then looked at the trends of SIC and MPF. SIC was high in the beginning of the season and became more variable and decreased throughout the melt season. MPF began low, increased sharply on 17-24 June, peaks at 16.0% on 24 June, and then slowly decreased throughout the remainder of the season.

We conducted an analysis of melt pond size distribution in WorldView imagery (Section 6.4.2) and quantified the impact of sub-pixel melt ponds on Sentinel-2 MPF. We found that although accounting for the area of the sub pixel melt ponds found in WorldView imagery in the calculation of the Sentinel-2 MPF improved the estimates of the Sentinel-2 MPF, it did not make up the entire

discrepancy, suggesting other sources of error contribute to the Sentinel-2 low MPF bias.

We then derived melt pond depth from ICESat-2 photon data. We applied the MPA to 477 ponds distributed in space and time. The DDA is fully automated and when applied to 87 ICESat-2 tracks, we found over 7,000 melt ponds. In both the MPA and DDA- tracked ponds, the melt pond depth increased through mid-June when it decreased in the DDA ponds and continued to increase in the MPA ponds. We found good agreement in the ponds that both algorithms tracked, but the DDA demonstrated the ability to automatically detect ponds that we may have missed in the manual MPA pond identification. We conclude that although the MPA may under-sample shallow ponds, it is able to effectively track the evolution of the largest ponds. Using the melt pond size distribution analysis described in Section 6.4.2, we quantified the percentage of melt pond area that may not be captured by the two algorithms. Given the minimum trackable ponds width of 20 m and 7.5 m for the MPA and DDA, respectively, we found that the MPA may miss as much as 70% of melt ponds, by pond area, and DDA 20%.

We discussed the evolution of MPF, SIC and melt pond depth in context of previous in situ, airborne, and modeling studies of melt evolution. Conclusions and a discussion of the impact of this work are offered in Chapter 7.

Chapter 7: Summary and Conclusions

The goal of the work presented in this thesis was to utilize new, high-resolution remote sensing observations of Arctic summer sea ice to enhance our understanding of summer melt processes and patterns. Considering the observed negative and accelerating trends in the end of summer sea ice extent, we are motivated to understand the evolution of summer sea ice throughout the melt season. This chapter provides a summary of the work conducted in reaching this goal, and the impact of our findings. First, we summarize the major algorithm development activities undertaken for the classification of melt features in airborne imagery collected during the NASA IceBridge mission (section 7.1) and we discuss the results of the classification process. Second, we discuss our approach to tracking the evolution of summer melt on multiyear sea ice in the Arctic (section 7.2) using a combination of active and passive remote sensing. We discuss the application of our ice type classification algorithm to widespread satellite imagery and the novel use of satellite laser altimeter observations of ice elevation and melt pond bathymetry to track melt pond depth development during summer. We discuss avenues for potential future research in section 7.3, and final conclusions are offered in section 7.4.

7.1 Classification of Melt Features in IceBridge Imagery

7.1.1 Summary of Work

In Chapters 3 and 4 we describe our work using high-resolution (0.1 m) IceBridge imagery to conduct a detailed assessment of the summer sea ice cover of

the Arctic Ocean. Surveys of two distinct regions allowed for the comparison of melt pond conditions with respect to ice type. A 2016 survey focused on the marginal ice zone in the Beaufort and Chukchi Seas and comprised predominantly first year ice, while in 2017, data over the consolidated multiyear ice of the Central Arctic region were collected. MacGregor et al., (2021) describes the success of these summer campaigns despite the persistent cloud coverage in the Arctic summer, and highlights our ability to derive melt parameters from the DMS data (Buckley et al., 2020a).

In Chapter 3, we describe the development of an automated, pixel-based algorithm (Chapter 3) that effectively classifies summer sea ice features in DMS imagery, including undeformed sea ice, deformed sea ice, melt ponds, and open water (Buckley et al., 2020a). Our algorithm was a new approach in that it adapts to the variable overhead lighting conditions in DMS imagery. We created this algorithm so that it may be used for application to other high resolution imagery datasets. The scheme was applied to thousands of DMS images and the sea ice concentration (SIC), melt pond fraction (MPF), and pond color fraction (PCF) were derived on a per-image basis (Chapter 4). These parameters are important aspects of summer sea ice; SIC, MPF and PCF all provide information on the albedo of the Arctic sea ice and in turn, the absorption of incoming solar radiation.

These regional differences in MPF are related to the distinct ice type at the survey site, and our results conclusively show that MPF is greater on first year ice than on multiyear ice (Buckley et al., 2020a). In the Beaufort and Chukchi Seas, SIC averaged 69%, MPF averaged 25% and dark ponds dominated and had a PCF of 60%,

compared to a PCF of 9% and 31%, for medium and light ponds, respectively. In the Central Arctic, SIC averaged 90%, MPF averaged 14% and the PCF of light ponds was 68%, compared with 16% for both medium and dark ponds.

We examined our findings in context of previous studies of melt pond fraction on first year and multiyear ice and found good agreement. When compared with lower resolution datasets, we found our DMS-derived SIC is able to capture more variability in the sea ice cover, and the lower resolution passive microwave datasets may be biased high.

7.1.2 Impact of Findings

Our results have important implications for the study of Arctic-wide albedo in summer. Since 1985 the summer ice cover has transitioned from a predominantly multiyear ice cover to a seasonal ice cover (Comiso, 2012, Tschudi et al., 2020). The first year ice comprised 55% of the ice cover in the mid-1980s, compared to 77% in 2018 (Perovich et al., 2018). Thick multiyear ice is more resilient than the thinner younger ice, and is more likely to survive the summer melt season. First year ice is more likely to melt out during the Arctic summer, increasing the albedo of the Arctic.

As the multiyear ice of the Arctic Ocean is replaced by a younger, more seasonal ice cover, our results suggest that MPF will increase, and melt pond color will darken. The higher overall MPF and prevalence of dark MPs on first year ice discovered in our analysis of the 2016 and 2017 IceBridge imagery (Buckley et al., 2020a) demonstrate the critical control that melt ponds have on overall albedo of the

Arctic Ocean in summer. Lower albedo surfaces, including dark melt ponds, allow for more absorption of incoming solar radiation. Pond albedo typically ranges from 0.1 to 0.3 for dark ponds, approximately 50% lower than the albedo of light ponds which ranges 0.35-0.55 (Perovich, et al. 2002). Our results show ponds are darker and more widespread in the Beaufort and Chukchi Seas consisting of predominantly first year ice. We therefore expect changes in pond fraction and color to accompany changes in ice type. This, in conjunction with a diminishing ice extent, would exacerbate the ice albedo feedback, increasing Arctic-wide solar absorption. In addition, melt ponds create a weaker ice pack, making the ice more vulnerable to break up in Arctic storms, such as occurred in summer 2012 (Parkinson and Comiso, 2013). The precise nature of future changes in the Arctic sea ice cover will also be influenced by the latitudinal location of the remaining summer sea ice.

The summer melt data products derived in this study are available as HDF5 files (one per image) containing the classification dataset with the dimensions of the original DMS GeoTIFF where each value indicates the pixel classification (Buckley et al., 2020b). There are also ASCII text files (one per flight) with the SIC, MPF, and PCF derived from the classification masks. These data are of keen interest to the community for a number of related studies. Our findings were incorporated in a review of IceBridge science results (MacGregor et al., 2021) to demonstrate the utility of airborne surveys of summer Arctic sea ice. Sea ice modelers may find these parameters useful for understanding melt pond shapes and fractions in initialization and validation of models. The melt pond shapes and areas (see Figure 3.6) can provide information on transmission of light through the ice pack (Light et al., 2015)

for those who study under ice ecology. The MPF product can be used to validate satellite MP products, for example, the MODIS MPF as described in Rösel and Kaleschke (2012). Similarly, the SIC product could be used for validation of the AMSR2 and CDR SIC (Meier et al., 2018, Meier et al., 2017). As we evaluate lower resolution data products with longer records and Arctic-wide observations, we can quantify summer-specific uncertainties, that may be considered to improve these datasets.

The classification algorithm developed and described in Buckley et al., 2020a is design to adjust automatically to pixel size and light conditions, and therefore has application to other remote sensing datasets. In fact, this algorithm with minor modifications was applied to Sentinel-2 and WorldView imagery for the melt evolution study (Buckley et al., 2022), detailed in Chapter 6. The automated classification approach opens up the possibility of processing and analyzing imagery data sets that span multiple years and various regions. This provides potential to investigate the variability and trends in MPF with time as sea ice conditions in the Arctic change. We will discuss this further in section 7.3 below.

7.2 Observations of Melt Evolution on Multiyear Sea Ice

7.2.1 Summary of Work

We have synthesized passive and active remote sensing observations of the summer sea ice to monitor the summer sea ice evolution in a new way. By combining observations from different platforms, we are able to weave together independent

measurements to optimize our understanding of sea ice melt. The goal of this work was to glean information from high resolution summer sea ice observations throughout the 2020 melt season. In section 7.1 we summarized the development of the image classification algorithm for the initial analysis focused on airborne observations. Here, we have applied the image classification algorithm to a seasonal study, expanding beyond the airborne study, and covering a full melt season at a basin-scale. ICESat-2 measures the sea ice surface at higher resolution that any satellite altimeter, providing the most detailed and precise elevation measurements to date (Farrell et al., 2020). We take advantage of these capabilities to measure melt pond depth from space for the first time. We utilize Sentinel-2 imagery and ICESat-2 altimetry to measure the melting sea ice in three dimensions from 1 June 2020 through 30 September 2020.

We have developed an algorithm to track the melt ponds observed in the ICESat-2 photon cloud for the first time (Chapter 5, Buckley et al., 2022). The UMD Melt Pond Algorithm (MPA), is able to track the surface and bathymetry of the pond enabling derivation of melt pond depth. The manual MPA was used to validate the results of a related automatic algorithm developed in collaboration with a team at UC Boulder. This algorithm, the DDA-bifurcate-sea ice (DDA), was developed as a member of a family of algorithms designed to track surfaces in a photon cloud at high resolution (Herzfeld et al., 2017, 2021). The DDA has the ability to track multiple reflectors (such as a pond surface and bathymetry) and is auto-adaptive, and different from the MPA in that it does not require manual input, thus, is much more efficient.

We applied the image classification algorithm (Chapter 3) to cloud-free Sentinel-2 imagery acquired 1 June 2020 through 30 September 2020. We derived MPF and SIC from over 1,000 images to understand the evolution of the sea ice throughout the summer. The MPA is used to track hundreds of ponds throughout our study region and period. The DDA is applied to 87 ICESat-2 tracks across our multiyear ice study region, tracking thousands of melt ponds. We follow the evolution of the sea ice parameters throughout the melt season.

We find the melt pond fraction increasing until June 24, peaking at 16 % and then decreasing for the remainder of the summer due to melt pond drainage. Melt pond fraction results are consistent with other studies conducted on multiyear ice (e.g., Buckley et al., 2020a; Rösel and Kaleschke, 2012; Mäkynen et al., 2014). We find the median depths of individual ponds tracked by the algorithms as 0.81 m and 0.54 m on average from the MPA and DDA, respectively. In both the MPA and DDA results, the median pond depth increases throughout July. The melt pond depth evolution follows a similar pattern to other studies of pond depth (Perovich et al., 2003; Morassutti and LeDrew, 1996), but the depth values we find with the MPA are higher compared to other studies.

7.2.2 Impact of Findings

The approach taken in this work allows us to track melt evolution using multiple remote sensing datasets together, whereas previous work relied solely on one remote sensing technique. This new way of observing the Arctic will be critical for tracking pan-Arctic melt processes and assessing earth system model simulations.

The high-resolution summer sea ice properties derived in this work are of interest to the modeling community. We have demonstrated the novelty of ICESat-2 bathymetric mapping of melt ponds at a basin-scale. The heterogenous properties of melting summer sea ice occur at spatial scales smaller than the size of a model grid cell (Perovich et al., 2002), and these unresolved properties are in need of parameterization. The melt pond depth and melt pond fraction derived in this work will allow us the opportunity to reevaluate the relationship between pond fraction and depth and reassess parameterization schemes used in models. Integrating models and observations is essential for improved predictions and understanding observation needs.

These observations will point us towards a better understanding of summer surface melt, an important component of the thermodynamic mass balance of sea ice (Perovich and Richter-Menge, 2015). The pond depth and area measurements provide a three-dimensional view of the ponds and is valuable information for quantifying the volume of meltwater stored by the ice. Pond meltwater affects the freshwater budget of the upper ocean when it drains vertically through the ice and laterally off the ice. With simultaneous and continuous measurements of pond fraction and pond depth, we may estimate the evolution of meltwater storage, and thus meltwater flux to the ocean (as in Webster et al., 2022a). Further, the presence of ponds alters the hydrostatic balance assumed when deriving sea ice thickness from altimetry measurements of sea ice freeboard, and pond depth and fraction may be used to quantify how melt ponds affect this calculation (Chapter 2, Figure 2.6).

7.3 Suggested Future Work

Despite the advances in remote sensing techniques and studies like the work presented in this thesis, there remains a gap in our knowledge of summer sea ice. Remote sensing provides an opportunity for longer-term and larger-scale observations as compared to field studies. Here we suggest studies with the techniques and datasets developed in this thesis to expand our understanding of summer melt, and further validate the findings we have presented.

7.3.1 Melt Pond Depth and Volume

The DMS-derived data products (Chapter 4, Buckley et al., 2020a, 2020b) may be used in conjunction with high-resolution laser altimetry to understand the surface which the laser is measuring. We have demonstrated the feasibility of utilizing ATM waveform data to identify melt ponds and derive their depth in Chapter 5, section 5.2 (Buckley et al., 2019). While this technique was demonstrated in a small case study it may be applied more widely to ponds observed throughout the 2017 OIB campaign. Using melt pond fraction derived from imagery, with coincident estimates of pond depth derived from laser altimetry we can estimate pond volume. Obtaining widespread estimates of pond volume across multiyear ice during summer would provide an important observation for constraining freshwater fluxes in summer (Zhang et al., 2018). The freshwater layer in the upper level of the Arctic Ocean is crucial for preventing mixing with the warmer but denser ocean water below. The timing and magnitude of the freshwater flux from the sea ice to the ocean is essential for understanding and predicting the formation of under-ice blooms.

7.3.2 Under Ice Light Environment

The distribution of melt ponds on sea ice controls the partitioning of light and shortwave radiation through the ice pack (Light et al., 2008). Approximately four times more light is transmitted through ponds than bare ice (Arrigo et al., 2012). The availability of light is important when considering the ability for phytoplankton growth in the upper ocean (Arrigo et al., 2012). With the classified data arrays derived for each DMS image (Buckley et al., 2020), we have information on the spatial distribution of melt ponds across the sea ice surface, and can use this information to infer the light distribution beneath individual ice floes. Horvat et al. (2020) investigated the under-ice light field with synthetically generated melt ponds. They modeled the partitioning of light through a single number connected to the fractal dimension of the modeled (or observed) pond distribution. Estimating light penetration from our existing dataset can be used to validate the light field predicted by Horvat et al. (2020) and refine the understanding how melt pond distribution controls the under-ice light environment. The DMS dataset can be used to refine the model predictions of melt pond distribution and, in combination with measurements of under ice light, can quantify the differences between light penetration through ponded multiyear ice and first year ice. This is an important topic as 'massive' (>100 km) phytoplankton blooms have been observed beneath ponded first year ice (Arrigo et al., 2012). We have shown the different melt pond coverage on first year ice and multiyear ice, and expect changes in the under-ice light field as first year replaces multiyear ice in the sea ice cover.

7.3.3 Validation of Satellite-Derived Pond Depth

Remotely sensed data requires in situ validation (Buckley et al., 2022), and on summer sea ice, this is difficult to collect (see Chapter 1 section 1.5.4). In situ and airborne studies can help us understand the accuracy and limitations of satellite datasets (e.g., King et al., 2018, MacGregor et al., 2021). These airborne and in situ surveys provide the opportunity to obtain higher-resolution observations that may inform us of biases or errors associated with the lower resolution satellite products as in as in Cavalieri et al. (1991), Rösel et al., (2012), Connor et al. (2012), and Kwok et al. (2019).

The ICESat-2 Summer Sea Ice Campaign (ISSIC) 2022 is planned for mid-July 2022 with the explicit objectives to improve and assess the higher level ICESat-2 data products (ATL07 and ATL10), and develop a melt pond retrieval algorithm that can be integrated to the systematic production of ICESat-2 data products. The campaign includes the collection of lidar measurements and high resolution imagery from the Land, Vegetation, and Ice Sensor (LVIS) a 1064 nm wavelength lidar with a high resolution camera, and Chiroptera, operating at both green (515 nm) and infrared (1064 nm).

The algorithms and methodology derived in this work can be applied to the airborne data that will be acquired during the ISSIC 2022 campaign. The image classification algorithm can be applied to ISSIC 2022 airborne imagery to derive MPF and SIC, and the pond depth algorithm can be applied to the Chiroptera green lidar to obtain pond depths. The LVIS infrared lidar will provide surface elevation,

from which lead locations and freeboard can be determined. These data may be combined for estimated of pond locations, fraction, depth and volume. In the case of a successful ICESat-2 underflight, these data will be invaluable, providing insight into the ICESat-2 response to different surfaces present in the summer melt season.

Even more powerful will be the combination of ISSIC 2022 airborne observations with coincident or near coincident ICESat-2, Sentinel-2 and WV observations. Since the specific objectives of the summer campaign are to assess the utility of existing ICESat-2 algorithms for describing summer sea ice conditions, flight survey lines will be designed to target specific ICESat-2 overpasses and obtain spatially and temporally coincident satellite and airborne acquisitions. This will also provide the opportunity to validate the derived ICESat-2 melt pond depth and width using the existing MPA and DDA algorithms. Measurements of pond depth from the airborne instruments will improve our understanding of the ICESat-2 measurements, and in turn can help to improve our algorithms. For example, there is uncertainty in the vertical location of the true melt pond bottom. The MPA and DDA track this location differently leading to a discrepancy in the pond depths measured with these two algorithms. This campaign has the potential to clarify where the pond bottom exists within the photon cloud, and we may be able to adjust the pond tracking algorithms accordingly. ISSIC has the potential to clarify a number of the remaining questions about the ICESat-2 laser response during the melt season and this information will certainly improve the accuracy of ICESat-2 products and allow for a better quantification of uncertainty. These studies will allow us to better understand the ICESat-2 laser response to different melt conditions and improve the algorithms

so that their pond discrimination and depth retrievals are robust and accurate. Moreover, characterizing the response of the ICESat-2 laser altimeter in the summer is an essential step towards extending sea ice products (such as thickness) into the melt season, a critical component for improving summer Arctic sea ice predictions (Bushuk et al., 2020).

7.3.4 Basin-scale Studies

In this work, we have demonstrated the ability to develop algorithms that can be applied to various datasets (Buckley et al., 2020, 2022; Farrell et al., 2020). Future work involves applying these algorithms over larger regions, longer time series and to additional remote sensing datasets.

We have applied the UMD Melt Pond Algorithm and the Density Dimension Algorithm – bifurcate – sea ice to ICESat-2 tracks over the region of thick, rough and predominantly multiyear ice (Buckley et al., 2022). There is potential to extend investigations of summer melt by including ICESat-2 and Sentinel-2 observations over thinner, level ice. At this point we have applied to algorithm to primarily multiyear ice. Our ability to track shallow ponds is limited to some extent by the vertical resolution of the ICESat-2 photon cloud data, and the capabilities of the current tracking algorithms. We are also limited by Sentinel-2 data over first year ice, because during the summer, first year ice area retreats off the coast of western Canada and Alaska, to latitudes north of the data availability which is limited to within 20 km from the coast.

Despite these limitations, we are keen to apply the DDA algorithm to all summer sea ice tracks over multiyear ice, as we have only tracked about 10% of the summer 2020 tracks and no 2021 tracks thus far. We can also apply our classification algorithm (Buckley et al., 2020, Chapter 3) to all available high resolution summer imagery datasets. And finally, we look to improve our tracking algorithms so that it may resolve shallower ponds present on first year ice. With a higher density of pond observations spread through time and space, we will be able to analyze these observations at multiple scales and understand spatial patterns. The algorithms developed in this thesis are tools available for future projects.

7.3.5 Integrating Sea Ice Models and Observations

We have widely disseminated our work through presentations and attendances at workshops and conferences and through publications (Buckley et al. 2020, 2022; Farrell et al., 2020, MacGregor et al., 2021, Herzfeld et al. 2022). We will continue to circulate our work and engage with other researchers in the sea ice community to explore avenues for incorporating remote sensing observations in sea ice forecasting and prediction. As we work to expand our observational knowledge of summer sea ice, it is essential we collaborate and communicate with the sea ice modeling community, to understand required remote sensing observations. Long-term observations, over the large spatial extents of summer sea ice, will allow for an improvement in the characterization of sea ice properties for parameterization in climate models. The observed summer sea ice state acts as a basis for comparison with model output. With a better understanding of the summer sea ice processes, we

may be able to improve the model representation of the interconnected and complex processes that occur in the summer Arctic. Similarly, models provide an idea of the observations required to expand our understanding. Models may discover specific feedbacks or relationships that require further knowledge. Sensitivity studies can determine the relative importance of specific processes that the observational community may need to focus on. It has been shown that the reduction in uncertainties of satellite retrievals and potential to expand datasets throughout the melt season, will improve initial conditions in models and advance the summer ice forecasts (Bushuk et al., 2020). We continue to look to contribute to a strong connection between observation-focused scientists and modelers to efficiently move forward the field of Arctic sea ice science and in particular improve our understanding of the summer sea ice characteristics and processes.

7.4 Conclusions

This work contributes to the knowledge of summer sea ice and the evolution of melt pond properties such as melt pond depth and melt pond fraction. The techniques we have developed may be applied on a larger scale to extract more summer melt information from high resolution remote sensing datasets. Specifically, we have:

- Developed techniques for deriving melt parameters from new high resolution remote sensing imagery and altimetry
- Drawn conclusions about MPF on first year ice and multiyear ice

- Followed the evolution of melt through the 2020 summer season, and assessed the magnitude of MPF and melt pond depth in context of previous studies.
- Produced data products describing the summer sea ice to help inform new scientific studies of melt season processes.

Appendix 1: Sentinel-2 and WorldView Classifications

This appendix provides the Sentinel-2 and WorldView images used for the Sentinel-2 classification validation. Figures A1-18 show a) the original Sentinel-2 tile clipped to the extent of the coincident WorldView image, b) shows the classified Sentinel-2 image, where pixel classification is as follows: border (gray), sea ice (red), open water (blue), melt pond (yellow), other (green). c-d) are the same as in a) and b) but for the WorldView images. The figure number corresponds to the image number in Table 6.1 and Table 6.3.

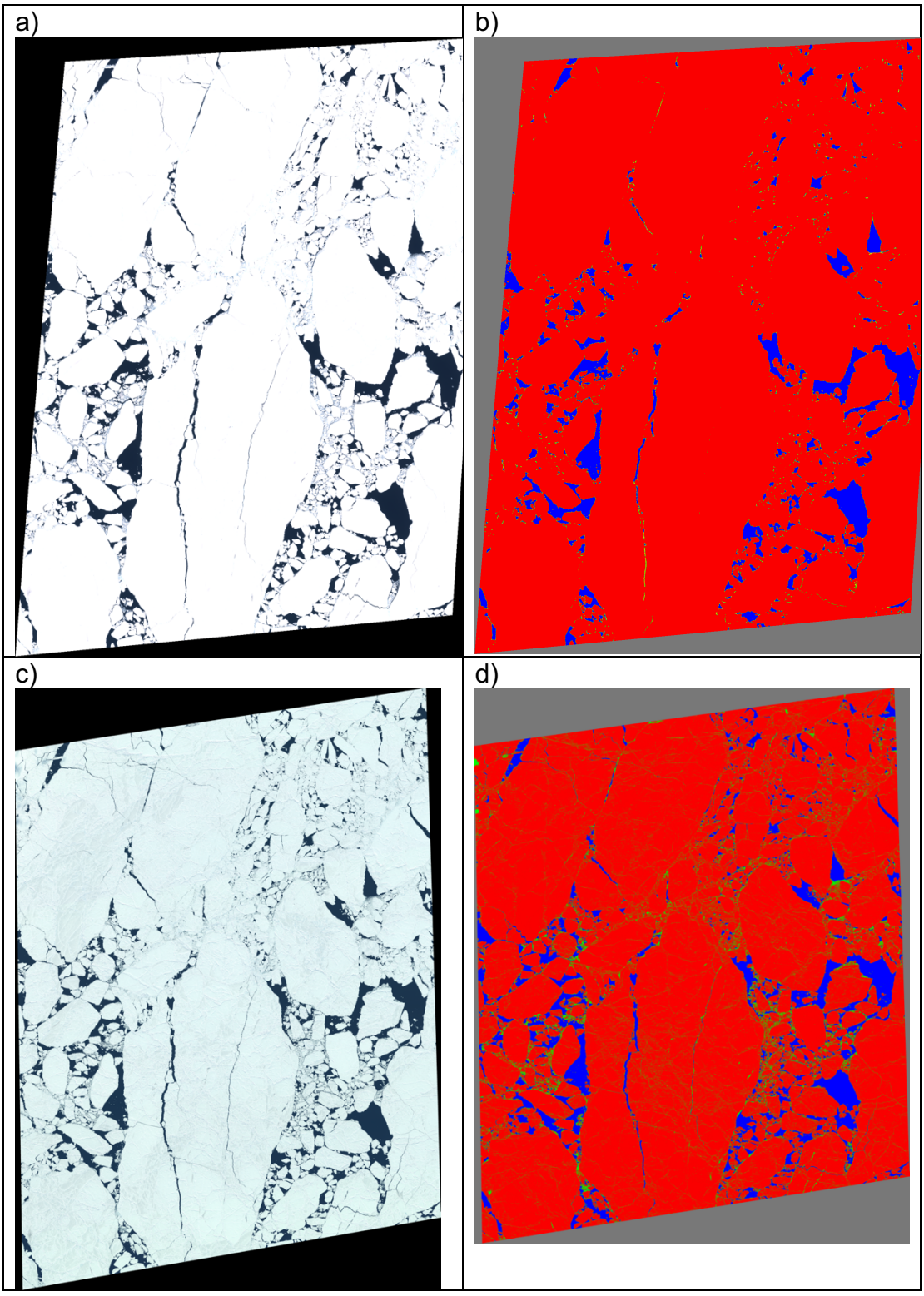

Figure 1. Images captured on 9 June 2020.

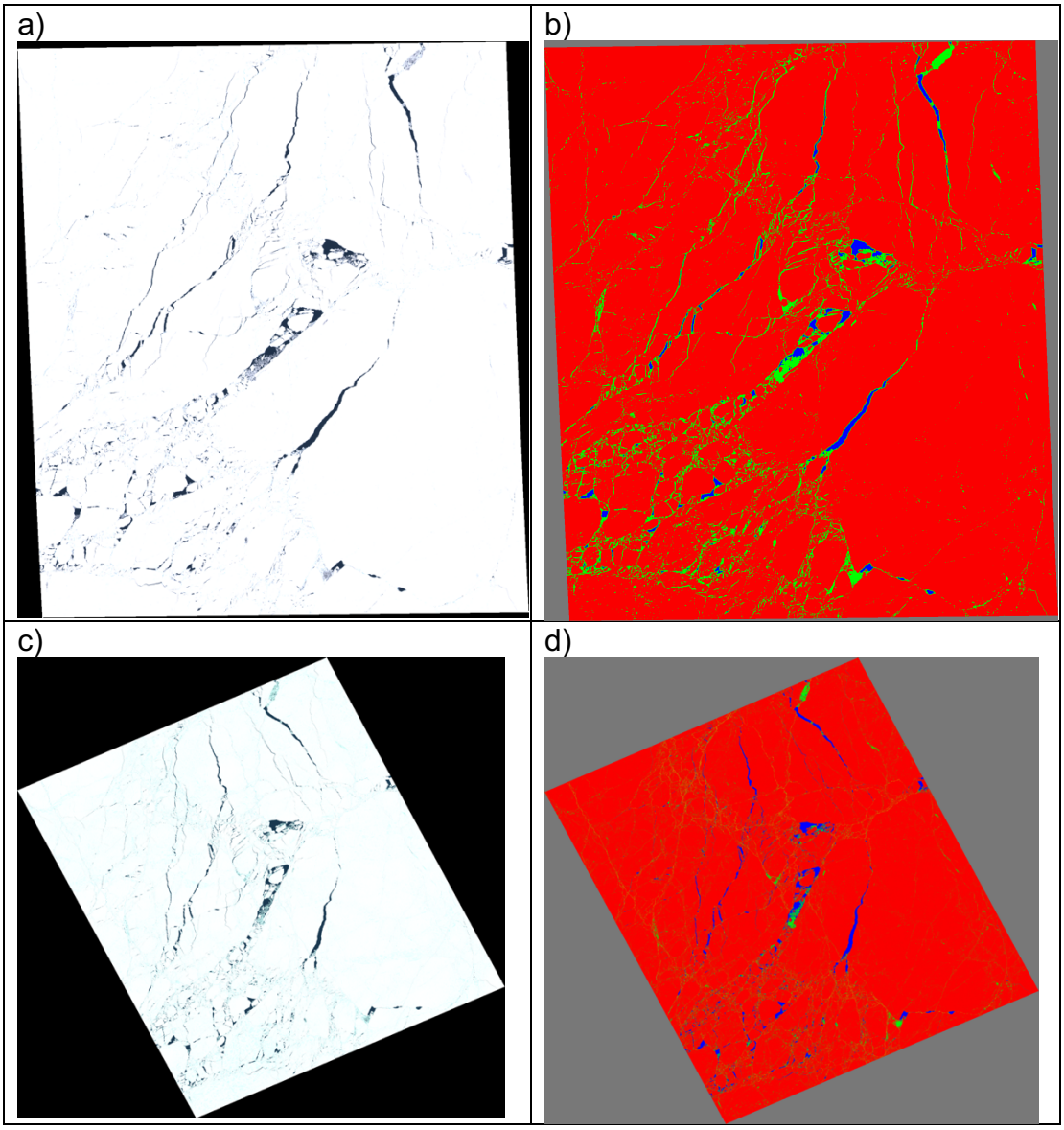

Figure 2. Images captured on 11 June 2020.

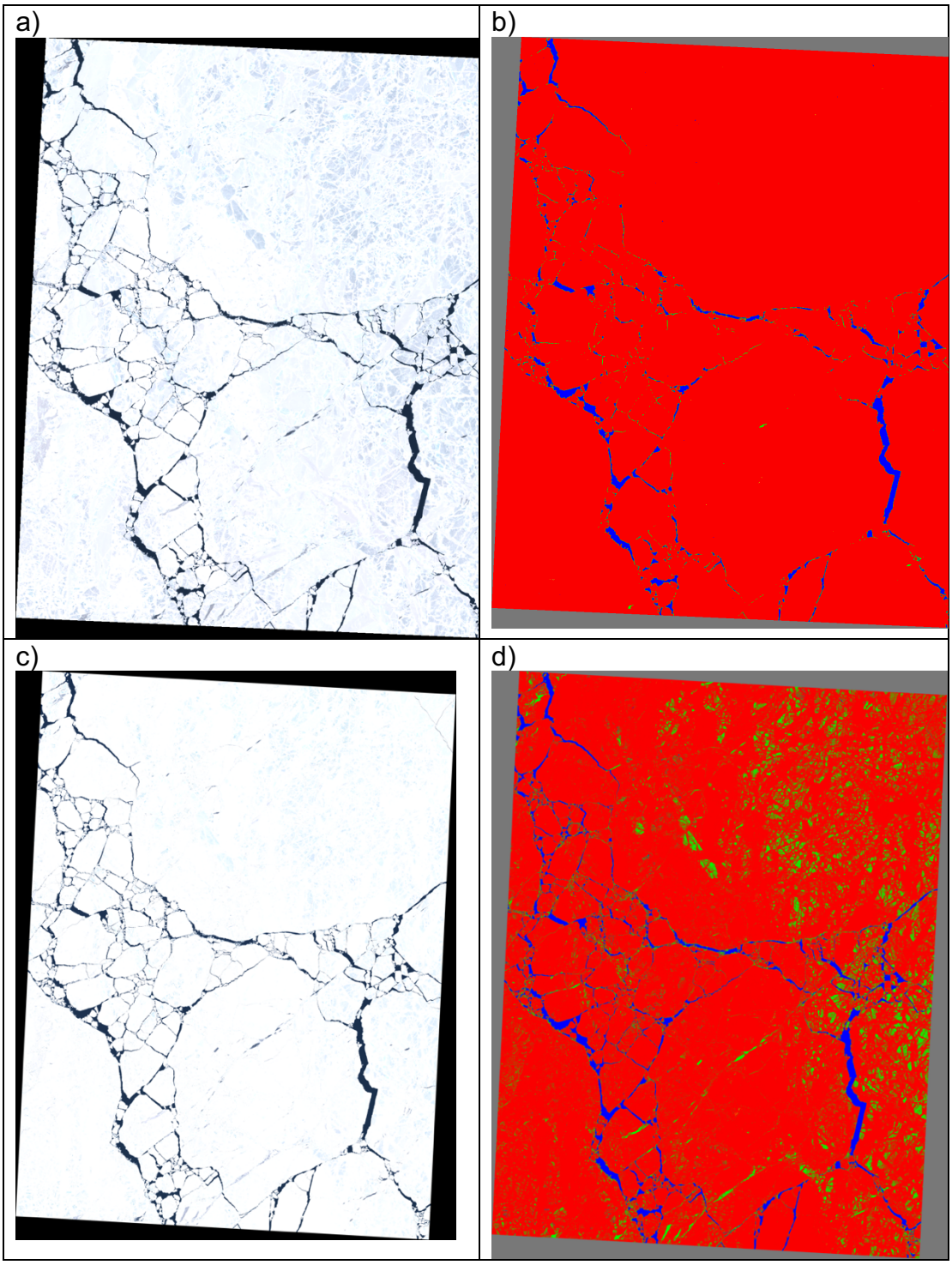

Figure 3. Images captured on 12 June 2020.

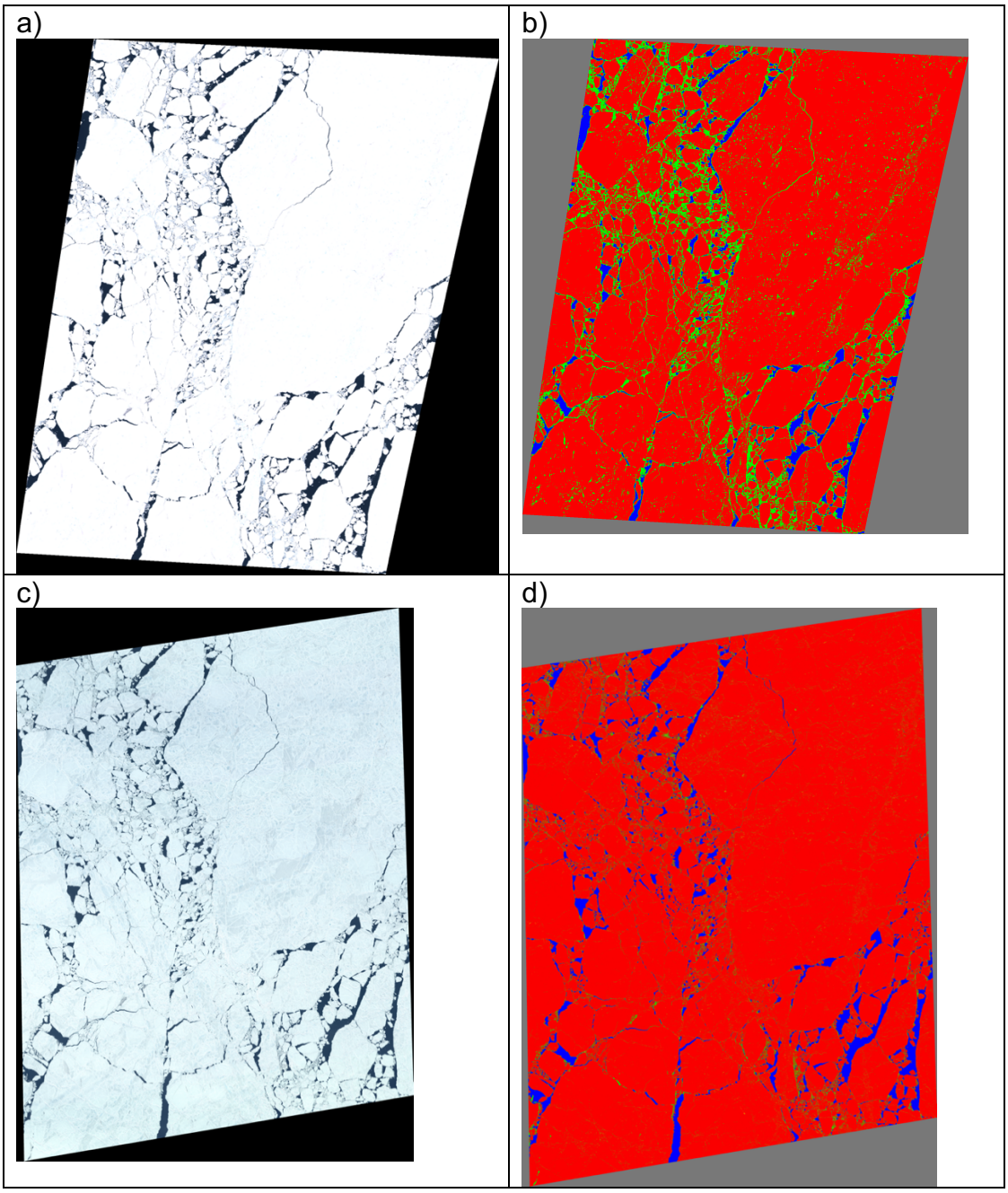

Figure 4. Images captured on 14 June 2020.

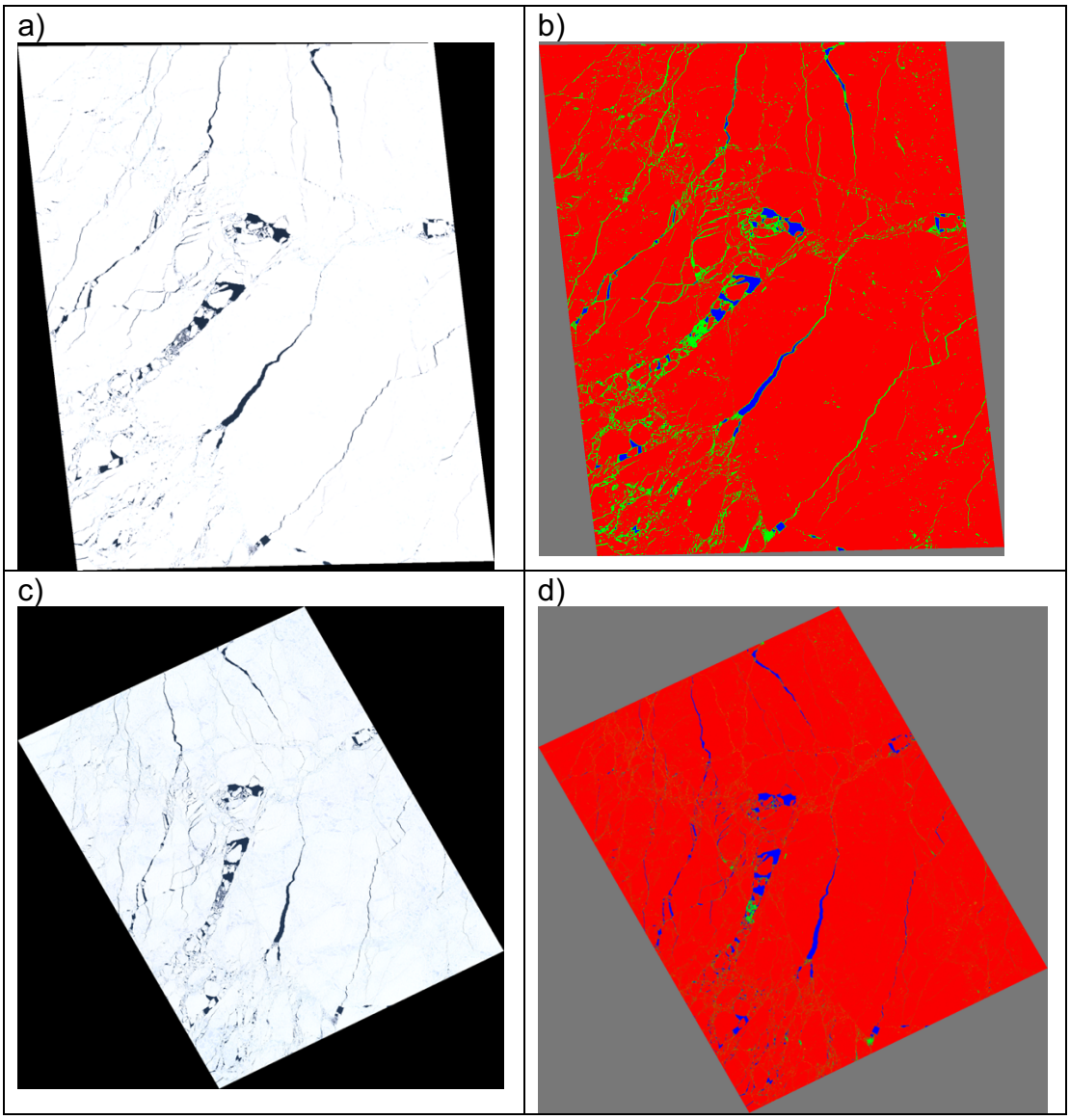

Figure 5. Images captured on 12 June 2020.

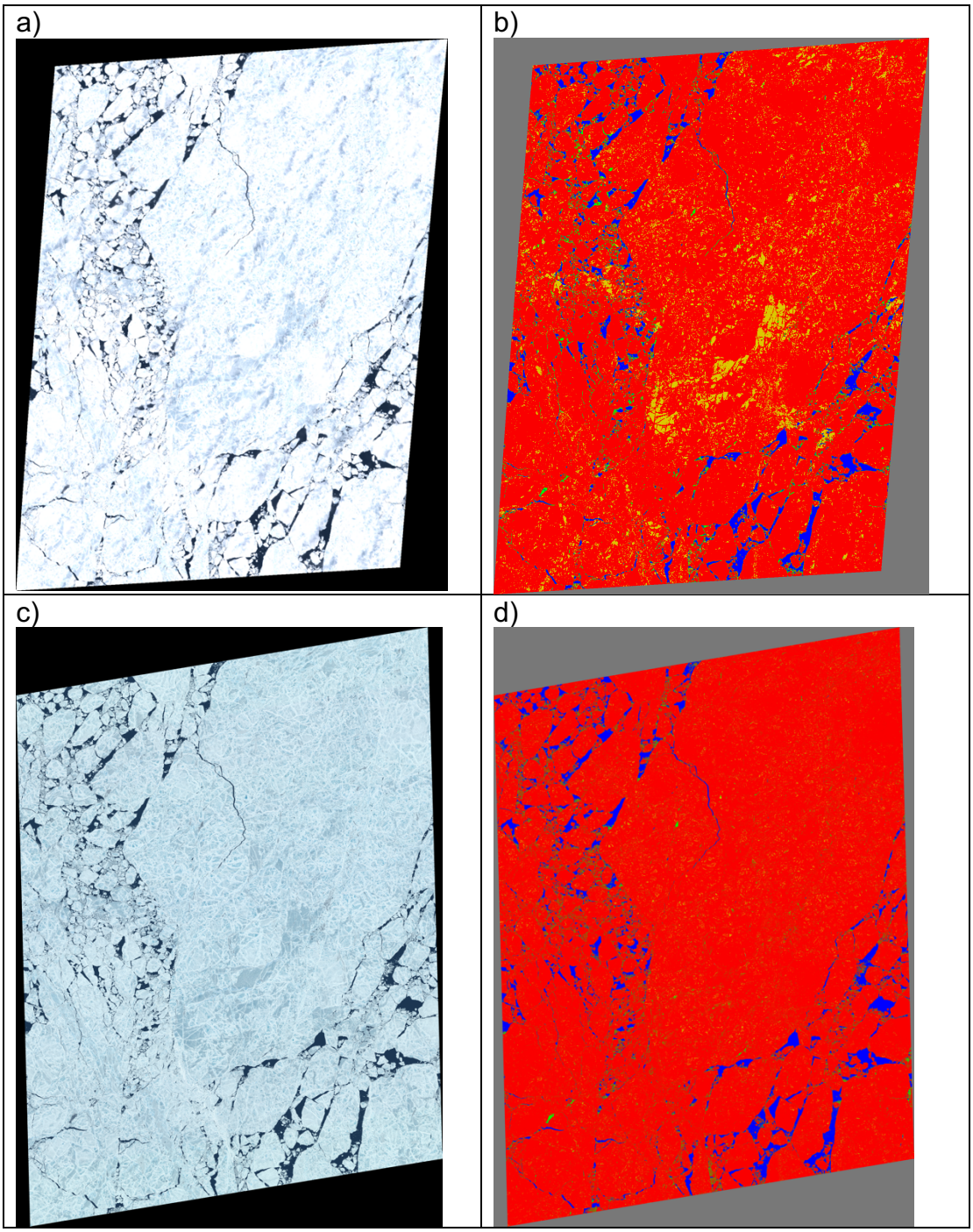

Figure 6. Images captured on 17 June 2020.

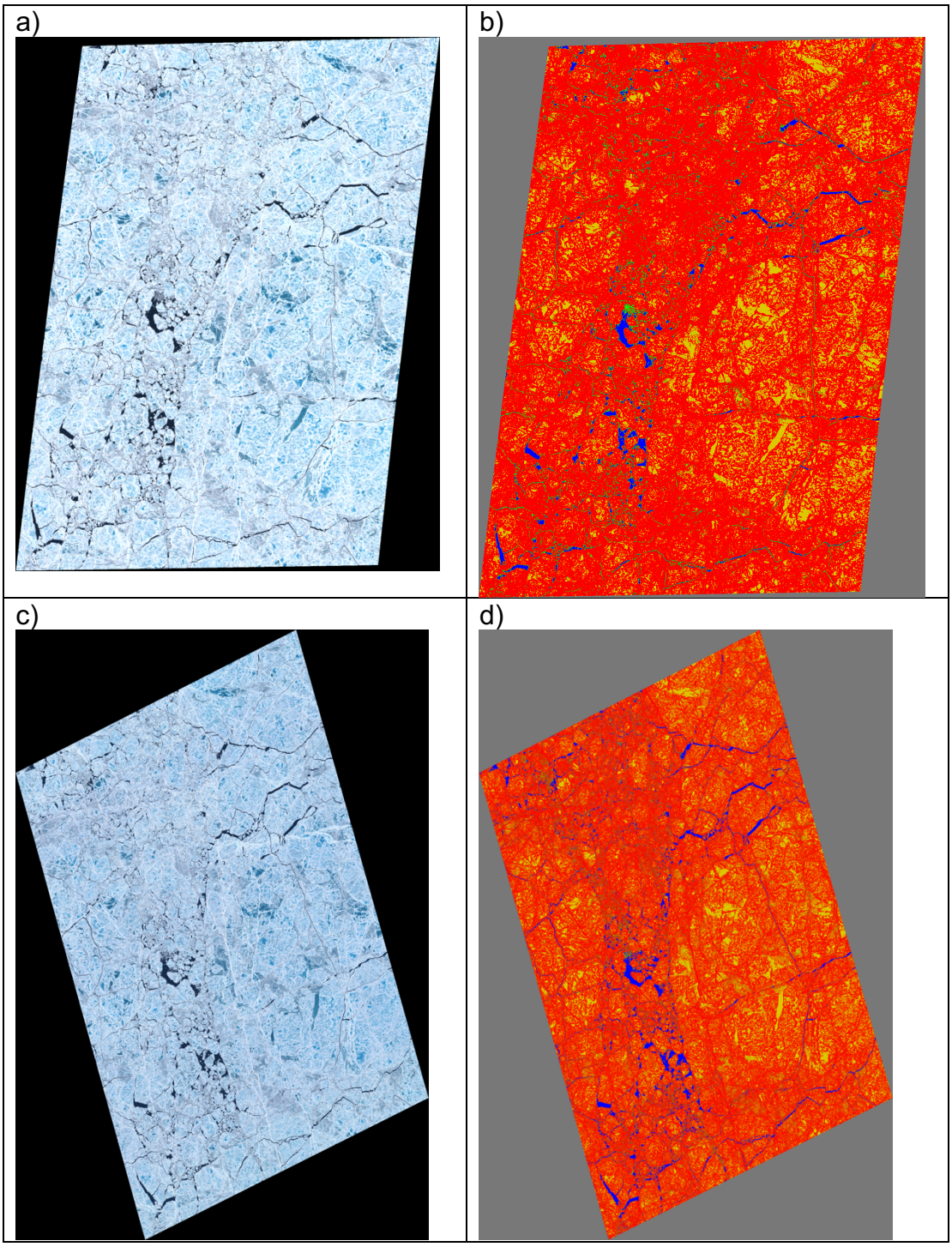

Figure 7. Images captured on 30 June 2020.

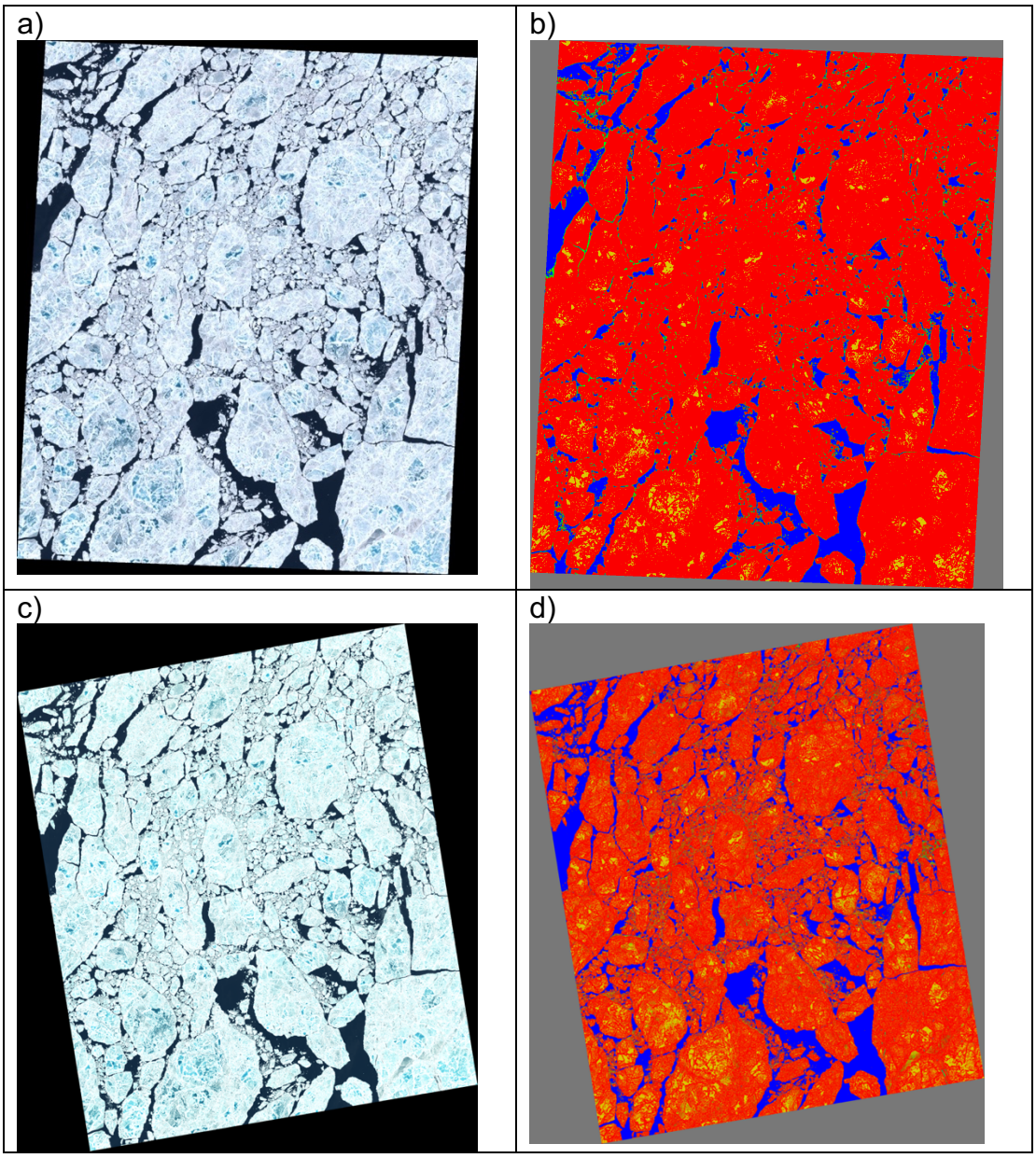

Figure 8. Images captured on 2 July 2020.

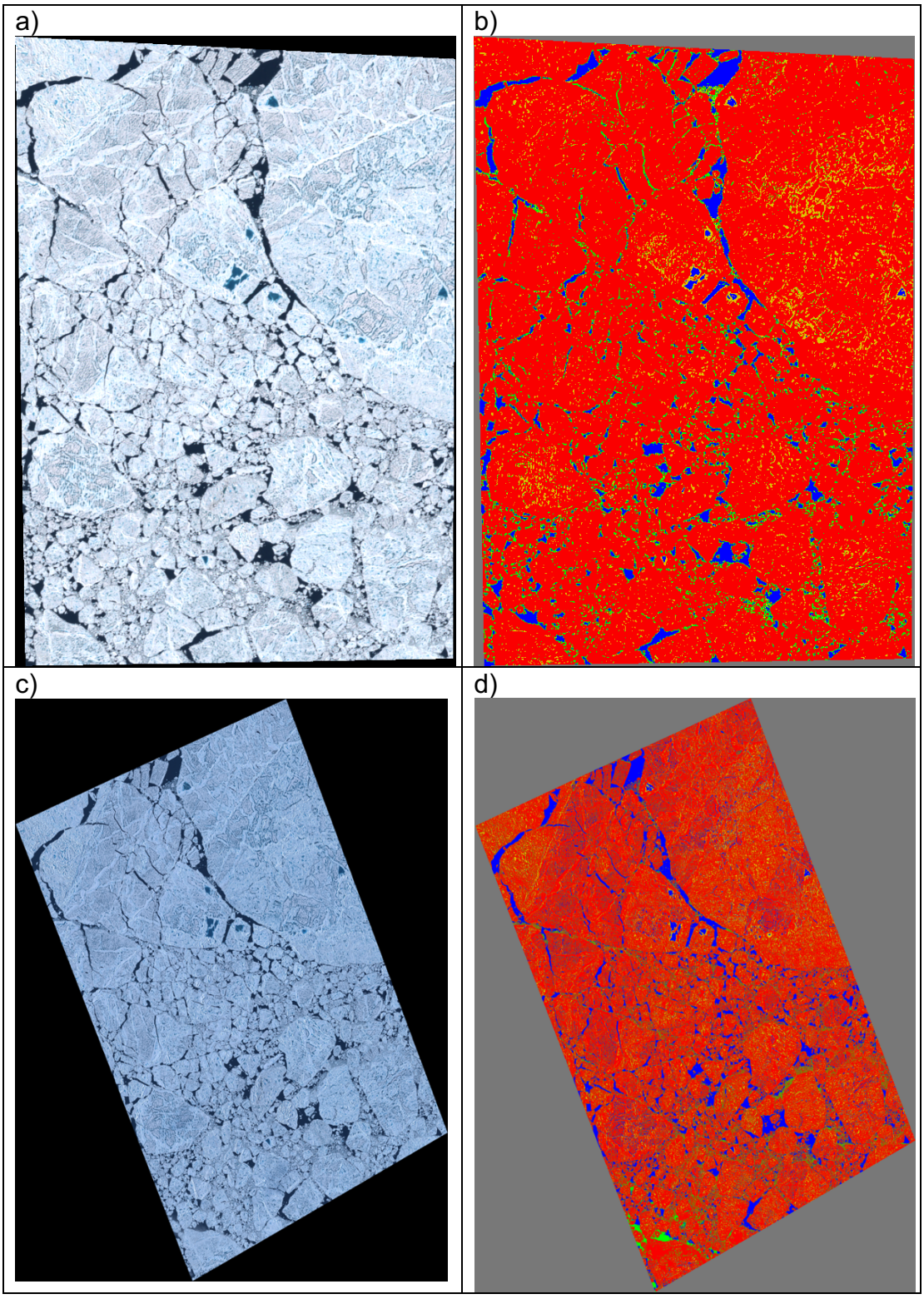

Figure 9. Images captured on 22 July 2020.

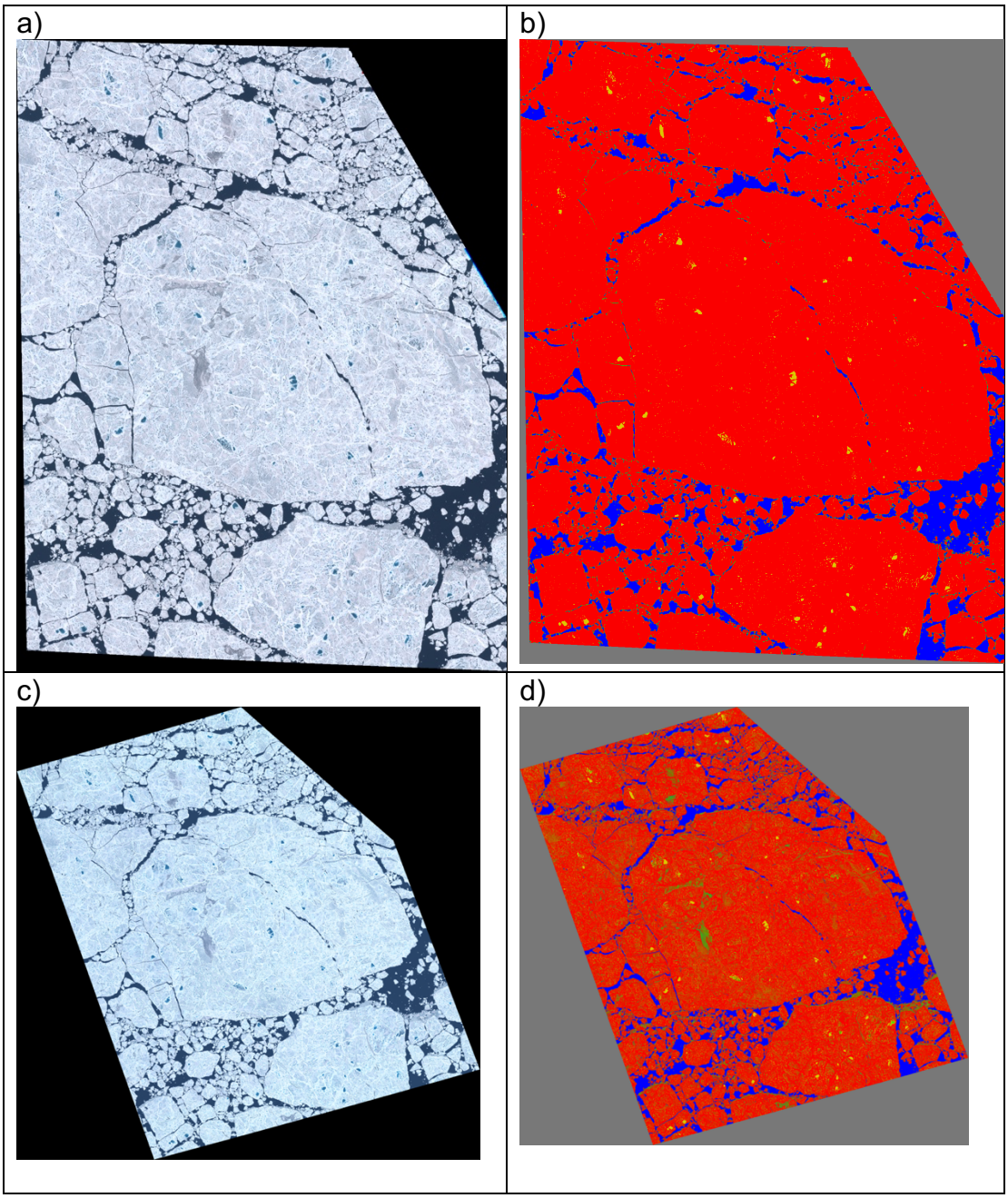

Figure 10. Images captured on 24 July 2019.

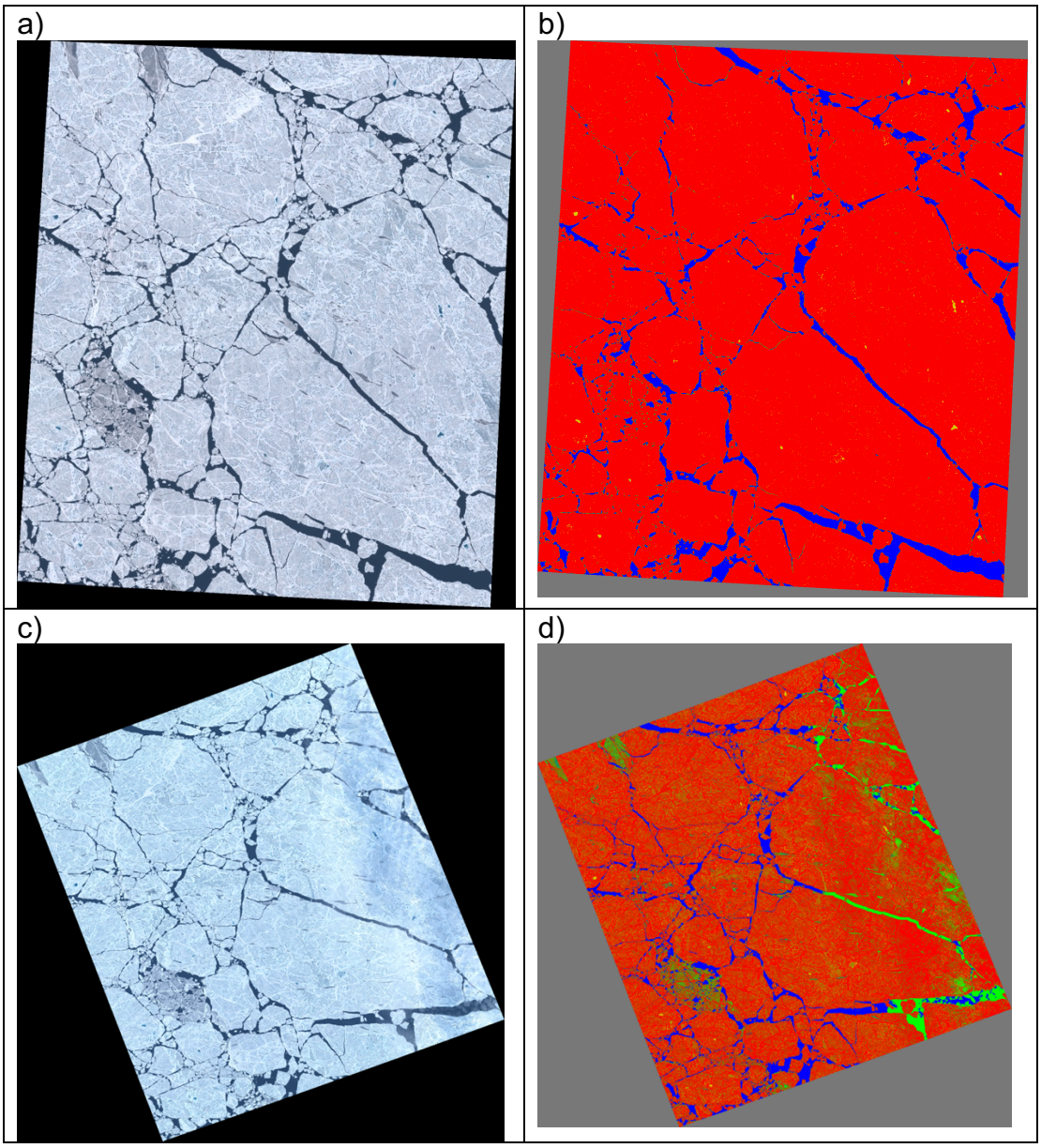

Figure 11. Images captured on 24 July 2019.

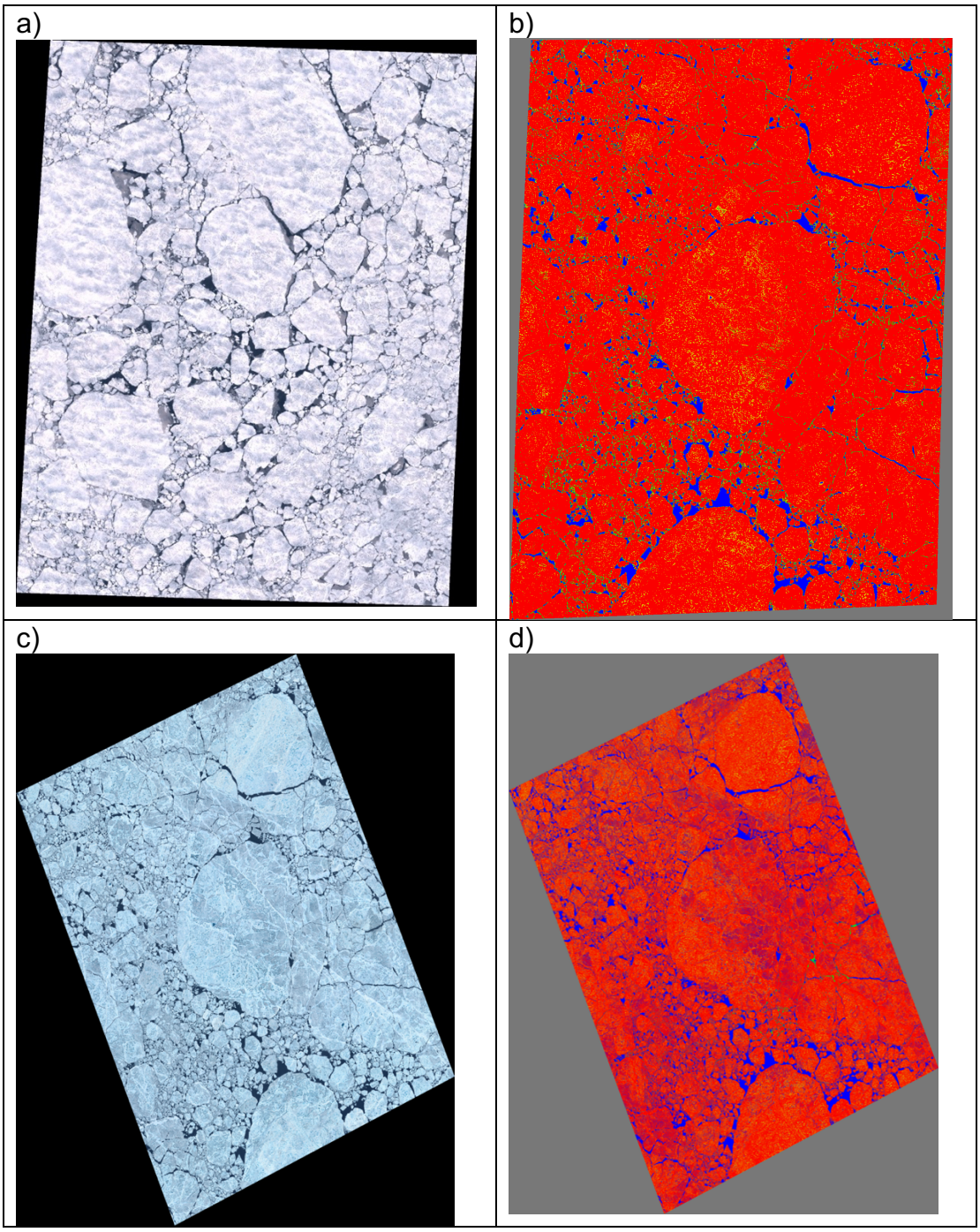

Figure 12. Images captured on 26 July 2019.

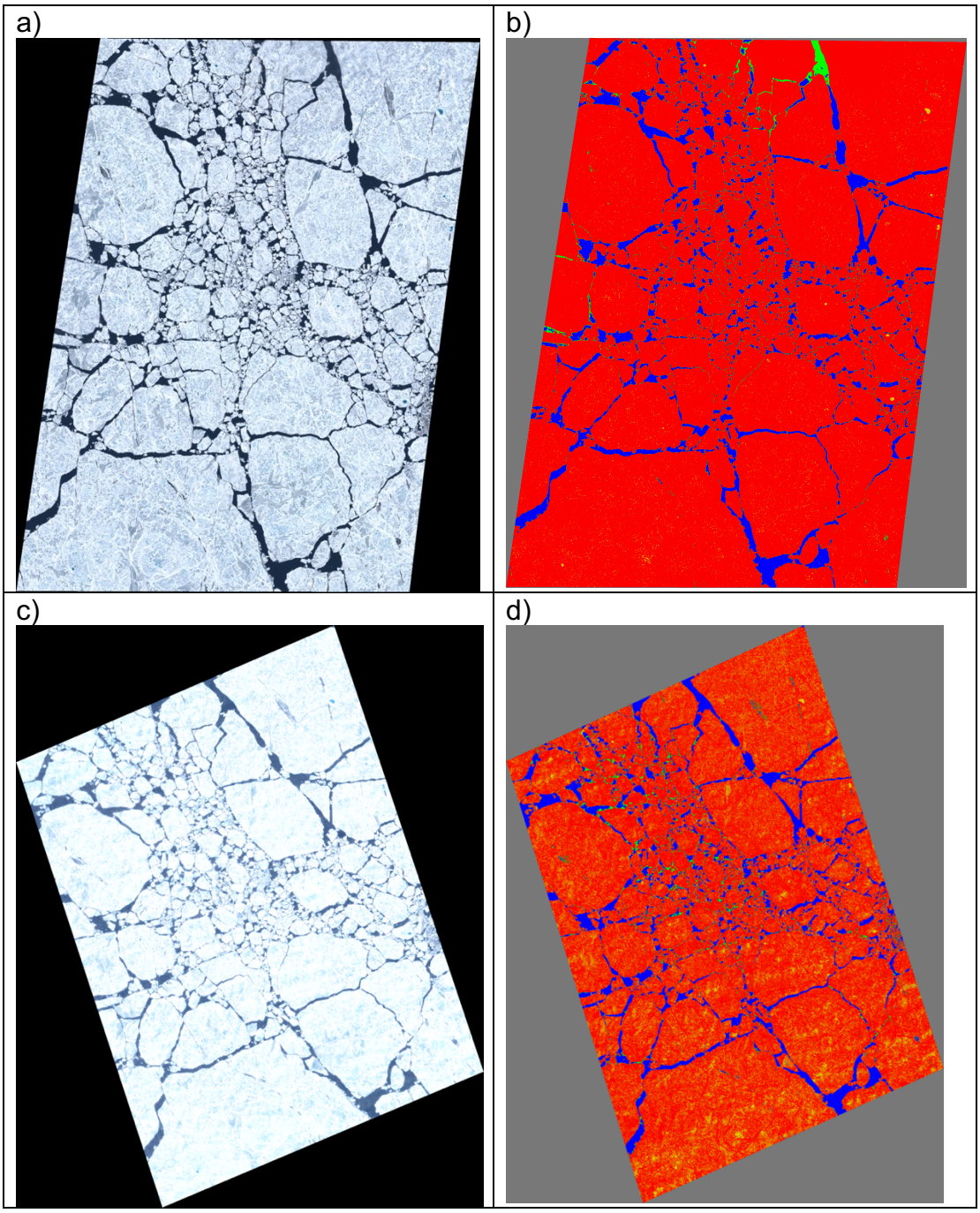

Figure 13. Images captured on 27 July 2020.

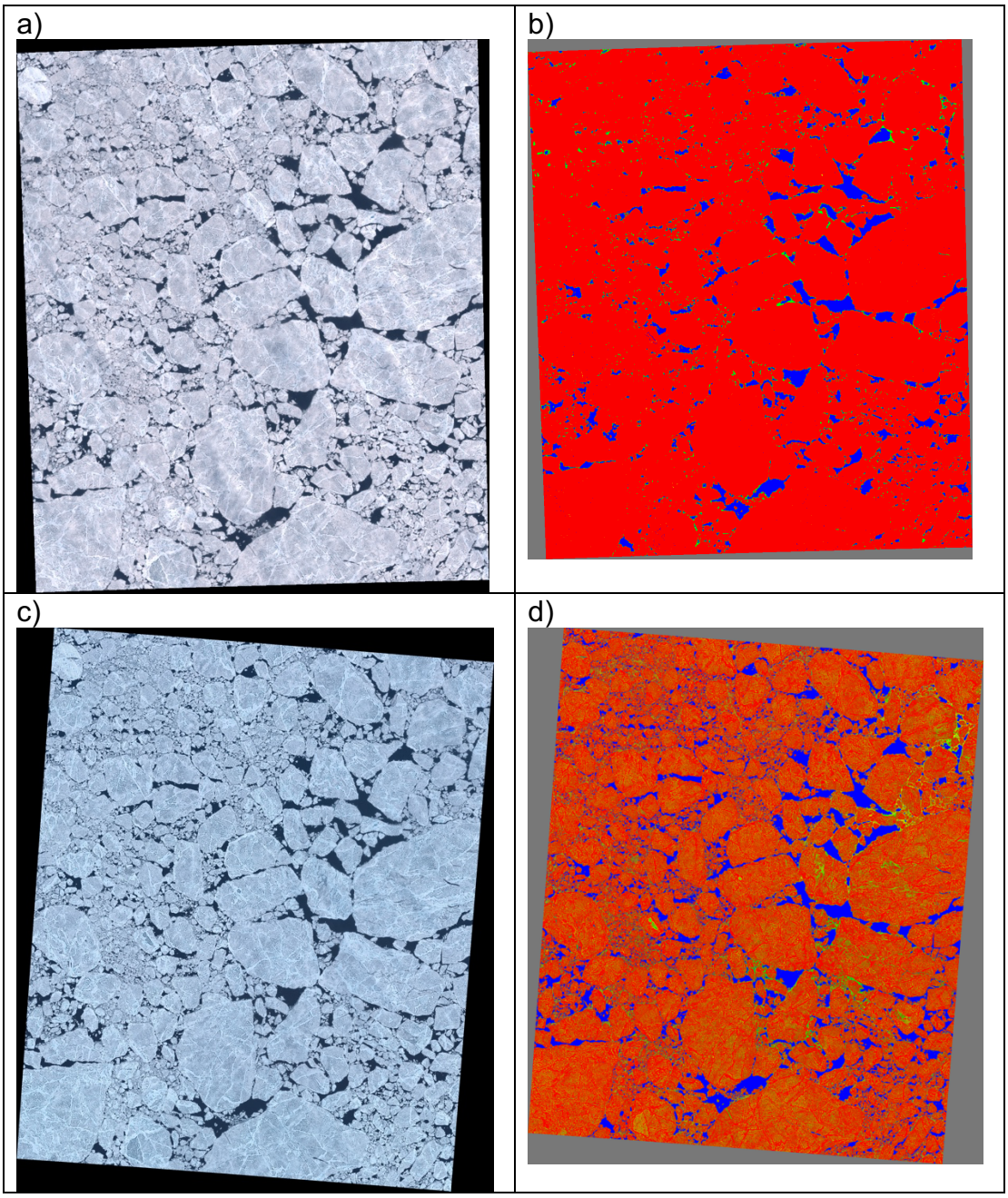

Figure 14. Images captured on 31 July 2020.

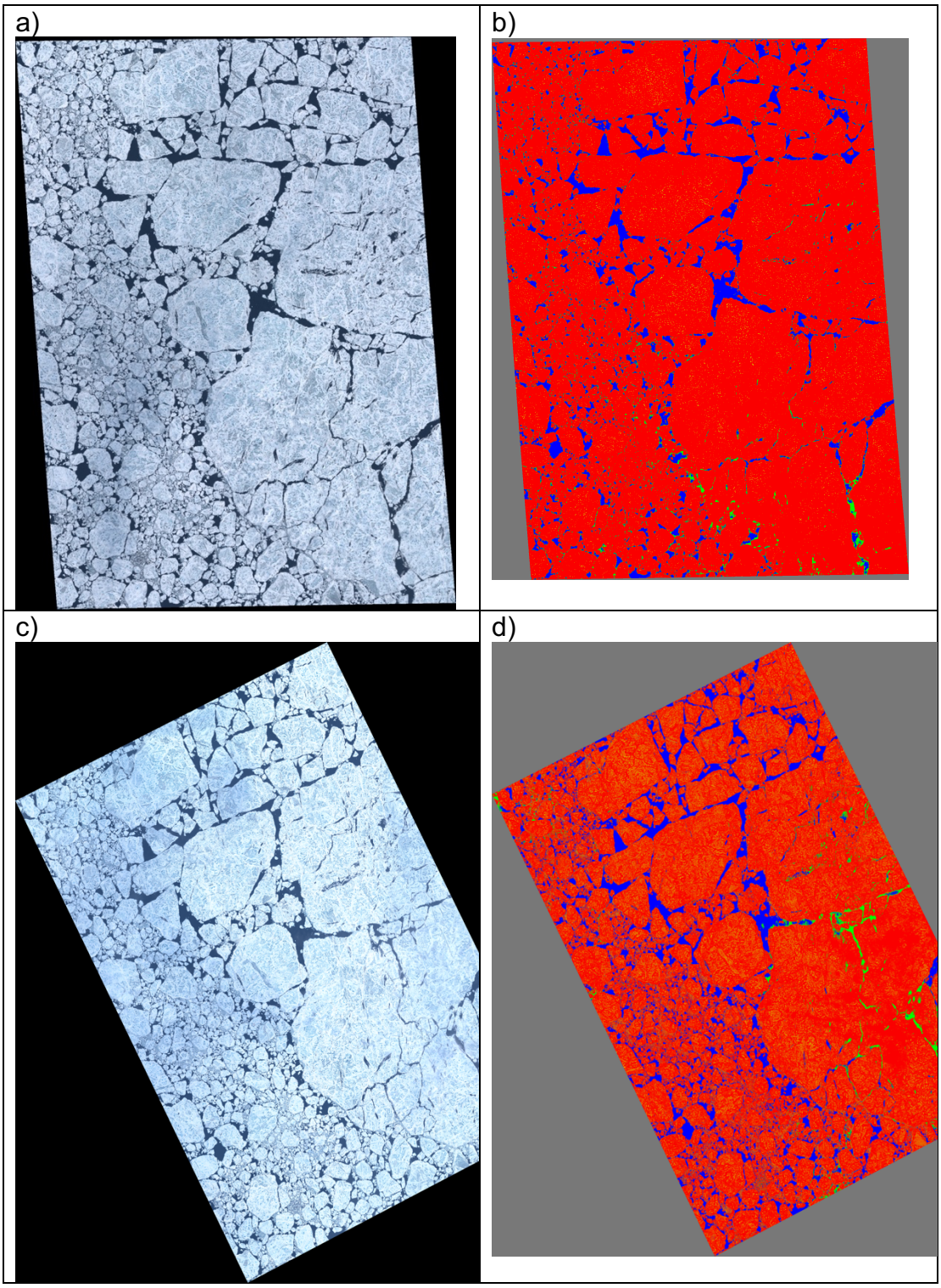

Figure 15. Images captured on 4 August 2019.

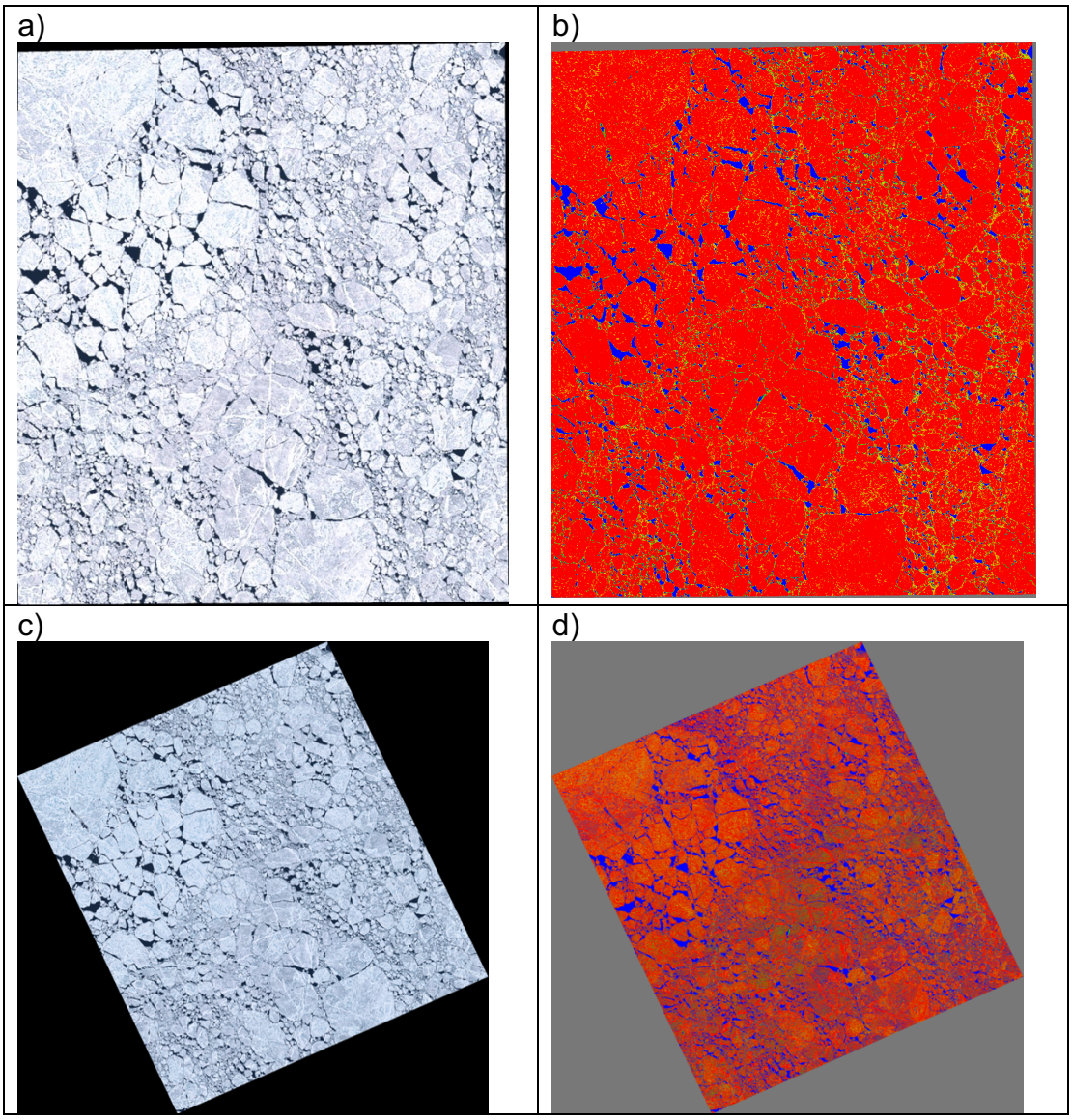

Figure 16. Images captured on 7 August 2020.

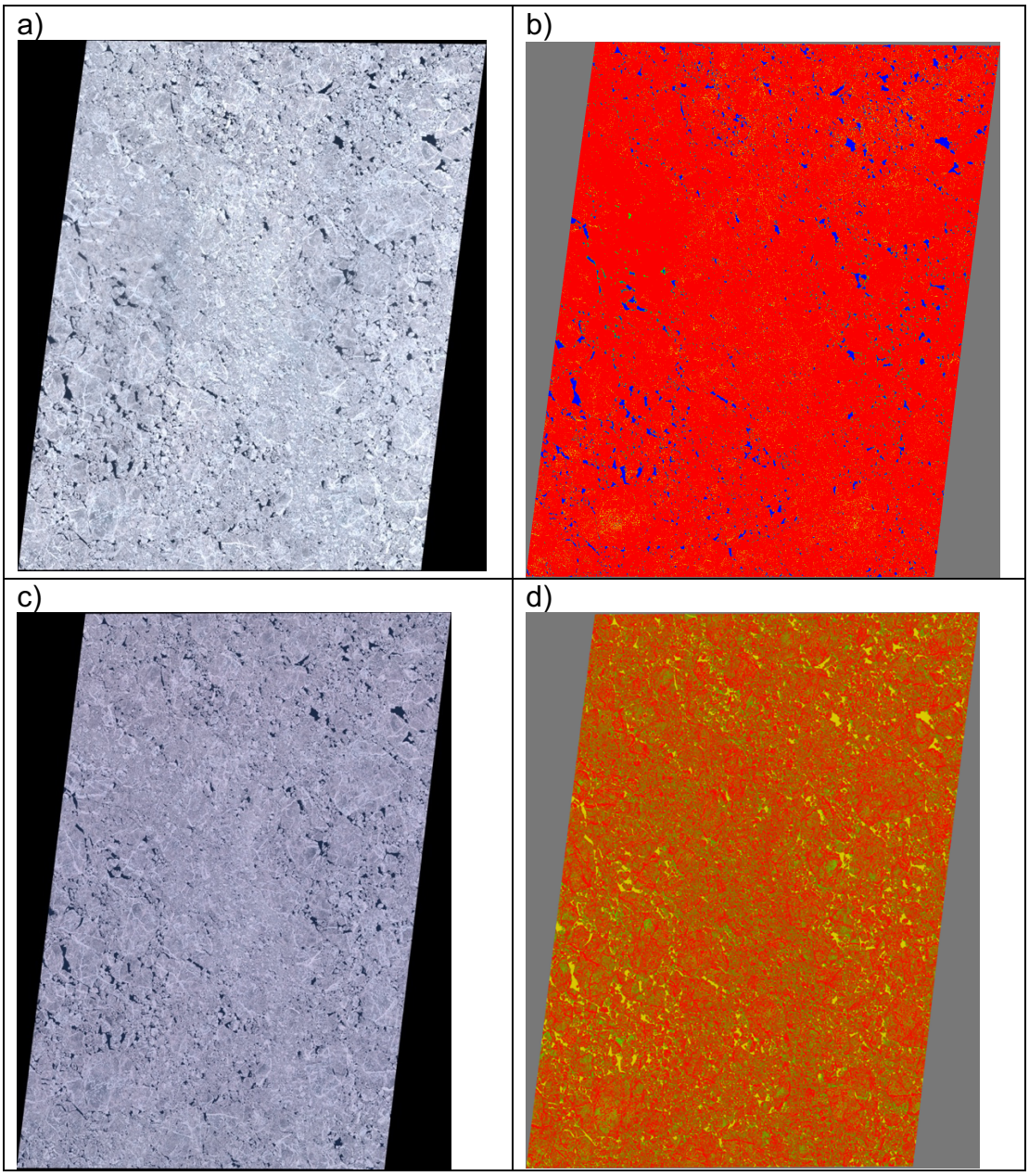

Figure 17. Images captured on 9 August 2020.

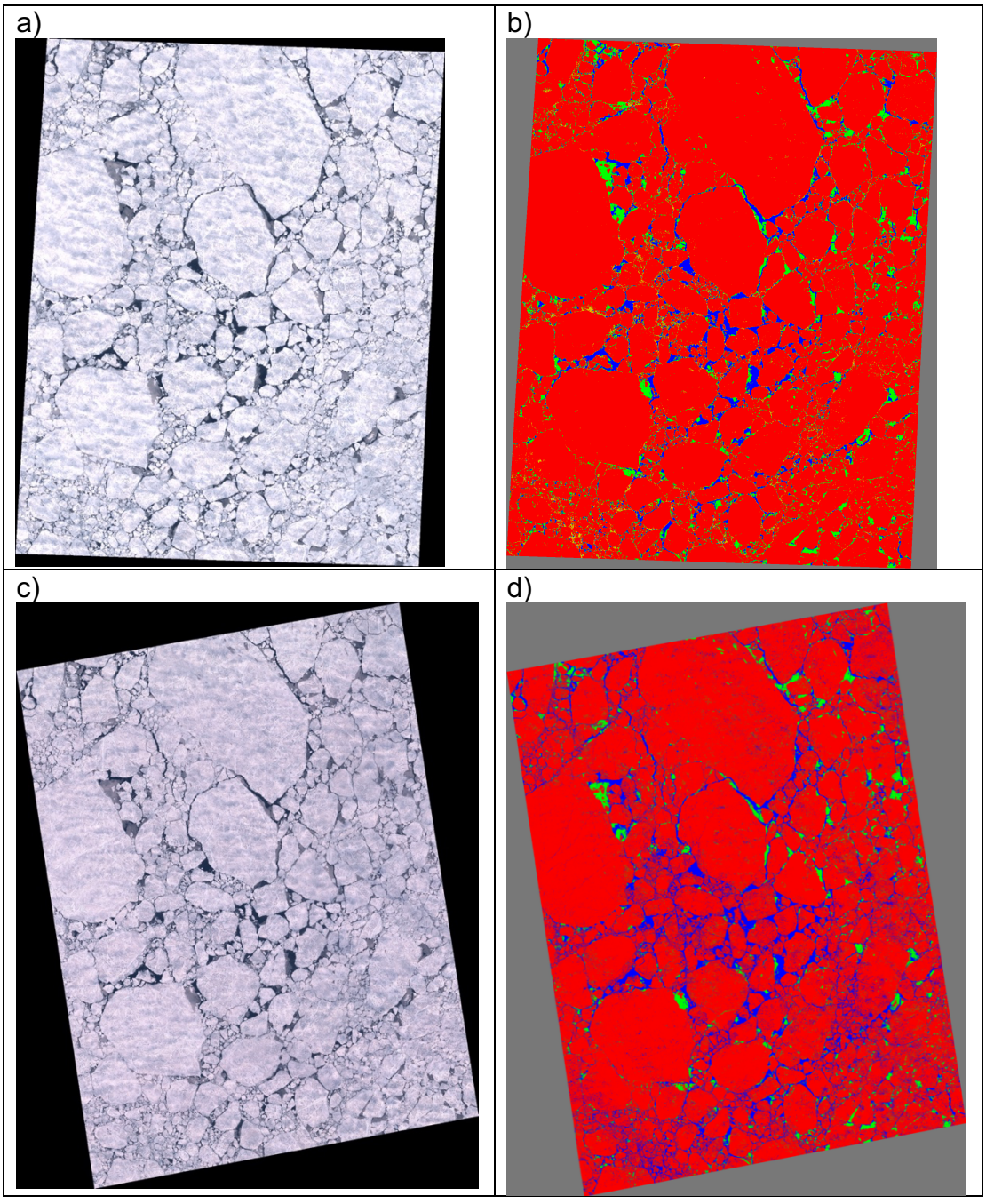

Figure 18. Images captured on 3 September 2020.

Bibliography

Aaboe, S., Down, E. J., & Eastwood, S. (n.d.). *Product User Manual for the Global sea-ice edge and type Product*. 36.

Aagaard, K., & Carmack, E. C. (1989). The role of sea ice and other fresh water in the Arctic circulation. *Journal of Geophysical Research: Oceans*, *94*(C10), 14485–14498. https://doi.org/10.1029/JC094iC10p14485

Aagaard, K., Coachman, L. K., & Carmack, E. (1981). On the halocline of the Arctic Ocean. *Deep Sea Research Part A. Oceanographic Research Papers*, *28*(6), 529–545. https://doi.org/10.1016/0198-0149(81)90115-1

Anderson, M., & Bliss, A. (2019). *Snow Melt Onset Over Arctic Sea Ice from SMMR and SSM/I-SSMIS Brightness Temperatures* [Data set]. NASA National Snow and Ice Data Center DAAC. https://doi.org/10.5067/A9YK15H5EBHK

Andreas, E. L., & Ackley, S. F. (1982). On the Differences in Ablation Seasons of Arctic and Antarctic Sea Ice. *Journal of the Atmospheric Sciences*, *39*(2), 440–447. https://doi.org/10.1175/1520-0469(1982)039<0440:OTDIAS>2.0.CO;2

Armstrong, T. (1972). World Meteorological Organization. WMO sea-ice nomenclature. Terminology, codes and illustrated glossary. Edition 1970. Geneva, Secretariat of the World Meteorological Organization, 1970. [Ix], 147 p. [Including 175 photos] + corrigenda slip. (WMO/OMM/BMO, No. 259, TP. 145.). *Journal of Glaciology*, *11*(61), 148–149. https://doi.org/10.3189/S0022143000022577

Arntsen, A. E., Song, A. J., Perovich, D. K., & Richter-Menge, J. A. (2015). Observations of the summer breakup of an Arctic sea ice cover. *Geophysical Research Letters*, *42*(19), 8057–8063. https://doi.org/10.1002/2015GL065224

Arrigo, K. R. (2017). Sea ice as a habitat for primary producers. In *Sea Ice* (pp. 352–369). John Wiley & Sons, Ltd. https://doi.org/10.1002/9781118778371.ch14

Arrigo, K. R., Perovich, D. K., Pickart, R. S., Brown, Z. W., van Dijken, G. L., Lowry, K. E., Mills, M. M., Palmer, M. A., Balch, W. M., Bahr, F., Bates, N. R., Benitez-Nelson, C., Bowler, B., Brownlee, E., Ehn, J. K., Frey, K. E., Garley, R., Laney, S. R., Lubelczyk, L., … Swift, J. H. (2012). Massive Phytoplankton Blooms Under Arctic Sea Ice. *Science*, *336*(6087), 1408–1408. https://doi.org/10.1126/science.1215065

Blanchard-Wrigglesworth, E., Webster, M. A., Farrell, S. L., & Bitz, C. M. (2018). Reconstruction of Snow on Arctic Sea Ice. *Journal of Geophysical Research: Oceans*, *123*(5), 3588–3602. https://doi.org/10.1002/2017JC013364

Boisvert, L. N., Markus, T., & Vihma, T. (2013). Moisture flux changes and trends for the entire Arctic in 2003–2011 derived from EOS Aqua data. *Journal of Geophysical Research: Oceans*, *118*(10), 5829–5843. https://doi.org/10.1002/jgrc.20414

Boisvert, L. N., & Stroeve, J. C. (2015). The Arctic is becoming warmer and wetter as revealed by the Atmospheric Infrared Sounder. *Geophysical Research Letters*, *42*(11), 4439–4446. https://doi.org/10.1002/2015GL063775

Bojinski, S., Verstraete, M., Peterson, T. C., Richter, C., Simmons, A., & Zemp, M. (2014). The Concept of Essential Climate Variables in Support of Climate Research, Applications, and Policy. *Bulletin of the American Meteorological Society*, *95*(9), 1431–1443. https://doi.org/10.1175/BAMS-D-13-00047.1

Breivik, L.-A., Eastwood, S., & Lavergne, T. (2012). Use of C-Band Scatterometer for Sea Ice Edge Identification. *IEEE Transactions on Geoscience and Remote Sensing*, *50*(7), 2669–2677. https://doi.org/10.1109/TGRS.2012.2188898

Brunt, K. M., Neumann, T. A., & Smith, B. E. (2019). Assessment of ICESat-2 Ice Sheet Surface Heights, Based on Comparisons Over the Interior of the Antarctic Ice Sheet. *Geophysical Research Letters*, *46*(22), 13072–13078. https://doi.org/10.1029/2019GL084886

Buckley, E., Farrell, S. L., Duncan, K., Herzfeld, U. C., & Webster, M. (2019). *Sea Ice Melt Pond Properties as Observed by ICESat-2*. *2019*, C32B-08.

Buckley, E. M., Farrell, S. L., Duncan, K., Connor, L. N., Kuhn, J. M., & Dominguez, R. T. (2020a). Classification of Sea Ice Summer Melt Features in High-Resolution IceBridge Imagery. *Journal of Geophysical Research: Oceans*, *125*(5), e2019JC015738. https://doi.org/10.1029/2019JC015738

Buckley, Ellen; Farrell, Sinead; Duncan, Kyle; Connor, Laurence; Kuhn, John; Dominguez, Roseanne (2020b). Arctic Sea Ice Summer Melt Feature Classification from Operation IceBridge High-Resolution Optical Imagery, July 2016 and July 2017 (NCEI Accession 0209246). NOAA National Centers for Environmental Information. [Dataset]. https://doi.org/10.25921/cp7t-7118

Buckley, E., S.L. Farrell, K. Duncan, L.N. Connor, J.M. Kuhn, R. Dominguez (2019), Analysis of the Airborne Topographic Mapper (ATM) Response over Melt Ponds on Sea Ice, Abstract 82A3250, presented at 2019 International Glaciological Society Sea Ice Symposium, Winnipeg, Manitoba, CAN, August

Buckley, E., Farrell, S. L., Herzfeld, U., Trantow, T., Baney, O. N., Duncan, K., Lawson M., (in prep). Observing the Evolution of Summer Melt on Perennial Sea Ice with ICESat-2 and Sentinel-2.

Bufton, J. L. (1989). Laser altimetry measurements from aircraft and spacecraft. *Proceedings of the IEEE*, *77*(3), 463–477. https://doi.org/10.1109/5.24131

Bushuk, M., Winton, M., Bonan, D. B., Blanchard-Wrigglesworth, E., & Delworth, T. L. (2020). A Mechanism for the Arctic Sea Ice Spring Predictability Barrier. *Geophysical Research Letters*, *47*(13), e2020GL088335. https://doi.org/10.1029/2020GL088335

Carmack, E., Polyakov, I., Padman, L., Fer, I., Hunke, E., Hutchings, J., Jackson, J., Kelley, D., Kwok, R., Layton, C., Melling, H., Perovich, D., Persson, O., Ruddick, B., Timmermans, M.-L., Toole, J., Ross, T., Vavrus, S., & Winsor, P. (2015). Toward Quantifying the Increasing Role of Oceanic Heat in Sea Ice Loss in the New Arctic. *Bulletin of the American Meteorological Society*, *96*(12), 2079–2105. https://doi.org/10.1175/BAMS-D-13-00177.1

Cavalieri, D. J., Crawford, J. P., Drinkwater, M. R., Eppler, D. T., Farmer, L. D., Jentz, R. R., & Wackerman, C. C. (1991). Aircraft active and passive microwave validation of sea ice concentration from the Defense Meteorological Satellite

Program special sensor microwave imager. *Journal of Geophysical Research: Oceans*, *96*(C12), 21989–22008. https://doi.org/10.1029/91JC02335

Chelton, D. B., Ries, J. C., Haines, B. J., Fu, L.-L., & Callahan, P. S. (2001). Satellite altimetry. In *International geophysics* (Vol. 69, pp. 1–ii). Elsevier.

Clark, P. U., Pisias, N. G., Stocker, T. F., & Weaver, A. J. (2002). The role of the thermohaline circulation in abrupt climate change. *Nature*, *415*(6874), 863–869. https://doi.org/10.1038/415863a

Cohen, J., Zhang, X., Francis, J., Jung, T., Kwok, R., Overland, J., Ballinger, T., Blackport, R., Bhatt, U. S., Chen, H., Coumou, D., Feldstein, S., Handorf, D., Hell, M., Henderson, G., Ionita, M., Kretschmer, M., Laliberte, F., Lee, S., … Yoon, J. (2018). Arctic Change and Possble Influence on Mid-latitude Climate and Weather. *US CLIVAR Reports*, *N/A*, 10.5065/D6TH8KGW. https://doi.org/10.5065/D6TH8KGW

Comiso, J. C. (2009). Variability and Trends of the Global Sea Ice Cover. In *Sea Ice* (pp. 205–246). John Wiley & Sons, Ltd. https://doi.org/10.1002/9781444317145.ch6

Comiso, J. C. (2012). Large Decadal Decline of the Arctic Multiyear Ice Cover. *Journal of Climate*, *25*(4), 1176–1193. https://doi.org/10.1175/JCLI-D-11-00113.1

Comiso, J. C., & Kwok, R. (1996). Surface and radiative characteristics of the summer Arctic sea ice cover from multisensor satellite observations. *Journal of Geophysical Research: Oceans*, *101*(C12), 28397–28416. https://doi.org/10.1029/96JC02816

Comiso, J. C., Parkinson, C. L., Gersten, R., & Stock, L. (2008). Accelerated decline in the Arctic sea ice cover. *Geophysical Research Letters*, *35*(1). https://doi.org/10.1029/2007GL031972

Connor, L. N., Farrell, S. L., McAdoo, D. C., Krabill, W. B., & Manizade, S. (2012). Validating ICESat over thick sea ice in the Northern Canada Basin. *IEEE Transactions on Geoscience and Remote Sensing*, *51*(4), 2188–2200.

Cottier, F., Steele, M., & Nilsen, F. (2017). Sea ice and Arctic Ocean oceanography. In *Sea Ice* (pp. 197–215). John Wiley & Sons, Ltd. https://doi.org/10.1002/9781118778371.ch7

Curcio, J. A., & Petty, C. C. (1951). The Near Infrared Absorption Spectrum of Liquid Water. *JOSA*, *41*(5), 302–304. https://doi.org/10.1364/JOSA.41.000302

Curry, J. A., Schramm, J. L., & Ebert, E. E. (1995). Sea Ice-Albedo Climate Feedback Mechanism. *Journal of Climate*, *8*(2), 240–247. https://doi.org/10.1175/1520-0442(1995)008<0240:SIACFM>2.0.CO;2

Curry, J. A., Schramm, J. L., Perovich, D. K., & Pinto, J. O. (2001). Applications of SHEBA/FIRE data to evaluation of snow/ice albedo parameterizations. *Journal of Geophysical Research: Atmospheres*, *106*(D14), 15345–15355. https://doi.org/10.1029/2000JD900311

Curry, J. A., Schramm, J. L., Rossow, W. B., & Randall, D. (1996). Overview of Arctic Cloud and Radiation Characteristics. *Journal of Climate*, *9*(8), 1731–1764. https://doi.org/10.1175/1520-0442(1996)009<1731:OOACAR>2.0.CO;2

Dammann, D. O., Eicken, H., Mahoney, A. R., Meyer, F. J., & Betcher, S. (2018). Assessing Sea Ice Trafficability in a Changing Arctic. *Arctic*, *71*(1), 59–75.

Defries, R. (2008). Terrestrial Vegetation in the Coupled Human-Earth System: Contributions of Remote Sensing. *Annual Review of Environment and Resources*, *33*. https://doi.org/10.1146/annurev.environ.33.020107.113339

Dominguez, Roseanne. (2010). *IceBridge DMS L1B Geolocated and Orthorectified Images, Version 1* [Data set]. NASA National Snow and Ice Data Center DAAC. https://doi.org/10.5067/OZ6VNOPMPRJ0

Drusch, M., Del Bello, U., Carlier, S., Colin, O., Fernandez, V., Gascon, F., Hoersch, B., Isola, C., Laberinti, P., Martimort, P., Meygret, A., Spoto, F., Sy, O., Marchese, F., & Bargellini, P. (2012). Sentinel-2: ESA's Optical High-Resolution Mission for GMES Operational Services. *Remote Sensing of Environment*, *120*, 25–36. https://doi.org/10.1016/j.rse.2011.11.026

Duncan, K., Farrell, S. L., Connor, L. N., Richter-Menge, J., Hutchings, J. K., & Dominguez, R. (2018). High-resolution airborne observations of sea-ice pressure ridge sail height. *Annals of Glaciology*, *59*(76pt2), 137–147. https://doi.org/10.1017/aog.2018.2

Eastman, R., & Warren, S. G. (2010). Interannual Variations of Arctic Cloud Types in Relation to Sea Ice. *Journal of Climate*, *23*(15), 4216–4232. https://doi.org/10.1175/2010JCLI3492.1

Ebert, E. E., & Curry, J. A. (1993). An intermediate one-dimensional thermodynamic sea ice model for investigating ice-atmosphere interactions. *Journal of Geophysical Research: Oceans*, *98*(C6), 10085–10109. https://doi.org/10.1029/93JC00656

Eicken, H., Grenfell, T. C., Perovich, D. K., Richter-Menge, J. A., & Frey, K. (2004). Hydraulic controls of summer Arctic pack ice albedo. *Journal of Geophysical Research: Oceans*, *109*(C8). https://doi.org/10.1029/2003JC001989

Eicken, H., Krouse, H. R., Kadko, D., & Perovich, D. K. (2002). Tracer studies of pathways and rates of meltwater transport through Arctic summer sea ice. *Journal of Geophysical Research: Oceans*, *107*(C10), SHE 22-1-SHE 22-20. https://doi.org/10.1029/2000JC000583

European Space Agency. (2015). Sentinel-2 user handbook. *Standard Document, Issue 1 Rev 2*.

Farrell, S. L., Brunt, K. M., Ruth, J. M., Kuhn, J. M., Connor, L. N., & Walsh, K. M. (2015). Sea-ice freeboard retrieval using digital photon-counting laser altimetry. *Annals of Glaciology*, *56*(69), 167–174. https://doi.org/10.3189/2015AoG69A686

Farrell, S. L., Duncan, K., Buckley, E. M., Richter-Menge, J., & Li, R. (2020). Mapping Sea Ice Surface Topography in High Fidelity With ICESat-2. *Geophysical Research Letters*, *47*(21), e2020GL090708. https://doi.org/10.1029/2020GL090708

Farrell, S. L., Kurtz, N., Connor, L. N., Elder, B. C., Leuschen, C., Markus, T., McAdoo, D. C., Panzer, B., Richter-Menge, J., & Sonntag, J. G. (2012). A First Assessment of IceBridge Snow and Ice Thickness Data Over Arctic Sea Ice. *IEEE Transactions on Geoscience and Remote Sensing*, *50*(6), 2098–2111. https://doi.org/10.1109/TGRS.2011.2170843

Farrell, S. L., Markus, T., Kwok, R., & Connor, L. (2011). Laser altimetry sampling strategies over sea ice. *Annals of Glaciology*, *52*(57), 69–76. https://doi.org/10.3189/172756411795931660

Fetterer, F.; Knowles K.; Meier W.; Savoie M.; Windnagel A. (2017). *Sea Ice Index, Version 3* [Data set]. NSIDC. https://doi.org/10.7265/N5K072F8

Fetterer, F., & Untersteiner, N. (1998). Observations of melt ponds on Arctic sea ice. *Journal of Geophysical Research: Oceans*, *103*(C11), 24821–24835. https://doi.org/10.1029/98JC02034

Flocco, D., Feltham, D. L., Bailey, E., & Schroeder, D. (2015). The refreezing of melt ponds on Arctic sea ice. *Journal of Geophysical Research: Oceans*, *120*(2), 647–659. https://doi.org/10.1002/2014JC010140

Flocco, D., Feltham, D. L., & Turner, A. K. (2010). Incorporation of a physically based melt pond scheme into the sea ice component of a climate model. *Journal of Geophysical Research: Oceans*, *115*(C8). https://doi.org/10.1029/2009JC005568

Flocco, D., Schroeder, D., Feltham, D. L., & Hunke, E. C. (2012). Impact of melt ponds on Arctic sea ice simulations from 1990 to 2007. *Journal of Geophysical Research: Oceans*, *117*(C9). https://doi.org/10.1029/2012JC008195

Freeman, H. (1961). On the encoding of arbitrary geometric configurations. *IRE Transactions on Electronic Computers*, (2), 260-268.

Fricker, H. A., Arndt, P., Brunt, K. M., Datta, R. T., Fair, Z., Jasinski, M. F., Kingslake, J., Magruder, L. A., Moussavi, M., & Pope, A. (2021). ICESat-2

Meltwater Depth Estimates: Application to Surface Melt on Amery Ice Shelf, East Antarctica. *Geophysical Research Letters*, *48*(8), e2020GL090550.

Giles, K. A., Laxon, S. W., Wingham, D. J., Wallis, D. W., Krabill, W. B., Leuschen, C. J., McAdoo, D., Manizade, S. S., & Raney, R. K. (2007). Combined airborne laser and radar altimeter measurements over the Fram Strait in May 2002. *Remote Sensing of Environment*, *111*(2), 182–194. https://doi.org/10.1016/j.rse.2007.02.037

Grenfell, T. C., & Perovich, D. K. (2004). Seasonal and spatial evolution of albedo in a snow-ice-land-ocean environment. *Journal of Geophysical Research: Oceans*, *109*(C1). https://doi.org/10.1029/2003JC001866

Haas, C. (2009). Dynamics Versus Thermodynamics: The Sea Ice Thickness Distribution. In *Sea Ice* (pp. 113–151). John Wiley & Sons, Ltd. https://doi.org/10.1002/9781444317145.ch4

Haas, C. (2017). Sea ice thickness distribution. In *Sea Ice* (pp. 42–64). John Wiley & Sons, Ltd. https://doi.org/10.1002/9781118778371.ch2

Herzfeld, U. C., Trantow, T., Lawson, M., Hans, J., & Medley, G. (2021). Surface heights and crevasse morphologies of surging and fast-moving glaciers from ICESat-2 laser altimeter data—Application of the density-dimension algorithm (DDA-ice) and evaluation using airborne altimeter and Planet SkySat data. *Science of Remote Sensing*, *3*, 100013. https://doi.org/10.1016/j.srs.2020.100013

Herzfeld, U., Trantow, T., Buckley, E., Farrell, S., and Lawson, M. (in prep). Automated detection and depth measurement of melt ponds on sea ice from ICESat-2 ATLAS data — the DDA-bifurcate-seaice.

Herzfeld, U. C., Trantow, T. M., Harding, D., & Dabney, P. W. (2017). Surface-Height Determination of Crevassed Glaciers—Mathematical Principles of an Autoadaptive Density-Dimension Algorithm and Validation Using ICESat-2 Simulator (SIMPL) Data. *IEEE Transactions on Geoscience and Remote Sensing*, *55*(4), 1874–1896. https://doi.org/10.1109/TGRS.2016.2617323

Holland, M. M., Bailey, D. A., Briegleb, B. P., Light, B., & Hunke, E. (2012). Improved Sea Ice Shortwave Radiation Physics in CCSM4: The Impact of Melt Ponds and Aerosols on Arctic Sea Ice. *Journal of Climate*, *25*(5), 1413–1430. https://doi.org/10.1175/JCLI-D-11-00078.1

Horvat, C., Flocco, D., Rees Jones, D. W., Roach, L., & Golden, K. M. (2020). The Effect of Melt Pond Geometry on the Distribution of Solar Energy Under First-Year Sea Ice. *Geophysical Research Letters*, *47*(4), e2019GL085956. https://doi.org/10.1029/2019GL085956

Horvat, C., Jones, D. R., Iams, S., Schroeder, D., Flocco, D., & Feltham, D. (2017). The frequency and extent of sub-ice phytoplankton blooms in the Arctic Ocean. *Science Advances*, *3*(3), e1601191. https://doi.org/10.1126/sciadv.1601191

Huete, A., Didan, K., Miura, T., Rodriguez, E. P., Gao, X., & Ferreira, L. G. (2002). Overview of the radiometric and biophysical performance of the MODIS vegetation indices. *Remote Sensing of Environment*, *83*(1), 195–213. https://doi.org/10.1016/S0034-4257(02)00096-2

Hunke, E. C., Hebert, D. A., & Lecomte, O. (2013). Level-ice melt ponds in the Los Alamos sea ice model, CICE. *Ocean Modelling*, *71*, 26–42. https://doi.org/10.1016/j.ocemod.2012.11.008

Hunke, E. C., Lipscomb, W. H., & Turner, A. K. (2010). Sea-ice models for climate study: Retrospective and new directions. *Journal of Glaciology*, *56*(200), 1162–1172. https://doi.org/10.3189/002214311796406095

Huntington, H. P., Gearheard, S., Holm, L. K., Noongwook, G., Opie, M., & Sanguya, J. (2017). Sea ice is our beautiful garden: Indigenous perspectives on sea ice in the Arctic. In *Sea Ice* (pp. 583–599). John Wiley & Sons, Ltd. https://doi.org/10.1002/9781118778371.ch25

Imaoka, K., Maeda, T., Kachi, M., Kasahara, M., Ito, N., & Nakagawa, K. (2012). Status of AMSR2 instrument on GCOM-W1. *Earth Observing Missions and Sensors: Development, Implementation, and Characterization II*, *8528*, 201–206. https://doi.org/10.1117/12.977774

Istomina, L., Heygster, G., Huntemann, M., Schwarz, P., Birnbaum, G., Scharien, R., Polashenski, C., Perovich, D., Zege, E., Malinka, A., Prikhach, A., & Katsev, I. (2015). Melt pond fraction and spectral sea ice albedo retrieval from MERIS data – Part 1: Validation against in situ, aerial, and ship cruise data. *The Cryosphere*, *9*(4), 1551–1566. https://doi.org/10.5194/tc-9-1551-2015

Ivanova, N., Pedersen, L. T., Tonboe, R. T., Kern, S., Heygster, G., Lavergne, T., Sørensen, A., Saldo, R., Dybkjær, G., Brucker, L., & Shokr, M. (2015). Inter-comparison and evaluation of sea ice algorithms: Towards further identification of challenges and optimal approach using passive microwave observations. *The Cryosphere*, *9*(5), 1797–1817. https://doi.org/10.5194/tc-9-1797-2015

Kacimi, S., & Kwok, R. (2022). Arctic Snow Depth, Ice Thickness, and Volume From ICESat-2 and CryoSat-2: 2018–2021. *Geophysical Research Letters*, *49*(5), e2021GL097448. https://doi.org/10.1029/2021GL097448

Kalnay, E., Kanamitsu, M., Kistler, R., Collins, W., Deaven, D., Gandin, L., Iredell, M., Saha, S., White, G., Woollen, J., Zhu, Y., Chelliah, M., Ebisuzaki, W., Higgins, W., Janowiak, J., Mo, K. C., Ropelewski, C., Wang, J., Leetmaa, A., … Joseph, D. (1996). The NCEP/NCAR 40-Year Reanalysis Project. *Bulletin of the American Meteorological Society*, *77*(3), 437–472. https://doi.org/10.1175/1520-0477(1996)077<0437:TNYRP>2.0.CO;2

Kern, S., Lavergne, T., Notz, D., Pedersen, L. T., & Tonboe, R. (2020). Satellite passive microwave sea-ice concentration data set inter-comparison for Arctic summer conditions. *The Cryosphere*, *14*(7), 2469–2493. https://doi.org/10.5194/tc-14-2469-2020

King, J., Derksen, C., Toose, P., Langlois, A., Larsen, C., Lemmetyinen, J., Marsh, P., Montpetit, B., Roy, A., Rutter, N., & Sturm, M. (2018). The influence of snow microstructure on dual-frequency radar measurements in a tundra environment. *Remote Sensing of Environment*, *215*, 242–254. https://doi.org/10.1016/j.rse.2018.05.028

Koenig, L., Martin, S., Studinger, M., & Sonntag, J. (2010). Polar Airborne Observations Fill Gap in Satellite Data. *Eos, Transactions American Geophysical Union*, *91*(38), 333–334. https://doi.org/10.1029/2010EO380002

Krabill, W. B., Abdalati, W., Frederick, E. B., Manizade, S. S., Martin, C. F., Sonntag, J. G., Swift, R. N., Thomas, R. H., & Yungel, J. G. (2002). Aircraft

laser altimetry measurement of elevation changes of the greenland ice sheet: Technique and accuracy assessment. *Journal of Geodynamics*, *34*(3), 357–376. https://doi.org/10.1016/S0264-3707(02)00040-6

Kurtz, N. T., Farrell, S. L., Studinger, M., Galin, N., Harbeck, J. P., Lindsay, R., Onana, V. D., Panzer, B., & Sonntag, J. G. (2013). Sea ice thickness, freeboard, and snow depth products from Operation IceBridge airborne data. *The Cryosphere*, *7*(4), 1035–1056.

Kwok, R. (2015). Sea ice convergence along the Arctic coasts of Greenland and the Canadian Arctic Archipelago: Variability and extremes (1992–2014). *Geophysical Research Letters*, *42*(18), 7598–7605. https://doi.org/10.1002/2015GL065462

Kwok, R. (2018). Arctic sea ice thickness, volume, and multiyear ice coverage: Losses and coupled variability (1958–2018). *Environmental Research Letters*, *13*(10), 105005. https://doi.org/10.1088/1748-9326/aae3ec

Kwok, R., A. A. Petty, G. Cunningham, T. Markus, D. Hancock, A. Ivanoff, J. Wimert, M. Bagnardi, N. Kurtz, & Team, T. Ices.-2 S. (2021). *ATLAS/ICESat-2 L3A Sea Ice Height, version 5* [Data set]. NASA National Snow and Ice Data Center DAAC. https://doi.org/10.5067/ATLAS/ATL07.005

Kwok, R., & Cunningham, G. F. (2015). Variability of Arctic sea ice thickness and volume from CryoSat-2. *Philosophical Transactions of the Royal Society A: Mathematical, Physical and Engineering Sciences*, *373*(2045), 20140157. https://doi.org/10.1098/rsta.2014.0157

Kwok, R., Kacimi, S., Markus, T., Kurtz, N. T., Studinger, M., Sonntag, J. G., Manizade, S. S., Boisvert, L. N., & Harbeck, J. P. (2019). ICESat-2 Surface Height and Sea Ice Freeboard Assessed With ATM Lidar Acquisitions From Operation IceBridge. *Geophysical Research Letters*, *46*(20), 11228–11236. https://doi.org/10.1029/2019GL084976

Kwok, R., Kacimi, S., Webster, M. A., Kurtz, N. T., & Petty, A. A. (2020a). Arctic snow depth and sea ice thickness from ICESat-2 and CryoSat-2 freeboards: A first examination. *Journal of Geophysical Research: Oceans*, *125*(3), e2019JC016008.

Kwok, R., Kacimi, S., Webster, M. a., Kurtz, N. t., & Petty, A. a. (2020b). Arctic Snow Depth and Sea Ice Thickness From ICESat-2 and CryoSat-2 Freeboards: A First Examination. *Journal of Geophysical Research: Oceans*, *125*(3), e2019JC016008. https://doi.org/10.1029/2019JC016008

Kwok, R., Markus, T., Kurtz, N. T., Petty, A. A., Neumann, T. A., Farrell, S. L., Cunningham, G. F., Hancock, D. W., Ivanoff, A., & Wimert, J. T. (2019). Surface Height and Sea Ice Freeboard of the Arctic Ocean From ICESat-2: Characteristics and Early Results. *Journal of Geophysical Research: Oceans*, *124*(10), 6942–6959. https://doi.org/10.1029/2019JC015486

Kwok, R., Petty, A., Bagnardi, M., Wimert, J. T., Cunningham, G. F., Hancock, D. W., Ivanoff, A., & Kurtz, N. (n.d.). *Algorithm Theoretical Basis Document (ATBD) For Sea Ice Products*. 129.

Kwok, R., & Rothrock, D. A. (2009). Decline in Arctic sea ice thickness from submarine and ICESat records: 1958–2008. *Geophysical Research Letters*, *36*(15). https://doi.org/10.1029/2009GL039035

Kwok, R., & Sulsky, D. (2010). Arctic Ocean Sea Ice Thickness and Kinematics: SATELLITE RETRIEVALS AND MODELING. *Oceanography*, *23*(4), 134–143.

Kwok, R., Zwally, H. J., & Yi, D. (2004). ICESat observations of Arctic sea ice: A first look. *Geophysical Research Letters*, *31*(16). https://doi.org/10.1029/2004GL020309

Laidre, K. L., & Regehr, E. V. (2017). Arctic marine mammals and sea ice. In *Sea Ice* (pp. 516–533). John Wiley & Sons, Ltd. https://doi.org/10.1002/9781118778371.ch21

Laidre, K. L., Stern, H., Kovacs, K. M., Lowry, L., Moore, S. E., Regehr, E. V., Ferguson, S. H., Wiig, Ø., Boveng, P., Angliss, R. P., Born, E. W., Litovka, D., Quakenbush, L., Lydersen, C., Vongraven, D., & Ugarte, F. (2015). Arctic marine mammal population status, sea ice habitat loss, and conservation recommendations for the 21st century. *Conservation Biology*, *29*(3), 724–737. https://doi.org/10.1111/cobi.12474

Launiainen, J., & Vihma, T. (1994). On the surface heat fluxes in the Weddell Sea. *Washington DC American Geophysical Union Geophysical Monograph Series*, *85*, 399–419. https://doi.org/10.1029/GM085p0399

Lavergne, T., Eastwood, S., Teffah, Z., Schyberg, H., & Breivik, L.-A. (2010). Sea ice motion from low-resolution satellite sensors: An alternative method and its

validation in the Arctic. *Journal of Geophysical Research: Oceans*, *115*(C10). https://doi.org/10.1029/2009JC005958

Laxon, S., Peacock, N., & Smith, D. (2003). High interannual variability of sea ice thickness in the Arctic region. *Nature*, *425*(6961), 947–950. https://doi.org/10.1038/nature02050

Laxon, S. W., Giles, K. A., Ridout, A. L., Wingham, D. J., Willatt, R., Cullen, R., Kwok, R., Schweiger, A., Zhang, J., Haas, C., Hendricks, S., Krishfield, R., Kurtz, N., Farrell, S., & Davidson, M. (2013). CryoSat-2 estimates of Arctic sea ice thickness and volume. *Geophysical Research Letters*, *40*(4), 732–737. https://doi.org/10.1002/grl.50193

Light, B., Grenfell, T. C., & Perovich, D. K. (2008). Transmission and absorption of solar radiation by Arctic sea ice during the melt season. *Journal of Geophysical Research: Oceans*, *113*(C3). https://doi.org/10.1029/2006JC003977

Light, B., Perovich, D. K., Webster, M. A., Polashenski, C., & Dadic, R. (2015). Optical properties of melting first-year Arctic sea ice. *Journal of Geophysical Research: Oceans*, *120*(11), 7657–7675. https://doi.org/10.1002/2015JC011163

Light, B., Smith, M. M., Perovich, D. K., Webster, M. A., Holland M., Linhardt, F., Raphael I. A., Clemens-Sewall D., Macfarlane, A R., Anhaus P., Bailey D. (submitted). Arctic sea ice albedo: spectral composition, spatial heterogeneity, and temporal evolution observed during the MOSAiC drift.

Lu, D., & Weng, Q. (2007). A survey of image classification methods and techniques for improving classification performance. *International Journal of Remote Sensing*, *28*(5), 823–870. https://doi.org/10.1080/01431160600746456

Lu, P., Leppäranta, M., Cheng, B., Li, Z., Istomina, L., & Heygster, G. (2018). The color of melt ponds on Arctic sea ice. *The Cryosphere*, *12*(4), 1331–1345. https://doi.org/10.5194/tc-12-1331-2018

Lüthje, M., Feltham, D. L., Taylor, P. D., & Worster, M. G. (2006). Modeling the summertime evolution of sea-ice melt ponds. *Journal of Geophysical Research: Oceans*, *111*(C2). https://doi.org/10.1029/2004JC002818

MacGregor, J. A., Boisvert, L. N., Medley, B., Petty, A. A., Harbeck, J. P., Bell, R. E., Blair, J. B., Blanchard-Wrigglesworth, E., Buckley, E. M., Christoffersen, M. S., Cochran, J. R., Csathó, B. M., De Marco, E. L., Dominguez, R. a. T., Fahnestock, M. A., Farrell, S. L., Gogineni, S. P., Greenbaum, J. S., Hansen, C. M., … Yungel, J. K. (2021). The Scientific Legacy of NASA's Operation IceBridge. *Reviews of Geophysics*, *59*(2). https://doi.org/10.1029/2020RG000712

Magruder, L. A., Brunt, K. M., & Alonzo, M. (2020). Early ICESat-2 on-orbit Geolocation Validation Using Ground-Based Corner Cube Retro-Reflectors. *Remote Sensing*, *12*(21), 3653. https://doi.org/10.3390/rs12213653

Mäkynen, M., Kern, S., Rösel, A., & Pedersen, L. T. (2014). On the Estimation of Melt Pond Fraction on the Arctic Sea Ice With ENVISAT WSM Images. *IEEE Transactions on Geoscience and Remote Sensing*, *52*(11), 7366–7379. https://doi.org/10.1109/TGRS.2014.2311476

Markus, T., & Cavalieri, D. J. (2009). *The AMSR-E NT2 Sea Ice Concentration Algorithm: Its Basis and Implementation*. The Remote Sensing Society of Japan. https://doi.org/10.11440/rssj.29.216

Markus, T., Cavalieri, D. J., & Ivanoff, A. (2002). The potential of using Landsat 7 ETM+ for the classification of sea-ice surface conditions during summer. *Annals of Glaciology*, *34*, 415–419. https://doi.org/10.3189/172756402781817536

Markus, T., Cavalieri, D. J., Tschudi, M. A., & Ivanoff, A. (2003). Comparison of aerial video and Landsat 7 data over ponded sea ice. *Remote Sensing of Environment*, *86*(4), 458–469. https://doi.org/10.1016/S0034-4257(03)00124-X

Markus, T., Neumann, T., Martino, A., Abdalati, W., Brunt, K., Csatho, B., Farrell, S., Fricker, H., Gardner, A., Harding, D., Jasinski, M., Kwok, R., Magruder, L., Lubin, D., Luthcke, S., Morison, J., Nelson, R., Neuenschwander, A., Palm, S., … Zwally, J. (2017). The Ice, Cloud, and land Elevation Satellite-2 (ICESat-2): Science requirements, concept, and implementation. *Remote Sensing of Environment*, *190*, 260–273. https://doi.org/10.1016/j.rse.2016.12.029

Markus, T., Stroeve, J. C., & Miller, J. (2009). Recent changes in Arctic sea ice melt onset, freezeup, and melt season length. *Journal of Geophysical Research: Oceans*, *114*(C12). https://doi.org/10.1029/2009JC005436

Maslanik, J. A., Fowler, C., Stroeve, J., Drobot, S., Zwally, J., Yi, D., & Emery, W. (2007). A younger, thinner Arctic ice cover: Increased potential for rapid, extensive sea-ice loss. *Geophysical Research Letters*, *34*(24). https://doi.org/10.1029/2007GL032043

Maxar. (2020a). *WorldView-2*. https://resources.maxar.com/data-sheets/worldview-2

Maxar. (2020b). *WorldView-3*. https://resources.maxar.com/data-sheets/worldview-3

McFeeters, S. K. (1996). The use of the Normalized Difference Water Index (NDWI) in the delineation of open water features. *International Journal of Remote Sensing*, *17*(7), 1425–1432. https://doi.org/10.1080/01431169608948714

McFeeters, S. K. (2013). Using the Normalized Difference Water Index (NDWI) within a Geographic Information System to Detect Swimming Pools for Mosquito Abatement: A Practical Approach. *Remote Sensing*, *5*(7), 3544–3561. https://doi.org/10.3390/rs5073544

McGill, M., Markus, T., Scott, V. S., & Neumann, T. (2013). The Multiple Altimeter Beam Experimental Lidar (MABEL): An Airborne Simulator for the ICESat-2 Mission. *Journal of Atmospheric and Oceanic Technology*, *30*(2), 345–352. https://doi.org/10.1175/JTECH-D-12-00076.1

Meier, W., Markus, T., & Comiso, J. C. (2017). *AMSR-E/AMSR2 Unified L3 Daily 12.5 km Polar Gridded Brightness Temperatures, Sea Ice Concentration, & Snow Depth, Version 1* [Data set]. NASA National Snow and Ice Data Center DAAC. https://doi.org/10.5067/RA1MIJOYPK3P

Meier, W. N., & Ivanoff, A. (2017). Intercalibration of AMSR2 NASA Team 2 Algorithm Sea Ice Concentrations With AMSR-E Slow Rotation Data. *IEEE Journal of Selected Topics in Applied Earth Observations and Remote Sensing*, *10*(9), 3923–3933. https://doi.org/10.1109/JSTARS.2017.2719624

Meier, W. N., Markus, T., Comiso, J., Ivanoff, A., & Miller, J. (2017). *SEA ICE ALGORITHM THEORETICAL BASIS DOCUMENT*. 24.

Meier, W. N., Stewart, J. S., Liu, Y., Key, J., & Miller, J. A. (2017). Operational Implementation of Sea Ice Concentration Estimates From the AMSR2 Sensor.

IEEE Journal of Selected Topics in Applied Earth Observations and Remote Sensing, *10*(9), 3904–3911. https://doi.org/10.1109/JSTARS.2017.2693120

Meier, W. N., Stewart, J. S., Windnagel, A., & Fetterer, F. M. (2022). Comparison of Hemispheric and Regional Sea Ice Extent and Area Trends from NOAA and NASA Passive Microwave-Derived Climate Records. *Remote Sensing*, *14*(3), 619. https://doi.org/10.3390/rs14030619

Meier, W., Perovich, D., Farrell, S., Haas, C., Hendricks, S., Petty, A., Webster, M., Divine, D., Gerland, S., Kaleschke, L., Ricker, R., Steer, A., Tian-Kunze, X., Tschudi, M., & Wood, K. (2021). *Sea ice* (Arctic Report Card 2021).

Menne, M. J., Durre, I., Korzeniewski, B., McNeill, S., Thomas, K., Yin, X., Anthony, S., Ray, R., Vose, R. S., Gleason, B. E., & Houston, T. G. (2012). *Global Historical Climatology Network—Daily (GHCN-Daily), Version 3* [Data set]. NOAA National Centers for Environmental Information. https://doi.org/10.7289/V5D21VHZ

Miao, X., Xie, H., Ackley, S. F., Perovich, D. K., & Ke, C. (2015). Object-based detection of Arctic sea ice and melt ponds using high spatial resolution aerial photographs. *Cold Regions Science and Technology*, *119*, 211–222. https://doi.org/10.1016/j.coldregions.2015.06.014

Mobley, C. D. (1995). The optical properties of water. In *Handbook of Optics Vol. I* (p. 43.3-43.56). McGraw-Hill.

Morassutti, M. P., & Ledrew, E. F. (1996). Albedo and Depth of Melt Ponds on Sea-Ice. *International Journal of Climatology*, *16*(7), 817–838.

https://doi.org/10.1002/(SICI)1097-0088(199607)16:7<817::AID-JOC44>3.0.CO;2-5

Mortin, J., Svensson, G., Graversen, R. G., Kapsch, M.-L., Stroeve, J. C., & Boisvert, L. N. (2016). Melt onset over Arctic sea ice controlled by atmospheric moisture transport. *Geophysical Research Letters*, *43*(12), 6636–6642. https://doi.org/10.1002/2016GL069330

Myneni, R. B., Hall, F. G., Sellers, P. J., & Marshak, A. L. (1995). The interpretation of spectral vegetation indexes. *IEEE Transactions on Geoscience and remote Sensing*, *33*(2), 481-486.

Neuenschwander, A., Guenther, E., White, J. C., Duncanson, L., & Montesano, P. (2020). Validation of ICESat-2 terrain and canopy heights in boreal forests. *Remote Sensing of Environment*, *251*, 112110. https://doi.org/10.1016/j.rse.2020.112110

Neumann, T. A., A. Brenner, D. Hancock, J. Robbins, J. Saba, K. Harbeck, A. Gibbons, J. Lee, S. B. Luthcke, & T. Rebold. (2021). *ATLAS/ICESat-2 L2A Global Geolocated Photon Data, version 5* [Data set]. NASA National Snow and Ice Data Center DAAC. https://doi.org/10.5067/ATLAS/ATL03.005

Neumann, T. A., Martino, A. J., Markus, T., Bae, S., Bock, M. R., Brenner, A. C., Brunt, K. M., Cavanaugh, J., Fernandes, S. T., Hancock, D. W., Harbeck, K., Lee, J., Kurtz, N. T., Luers, P. J., Luthcke, S. B., Magruder, L., Pennington, T. A., Ramos-Izquierdo, L., Rebold, T., … Thomas, T. C. (2019). The Ice, Cloud, and Land Elevation Satellite – 2 mission: A global geolocated photon product

derived from the Advanced Topographic Laser Altimeter System. *Remote Sensing of Environment*, *233*, 111325. https://doi.org/10.1016/j.rse.2019.111325

Newman, T., Farrell, S. L., Richter-Menge, J., Connor, L. N., Kurtz, N. T., Elder, B. C., & McAdoo, D. (2014). Assessment of radar-derived snow depth over Arctic sea ice. *Journal of Geophysical Research: Oceans*, *119*(12), 8578–8602. https://doi.org/10.1002/2014JC010284

Notz, D., & Community, S. (2020). Arctic Sea Ice in CMIP6. *Geophysical Research Letters*, *47*(10), e2019GL086749. https://doi.org/10.1029/2019GL086749

Onana, V.-D.-P., Kurtz, N. T., Farrell, S. L., Koenig, L. S., Studinger, M., & Harbeck, J. P. (2013). A Sea-Ice Lead Detection Algorithm for Use With High-Resolution Airborne Visible Imagery. *IEEE Transactions on Geoscience and Remote Sensing*, *51*(1), 38–56. https://doi.org/10.1109/TGRS.2012.2202666

Palm, S. P., Yang, Y., Herzfeld, U., Hancock, D., Hayes, A., Selmer, P., Hart, W., & Hlavka, D. (2021). ICESat-2 Atmospheric Channel Description, Data Processing and First Results. *Earth and Space Science*, *8*(8), e2020EA001470. https://doi.org/10.1029/2020EA001470

Parkinson, C. L. (2014). Global Sea Ice Coverage from Satellite Data: Annual Cycle and 35-Yr Trends. *Journal of Climate*, *27*(24), 9377–9382. https://doi.org/10.1175/JCLI-D-14-00605.1

Parkinson, C. L. (2019). A 40-y record reveals gradual Antarctic sea ice increases followed by decreases at rates far exceeding the rates seen in the Arctic. *Proceedings of the National Academy of Sciences*, *116*(29), 14414–14423. https://doi.org/10.1073/pnas.1906556116

Parkinson, C. L., & Comiso, J. C. (2013). On the 2012 record low Arctic sea ice cover: Combined impact of preconditioning and an August storm. *Geophysical Research Letters*, *40*(7), 1356–1361. https://doi.org/10.1002/grl.50349

Parrish, C. E., Magruder, L. A., Neuenschwander, A. L., Forfinski-Sarkozi, N., Alonzo, M., & Jasinski, M. (2019). Validation of ICESat-2 ATLAS Bathymetry and Analysis of ATLAS's Bathymetric Mapping Performance. *Remote Sensing*, *11*(14), 1634. https://doi.org/10.3390/rs11141634

Perovich, D. K. (2017). Sea ice and sunlight. In *Sea Ice* (pp. 110–137). John Wiley & Sons, Ltd. https://doi.org/10.1002/9781118778371.ch4

Perovich, D. K., Grenfell, T. C., Light, B., & Hobbs, P. V. (2002). Seasonal evolution of the albedo of multiyear Arctic sea ice. *Journal of Geophysical Research: Oceans*, *107*(C10), SHE 20-1-SHE 20-13. https://doi.org/10.1029/2000JC000438

Perovich, D. K., Grenfell, T. C., Richter-Menge, J. A., Light, B., Tucker III, W. B., & Eicken, H. (2003). Thin and thinner: Sea ice mass balance measurements during SHEBA. *Journal of Geophysical Research: Oceans*, *108*(C3). https://doi.org/10.1029/2001JC001079

Perovich, D. K., Light, B., Eicken, H., Jones, K. F., Runciman, K., & Nghiem, S. V. (2007). Increasing solar heating of the Arctic Ocean and adjacent seas, 1979–2005: Attribution and role in the ice-albedo feedback. *Geophysical Research Letters*, *34*(19). https://doi.org/10.1029/2007GL031480

Perovich, D. K., & Maykut, G. A. (1990). Solar heating of a stratified ocean in the presence of a static ice cover. *Journal of Geophysical Research: Oceans*, *95*(C10), 18233–18245. https://doi.org/10.1029/JC095iC10p18233

Perovich, D. K., & Polashenski, C. (2012). Albedo evolution of seasonal Arctic sea ice. *Geophysical Research Letters*, *39*(8). https://doi.org/10.1029/2012GL051432

Perovich, D. K., & Richter-Menge, J. A. (2015). Regional variability in sea ice melt in a changing Arctic. *Philosophical Transactions of the Royal Society A: Mathematical, Physical and Engineering Sciences*, *373*(2045), 20140165. https://doi.org/10.1098/rsta.2014.0165

Perovich, D. K., Roesler, C. S., & Pegau, W. S. (1998). Variability in Arctic sea ice optical properties. *Journal of Geophysical Research: Oceans*, *103*(C1), 1193–1208. https://doi.org/10.1029/97JC01614

Perovich, D. K., Tucker III, W. B., & Ligett, K. A. (2002). Aerial observations of the evolution of ice surface conditions during summer. *Journal of Geophysical Research: Oceans*, *107*(C10), SHE 24-1-SHE 24-14. https://doi.org/10.1029/2000JC000449

Perovich, D., Meier, W. N., Tschudi, M., Farrell, S. L., Hendricks, S., Gerland, S., Haas, C., Krumpen, T., Polashenski, C., Ricker, R., & Webster, M. (2018). *Sea Ice* (Arctic Report Card 2018). https://www.arctic.noaa.gov/Report-card

Perovich, D., Smith, M., Light, B., & Webster, M. (2021). Meltwater sources and sinks for multiyear Arctic sea ice in summer. *The Cryosphere*, *15*(9), 4517–4525. https://doi.org/10.5194/tc-15-4517-2021

Petrich, C., & Eicken, H. (2017). Overview of sea ice growth and properties. *Sea Ice*, 1–41.

Petrich, C., Eicken, H., Polashenski, C. M., Sturm, M., Harbeck, J. P., Perovich, D. K., & Finnegan, D. C. (2012). Snow dunes: A controlling factor of melt pond

distribution on Arctic sea ice. *Journal of Geophysical Research: Oceans*, *117*(C9). https://doi.org/10.1029/2012JC008192

Polashenski, C., Perovich, D., & Courville, Z. (2012). The mechanisms of sea ice melt pond formation and evolution. *Journal of Geophysical Research: Oceans*, *117*(C1). https://doi.org/10.1029/2011JC007231

Rampal, P., Weiss, J., Dubois, C., & Campin, J.-M. (2011). IPCC climate models do not capture Arctic sea ice drift acceleration: Consequences in terms of projected sea ice thinning and decline. *Journal of Geophysical Research: Oceans*, *116*(C8). https://doi.org/10.1029/2011JC007110

Richter-Menge, J. A., & Farrell, S. L. (2013). Arctic sea ice conditions in spring 2009–2013 prior to melt. *Geophysical Research Letters*, *40*(22), 5888–5893. https://doi.org/10.1002/2013GL058011

Rösel, A., & Kaleschke, L. (2012). Exceptional melt pond occurrence in the years 2007 and 2011 on the Arctic sea ice revealed from MODIS satellite data. *Journal of Geophysical Research: Oceans*, *117*(C5). https://doi.org/10.1029/2011JC007869

Rösel, A., Kaleschke, L., & Birnbaum, G. (2012). Melt ponds on Arctic sea ice determined from MODIS satellite data using an artificial neural network. *The Cryosphere*, *6*(2), 431–446. https://doi.org/10.5194/tc-6-431-2012

Sallila, H., Farrell, S. L., McCurry, J., & Rinne, E. (2019). Assessment of contemporary satellite sea ice thickness products for Arctic sea ice. *The Cryosphere*, *13*(4), 1187–1213. https://doi.org/10.5194/tc-13-1187-2019

Scharien, R. K., & Yackel, J. J. (2005). Analysis of surface roughness and morphology of first-year sea ice melt ponds: Implications for microwave scattering. *IEEE Transactions on Geoscience and Remote Sensing*, *43*(12), 2927–2939. https://doi.org/10.1109/TGRS.2005.857896

Schröder, D., Feltham, D. L., Flocco, D., & Tsamados, M. (2014). September Arctic sea-ice minimum predicted by spring melt-pond fraction. *Nature Climate Change*, *4*(5), 353–357. https://doi.org/10.1038/nclimate2203

Schutz, B. E., Zwally, H. J., Shuman, C. A., Hancock, D., & DiMarzio, J. P. (2005). Overview of the ICESat Mission. *Geophysical Research Letters*, *32*(21). https://doi.org/10.1029/2005GL024009

Scott, F., & Feltham, D. L. (2010). A model of the three-dimensional evolution of Arctic melt ponds on first-year and multiyear sea ice. *Journal of Geophysical Research: Oceans*, *115*(C12). https://doi.org/10.1029/2010JC006156

Shu, Q., Wang, Q., Song, Z., Qiao, F., Zhao, J., Chu, M., & Li, X. (2020). Assessment of Sea Ice Extent in CMIP6 With Comparison to Observations and CMIP5. *Geophysical Research Letters*, *47*(9), e2020GL087965. https://doi.org/10.1029/2020GL087965

Shuchman, R. A., & Onstott, R. G. (1990). Remote sensing of the polar oceans. In *Polar oceanography, part A, Physical Science* (pp. 123–169). Academic Press, Inc.

Shupe, M. D., Rex, M., Dethloff, K., Damm, E., Fong, A. A., Gradinger, R., Heuze, C., Loose, B., Makarov, A., Maslowski, W., Nicolaus, M., Perovich, D., Rabe, B., Rinke, A., Sokolov, V., & Sommerfeld, A. (2020). The MOSAiC Expedition:

A Year Drifting with the Arctic Sea Ice. *Arctic Report Card*. https://doi.org/10.25923/9g3v-xh92

Simmonds, I. (2015). Comparing and contrasting the behaviour of Arctic and Antarctic sea ice over the 35 year period 1979-2013. *Annals of Glaciology*, *56*(69), 18–28. https://doi.org/10.3189/2015AoG69A909

Skyllingstad, E. D., Paulson, C. A., & Perovich, D. K. (2009). Simulation of melt pond evolution on level ice. *Journal of Geophysical Research: Oceans*, *114*(C12). https://doi.org/10.1029/2009JC005363

Smith, B., Fricker, H. A., Holschuh, N., Gardner, A. S., Adusumilli, S., Brunt, K. M., Csatho, B., Harbeck, K., Huth, A., Neumann, T., Nilsson, J., & Siegfried, M. R. (2019). Land ice height-retrieval algorithm for NASA's ICESat-2 photon-counting laser altimeter. *Remote Sensing of Environment*, *233*, 111352. https://doi.org/10.1016/j.rse.2019.111352

Smith, S. D., Muench, R. D., & Pease, C. H. (1990). Polynyas and leads: An overview of physical processes and environment. *Journal of Geophysical Research: Oceans*, *95*(C6), 9461–9479. https://doi.org/10.1029/JC095iC06p09461

Stroeve, J. C., Markus, T., Boisvert, L., Miller, J., & Barrett, A. (2014). Changes in Arctic melt season and implications for sea ice loss. *Geophysical Research Letters*, *41*(4), 1216–1225. https://doi.org/10.1002/2013GL058951

Stroeve, J. C., Serreze, M. C., Holland, M. M., Kay, J. E., Malanik, J., & Barrett, A. P. (2012). The Arctic's rapidly shrinking sea ice cover: A research synthesis.

Climatic Change, *110*(3), 1005–1027. https://doi.org/10.1007/s10584-011-0101-1

Stroeve, J., Holland, M. M., Meier, W., Scambos, T., & Serreze, M. (2007). Arctic sea ice decline: Faster than forecast. *Geophysical Research Letters*, *34*(9). https://doi.org/10.1029/2007GL029703

Stroeve, J., & Notz, D. (2018). Changing state of Arctic sea ice across all seasons. *Environmental Research Letters*, *13*(10), 103001. https://doi.org/10.1088/1748-9326/aade56

Studinger, Michael, & Linkswiler, Matthew. (2017). *IceBridge ATM L1B Elevation and Return Strength with Waveforms, Version 1* [Data set]. NASA National Snow and Ice Data Center DAAC. https://doi.org/10.5067/EZQ5U3R3XWBS

Tilling, R., Kurtz, N. T., Bagnardi, M., Petty, A. A., & Kwok, R. (2020). Detection of Melt Ponds on Arctic Summer Sea Ice From ICESat-2. *Geophysical Research Letters*, *47*(23), e2020GL090644. https://doi.org/10.1029/2020GL090644

Tsamados, M., Feltham, D., Petty, A., Schroeder, D., & Flocco, D. (2015). Processes controlling surface, bottom and lateral melt of Arctic sea ice in a state of the art sea ice model. *Philosophical Transactions of the Royal Society A: Mathematical, Physical and Engineering Sciences*, *373*(2052), 20140167. https://doi.org/10.1098/rsta.2014.0167

Tschudi, M. A., Curry, J. A., & Maslanik, J. A. (2001). Airborne observations of summertime surface features and their effect on surface albedo during FIRE/SHEBA. *Journal of Geophysical Research: Atmospheres*, *106*(D14), 15335–15344. https://doi.org/10.1029/2000JD900275

Tschudi, M. A., Maslanik, J. A., & Perovich, D. K. (2008). Derivation of melt pond coverage on Arctic sea ice using MODIS observations. *Remote Sensing of Environment*, *112*(5), 2605–2614. https://doi.org/10.1016/j.rse.2007.12.009

Tschudi, M. A., Meier, W. N., & Stewart, J. S. (2020). An enhancement to sea ice motion and age products at the National Snow and Ice Data Center (NSIDC). *The Cryosphere*, *14*(5), 1519–1536. https://doi.org/10.5194/tc-14-1519-2020

Tucker, C. J. (1979). Red and photographic infrared linear combinations for monitoring vegetation. *Remote Sensing of Environment*, *8*(2), 127–150. https://doi.org/10.1016/0034-4257(79)90013-0

Uttal, T., Curry, J. A., McPhee, M. G., Perovich, D. K., Moritz, R. E., Maslanik, J. A., Guest, P. S., Stern, H. L., Moore, J. A., Turenne, R., Heiberg, A., Serreze, M. C., Wylie, D. P., Persson, O. G., Paulson, C. A., Halle, C., Morison, J. H., Wheeler, P. A., Makshtas, A., Grenfeld, T. C. (2002). Surface Heat Budget of the Arctic Ocean. *Bulletin of the American Meteorological Society*, *83*(2), 255–276. https://doi.org/10.1175/1520-0477(2002)083<0255:SHBOTA>2.3.CO;2

Vermote, E., & Wolfe, R. (2021). *MODIS/Aqua Surface Reflectance Daily L2G Global 250m SIN Grid V061* [Data set]. NASA EOSDIS Land Processes DAAC. https://doi.org/10.5067/MODIS/MYD09GQ.061

Vihma, T. (2014). Effects of Arctic Sea Ice Decline on Weather and Climate: A Review. *Surveys in Geophysics*, *35*(5), 1175–1214. https://doi.org/10.1007/s10712-014-9284-0

von Albedyll, L., Haas, C., & Dierking, W. (2021). Linking sea ice deformation to ice thickness redistribution using high-resolution satellite and airborne observations. *The Cryosphere*, *15*(5), 2167–2186. https://doi.org/10.5194/tc-15-2167-2021

Wang, M., & Overland, J. E. (2012). A sea ice free summer Arctic within 30 years: An update from CMIP5 models. *Geophysical Research Letters*, *39*(18). https://doi.org/10.1029/2012GL052868

Warren, S. G., Rigor, I. G., Untersteiner, N., Radionov, V. F., Bryazgin, N. N., Aleksandrov, Y. I., & Colony, R. (1999). Snow Depth on Arctic Sea Ice. *Journal of Climate*, *12*(6), 1814–1829. https://doi.org/10.1175/1520-0442(1999)012<1814:SDOASI>2.0.CO;2

Webster, M. A., Holland, M., Wright, N. C., Hendricks, S., Hutter, N., Itkin, P., Light, B., Linhardt, F., Perovich, D. K., Raphael, I. A., Smith, M. M., von Albedyll, L., & Zhang, J. (2022a). Spatiotemporal evolution of melt ponds on Arctic sea ice: MOSAiC observations and model results. *Elementa: Science of the Anthropocene*, *10*(1), 000072. https://doi.org/10.1525/elementa.2021.000072

Webster, M. A., Rigor, I. G., Perovich, D. K., Richter-Menge, J. A., Polashenski, C. M., & Light, B. (2015). Seasonal evolution of melt ponds on Arctic sea ice. *Journal of Geophysical Research: Oceans*, *120*(9), 5968–5982. https://doi.org/10.1002/2015JC011030

Webster, M., Rigor, I., & Wright, N. (2022b). Observing Arctic Sea Ice. *Oceanography*. https://doi.org/10.5670/oceanog.2022.115

World Meteorological Organization (WMO) (1970). Sea ice nomenclature. Geneva, Switzerland: Terminology, codes and illustrated glossary.No. 259.

Wright, N. C., & Polashenski, C. M. (2018). Open-source algorithm for detecting sea ice surface features in high-resolution optical imagery. *The Cryosphere*, *12*(4), 1307–1329. https://doi.org/10.5194/tc-12-1307-2018

Wright, N. C., Polashenski, C. M., McMichael, S. T., & Beyer, R. A. (2020). Observations of sea ice melt from Operation IceBridge imagery. *The Cryosphere*, *14*(10), 3523–3536. https://doi.org/10.5194/tc-14-3523-2020

Yan, J.-B., Gogineni, S., Rodriguez-Morales, F., Gomez-Garcia, D., Paden, J., Li, J., Leuschen, C. J., Braaten, D. A., Richter-Menge, J. A., Farrell, S. L., Brozena, J., & Hale, R. D. (2017). Airborne Measurements of Snow Thickness: Using ultrawide-band frequency-modulated-continuous-wave radars. *IEEE Geoscience and Remote Sensing Magazine*, *5*(2), 57–76. https://doi.org/10.1109/MGRS.2017.2663325

Zege, E., Malinka, A., Katsev, I., Prikhach, A., Heygster, G., Istomina, L., Birnbaum, G., & Schwarz, P. (2015). Algorithm to retrieve the melt pond fraction and the spectral albedo of Arctic summer ice from satellite optical data. *Remote Sensing of Environment*, *163*, 153–164. https://doi.org/10.1016/j.rse.2015.03.012

Zhang, J., Schweiger, A., Webster, M., Light, B., Steele, M., Ashjian, C., Campbell, R., & Spitz, Y. (2018). Melt Pond Conditions on Declining Arctic Sea Ice Over 1979–2016: Model Development, Validation, and Results. *Journal of Geophysical Research: Oceans*, *123*(11), 7983–8003. https://doi.org/10.1029/2018JC014298

Zhang, Z., Huisingh, D., & Song, M. (2019). Exploitation of trans-Arctic maritime transportation. *Journal of Cleaner Production*, *212*, 960–973. https://doi.org/10.1016/j.jclepro.2018.12.070